Title

Quasars Probing Quasars: The Circumgalactic Medium Surrounding z ~ 2 Quasars

Author

Lau, Marie Wingyee

Publication Date

2017

UNIVERSITY OF CALIFORNIA
SANTA CRUZ

QUASARS PROBING QUASARS: THE CIRCUMGALACTIC MEDIUM SURROUNDING $Z \sim 2$ QUASARS

A dissertation submitted in partial satisfaction of the
requirements for the degree of

DOCTOR OF PHILOSOPHY

in

ASTRONOMY AND ASTROPHYSICS

by

Marie Wingyee Lau

December 2017

The Dissertation of Marie Wingyee Lau
is approved:

Professor J. Xavier Prochaska, Chair

Professor Joseph F. Hennawi

Professor Graeme H. Smith

Dean Tyrus Miller
Vice Provost and Dean of Graduate Studies

Table of Contents

List of Figures

List of Tables

Abstract

Quasars Probing Quasars: The Circumgalactic Medium Surrounding $z \sim 2$ Quasars

by

Marie Wingyee Lau

Models of galaxy formation make the most direct predictions on gas related processes. Specifically, a picture on how gas flows through dark matter halos and onto galaxies to fuel star formation. A major prediction is that massive halos, including those hosting the progenitors of massive elliptical galaxies, exhibit a higher fraction of hot gas with $T \sim 10^7\,\mathrm{K}$. Another prediction is that some mechanism must be invoked to quench the supply of cool gas in massive systems. Under the current galaxy formation paradigm, every massive galaxy has undergone a quasar phase, making high-redshift quasars the progenitors of inactive supermassive black holes found in the center of nearly all galaxies. Moreover, quasars clustering implies $M_{\mathrm{halo}} \approx 10^{12.5}\,\mathrm{M}_{\odot}$, making quasar-host galaxies the progenitors of present day, massive, red and dead galaxies.

The Quasars Probing Quasars survey is well-suited to examine gas related processes in the context of massive galaxy formation, as well as quasar feedback. To date the survey has selected 700 closely projected quasar pairs. To study the circumgalactic medium, a sub-sample of pairs with projected separation within 300 kpc at the foreground quasar's redshift are selected. From the first to seventh paper in the Quasars Probing Quasars series, the statistical results had been limited to covering fractions, equivalent widths, and without precise redshift measurements of the foreground quasars. Signatures of quasar feedback in the cool circumgalactic medium had not been identified. Hence, a sub-sample of 14 pairs with echellette spectra are selected for more detailed analysis. It is found that the low and high ions roughly trace each other in velocity structure. The H I and low ion surface densities decline with projected distance. H I absorption is strong even beyond the virial radius. Unresolved Lyα emission in one case and N V detection in another case together imply that a fraction of transverse sightlines are illuminated. The ionization parameter U positively correlates with impact parameter, which implies the foreground quasar does not dominate the radiation field. The circumgalactic medium is significantly enriched even beyond the virial radius, and has median [M/H] $= -0.6$. O/Fe is supersolar. No evolution in the total H column is found up to projected distance of 200 kpc, within which the median $N_{\rm H} \approx 10^{20.5}\,{\rm cm}^{-2}$. Within the virial radius, the mass of the cool CGM is estimated at $M_{\rm cool}^{\rm CGM} \approx 1.5 \times 10^{11}\,{\rm M}_\odot$. In two cases, detection of C II* implies electron density $n_{\rm e} > 10\,{\rm cm}^{-3}$. Motivated by the preliminary kinematic results from this high-resolution sample, kinematic analysis of 148 pairs with precise foreground quasar redshifts is performed. The background spectra of this sample are of low and high resolution. The mean absorptions in metals exhibit velocity widths $\sigma_v \approx 300\,{\rm km\,s^{-1}}$, however the large widths do not require outflows. The mean absorptions have centroids redshifted from the systemic redshift by $+200\,{\rm km\,s^{-1}}$. The asymmetry may be explained if the quasars are anisotropic or intermittent, and the gas is not flowing onto the galaxy.

Finally, several observational and theoretical lines of future inquiry using multiwavelength data are presented.

To the brilliant scientist and human,

whom I named myself after,

who had said, “Nothing in life is to be feared. It is only to be understood. Now it’s the time to understand more, so that we may fear less.”

Acknowledgments

Given my humble background, I must thank my hometown for providing me basic necessities and an education, without which I could not become a useful member of the society.

I thank the Department of Physics of the Chinese University of Hong Kong, for providing a solid training of mathematical and computational methods, as well as all-rounded development. I have learned the most from Prof. Kenneth Young, Dr. S.S. Tong, and Prof. M.-C. Chu. From them I have obtained career and personal development guidance. I am grateful for the alumni network in United States.

Before coming to UCSC, I was given a foretaste of astronomy research by Prof. Peng Oh of UC Santa Barbara, Prof. Kristian Finlator of New Mexico State University. Prof. Oh and Prof. Finlator, together with and Prof. Yuk L. Yung of Caltech, put trust in my potentials before I did. Prof. Yung's mentorship was crucial to my ability to navigate in US on my own later.

I am indebted to Prof. J. Xavier Prochaska for teaching me discipline by high standards and his own example, and for providing clear and target-oriented guidance and scientific expertise. During my more senior years when I have the opportunity to co-mentor undergraduate and high school students, I recall Prof. Prochaska's pedagogical approach and pass it on. I thank Prof. Joseph F. Hennawi of UC Santa Barbara, for his insightful and helpful input, and for pleasant scientific and personal conversations. Together, Prof. Prochaska and Prof. Hennawi have allowed me the opportunity to contribute to an important line of research. I thank Prof. Graeme Smith for financial and humanity support, and for broadening my horizon to near-field astronomy. I thank Prof. Enrico Ramirez-Ruiz for academic advising, and for broadening my horizon to transient events. I thank Prof. Puragra Guhathakurta for mentoring me to become a mentor myself.

I want to thank everyone else that has worked in UCSC Astronomy and UCO Lick. Within this community, I extend special thanks to Prof. Alexie Leauthaud, Prof. Ruth Murray-Clay, Prof. Constance Rockosi, Prof. Bruce Margon, Prof. Jean

Brodie, Prof. Greg Laughlin, Prof. Jessica Werk, Dr. Martin Gaskell, Dr. Zheng Cai, Dr. Marcel Neeleman, Dr. Nicolas Tejos, Dr. Robert da Silva, Dr. Song Huang, Dr. Yicheng Guo, Dr. Shawfeng Dong, Dr. Sijing Shen, Dr. Guillermo Barro, Dr. Ryan Cooke, Dr. Hassen Yesuf, Dr. Rosalie McGurk, Dr. Claire Dorman, Dr. Srikar Srinath, Prof. Fulai Guo, Dr. Peter Gao, Prof. Michael Line, Prof. Xi Zhang, Dr. Elinor Gates, Dr. Paul Lynam, Pavl Zachary, Wayne Earthman, Erik Kovacs, Shawn Stone, Donnie Redel, Matt Brooks, Dan Espinosa, Steve Allen, Patrick Maloney, Rion Parsons, Ramon Berger, Jenna Scarpelli, David Sugg, Maria Sliwinski, Camille Leibler, Tiffany Hsyu, Brittany Miles, Asher Wasserman, Platon Karpov, Namrata Roy, Diana Powell, Nicolas Fernandez, and Caitlin Johnson. In the broader Astronomy community, I want to thank Prof. George Becker, Prof. Jane Lixin Dai, Prof. Lancelot Kao, Dr. Kenny C. Y. Ng, Dr. Alessandro Sonnenfeld, Dr. George Becker, Dr. Taysun Kimm, Stephanie H. Ho, T.-K. Chan, (Kenny) King Lau, and Chi Po Choi. I thank the above people for the time we spent together, on top of collaboration.

I thank all the international scholars for tips on job and funding eligibility, and on navigating through the rules of United States. I also want to thank everyone who has contributed to this land of opportunity, where incremental progress is possible.

I thank the Graduate Student Housing community for five years of homely experience. My former house mates Daphne Gorman, Sara Nasab, Jianan Liu, Annalisa Cadonna, Eilin Francis, Meng Gu, and Jeremy Baumgartner, and the resident assistants Barrett Anderson and Jo Mazeika have taken care of me. I need to name a few personal friends outside of UCSC: my godsister Sprite Chu, my godbrother Clare S. Y. Huang, Cathie (Tsz Yan) So, Sze Ning Mak, Cheng Shan, and Shiori Sato. I am blessed to have my brother, Steven Chi Yung Lau the brilliant programmer-in-training, who has made the conscious decision to love me.

The text of this dissertation includes a reprint of the following previously published material: Lau, M. W., Prochaska, J. X., & Hennawi, J. F. 2016, ApJS, 226, 25, and a preprint of the following material submitted for publication: Lau, M. W., Prochaska, J. X., & Hennawi, J. F. 2017, submitted to ApJ. The co-author listed in the above papers directed and supervised the research which forms the basis for Chapter 2 and 3 of the dissertation.

Chapter 1

Introduction

1.1 Galaxies and their Supermassive Black Holes

1.1.1 Massive Galaxy Formation

Although some details of the astrophysical processes are not well understood, models of galaxy formation have converged on a standard picture about how gas flows through dark matter halos and onto galaxies to fuel star formation (for a review see Somerville & Davé 2015). It is predicted that a substantial reservoir of $T \sim 10^4\,\mathrm{K}$ cool gas is embedded within a $T \sim 10^7\,\mathrm{K}$ hot, diffuse, and virialized gas. Cosmological hydrodynamic zoom-in simulations have shown that the cool gas can be probed by absorption- and emission-line spectroscopy in the rest-frame ultraviolet (Fumagalli et al. 2011; Shen et al. 2013; Faucher-Giguère et al. 2010), and observational signatures of these cold flows have been reported (Johnson et al. 2015; Cantalupo et al. 2014; Hennawi et al. 2015). Another major prediction of the models is that massive halos, including those hosting the progenitors of massive elliptical galaxies or are members of a protocluster, exhibit a higher fraction of hot gas owing to greater virialization of the medium. Moreover, some mechanism must be invoked to quench the supply of cool gas to progenitors of present-day, massive, red and dead galaxies, leaving only a hot gas phase known as the intragroup or intracluster medium. Such quenching mechanism is likely to be "maintenance" radio-mode feedback from active galactic nuclei (for reviews see Fabian 2012; Heckman & Best 2014). Forward progress demands that one studies the physical state of gas on 10 kpc–1 Mpc scales, at the formation epoch of present-day massive galaxies.

The Quasars Probing Quasars survey is designed to examine these gas related processes, which are the most direct predictions from physical models of galaxy formation. Details of the experimental design will be presented in section 1.3.

1.1.2 Feedback from Supermassive Black Holes on Galaxies

Under the current galaxy formation paradigm, every massive galaxy has undergone a luminous quasar phase. High-redshift quasars are thus the progenitors of inactive supermassive black holes found in the center of nearly all spheroid-dominated, massive galaxies (for a review see Kormendy & Ho 2013). Moreover, luminous quasars demonstrate strong clustering that has been measured in various quasar surveys. Eftekharzadeh et al. (2015) found that at $z \approx 2.4$, when star-forming activity peaks, the projected autocorrelation function implies dark halo masses of $M_{\rm halo} = 10^{12.5}\,{\rm M}_{\odot}$. Thus quasar-host galaxies are the progenitors of the present-day, massive, red and dead galaxies. The physical processes that quench their star formation remain poorly constrained to date.

To test the cold-flow paradigm for any galaxies, the community has generally relied on absorption-line spectroscopy (e.g., Steidel et al. 2010; Tumlinson et al. 2013). This is because direct detection of the line-emission from diffuse gas in the interstellar medium and gaseous halo of galaxies is difficult far beyond the Local Group. At $z \sim 2$, under the diffuse UV background, the densest part of the intergalactic medium has a Lyα surface brightness of ${\rm SB}_{{\rm Ly}\alpha} \approx 10^{-20}\,{\rm erg\,cm^{-2}\,s^{-1}\,arcsec^{-2}}$ (Cantalupo et al. 2005), far below the sensitivity of current instruments.

However, besides the Quasars Probing Quasars survey, quasar absorption-line studies have provided little insight into the physical state of the gaseous halo surrounding the quasar-host galaxies. The reasons are twofold. Firstly, the large ionizing flux from a quasar photoionizes most of the hydrogen and highly photoionizes the metals in and around its host galaxy (e.g., D'Odorico et al. 2008; Misawa et al. 2007). Secondly, the absorbers detected along the line-of-sight to a quasar generally have poor distance constraints, making their interpretation difficult (e.g., D'Odorico et al. 2004).

The Quasars Probing Quasars survey probes gas transverse to a quasar detected in absorption in background sightlines. If the transvere proximity effect is suppressed relative to the line-of-sight proximity, then larger amounts of neutral hydrogen and low ions may be detected. Furthermore, transverse sightlines will provide one-dimensional distance information.

1.2 Optical and Near-infrared Spectroscopy Techniques

For the Quasars Probing Quasars survey, rest-frame UV transitions of the H I and metal ions in absorption in the background quasar spectra, are redshifted to the optical in the observer's frame. They are analyzed for the ionization state, chemical abundances, and baryonic budget of the circumgalactic medium. The Mg II emission of the foreground quasars are redshifted to the optical in the observer's frame, and the narrow nebular emission-lines [O III] 5007 and Hα are redshifted to the near-infrared. They are analyzed for the systemic redshift of the foreground quasars. The work that culminated in the eighth and ninth paper in the series employed the optical instruments Gemini/GMOS-N, Gemini/GMOS-S, Keck/ESI, Keck/HIRES, Keck/LRIS, LBT/MODS1, Magellan/MagE, Magellan/MIKE, and VLT/XSHOOTER, and the near-infrared instruments Gemini-N/GNIRS, Gemini/NIRI, Keck/MOSFIRE, Keck/NIRSPEC,

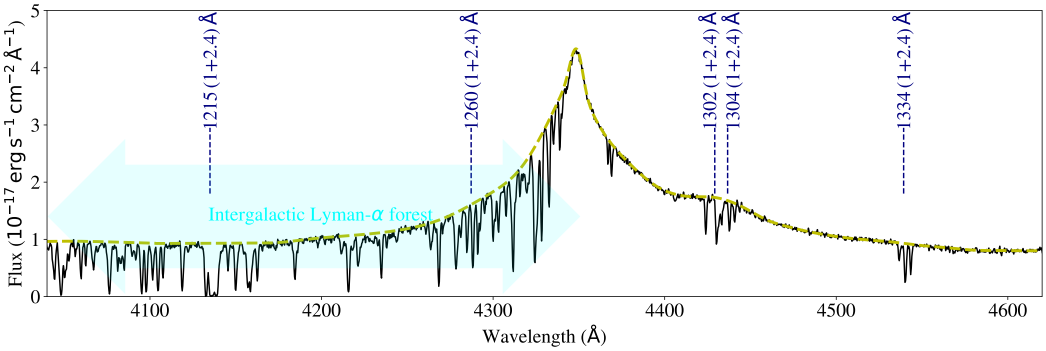

Figure 1.1 Spectrum of a typical quasar to illustrate absorption-line spectroscopy. The quasar is at redshift $z \sim 2.6$. The dashed line is an estimate of the continuum emission. The strong, broad emission is H I Lyman-α. Blueward of it are Lyman-α absorption-lines at different redshifts imprinted by intergalactic gas. There is one strong absorption system at $z \sim 2.4$ that absorbs at Lyman-α, Si II 1260, O I 1302, Si II 1304, and C II 1334.

Palomar/TripleSpec, and VLT/XSHOOTER.

To illustrate quasar absorption-line spectroscopy, a spectrum of a typical quasar is presented in Figure 1.1. The quasar has a redshift $z \sim 2.6$. The estimated continuum emission is shown. The strong, broad emission is H I Lyman-α. Blueward of it, there are many Lyman-α absorption-lines at different redshifts imprinted by intergalactic gas. There is one strong absorption system at $z \sim 2.4$. The system absorbs at its rest-frame Lyman-α, Si II 1260, O I 1302, Si II 1304, and C II 1334.

With absorption-line spectroscopy, if the line profile of an absorber is resolved, its column density and Doppler b-parameter can be modeled via Voigt profile fitting. If a line is only marginally resolved, a lower limit to its column density may be estimated by integrated the apparent optical depths over its velocity span (Savage & Sembach 1991), where the pixel optical depth is obtained from the normalized flux by $\tau(v) = -\ln(F(v)/F_{\text{continuum}})$. The strength of an absorption line is proportional to the oscillator of the transition and the column density of the absorber. For H I Lyman-α absorption, the curve-of-growth is linear for $N_{\text{HI}} \lesssim 10^{14}\,\text{cm}^{-2}$ and is logarithmic for $10^{14}\,\text{cm}^{-2} \lesssim N_{\text{HI}} \lesssim 10^{19}\,\text{cm}^{-2}$. For

$N_{\rm HI} \gtrsim 10^{19}\,{\rm cm^{-2}}$, damping wings become noticeable. Hence for $N_{\rm HI} \lesssim 10^{14}\,{\rm cm^{-2}}$ and $N_{\rm HI} \gtrsim 10^{19}\,{\rm cm^{-2}}$, reliable column density estimates may be obtained. If the Lyman limit at 912 Å is covered, another column density constraint may be obtained by assessing whether the absorber shows continuum opacity at the Lyman limit ("optically thick", $N_{\rm HI} \gtrsim 10^{17.3}\,{\rm cm^{-2}}$) or not ("optically thin", $N_{\rm HI} \lesssim 10^{17.3}\,{\rm cm^{-2}}$).

On the other hand, if an absorption-line system cannot be resolved into its individual lines, equivalent width may be calculated to quantify the absorption strength. The observed equivalent width is calculated from $W(\lambda_0) = (\lambda_0/c)\int_{-\infty}^{\infty}(1- F(v)/F_{\rm continuum})dv$, where λ_0 is the wavelength at the line center. The rest-frame equivalent width is calculated from the observed equivalent width divided by $(1+z)$.

Time variability of lines is an important diagnostic that will be used in future studies of quasar associated absorbers, that will be natural extension to the Quasars Probing Quasars survey. Time variability can be constrained from observing the same emitting or absorbing source in multiple epochs. The recombination time is inversely proportional to the electron density of a gas. Variability on time scale of years demands that the absorbing region is rather compact. For gas clumps intrinsic to a quasar, where high ions such as O VI are frequently detected and with absorption strengths that vary with time, the elctron density is typically $n_e > 5000\,{\rm cm^{-3}}$.

The line ratio of a doublet, in absorption or emission, is another important diagnostic that is used in the Quasars Probing Quasars survey, and will be used in future studies of quasar associated absorbers. The higher the optical depth ratio of the weaker line to the stronger line, the more optically thick is the gas producing the line transition. For absorption-lines, if the ratio of the weaker line to the stronger line is greater than permitted by the ratio of their oscillator strengths, then either there exists unresolved hidden saturation or there is partial coverage of the continuum-emitting source. The latter scenario in turn constrains the projected size of the absorber.

1.3 The Quasars Probing Quasars Experimental Design

The Quasars Probing Quasars survey [1] investigates massive galaxy formation and quasar feedback. It is an ongoing survey that selects closely projected quasar pairs from 10^6 quasars from the Sloan Digital Sky Survey, the Baryon Oscillation Spectroscopy Survey, and the 2dF Galaxy Redshift Survey. Pair candidates are followed-up and confirmed on 4m class telescopes. To date, the survey has confirmed ≈ 700 pairs to within 1 Mpc projected separation. The amount of observing time that has gone into this survey and the methodology is described in Prochaska et al. (2013a). Figure 1.2 is a cartoon showing the experimental design for using closely projected quasar pairs to study circumgalactic medium. The circumgalactic medium is loosely defined as the gaseous halo extending to 300 kpc from a galaxy, and is the site of interplay between gas accretion onto and gas flows from the galaxy. For each quasar pair, the line-of-sight to the background quasar is transverse to the foreground quasar at an impact parameter that is less than 300 kpc. The ionizing flux of the foreground quasar may not have an opening angle of 4π, and hence may not suppress the cool, $T \sim 10^4\,\mathrm{K}$ circumgalactic medium in the transverse direction. As the background sightline intercepts the gaseous halo surrounding the foreground quasar, strong absorption from low to intermediate ions are frequently detected in the background quasar spectrum that coincides with the foreground quasar's redshift.

Nine papers have resulted from the Quasars Probing Quasars survey. Before the work presented in the eighth and the ninth paper was performed, statistical inferences of the gas studied in absorption had been limited to low-resolution stacked spectra. The diagnostics had been limited to covering fractions, equiva-

---

[1] http://www.qpqsurvey.org

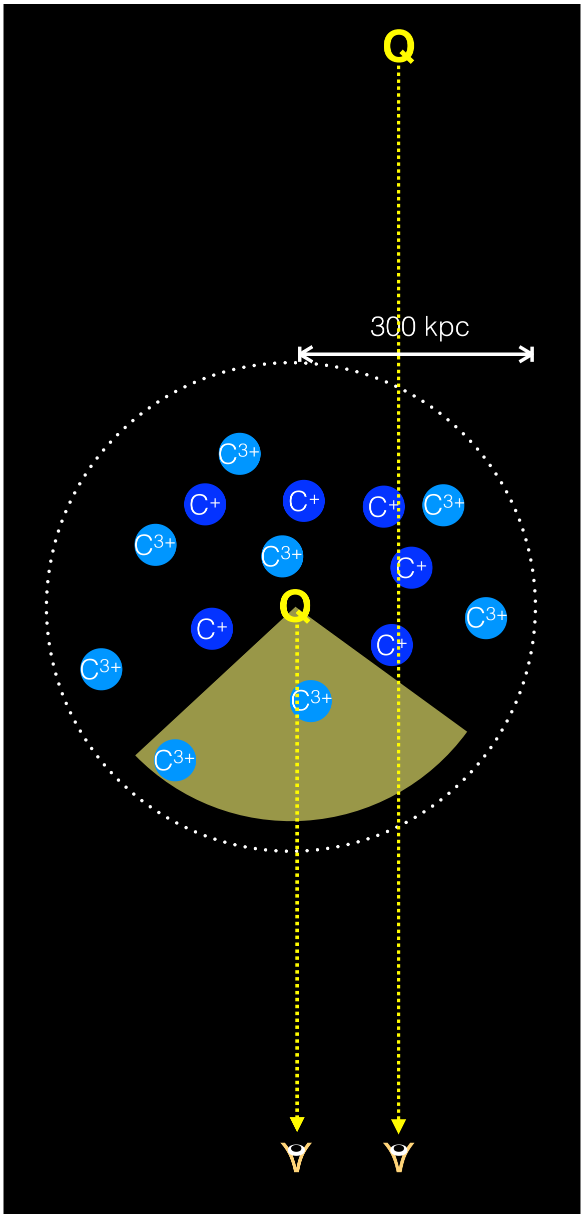

Figure 1.2 A cartoon showing the Quasars Probing Quasars experimental design for studying circumgalactic medium. The line-of-sight to the background quasar is transverse to the foreground quasar at a projected distance $< 300\,\mathrm{kpc}$. The ionizing flux of the foreground quasar may not have an opening angle that is wide enough to suppress the cool circumgalactic medium in the transverse direction. Strong absorption from low to intermediate ions are frequently detected in the background quasar spectrum near the foreground quasar's redshift.

lent widths, and without precise redshift measurements of the foreground quasars (Hennawi et al. 2006a; Hennawi & Prochaska 2007; Prochaska et al. 2013b,a). Exception to these limitations had been one quasar pair only, named J1204+0221. For this pair, a detailed analysis of the circumgalactic medium surrounding the foreground quasar is performed using an echelle, high signal-to-noise ratio spectrum of the background quasar, and a near-infrared spectrum of the foreground quasar for measuring the systemic redshift (Prochaska & Hennawi 2009). This quasar pair became the prototype for the eighth paper in the series. A Sloan Digital Sky Survey *gri* color composite image of the pair is shown in Figure 1.3. The background quasar has a systemic redshift $z_{\rm bg} \approx 2.5$, and the foreground quasar has a sytemic redshift $z_{\rm fg} \approx 2.4$. The pair is separated by 13.3", or a projected distance of 108 physical kpc at the foreground quasar's redshift.

The work presented in the first to seventh paper in the Quasars Probing Qusaars series suggests that the circumgalactic medium studied in the survey is different from that of the Lyman-break galaxies, which provoked questions about massive galaxy formation. Furthermore, the work presented in the first to seventh paper had yet to find signature of quasar feedback in the cool circumgalactic medium, which provoked questions about quasar feedback. The influence of a quasar on kpc scales is not so clear. Line-of-sight proximity supresses H I gas, enhances photoionization rate rate, and leads to greater abundance of highly ionized gas in N V and O VI. A transverse proximity effect would be the expected suppression in the Lyman-α forest opacity in the background sightline by the foreground quasar. This may not hold if the quasar is anisotropic or episodic.

A limitation of absorption-line analysis of transverse sightlines, regarding galactic scale flows, is the inherent symmetry of the experiment. One lacks constraint on the distance of the gas along the sightline. Positive or negative velocities may be interpreted as flow to or away from the system. Presented in the ninth paper in the series is a unique aspect of the Quasars Probing Quasars experiment that may break the symmetry in the velocity field of circumgalactic absorbers.

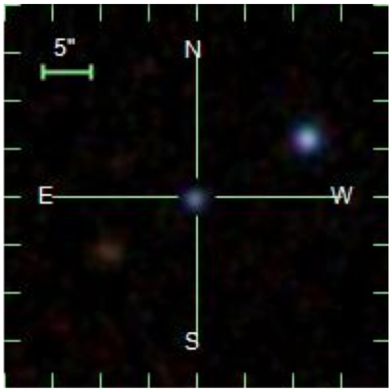

Figure 1.3 A Sloan Digital Sky Survey *gri* color composite image of the quasar pair J1204+0221 (Alam et al. 2015). The background quasar has a systemic redshift $z_{\rm bg} \approx 2.5$, and is unassociated with the foreground quasar that has a systemic redshift $z_{\rm fg} \approx 2.4$. The projected separation between the pair is 108 physical kpc at $z_{\rm fg}$.

1.4 Organization of the Thesis

This thesis is organized as follows.

Chapter 2 is a reprint of the paper "Quasars Probing Quasars VIII. The Physical Properties of the Cool Circumgalactic Medium Surrounding $z \sim 2$–3 Massive Galaxies Hosting Quasars" by Lau et al. (2016). This work employs echellette, optical spectra and low-resolution, near-infrared spectra, to analyze a statistical sample of 14 quasar pairs with projected separation $< 300\,$kpc. The results include ionization state modeling, chemical abundances, baryonic budget, peculiarities, and preliminary kinematics.

The content of Chapter 3 has been submitted as "Quasars Probing Quasars IX. The Kinematics of the Circumgalactic Medium Surrounding $z \sim 2$ Quasars" by Lau et al. to The Astrophysical Journal. This work employs low-resolution, optical and near-infrared spectra, to analyze 148 closely projected quasar pairs. Thee results are on precision kinematics and their interpretaton.

Chapter 4 summarizes the work that has been presented in this thesis, and concludes with future directions.

1.5 Acknowledgements

Funding for SDSS-III has been provided by the Alfred P. Sloan Foundation, the Participating Institutions, the National Science Foundation, and the U.S. Department of Energy Office of Science. The SDSS-III web site is http://www.sdss3.org/. SDSS-III is managed by the Astrophysical Research Consortium for the Participating Institutions of the SDSS-III Collaboration, including the University of Arizona, the Brazilian Participation Group, Brookhaven National Laboratory, Carnegie Mellon University, University of Florida, the French Participation Group, the German Participation Group, Harvard University, the Instituto de Astrofisica de Canarias, the Michigan State/Notre Dame/JINA Participation Group, Johns Hopkins University, Lawrence Berkeley National Laboratory, Max Planck Institute for Astrophysics, Max Planck Institute for Extraterrestrial Physics, New Mexico State University, New York University, Ohio State University, Pennsylvania State University, University of Portsmouth, Princeton University, the Spanish Participation Group, University of Tokyo, University of Utah, Vanderbilt University, University of Virginia, University of Washington, and Yale University.

Chapter 2

Quasars Probing Quasars: the Physical Properties of the Cool Circumgalactic Medium Surrounding $z \sim 2$–3 Massive Galaxies Hosting Quasars

We characterize the physical properties of the cool $T \sim 10^4\,\mathrm{K}$ circumgalactic medium (CGM) surrounding z ∼2–3 quasar host galaxies, which are predicted to evolve into present-day massive ellipticals. Using a statistical sample of 14 quasar pairs with projected separation < 300 kpc and spectra of high dispersion and high signal-to-noise ratio, we find extreme kinematics with low metal ion lines typically spanning $\approx 500\ \mathrm{km\,s^{-1}}$, exceeding any previously studied galactic population. The CGM is significantly enriched, even beyond the virial radius, with a median metallicity $[\mathrm{M/H}] \approx -0.6$. The α/Fe abundance ratio is enhanced, suggesting that halo gas is primarily enriched by core-collapse supernovae. The projected cool gas mass within the virial radius is estimated to be $1.9 \times 10^{11}\ \mathrm{M_\odot}\ (R_\perp/160\,\mathrm{kpc})^2$, accounting for $\approx 1/3$ of the baryonic budget of the

galaxy halo. The ionization state of CGM gas increases with projected distance from the foreground quasars, contrary to expectation if the quasar dominates the ionizing radiation flux. However, we also found peculiarities not exhibited in the CGM of other galaxy populations. In one absorption system, we may be detecting unresolved fluorescent Lyα emission, and another system shows strong N V lines. Taken together, these anomalies suggest that transverse sightlines are—at least in some cases—possibly illuminated. We also discovered a peculiar case where detection of the C II fine-structure line implies an electron density > 100 cm^{-3} and sub-parsec-scale gas clumps.

2.1 Introduction

The circumgalactic medium (CGM) is defined as the gaseous halo extending approximately 20–300 kpc from galaxies. It is the site of interplay between outflows from galaxies and accretion onto galaxies. Together these flows fuel, drain, heat, and enrich the CGM of dark matter halos. The impact of these processes on galaxy evolution and the enrichment of the intergalactic medium (IGM) remain open questions. The hot-phase CGM, or the intracluster medium, has been detected in X-rays at $z \lesssim 1$ from the halos of massive galaxy clusters (e.g. Mushotzky et al. 1996; Sato et al. 2007; Kravtsov & Borgani 2012). A warm-hot-phase CGM traced by O VI is also observed for individual galaxy halos (Tumlinson et al. 2011; Peeples et al. 2014). The cool-phase CGM, however, is typically too diffuse or low-mass to directly detect far beyond the Local Group (e.g. Oosterloo & van Gorkom 2005; Oosterloo et al. 2007). Instead, one is compelled to search in absorption using background sources whose sightlines pass close to foreground galaxies (e.g. Bergeron & Boisse 1991; Lanzetta et al. 1995; Chen et al. 2010; Prochaska et al. 2011).

Our understanding of the low-z CGM is greatly advanced by the COS-Halos survey. The survey presented a statistical sample of high-dispersion spectra that resolve the H I Lyman series and many diagnostic metal ion transition lines of the CGM surrounding L^* galaxies. The COS-Halos survey has demonstrated that, in addition to being a mediator for baryon recycling between galaxies and the IGM, the CGM also carries a significant portion of the baryonic budget of galaxy halos. Thus the CGM is essential in addressing the missing baryon problem in galaxy halos (Tumlinson et al. 2013; Werk et al. 2014).

In the low-z universe, outflows preferentially occur in star-forming galaxies with appreciable star formation rates (Martin 2005; Rupke et al. 2005; Rubin et al. 2014). At higher redshifts, when the star formation density is higher, these galactic winds occur for galaxies of a wide range in mass (Rubin et al. 2010; Steidel et al. 2010). The cold inflows onto galaxies are also predicted to be more important at higher redshifts as they feed and regulate the higher star formation rates (Kereš et al. 2005; Erb 2008). In addition, at $z \sim 2$–3, when both the universal star formation rate and the activitiy of active galactic nuclei (AGNs) peak, theories have predicted that quasar-driven outflows may couple with galaxy evolution by injecting heat into the CGM (Scannapieco & Oh 2004; Hopkins et al. 2008). Because of the difficulty in obtaining spectra of faint galaxies, previous studies of the CGM at high z have been largely confined to low-dispersion, stacked spectra (Adelberger et al. 2005a; Steidel et al. 2010; Crighton et al. 2011). Previous data obtained that are of sufficiently high quality for performing Voigt profile analysis have focused on modest samples of Lyman break galaxies (Simcoe et al. 2006; Rudie et al. 2012; Crighton et al. 2013, 2015; Turner et al. 2014).

It has been found the CGMs of Lyman break galaxies exhibit strong enhancement in metal ion absorption out to $\approx 200\,\mathrm{kpc}$ relative to the IGM average both in the transverse direction and in the line-of-sight direction to the galaxies. Because Lyman break galaxies inhabit dark matter halos $\lesssim 10^{12}$ $\mathrm{M}_\odot$ (Adelberger et al. 2005b), the majority of them are not predicted to evolve into the present-day, massive, "red and dead," elliptical galaxies. To study mechanisms for maintaining or quenching massive galaxy formation, one would preferably perform a similar experiment using background sightlines that pass close to more massive galaxies.

As a primary goal to assess the CGM of the most massive galaxies at $z \sim 2$–3, we have performed the "Quasars Probing Quasars" (QPQ) survey [1] to investigate the processes of massive galaxy formation. Quasars are bright and easily observed at cosmological distances. In an ongoing survey we select closely projected quasar pairs from $\sim 10^6$ quasars from SDSS, BOSS, and 2dF surveys (Bovy et al. 2011, 2012). We performed follow-up spectroscopy to confirm the pairs on 4 m class telescope including the 3.5 m telescope at Apache Point Observatory, the Mayall 4 m telescope at Kitt Peak National Observatory, the Multiple Mirror 6.5 m telescope, and the Calar Alto Observatory 3.5 m telescope. Our continuing effort to discover quasar pairs is described in Hennawi et al. (2006b, 2010). Detailed methodology of the QPQ experiment is described in Prochaska et al. (2013a, hereafter QPQ6). To date, we have confirmed ≈ 700 pairs to within 1 Mpc projected separation. In the series of QPQ papers, statistical inferences have generally been limited to results from low dispersion, stacked spectra, such as covering fractions and equivalent widths (Hennawi & Prochaska 2007; Prochaska et al. 2013b, 2014, hereafter QPQ2, QPQ5 and QPQ7). In the third paper of the QPQ series (Prochaska & Hennawi 2009, hereafter QPQ3), we have reported a detailed analysis of the CGM surrounding one foreground quasar, using spectra with echelle resolution, high signal-to-noise ratio. The previous QPQ studies, which suggested that properties of the CGM of QPQ are different from thosee of Lyman break galaxies, provoked questions about the physics of massive galaxy formation.

The previous QPQ studies have yet to find definitive signatures of quasar feedback in the cool CGM either. They provoked questions about the nature of quasar feedback. Quasars are the most luminous objects in the Universe and are thought to be powered by infall of matter onto a supermassive black hole at the center of a galaxy. On sub-kiloparsec scales, quasars may ionize and accelerate dense clumps of material, manifested as broad absorption line features (Weymann

---

[1] http://www.qpqsurvey.org

et al. 1991; Trump et al. 2006). Because of the enormous energy liberated by quasars, quasar feedback is often invoked on larger scales as the energy source that quench star formation in massive galaxies (Kimm et al. 2009; Lu et al. 2012) (but see Gabor et al. 2011).

The degree to which a quasar can influence its host galaxy on kiloparsec scales is less clear. The massive stars in the galaxy and the quasar may produce a significant flux of ionizing photons that would photoionize the surrounding gas on scales of at least tens of kiloparsecs. The line-of-sight proximity effect would suppress H I absorption along the line of sight to a quasar because of the enhanced photoionization rate in its vicinity, but may yield a greater abundance of highly ionized gas, manifested in, e.g., N V and O VI (Simcoe et al. 2002; D'Odorico et al. 2008; Tripp et al. 2008). The same may not hold for the transverse proximity effect, which is the expected suppression in Lyman-α forest opacity observed in another background sightline transverse to the quasar and is caused by the ionizing flux of the foregound quasar (Gonçalves et al. 2008). This will not occur if the quasar emits anisotropically due to obscuration effects in AGN unification models, where the accreting black hole is centered within a torus of dust and gas (Antonucci 1993), or if the quasar emits episodically in bursts of short duration (Croft 2004; Martini 2004; Hopkins et al. 2005). In Hennawi et al. (2006a, hereafter QPQ1), QPQ2 and Hennawi & Prochaska (2013, hereafter QPQ4), we discussed the transverse proximity effect as it applies to optically thick absorbers in the quasar environment, and argued that most of the optically thick systems observed in background sightlines are likely not illuminated by the quasar. These results are consistent with the results of complementary work done on $z \sim 1$ quasars using low-dispersion spectra of projected quasar pairs (Bowen et al. 2006; Farina et al. 2013, 2014; Johnson et al. 2015). They have revealed Mg II absorption in the CGM along the background sightlines coincident with the foreground quasar's redshift, of strengths consistent with the CGM surrounding non-quasar host galaxies of similar masses.

On the other hand, in the current galaxy formation paradigm, every massive galaxy has undergone a luminous quasar phase, making high-redshift quasars the progenitors of dormant supermassive black holes found in the center of nearly all bulge-dominated galaxies (Kormendy & Richstone 1995). Moreover, strong clustering of luminous quasars has been measured in various quasar surveys (e.g. Porciani et al. 2004; White et al. 2012). The recent work of White et al. (2012) found that at $z \approx 2.4$, when star forming activity peaks, the projected autocorrelation function takes the form $\xi_{\rm QQ} = (r/r_0)^{-1}$, where the correlation length $r_0 = 8.4\ h^{-1}$ comoving Mpc implies dark halo masses of $M_{\rm halo} \approx 10^{12.5}\ {\rm M}_\odot$. Thus quasar hosts are the progenitors of the present-day, massive, "red and dead" galaxies, whose physical processes that quench their star formation remain poorly constrained.

As we will frequently refer to other results from the QPQ series, we briefly review the methodology and the results of each paper. In QPQ1 (Hennawi et al. 2006a) we introduced a novel technique of using projected quasar pairs to study the physical state of the gas in $z \sim 2$–3 quasar environments. Spectroscopic observations of the background quasar in each pair reveal the nature of the IGM transverse to the foreground quasar on scales of tens of kiloparsecs to several megaparsecs. We searched 149 background quasar spectra for optically thick absorption in the vicinity of luminous foreground quasars, and found a high covering fraction to strong H I absorbers. In QPQ2 (Hennawi & Prochaska 2007) we compared the statistics of this optically thick absorption in background sightlines near the redshift of the foreground quasars to that observed along the line of sight to the foreground quasars. We found the clustering pattern of strong H I systems around quasars to be highly anisotropic, and we argued that the foreground quasars emit their ionizing radiation anisotropically or intermittently. In QPQ3 (Prochaska & Hennawi 2009) we presented an echelle spectrum of a projected quasar pair, which resolved the velocity field and revealed the physical properties of the gas at ≈ 100 kpc from the foreground quasar. This gas shows extreme kinematics, an enrichment exceeding 1/10 solar metallicity, and has a temperature $T \approx 10^4$ K. In QPQ4 (Hennawi & Prochaska 2013) we simultaneously studied the quasar CGM in absorption and emission. We found that quasar-powered Lyα fluorescence is generally absent from the absorbers observed in background sightlines, which implies that the foreground quasars do not illuminate the surrounding gas.In QPQ5 (Prochaska et al. 2013b) we used an enlarged sample of 74 closely projected quasar pair spectra to study the CGM of quasar host galaxies. We reported a covering fraction of $\approx 60\%$ to optically thick, metal-enriched gas within the virial radius ≈ 160 kpc. In QPQ6 (Prochaska et al. 2013a), with a sample enlarged to ≈ 650 quasar pairs, we confirmed that the high incidence of optically thick gas in excess of the IGM average extends to at least 1 physical Mpc transverse to the foreground quasars. The clustering found well exceeds CGM scales, which implies the gas may arise in large-scale structures. This enhanced H I absorption measured exceeds that of other galaxy populations, which is consistent with quasars being hosted by massive dark matter halos. In QPQ7 (Prochaska et al. 2014) we surveyed the incidence and absorption strength of metal line transitions. We found that the cool CGM around $z \sim 2$ quasars is the pinnacle amongst galaxies observed at all epochs, regarding covering fraction and equivalent width of H I Lyα and low ions.

To summarize, the QPQ series suggests a massive, enriched, and cool CGM surrounding massive galaxies at $z \sim 2$, despite the presence of a luminous quasar whose ionizing flux is sufficient to suppress the local H I Lyα opacity. Until recently, state-of-the-art cosmological (Meiksin et al. 2015; Rahmati et al. 2015) and zoom-in (Fumagalli et al. 2014; Faucher-Giguère et al. 2015) simulations of galaxy formation have had difficulties in reproducing the high covering fractions of optically thick gas seen in the QPQ work, even if one ignores quasar radiation. As explained in Faucher-Giguère et al. (2016), Rahmati et al. (2015) compared QPQ6 results with simulated halos that are typically more massive than the QPQ6 sample. We note the recent work Faucher-Giguère et al. (2016) were able to reproduce high covering fractions of optically thick gas in massive halos without invoking quasar feedback.

Questions raised by previous QPQ studies can be answered only if we can map the kinematics, ionization structure, relative chemical abundance patterns, the presence or absence of a hot collisionally ionized phase, and the volume density and size of the absorbing clouds, using a statistical sample of high dispersion spectra of high signal-to-noise ratio (S/N), which is the aim of the eighth paper in the series which forms the basis for this chapter. This chapter is summarized as follows. In Section 2.2, we describe the spectral data set that comprises QPQ8, including the criteria for selecting the subsample from the QPQ survey, the new observations and data reductions, and precise measurements of quasar redshift. In Section 3.3, we present the metal ion and H I absorption velocity profiles and their column density measurements, as we model of the ionization state of the absorption systems. In Section 2.4, we constrain the kinematics, the relative chemical abundances, the surface density profiles of the CGM gas, and the volume density and the linear size of the absorbers, and we discuss peculiarities of the QPQ8 sample compared to expectations for the $z \sim 2$ cool CGM surrounding quasars. In Section 4, we conclude with our key findings. In the Appendix, we describe our treatment of the self-blended C IV doublet in our kinematic analysis, and then we present figures and tables for the absorption associated with each of the foreground quasars in the sample. This is a lengthy chapter. The casual reader may wish to focus their attention on Section 2.4 which discusses the results and implications. Throughout this chapter we adopt a ΛCDM cosmology with $\Omega_M = 0.26$, $\Omega_\Lambda = 0.74$, and $H_0 = 70\,\mathrm{km\,s^{-1}\,Mpc^{-1}}$. All distances are proper unless otherwise stated.

2.2 Experimental Design

2.2.1 The QPQ8 Sample

The primary goal of this chapter is to conduct a detailed absorption line analysis of a statistical sample of CGM absorbers at proper impact parameters of 20–300 kpc from $z \sim 2$ quasars. The quasar pairs analyzed here are a subset of the sample studied previously for H I Lyα absorption and metal line absorption (C II and C IV) in QPQ6 and QPQ7 respectively. Imposed on this parent sample are selection criteria motivated by our detailed analysis of the quasar pair SDSSJ1204+0221 in QPQ3. We first required that the background quasar was observed with an echellette or echelle instrument, yielding a spectral resolution FWHM $\approx$ 60 km s^{-1} for echellette and $\approx$ 8 km s^{-1} for echelle. We further restricted the sample to those pairs where the average S/N at H I Lyα exceeds 9.5 per resolution element. Table 2.2 provides a summary of the basic specifications of different data sets, including spectral resolution, wavelength coverage, and S/N. Spectra of such quality roughly resolve the H I Lyman series and yield estimates of metallicity and relative chemical abundance to a precision of 0.3 dex, which would allow for the construction ofphotoionization models.

Together, these criteria imply a cut on the apparent magnitude of the background quasar of approximately 19.5 mag. We limited the selection to close quasar pairs with projected physical distance $R_\perp < 300$ kpc at the redshift of the foreground quasars to isolate the CGM. We imposed a cut on velocity difference between the redshifts of the two quasars > 3000 km s^{-1}, to avoid ambiguity in distinguishing absorption intrinsic to the background quasar from absorption associated with the foreground quasar. Finally, we required that the C II 1334 Å transition at the foreground quasar's redshift lie redward of the background quasar's Lyα forest, i.e. $(1+z_{\rm fg})1334.5323$ Å $>$ $(1+z_{\rm bg})1215.6701$ Å. By placing this metal transition outside of the Lyα forest, we ensure access to a suite of rest-frame far-UV diagnostics free from confusion with intergalactic Lyα absorption. This requirement

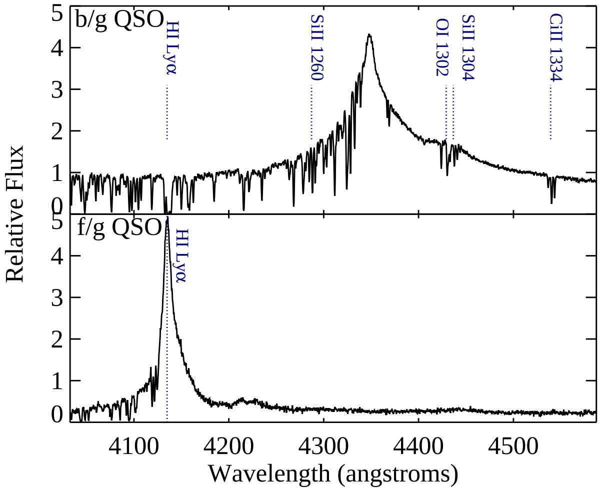

Figure 2.1 We show J0853−0011 as an example of a background-foreground quasar pair. Our line of sight to the background quasar is transverse to the foreground quasar at an impact parameter $R_\perp$, and intercepts its gaseous halo. The ionizing flux of the foreground quasar may or may not have an opening angle $< 4\pi$, and hence it may or may not suppress the cool CGM in the transverse direction. In the background quasar spectrum we see strong Lyα and metal ion absorption coincident with the foreground quasar's redshift.

corresponds to a relative velocity separation $\lesssim$ 20000–30000 $\mathrm{km\,s^{-1}}$. Figure 2.1 presents the spectra of J0853-0011 as an example of such a background-foreground quasar pair.

The final QPQ8 sample comprises 14 pairs. The observation journals and details related to data reduction and calibration of the 1D spectra are provided in QPQ6 and QPQ7. The spectra within the Lyα forest were previously continuum-normalized with an automated principal component analysis algorithm (Lee et al. 2012). To enable the search for weak absorption lines in our higher S/N QPQ8 sample, we here manually refitted the continua. We generated a high-order spline function that traces the obvious undulations and emission features of the background quasar. This analysis made use of the routine X_CONTINUUM, distributed as part of the XIDL software package.[2]

---

[2] http://www.ucolick.org/˜xavier/xidl

Table 2.1. QPQ8 Sample Summary

Name	FG Quasar	$z_{\rm fg}$	log L^a_{912}	log $L^b_{\rm bol}$	$g^c_{\rm UV}$	BG Quasar	$z_{\rm bg}$	$R_\perp$ (kpc)	θ^d (arcsec)
J0225+0048	J022517.68+004821.9	2.7265	30.33	46.34	535	J022519.50+004823.7	2.820	226	27.4
J0341+0000	J034138.15+000002.9	2.1233	29.92	46.07	274	J034139.19-000012.7	2.243	190	22.1
J0409−0411	J040955.87−041126.9	1.7155	30.34	46.42	516	J040954.21-041137.1	2.000	235	26.9
J0853−0011	J085358.36−001108.0	2.4014	29.82	45.86	645	J085357.49-001106.1	2.577	112	13.2
J0932+0925	J093226.34+092526.1	2.4170	30.27	46.31	402	J093225.60+092500.2	2.602	238	28.1
J1026+4614	J102618.80+461445.2	3.3401	30.79	46.79	1119	J102616.11+461420.8	3.421	288	37.1
J1038+5027	J103857.37+502707.9	3.1322	30.90	46.90	2069	J103900.01+502652.8	3.237	233	29.4
J1144+0959	J114435.53+095921.6	2.9731	30.63	46.55	1639	J114436.65+095904.9	3.160	189	23.5
J1145+0322	J114546.54+032236.7	1.7652	29.93	46.05	559	J114546.21+032251.9	2.011	139	15.9
J1204+0221	J120417.46+022104.7	2.4358	30.17	46.19	1424	J120416.68+022110.9	2.532	112	13.2
J1420+1603	J142054.42+160333.3	2.0197	30.58	46.54	4298	J142054.92+160342.9	2.057	104	12.0
J1427−0121	J142758.88−012130.3	2.2736	30.63	46.63	17964	J142758.73-012136.1	2.354	53	6.2
J1553+1921	J155325.60+192140.9	2.0098	29.70	45.81	3056	J155325.88+192137.6	2.098	44	5.1
J1627+4605	J162738.63+460538.3	3.8137	30.66	46.69	1222	J162737.24+460609.3	4.110	253	34.1

[a] Logarithm of the specific luminosity of the foreground quasar at the Lyman limit 912 Å, in unit of erg s^{-1} Hz^{-1}

[b] Logarithm of the bolometric luminosity of the foreground quasar, in unit of erg s^{-1} Hz^{-1}.

[c] The enhancement in flux relative to the extragalactic UV background, assuming that the foreground quasar emits isotropically and a distance equal to the impact parameter $R_\perp$.

[d] Angular separation between foreground and background quasars.

Table 3.1 lists the QPQ8 sample and summarizes key properties of the pairs and spectral data set. In cases where multiple spectra taken by different instruments covered the same transition, we gave preference to the higher-resolution spectra provided the S/N was sufficient. In terms of the spectral and photometric properties of the foreground quasar, the single sightline studied in QPQ3, J1204+0221, is unremarkable. J1204+0221FG has a systemic redshift of $z = 2.4358$, while the median of the QPQ8 sample is $z = 2.4$. J1204+0221FG has a bolometric luminosity of $10^{46.2}$ erg s^{-1}. Thus, J1204+0221 is representative of the larger statistical sample, and it is fair for us to rely on QPQ3 to form the selection criteria for QPQ8.

Table 2.2. QPQ8 Data Set Specifications

Name	BG Quasar Instrument	Resolution in FWHM ($\mathrm{km\,s^{-1}}$)	Wavelength Coverage (Å)	S/N per Å at Lyα at $z_{\rm fg}$
J0225+0048	ESI, GMOS	60, 125	3993–10556	76
J0341+0000	MagE	50	3044–10254	33
J0409−0411	MagE	62	3044–9459	15
J0853−0011	MagE	62	3042–10285	121
J0932+0925	MagE	51	3041–10284	74
J1026+4614	ESI	49	3994–10197	184
J1038+5027	ESI	48	3994–10197	70
J1144+0959	MIKE	9	3307–9167	205
J1145+0322	MagE	51	3042–10285	18
J1204+0221	HIRES	8	3448–6422	162
J1420+1603	MagE	51	3042–10285	74
J1427−0121	MIKE, MagE	8, 50	3309–9169	157
J1553+1921	MagE	51	3042–10285	33
J1627+4605	ESI	45	3989–10198	98

Table 2.3. Journal of Near-infrared Observations

Quasar	Observatory	Instrument	Date in UT	Exposure Time (s)	Line	$z_{\rm em}$	$\sigma(z_{\rm em})$ (km $\mathrm{s^{-1}}$)
J0341+0000FG	Keck	MOSFIRE	2014 Oct 1	960	Hβ	2.1233	272^a
J0409−0411FG	Keck	MOSFIRE	2014 Oct 1	960	Hα	1.7155	272^a
J0853−0011FG	Keck	NIRSPEC	2010 Jan 29	4800	[O III]	2.4014	44
J0932+0925FG	VLT	X-SHOOTER	2011 Apr 4	3600	[O III]	2.4170	44
J1038+5027FG	Gemini	NIRI	2006 May 9	4800	[O III]	3.1323	44
J1144+0959FG	Keck	NIRSPEC	2009 Jan 7	3000	[O III]	2.9731	44
J1204+0221FG	Gemini	GNIRS	2006 Mar 27	5440	[O III]	2.4358	44
J1420+1603FG	VLT	X-SHOOTER	2011 Apr 28	2400	Hα	2.0197	272^a
J1427−0121FG	Gemini	GNIRS	2006 Mar 12	7200	[O III]	2.2736	44
J1553+1921FG	VLT	X-SHOOTER	2007 Jul 17	2400	[O III]	2.0098	44
J1627+4605FG	Gemini	NIRI	2007 May 29	14400	[O III]	3.8137	44

[a] We quantified the uncertainties for Hα emission redshift and Hβ emission redshift to be 300 km $\mathrm{s^{-1}}$ and 392 km $\mathrm{s^{-1}}$ respectively. Hence when Mg II is detected, we adopted the Mg II emission redshift instead of the near IR redshift, for its smaller uncertainty of 272 km $\mathrm{s^{-1}}$.

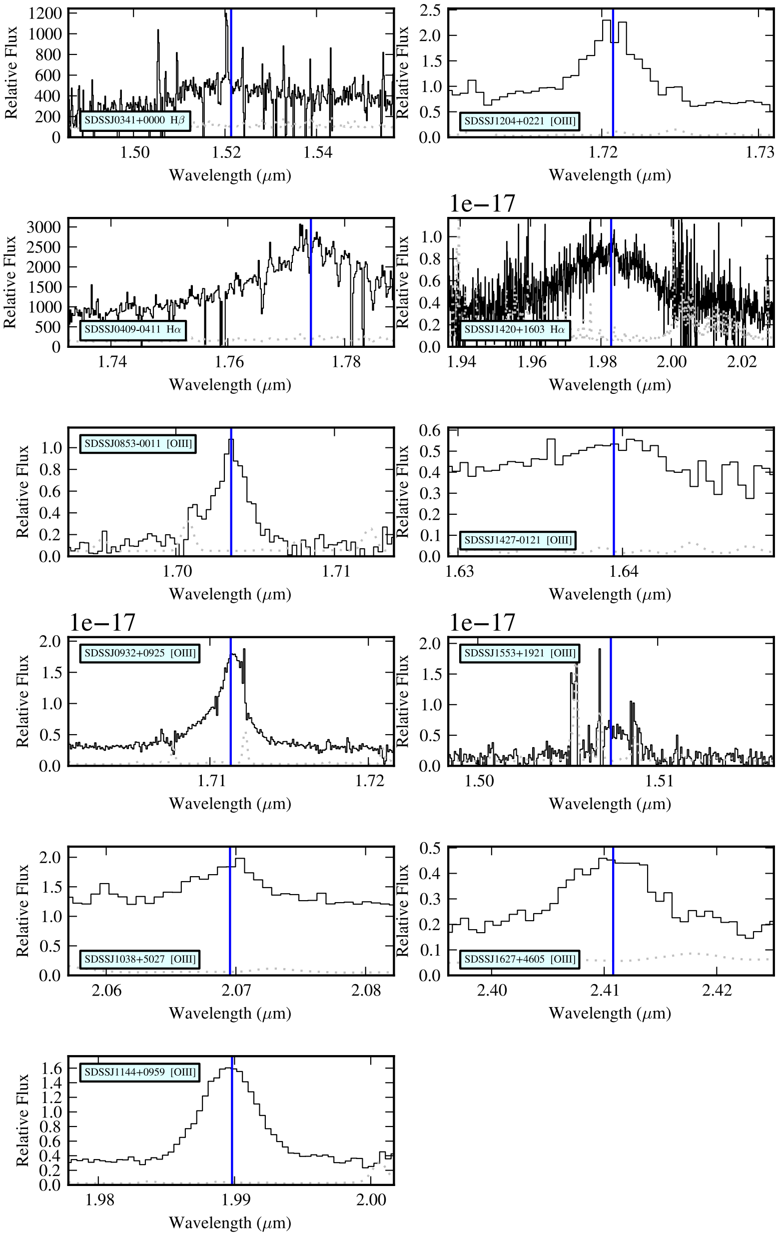

Figure 2.2 Near IR spectra of the foreground quasars for precisely determining the systemic redshift. The gray dotted curve is the 1σ uncertainty. We applied our custom algorithm for creating a centroid to the [O III] $\lambda5007$ emission line whenever it is present. When [O III] is not detectable we used Hα or Hβ. If no near IR data exists for the foreground quasar or no emission lines are found, we adopted the QPQ6 systemic redshift, which is obtained by fitting the full optical spectra.

2.2.2 Quasar Redshifts

The quasar emission redshifts $z_{\rm bg}$ were first taken directly from QPQ6. In QPQ6, the background quasar redshifts were taken from SDSS, while for the foreground quasars a custom line-centering algorithm was adopted to make a centroid of one or more rest-frame far-UV emission lines due to Mg II, [C III], Si IV and C IV. We iterated a flux-weighted, line-centering scheme until the centroid converged. Typical uncertainties range from $270\,{\rm km\,s^{-1}}$ to $790\,{\rm km\,s^{-1}}$. This precision is sufficient to define the QPQ8 sample. To establish a robust association of absorption with the foreground quasar, however, we desire the most precise assessment of its redshift $z_{\rm fg}$. Ideally, the uncertainties should be less than the peculiar motions of gas within the massive halos hosting quasars. This requires more precise measurements for $z_{\rm fg}$ than the QPQ6 results.

Our approach is to measure $z_{\rm fg}$ from rest-frame optical narrow forbidden emission lines such as [O III] $\lambda5007$, or the H I Balmer series. For $z \gtrsim 2$ quasars, these lines are shifted into the near infrared. These lines have smaller systematic uncertainties of $400\,{\rm km\,s^{-1}}$ or lower. [O III] has an average blueshift of $27\,{\rm km\,s^{-1}}$ and a dispersion of $44\,{\rm km\,s^{-1}}$ about this value (Richards et al. 2002; Boroson 2005). To account for this average shift due to the blue wing of the [O III] line, we added $27\,{\rm km\,s^{-1}}$ to the vacuum rest wavelength of 5008.24 Å when computing the redshift of the line. We have quantified the Hα and Hβ precision for an independent SDSS data set to be $300\,{\rm km\,s^{-1}}$ and $392\,{\rm km\,s^{-1}}$ respectively about the systemic value. We note that, in order to cover Hα in the optical, these SDSS quasars need to be at low redshift and hence are often not as luminous as the quasars in our QPQ sample. For fainter quasars, Hα is more peaked because of the narrow-line region, and hence the redshifts will be more accurate than for a luminous sample. We are not using these redshift uncertainties in a very quantitative manner, however. We observed 13 of the 14 foreground quasars using GNIRS (Elias et al. 2006) and NIRI (Hodapp et al. 2003) on the Gemini North telescope, NIRSPEC (McLean et al. 1998) on the Keck II telescope, and/or X-SHOOTER (Vernet et al. 2011) on the Very Large Telescope. Table 2.3 provides a journal of the near IR observations. When Mg II λ2800 is detected, the Mg II emission redshift is preferred over the Hα or Hβ emission redshifts for its smaller uncertainty of $272\,\mathrm{km\,s^{-1}}$. We have taken into account the median redshift of $97\,\mathrm{km\,s^{-1}}$ of Mg II from O III (Richards et al. 2002).

The X-SHOOTER spectra were reduced with a custom software package developed and kindly provided by George Becker, which includes nod sky subtraction on the slit and telluric corrections based on the European Southern Observatory SkyCalc sky model calculator (Noll et al. 2012; Jones et al. 2013; Moehler et al. 2014). Flat fielding of the detector was performed using dome flat exposures, and wavelength calibration of the near IR arm used night-sky emission features. Sky subtraction implements a two-dimensional b-spline algorithm and extraction was performed optimally. Significant residuals do persist at lines of the brightest sky emission. The remaining data were processed with algorithms in the LowRedux[3] package developed primarily by one of us (J.F.H.). The processes are similar to those for X-SHOOTER. The principal difference is sky subtraction, where the LowRedux algorithms first perform image subtraction of dithered (AB) exposures before fitting a b-spline to sky residuals. For all spectra, fluxing was performed with a telluric standard observed close in time and position on the sky to the scientific target.

In the following analysis, we omit the near-IR observations for (1) J1145+0322FG, whose Hβ λ4862 and [O III] λ5007 lines fall outside the transmitting infrared atmospheric windows. The emission line analyzed for redshift was Si IV, C IV, and C III, as described in QPQ6; (2) J0225+0048FG, whose Hβ λ4862, [O III] λ5007, and Hα are all redshifted to wavelengths of low atmospheric transmission. The emission lines analyzed for redshift were Si IV, C IV and [C III]. Although it has Mg II at observable wavelengths, it falls outside of our spectral coverage. (3) J1026+4614FG, whose Hβ λ4862 and [O III] λ5007 emission lines are weak and

---

[3] http://www.ucolick.org/∼xavier/LowRedux/index.html

yield redshift estimates that are inconsistent. The emission lines analyzed for redshift were Si IV and [C III]. This quasar too has Mg II at observable wavelengths but outside our coverage. For these sources, we adopted the $z_{\rm fg}$ measurements from QPQ6. Figure 2.2 presents the near IR spectra of the 11 foreground quasars with a near IR redshift measurement. We have analyzed these data with a custom algorithm that makes centroids of the emission lines and generates a best estimate for $z_{\rm fg}$. The results and adopted uncertainties are listed in Table 2.3.

2.3 Analysis

In this section, we present column density measurements for the gas associated with the foreground quasars in the QPQ8 sample. We begin with an analysis of associated metal line absorption, proceed to the H I analysis, and then describe ionization modeling of the systems. Details for the individual systems are provided in Appendix C. Here we describe the methodology and present representative examples.

2.3.1 Metals Absorption in Multiple Ionization States

We performed a search for associated metal line absorption within 1000 km s^{-1} of $z_{\rm fg}$. This search window allows for large peculiar motions in the gas, which may be common in the environments of these massive galaxies (e.g. QPQ3, Johnson et al. 2015). At the median $z_{\rm fg} = 2.4$ of our sample, this line-of-sight velocity window corresponds to 8 Mpc physical. We emphasize that systems of strong metal lines of equivalent width > 0.3 Å are rare in the intervening IGM along quasar sightlines and are dominated by C IV absorption. According to the calculations in QPQ7, the random incidence of C IV absorbers with equivalent width > 0.3 Å is 2.1 per unit redshift. QPQ6 measured a drop in H I equivalent width and QPQ7 measured a drop in C II and C IV equivalent width with impact parameter, especially at > 200 kpc. They suggest that the cool CGM gas is mostly contained near the central galaxy and argues against a large contribution from megaparsec scales. The positive detection of any such metals within 1000 km s^{-1} of $z_{\rm fg}$ is therefore unlikely to arise from gas at cosmological separations (see QPQ7 for further details). In Johnson et al. (2015), it was suggested that the CGM of neighboring galaxies of other host halos could contribute a significant portion of the Mg II absorption they observed around quasars. However, they plotted covering fractions due to all absorbers that fall within ±1500 km s^{-1}, which include contributions from galaxies that are actually within 300 kpc and hence are in the same host halo.

An absorption line system bearing heavy elements was detected in 12 out of 14 cases, an incidence that greatly exceeds random expectation. Furthermore, eight of these systems exhibit low ion transitions (e.g. C II λ1334), which occurs even more rarely in random sightlines. For complex profiles, metal ion absorptions well separated into distinct velocity intervals are grouped into subsystems A, B, C, etc, and are analyzed separately in what follows. Figure 2.3 shows the velocity profiles for the absorption associated with J0853$-$0011. The gas spans approximately 650 km s^{-1}, which we divided into three subsystems. Although multiple ionization states, e.g. C^{+} and C^{3+}, tend to have optical depth ratios that vary across velocity, they roughly trace one another in velocity structure.

For each subsystem associated with each foreground quasar, we measured the ionic column densities from commonly detected metal line transitions in CGM gas (e.g. Werk et al. 2013). For these measurements, we used the apparent optical depth method (AODM; Savage & Sembach 1991) which yields precise values for observations of high spectral resolution. For non-detections, we report 3σ upper limits on column densities, obtained by integrating over a velocity window that encompasses most of the apparent optical depths of a subsystem.

Line saturation, however, may affect the echellette spectra ($R_{\rm FWHM} \approx 6000$) and we conservatively report lower limits for cases where the minimum normalized flux is below ≈ 0.4. Metal absorption components are typically narrow,

< 10 km s^{-1}, which is evident in the three echelle spectra included in this study. In Appendix B we show that, where the minimum normalized flux is greater than 0.4, echellette quality spectra are sufficient for accurate column density measurements. Hence with our criterion on the normalized flux, using echellette quality spectra does not introduce systematic biases.

We verified that the velocity intervals of the subsystems are chosen in such a way that there is little apparent variation in the ionic ratios. The scientific results that involve assessing ionization do not sensitively depend on how many subsystems have been chosen, and we quote weighted average values of ionization parameter, chemical abundances, etc., for each quasar-pair absorption system in what follows. For one absorption system, J1427−0121, for which an echelle spectrum was obtained, we fitted Voigt profiles to the unsaturated metal absorption components as discussed in Appendix C. As expected for resolved lines, the total ion column densities recovered for each subsystem agree with measurements from integration of the apparent optical depths. In cases where there is no substantial ionization structure (as required for our subsystems), breaking down the absorption profile into individual components has limited scientific value. Uncertainties associated with ionization modeling and line saturation exceed the benefit gained from component-by-component fitting. Hence this study does not include a component-by-component analysis.

A brief description of each system, figures for the velocity plots, and tables of all line measurements are presented in Appendix C. Table 2.4 summarizes the integrated measurements for the QPQ8 sample.

2.3.2 Voigt Profile Modeling of the Lyman Series

For each system we measured the H I column density of the gas by modeling its Lyman series absorption. We have echellette or echelle resolution coverage of Lyα for every system. We also included higher-order Lyman series lines where the S/N estimated from the quasar continuum exceeds 5 per pixel. When the echellette or

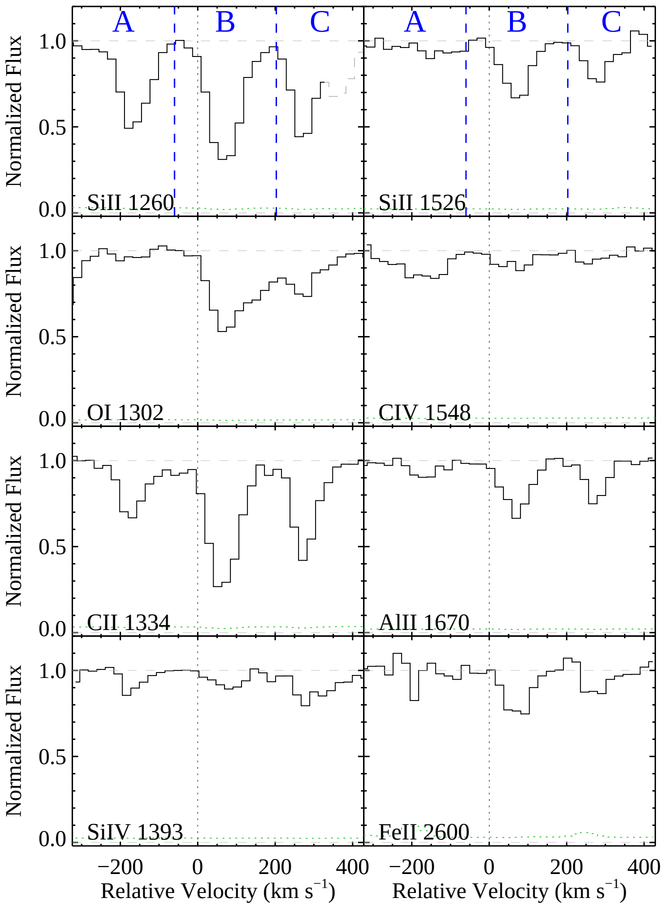

Figure 2.3 A subset of metal line transitions from the absorption associated with J0853−0011FG. The velocities are relative to the measured $z_{\rm fg} = 2.4014$. Absorptions well separated in distinct velocity intervals are designated as subsystems A, B, and C as denoted by the vertical dashed lines in the top subpanels. Absorption that is presumed to be unrelated to the foreground quasar, e.g. Lyα features from unrelated redshifts, is presented as dashed, gray lines. The gas shows multiple ionization states that roughly trace each other and span $\approx 650\,{\rm km\,s^{-1}}$. The green histogram shows the 1σ noise in the normalized flux.

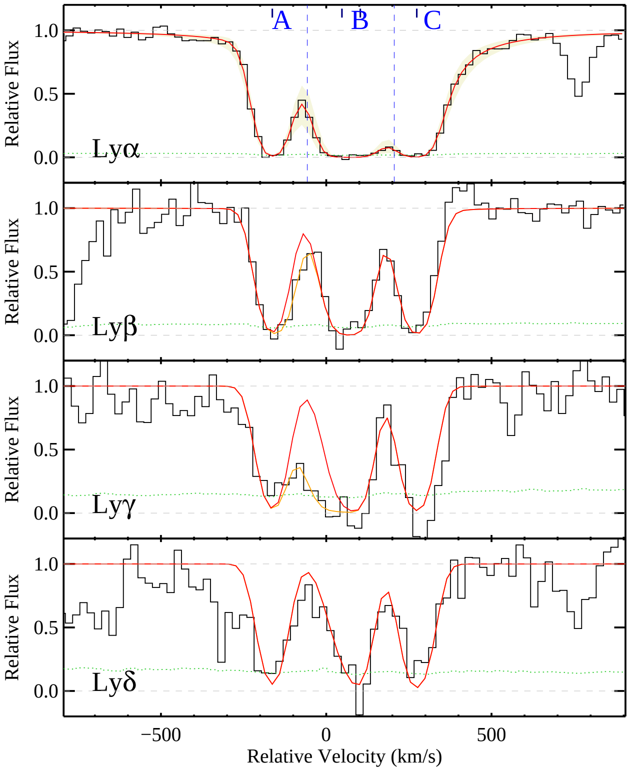

Figure 2.4 Example fit to H I Lyman series absorption profiles for J0853−0011. The black histograms show the Lyman series identified in the J0853−0011BG spectrum at velocities consistent with J0853−0011FG. The green dotted curves show the 1σ noise in the normalized flux. The relative velocity at $0\,\mathrm{km\,s^{-1}}$ corresponds to the redshift of J0853-0011FG. We performed Voigt profile modeling with χ^2 minimization to assess the H I column density. Specifically we introduced H I components centered at relative velocities traced by the peak optical depths of the associated set of metal ions. Note that in subsystem B there are two components. The navy ticks in the top subpanel mark the centroid redshifts for components traced by low ions. Figures of fits to Lyman series absorption for other QPQ8 systems, presented in Appendix C, will also show ticks that mark the centroids for components traced by high ions and ticks that mark H I components not associated with metal ions. Additional H I components introduced to model Lyα forest blending are omitted in the tick marks. The red curve is the summation of all H I components associated with J0853−0011FG, and the beige shades mark the estimated $\pm1\sigma$ errors in H I column densities. The orange curve is the summation of all H I components associated with J0853−0011FG and Lyα forest contamination.

echelle data do not cover blue enough wavelengths for these transitions, we also used lower dispersion data when available. For many of the systems the Lyman series lines are all saturated yet do not exhibit damping wings, i.e. the lines fall on the saturated portion of the curve of growth. A precise measurement of $N_{\rm HI}$ is therefore difficult and is degenerate with assumptions made about the component structure and Doppler b-values that one adopts in the modeling. Our general approach is to first set conservative bounds on $N_{\rm HI}$ based on a wide range of allowed Doppler parameters from $b = 15\,{\rm km\,s^{-1}}$ to $b = 60\,{\rm km\,s^{-1}}$. Such estimates are dependent, however, on the number of assumed components and their relative velocities.

We then performed Voigt profile modeling of the data by χ^2 minimization using the Absorption LIne Software (ALIS; Cooke et al. 2014). ALIS uses the MPFIT package (Markwardt 2009), which employs a Levenberg–Marquardt least-squares minimization algorithm, where the difference between the data and the model is weighted by the error in the data. We reduced the degrees of freedom by fixing the relative velocities of unblended H I components or H I components associated with metal absorption, preferably low ions, that show well matching velocity structures. The Doppler b parameter is allowed to vary freely between the values of $15\,{\rm km\,s^{-1}}$ and $60\,{\rm km\,s^{-1}}$, which are typical of the high-z Lyα forest (Kirkman & Tytler 1997). We adopted approximately the central $N_{\rm HI}$ values in the range of solutions allowed by ALIS that have nearly equivalent χ^2. Since possible damping wings of a Voigt profile may as well be explained by a weak component that is not introduced to the model, ALIS best-fit solutions tend to give biased high values. For this reason, our adopted $N_{\rm HI}$ and the ALIS best-fit $N_{\rm HI}$ values need not agree.

As an example, Figure 2.4 shows the Lyman series data and our fit for the J0853−0011 absorption system. For each subsystem we identified H I components at the velocities corresponding to the peak optical depths of its associated set of metal lines. The velocity centroids of H I components traced by low ions, e.g. C II and O I, are marked by navy ticks. In figures of Lyman series fits for other QPQ8 systems, presented in Appendix C, we also mark the centroids of H I components traced by high ions, primarily C IV, and centroids of H I components that have no associated metal ions. The red curve is the summation of all H I components associated with the foreground quasar, while the orange curve is the summation of all H I components associated with the foreground quasar and additional H I components introduced to model Lyα forest contamination.

From trial-and-error of introducing additional components in the modeling, we found that the possible presence of unresolved components introduces a systematic error of several tenths of 1 dex in the $N_{\rm HI}$ values. We also performed the same Lyman series modeling using a MagE spectrum of J1427$-$0121 and compared to the modeling results using the MIKE spectrum. We found that the best-fit $N_{\rm HI}$ values can be recovered within 1σ error, and hence spectra with echellette resolution does not introduce significantly larger errors than echelle spectra. Moreover we estimated a systematic error of ± 0.2 dex in the $N_{\rm HI}$ values due to quasar continuum placement. For H I components for which we did not fix the velocities, ALIS reported unphysically large uncertainties in $N_{\rm HI}$ values because of line blending when the uncertainties in the relative velocities of the components are large. The Voigt model parameters as well as the total $N_{\rm HI}$ of each absorption system and subsystems are tabulated in Table 2.21 in Appendix C. A detailed description of the model for each quasar pair is also presented in Appendix C.

2.3.3 Ionization Modeling: The Ionization Parameter U

As summarized in the previous subsections and presented in Figures 2.3 and 2.4, the CGMs of galaxies hosting quasars exhibit multiple ionization states (e.g. O^0, Si^+, S^{2+}, Si^{3+}), and the total H I column densities are generally less than $10^{19}\,{\rm cm}^{-2}$. Both of these observations imply a predominantly ionized gas. Even if the quasar's ionizing flux is not directly impinging on the gas (as we have previously argued in the QPQ series), the extragalactic ultraviolet background

(EUVB) may photoionize the medium, resulting in neutral fractions $x_{\mathrm{HI}} \ll 1$ (e.g. QPQ3). Therefore, we generated photoionization models for each of the systems exhibiting metal line absorption, to estimate x_{HI} and other physical properties of the gas. In the process, if we can make assumptions about the volume density of the gas or estimate it through fine-structure excitation lines, we may compare the intensity of the ionizing radiation field that produces the observed ionic ratios with the predicted flux of the quasar at the impact parameter of the sightline. In this way we may test the hypothesis of whether the nearby foreground quasars are shining on the gas.

There are two primary processes that produce an ionized gas: collisional ionization and photoionization. If we assume that the cooling function takes the form in Sutherland & Dopita (1993), the cooling time $t_{\mathrm{cool}} \lesssim 10^4$ yr is short for any reasonable density. A model where collisional ionization is the primary mechanism producing the observed ionic ratios would require a heat source to maintain the gas temperature in equilibrium. We therefore assumed that photoionization is the dominant mechanism for setting the ionization structure of the gas, and also the dominant source of heat. Furthermore we note that the analysis in QPQ3 shows that equilibrium solutions for collisional ionization with $T \sim 10^4\,\mathrm{K}$ give very similar results to the photoionization models presented here.

We calculated the ionization state of plane parallel-slabs with version 10.00 of the Cloudy software package last described by Ferland et al. (2013). The inputs to Cloudy are the N_{HI} of a subsystem, as modeled in the previous subsection, the total volume density (neutral plus ionized) n_{H} which we fix at a constant $0.1\ \mathrm{cm}^{-3}$, and an initial assumed metallicity $[\mathrm{M/H}] = -0.5\,\mathrm{dex}$. We then varied the ionization parameter $U \equiv \Phi / n_{\mathrm{H}} c$ where Φ is the flux of ionizing photons having $h\nu \geq 1$ Ryd, and iterated on [M/H] and U until the results converge. The results are largely insensitive to the choice of volume density because it is nearly homologous with U, but they do vary with metallicity because this affects the cooling rate of the gas. It is convenient to fix n_{H} and vary Φ, so that there is only one degree of freedom in the output, which is the ionization parameter. For these calculations, we assumed that the spectral shape of the extragalactic UV background field follows that computed by Haardt & Madau (2012) and we varied the amplitude. For radiation fields of $z \sim 2$ quasars at a few Ryd, the EUVB is very similar to a power-law spectrum $f_\nu \propto \nu^{-1.57}$. As the input U parameter changes, the Cloudy algorithm varies the number of gas slabs to maintain a constant $N_{\rm HI}$ at the input value. For optically thick systems the results are sensitive to the assumed $N_{\rm HI}$. Larger $N_{\rm HI}$ values imply more self-shielding of the inner regions, which in turn demand a more intense radiation field to explain the observed ionization states.

For each system, we considered a series of ionic ratios and a wide range of ionization parameters. Our analysis focused on multiple ionization states of individual elements, such as $\rm C^+/C^{3+}$ and $\rm Si^+/Si^{3+}$, to avoid uncertainties related to intrinsic abundance variations. We also considered ratios of low to high ion species of different elements for constraining U assuming solar relative abundances. We adopted a correspondingly higher uncertainty for such constraints.

Figure 2.5 presents the comparison of a series of Cloudy models with constraints from the ionic ratios of the three subsystems in J0853−0011. The observational constraints on the ionic ratios and the corresponding $\log U$ values are indicated by solid boxes, or arrows for lower or upper limits. The ionic ratios for these three subsystems can be described by a photoionization model with $\log U \approx -3.3$. Occasionally, the observational constraints are not fully consistent with a single U value, for example subsystem C of J0853−0011 shown in Figure 2.5. Although this inconsistency may suggest that the low and high ions arise in a multiphase or non-equilibrium medium, there are significant systematic uncertainties inherent to photoionization modeling, including the assumed spectral shape for the radiation field, the cloud geometry, and the atomic data. In such cases, we preferred constraints from ionic ratios that are more sensitive to U. For example, for subsystems of J0853−0011, observational constraints from

Table 2.4. Total Ionic Column Densities

QSO Pair	$z_{\rm fg}$	log $N(\rm C^+)$	log $N(\rm C^{+3})$	log $N(\rm O^0)$	log $N(\rm Si^+)$	log $N(\rm Si^{+3})$	log $N(\rm Fe^+)$
J0225+0048	2.7265	< 13.86	14.12 ± 0.02	...	< 12.76	13.39 ± 0.05	...
J0341+0000	2.1233	< 14.00	< 13.28	...	< 13.42	...	< 13.62
J0409-0411	1.7155	< 13.97	< 13.31	...	< 13.48	...	14.12 ± 0.08
J0853-0011	2.4014	> 14.11	13.25 ± 0.03	14.48 ± 0.01	13.36 ± 0.01	12.86 ± 0.03	13.01 ± 0.03
J0932+0925	2.4170	13.72 ± 0.11	13.93 ± 0.02	...	< 13.55	13.14 ± 0.04	< 13.19
J1026+4614	3.3401	< 13.14	13.43 ± 0.02	...	< 12.12	12.74 ± 0.04	...
J1038+5027	3.1323	< 13.38	14.08 ± 0.02	...	< 13.39	13.00 ± 0.10	...
J1144+0959	2.9731	> 13.26	> 13.84	13.16 ± 0.13	12.84 ± 0.03	> 13.06	13.25 ± 0.05
J1145+0322	1.7652	> 14.71	> 14.59	14.08 ± 0.14	13.97 ± 0.05	13.74 ± 0.03	13.53 ± 0.09
J1204+0221	2.4358	> 14.75	13.80 ± 0.01	> 14.46	> 14.27	13.06 ± 0.01	13.59 ± 0.04
J1420+1603	2.0197	> 14.22	> 14.12	> 14.61	13.25 ± 0.03	13.27 ± 0.03	13.59 ± 0.01
J1427-0121	2.2736	14.01 ± 0.02	14.40 ± 0.02	14.12 ± 0.03	12.75 ± 0.01	12.91 ± 0.03	< 12.58
J1553+1921	2.0098	> 14.92	14.57 ± 0.03	> 15.05	15.26 ± 0.14	13.82 ± 0.10	14.02 ± 0.03
J1627+4605	3.8137	< 13.17	13.63 ± 0.04	< 13.53	< 13.25	< 12.66	...

Note. — Total logarithmic column densities for the absorption associated with each QPQ8 pair. One should adopt a systematic uncertainty of 0.05 dex related to continuum placement.

$\rm C^+/C^{3+}$ and $\rm Si^+/Si^{3+}$ are preferred to $\rm Fe^+/Fe^{2+}$, and we adopted a U value that is between that constrained by $\rm C^+/C^{3+}$ and that by $\rm Si^+/Si^{3+}$. We then proceeded conservatively by allowing for a substantial error on U. The uncertainties in the adopted $\log U$ values in this study are set to be at least 0.3 dex. For J0853−0011, the adopted uncertainties in $\log U$ encompass constraints on U from all ionic ratios. The estimated U value will give a corresponding neutral fraction $x_{\rm HI}$ and a total hydrogen column density $N_{\rm H} \equiv N_{\rm HI}/x_{\rm HI}$. The error in the neutral fraction is roughly linear with the uncertainty in U for $\log U > -4$.

A discussion of the constraints and the results of ionization modeling for the individual absorption systems is presented in Appendix C. Figure 2.6 presents a scatter plot for all of the U values derived from the data set against the estimated H I column density. Despite the large uncertainties in the measurements, there is a statistically significant anticorrelation between U and $N_{\rm HI}$. A Spearman's rank correlation test rules out the null hypothesis at 99.99% confidence. This may be explained by either an increasing volume density $n_{\rm H}$ with increasing column density $N_{\rm HI}$ or a fixed volume density and a varying radiation field. In the latter

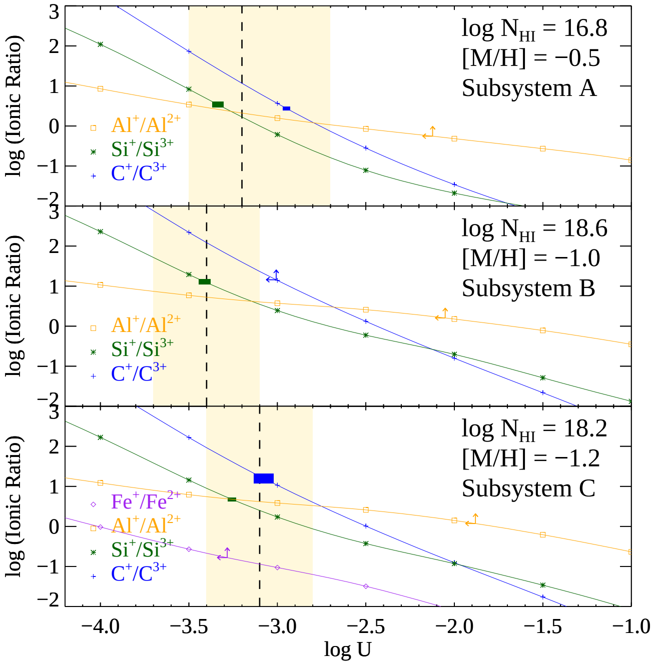

Figure 2.5 Cloudy example of constraining the ionization parameter $U = \Phi/n_{\rm H}c$ for J0853−0011, where Φ is the ionizing photon flux. This figure presents a comparison of a series of Cloudy models with constraints from the ionic ratios of the three subsystems A, B, and C. The observed ionic ratios and the corresponding $\log U$ are indicated by solid boxes, whose heights and breaths represent the 1σ uncertainties, or are indicated by arrows for lower or upper limits.

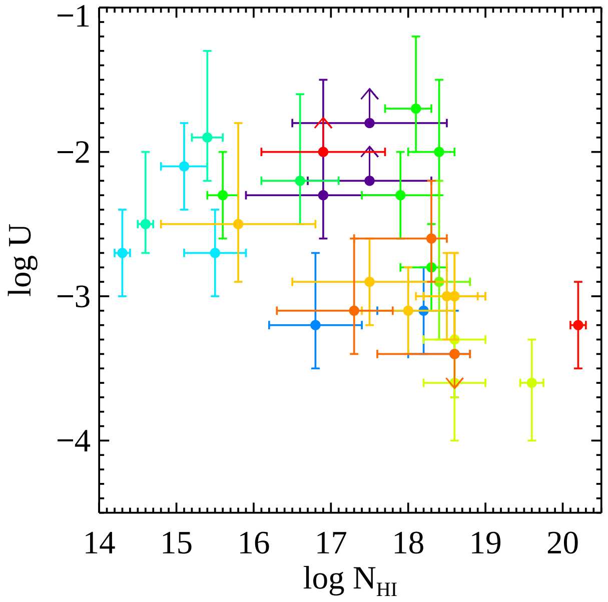

Figure 2.6 A scatter plot for all of the individual subsystems' U values against the estimated $N_{\rm HI}$. For clarity, subsystems associated with different quasars are coded in different colors. An anticorrelation is significant at $>99.99\%$ confidence.

case, when Φ decreases, U decreases and $N_{\rm HI}$ increases. This would be the scenario if there is gas with similar density at different distances or if there are illuminated and obscured systems.

Granted the focus of this chapter is on the cool CGM, we estimated a characteristic U value for each pair by weighting the U value of each subsystem by its corresponding $N_{\rm HI}$ value:

$$< U > \equiv \frac{\sum(U N_{\rm HI})}{\sum(N_{\rm HI})} \tag{2.1}$$

These values are listed in Table 2.5 together with the $N_{\rm HI}$-weighted neutral fractions $< x_{\rm HI} >$, and the individual constraints on U for each subsystem. We also derived $n_{\rm EUVB}$, the density one will require to give the $< U >$ value if the gas is illuminated only by an EUVB with normalization rescaled to match the mean opacity of the Lyα forest of Faucher-Giguère et al. (2008). We list the $n_{\rm EUVB}$ results in Table 2.5. In this scenario, one would require gas densities of 10^{-2} cm^{-3}

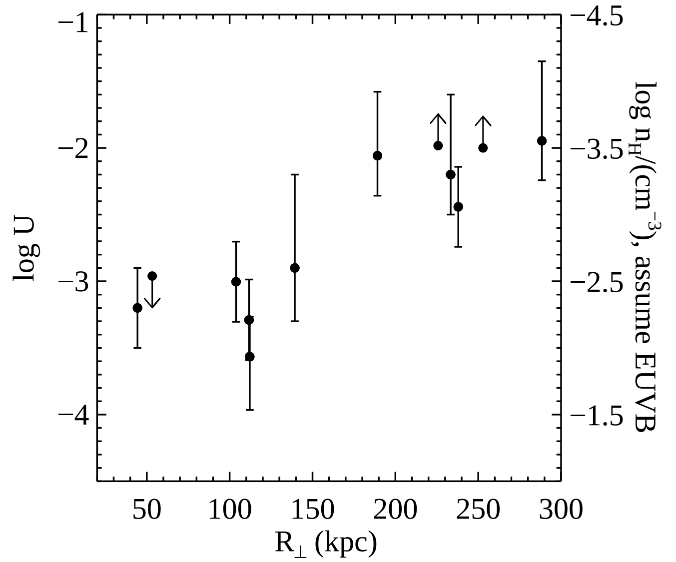

Figure 2.7 $< U >$ as a function of $R_\perp$. We estimated a characteristic average $< U >$ for each quasar-associated absorption system by weighting the U values of the subsystems by their $N_{\rm HI}$. The correlation between $< U >$ and $R_\perp$ is significant at 99.8% confidence. We also derived $n_{\rm EUVB}$, the density required to give $< U >$ if the gas is illuminated only by the extragalactic UV background and rescaled to match the mean opacity of the Lyα forest. These may be regarded as lower limits to the gas density.

or lower. These may be regarded as lower limits to the gas density. The results of n_{EUVB} together with $< U >$ as a function of the impact parameter $R_{\perp}$ are plotted in Figure 2.7. There is a statistically significant positive correlation between $< U >$ and $R_{\perp}$. A Spearman's rank correlation test rules out the null hypothesis at 99.8% confidence. This positive dependence of $< U >$ on $R_{\perp}$ runs contrary to expectation should the quasar dominate the ionizing flux received by the absorbers, unless the density profile is much steeper than that of n_{EUVB}. Moreover, we found no statistically significant correlation between U and quasar bolometric luminosity or the UV enhancement factor, again contrary to expectation if the quasar radiation dominates. The dependence of $< U >$ on $R_{\perp}$ further implies that n_{H} decreases with increasing $R_{\perp}$. This may also be explained as an increasing volume density with increasing neutral column density. Table 2.5 also lists n_{QSO}, the density required to yield $< U >$ assuming that the gas is located at a distance from the quasar equal to $R_{\perp}$ and that the quasar emits isotropically. We note that in QPQ2 we argued that the anisotropic clustering (i.e. transverse compared to line of sight) of optically thick absorbers around quasars suggests that most absorbers with $N_{\mathrm{HI}} \gtrsim 10^{17}\,\mathrm{cm}^{-2}$ detected in background sightlines are not illuminated by the foreground quasar, and we came to similar conclusions based on the absence of fluorescent recombination emission from these absorbers in QPQ4. The n_{QSO} values may be regarded as a rough upper bound to n_{H}, unless there is an extra local source of radiation, where the n_{H} values would need to be correspondingly higher as the U values are elevated. We discuss these values further in Section 2.4.4.

2.4 Results

2.4.1 Kinematics

We may precisely characterize the kinematics of the absorbing gas by Combining the high spectral resolution of the QPQ8 data set with our near-IR estimates

Table 2.5. Summary of physical conditions

Name	Subsystem	$\log U^a$	$\log <U>^b$	$\log <x_{\rm HI}>^c$	$\log n^d_{\rm EUVB}/{\rm cm}^{-3}$	$\log n^e_{\rm QSO}/{\rm cm}^{-3}$	$\log n^f_{\rm e}/{\rm cm}^{-3}$	Linear Size^g (pc)
J0225+0048	A	> -1.8	> -2.0	-3.4	-3.6	-0.8		
	B	$-2.3^{+0.8}_{-0.3}$						
	C	> -2.2						
J0853-0011	A	$-3.2^{+0.5}_{-0.3}$	-3.3	-1.2	-2.2	$+0.6$		
	B	$-3.4^{+0.3}_{-0.3}$						
	C	$-3.1^{+0.3}_{-0.3}$					< 0.9	> 3.8
J0932+0925	A	$-2.7^{+0.3}_{-0.3}$	-2.4	-2.8	-3.1	-0.5	< 1.8	> 0.01
	B	$-2.1^{+0.3}_{-0.3}$						
	C	$-2.7^{+0.3}_{-0.3}$						
J1026+4614	A	$-1.9^{+0.6}_{-0.3}$	-1.9	-3.3	-3.7	-0.6		
	B	$-2.5^{+0.5}_{-0.2}$						
J1038+5027	A	$-2.2^{+0.6}_{-0.3}$	-2.2	-3.3	-3.4	-0.1		
J1144+0959	A	$-1.5^{+0.3}_{-0.3}$	-2.1	-2.4	-3.5	-0.3		
	B	$-1.7^{+0.5}_{-0.3}$						
	C	$-2.8^{+0.3}_{-0.3}$						
	D	$-2.3^{+0.3}_{-0.3}$					< 1.3	> 11.2
	E	$-2.3^{+0.3}_{-0.3}$						
	F	$-2.0^{+0.5}_{-0.3}$					< 0.4	> 239.3
J1145+0322	A	$-2.9^{+0.7}_{-0.4}$	-2.9	-1.8	-2.6	$+0.1$	< 0.6	> 11.8
J1204+0221	A	$-3.3^{+0.3}_{-0.4}$	-3.6	-0.3	-1.9	$+1.2$		
	B	$-3.6^{+0.3}_{-0.4}$						
	C	$-3.6^{+0.3}_{-0.4}$					< 0.6	> 2.4
J1420+1603	A	$-2.5^{+0.7}_{-0.4}$	-3.0	-1.6	-2.5	$+1.1$		
	B	$-3.0^{+0.3}_{-0.3}$						
	C	$-3.1^{+0.3}_{-0.3}$						
	D	$-3.0^{+0.3}_{-0.3}$						
	E	$-3.0^{+0.3}_{-0.3}$						
	F	$-2.9^{+0.3}_{-0.3}$					2.2	0.17
J1427-0121	A	$-3.1^{+0.5}_{-0.3}$	< -3.0	-1.3	-2.5	$+1.7$		
	B	$-2.6^{+0.4}_{-0.3}$					< 0.7	> 23.5
	C	< -3.4					1.2	0.97
J1553+1921	A	$-3.2^{+0.3}_{-0.3}$	-3.2	-0.3	-2.3	$+1.2$	$< 2.5^h$	> 7.7
J1627+4605	A	> -2.0	> -2.0	-3.5	-3.7	-0.6		

[a] The ionization parameter U for each subsystem comes from Cloudy ionization modeling.

[b] The average ionization parameter $< U >$ for the absorption system associated with the foreground quasar is calculated as the U values of its subsystems weighted by their corresponding $N_{\rm HI}$ values.

[c] For each subsystem the estimated U will give a corresponding neutral fraction $x_{\rm HI}$. The average neutral fraction $< x_{\rm HI} >$ is calculated as the neutral fractions of the subsystems weighted by their $N_{\rm HI}$.

[d] The density required to give the $< U >$ value if the gas is illuminated only by the EUVB and rescaled to match the mean opacity of the Lyα forest.

[e] The density required to yield $< U >$ assuming that the gas is located at a distance from the quasar equal to the impact parameter and that the quasar emits isotropically.

[f] Electron volume density calculated from ratios of fine-structure excited state to ground state, under the assumption of collisional equilibrium.

[g] When the electron volume density is available, we estimated the linear size of the absorbing cloud from $\ell = N_{\rm H}/n_{\rm H}$, where $n_{\rm H} = n_e/(1 - x_{\rm HI})$, not compensating for the contribution of ionized helium to electron density.

[h] This is a damped Lyman α system and $n_{\rm HI}$ is reported instead of $n_{\rm e}$.

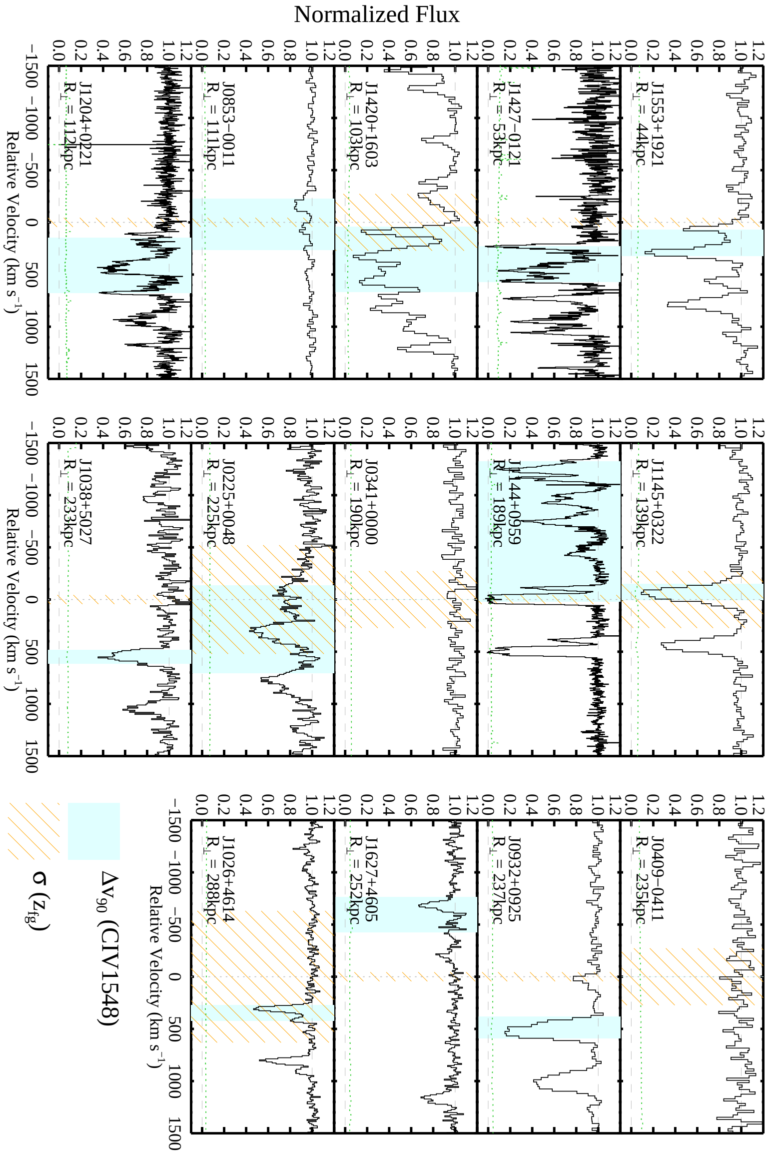

Figure 2.8 C IV $\lambda1548$ absorption profiles associated with the foreground quasars. The cyan shade encompasses 90% of the optical depth of the C IV $\lambda1548$ transition. The orange shade marks the 1σ uncertainty in $z_{\rm fg}$. When detected, the C II $\lambda1334$ profiles show similar velocity widths. The gas exhibits velocity widths ranging from $\approx 50\,{\rm km\,s^{-1}}$ to nearly $1500\,{\rm km\,s^{-1}}$. The centroids tend to occur within $500\,{\rm km\,s^{-1}}$. Significant absorption rarely occurs at negative velocities. The green histogram shows the 1σ noise in the normalized flux.

for $z_{\rm fg}$. Such measurements resolve the dynamics of the cool gas in the massive halos hosting quasars and constrain physical scenarios for the origin of this medium. In particular, one may search for evidence of non-gravitational motions, i.e. galactic-scale outflows powered by AGNs, that are regularly invoked as a critical process in galaxy formation theory (e.g. Faucher-Giguère & Quataert 2012).

In the following, we examine three statistical measures to characterize the kinematics: (i) the optical depth-weighted velocity offset of the gas relative to $z_{\rm fg}$:

$$\bar{\delta v} \equiv \frac{\sum\limits_i \tau_i \delta v_i}{\sum\limits_i \tau_i} \tag{2.2}$$

where f_i is the normalized flux and $\tau_i = -\ln(f_i)$ is the optical depth per pixel. In cases where the absorption saturates, we adopt a value equal to one half of the standard deviation in those pixels, $\sigma(f_i)/2$. This tends to limit τ_i to less than 4 per pixel; (ii) the velocity interval that encompasses 90% of the total optical depth, Δv_{90} (e.g. Prochaska & Wolfe 1997); (iii) the root mean square of the gas σ_v, measured from the optical depth weighted dispersion of the profiles. Figure 2.8 provides a qualitative picture of the kinematic characteristics. Plotted are the C IV doublets for the QPQ8 sightlines with $v = 0\,{\rm km\ s^{-1}}$ corresponding to $z_{\rm fg}$ for the C IV $\lambda1548$ transition. In each, we highlight the Δv_{90} interval relative to $z_{\rm fg}$. For the few absorption systems where Δv_{90} exceeds the velocity separation of the $\lambda\lambda\,1548, 1550$ doublet $\approx 500\,{\rm km\ s^{-1}}$, we estimated the kinematic measurements for C IV $\lambda1548$ as described in Appendix A. A few results are evident. First, the gas exhibits a dynamic range in the Δv_{90} widths ranging from $\approx 50\,{\rm km\ s^{-1}}$ to nearly $1500\,{\rm km\ s^{-1}}$. Second, the centroids of the absorption profiles tend to occur within $500\,{\rm km\ s^{-1}}$ of $z_{\rm fg}$. Third, significant absorption rarely occurs at negative velocities.

These results are further described in Figure 2.9 which presents the Δv_{90} and $\bar{\delta v}$ measurements for C II $\lambda1334$ and C IV $\lambda1548$ against impact parameter. These two ions generally exhibit similar kinematic characteristics, consistent with the high ionization fractions estimated for the gas. The Δv_{90} widths for the QPQ8 sample have median values of $555\,\mathrm{km\ s^{-1}}$ for C II and $342\,\mathrm{km\ s^{-1}}$ for C IV, and exhibit no strong correlation with $R_{\perp}$. These motions greatly exceed the values previously measured for gas tracing galaxies or CGM in absorption. This includes the damped Lyα systems, whose median Δv_{90} for low ion absorption $\approx 80\,\mathrm{km\ s^{-1}}$ and that for C IV $\approx 170\,\mathrm{km\ s^{-1}}$ (Prochaska & Wolfe 1997; Neeleman et al. 2013), and also the CGM of L^* galaxies in the low-z universe whose median $\Delta v_{90} \approx 100\,\mathrm{km\ s^{-1}}$ (Werk et al. 2013). Velocity widths exceeding several hundred $\mathrm{km\ s^{-1}}$ have only been routinely observed 'down-the-barrel' to star-forming galaxies and AGNs themselves, where one probes gas within the galaxy (e.g. Hamann 1998; Steidel et al. 2010). At present, the QPQ8 sample exhibits the largest velocity widths probed in absorption on CGM scales at any epoch. Existing studies that found large velocity spreads along transverse sightlines around galaxies are limited to single sightlines with most of the gas within a few hundred $\mathrm{km\,s^{-1}}$ (e.g. Tripp et al. 2011), or with gas tracing a higher ionization state (e.g. Churchill et al. 2012), or where the average velocity spread is smaller than that measured in QPQ8 (e.g. Gauthier 2013; Muzahid et al. 2015; Zahedy et al. 2016) or the velocity spreads are not well quantified (e.g. Johnson et al. 2015). We further emphasize that this result follows from the systematically large equivalent widths observed in the full QPQ sample (e.g. QPQ5, QPQ7). Therefore, despite the small sample size of QPQ8, we consider the distribution of large Δv_{90} values to be a statistically strong result.

The lower panel of Figure 2.9 shows the velocity offsets $\bar{\delta v}$ for the sample, restricted to absorption systems with precise Mg II or near IR measurements for $z_{\rm fg}$. The $\bar{\delta v}$ values range from $\approx -500\,\mathrm{km\ s^{-1}}$ to $\approx +500\,\mathrm{km\ s^{-1}}$ with rms values of 261 $\mathrm{km\ s^{-1}}$ and 408 $\mathrm{km\ s^{-1}}$ for C II and C IV respectively. The $\bar{\delta v}$ values frequently match or exceed the velocity width, implying that the absorption often occurs to only positive or negative velocities relative to $z_{\rm fg}$. Furthermore the $\bar{\delta v}$ values of our sample appear to preferentially exhibit positive values. For C IV,

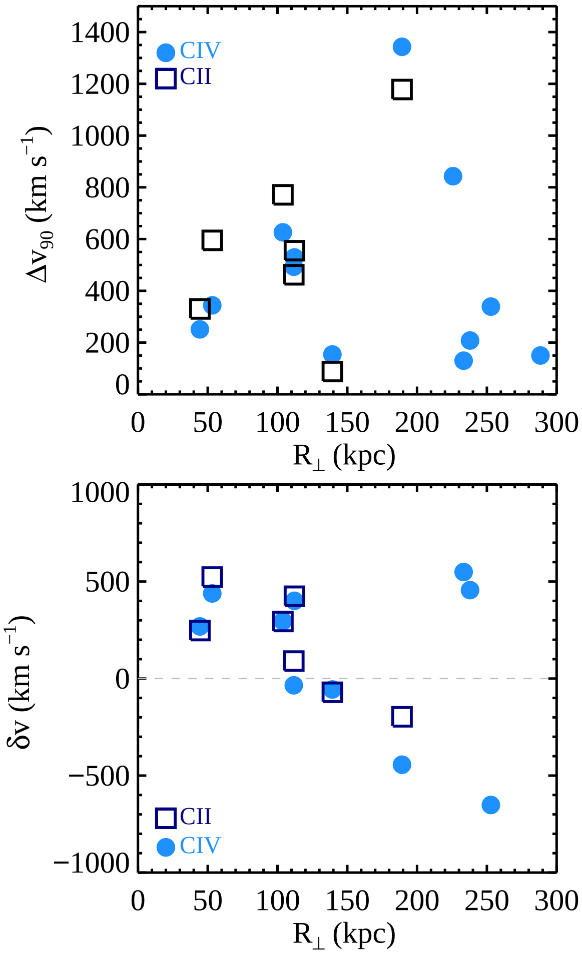

Figure 2.9 (Top) Measurements of the Δv_{90} statistic for low ion absorption (open squares) and high ion absorption (filled circles). The absorptions within $R_\perp \leq 200$ kpc show very large Δv_{90} values. This distribution exceeds all previous measurements for gas surrounding galaxies (e.g. Prochaska & Wolfe 1997; Neeleman et al. 2013; Werk et al. 2013). (Bottom) Velocity offsets $\bar{\delta} v$ between the optical depth-weighted centroid of the absorption profiles and the systemic redshift of the foreground quasar. The $\bar{\delta} v$ values typically match or exceed the Δv_{90} value, indicating that a majority of gas occurs at only positive or negative velocities relative to the systemic. In this small sample, there is an apparent bias to positive velocities.

only 2 of the 10 profiles have $\bar{\delta v} \ll 0\,\mathrm{km\ s^{-1}}$ and the median measurement is $+282\,\mathrm{km\ s^{-1}}$. Of course, the skewness of the $\bar{\delta v}$ distribution may be dominated by sample variance and therefore must be confirmed with a larger sample of pairs (see Lau et al. 2017, submitted; QPQ9). The result does follow, however, a reported asymmetry in H I in an independent quasar pair sample (Kirkman & Tytler 2008).

We further illustrate the kinematic characteristics of the gas by constructing the average optical depth profiles for the QPQ8 sample. We interpolated the apparent optical depth of each transition onto a fixed velocity grid with pixels of 25 km $\mathrm{s^{-1}}$ and normalized each to have a peak $\tau_i = 1$. We then performed a straight average of all the profiles. For systems where the C IV doublet self-blends, we estimated the optical depth of C IV $\lambda1548$ in the overlap spectral region from the unblended portions of the doublet. The details of the treatment are in Appendix A. Figure 2.10 shows the average optical depth profiles. These further emphasize the large velocity widths and the tendency toward positive velocities.

Taking the ensemble of QPQ8 data as a statistical representation of the CGM surrounding quasars, we may estimate the rms of the CGM surrounding quasars, σ_v from the average profile. Measuring this dispersion relative to the profile centroid, instead of $v = 0$ km $\mathrm{s^{-1}}$, we recovered $\sigma_v = 249\,\mathrm{km\ s^{-1}}$ for C II and $\sigma_v = 495\,\mathrm{km\ s^{-1}}$ for C IV. A large σ_v value for C IV is representative of the sample. Even if we take out the two sightlines with the largest velocity dispersion, i.e. J0225+0048 and J1144+0959, we still get $\sigma_v = 388\,\mathrm{km\ s^{-1}}$.

In QPQ3, we argued that the extreme kinematics of J1204+0221 ($\Delta v_{90} \approx 650\,\mathrm{km\ s^{-1}}$) could be consistent with the one-dimensional velocity dispersion of a massive dark matter halo. We assumed a dark matter halo mass of $10^{13.3}$ $\mathrm{M_\odot}$ and estimated a line-of-sight velocity dispersion of $\sigma_{\mathrm{1D}} \approx 431\,\mathrm{km\ s^{-1}}$ according to Tormen et al. (1997) and assuming a Navarro–Frenk–White (NFW) halo with concentration parameter $c = 4$. More recent analysis of quasar clustering prefers a lower typical mass ($10^{12.5}$ $\mathrm{M_\odot}$), giving $\sigma_{\mathrm{1D}} = 212\,\mathrm{km\ s^{-1}}$. At this mass scale, we

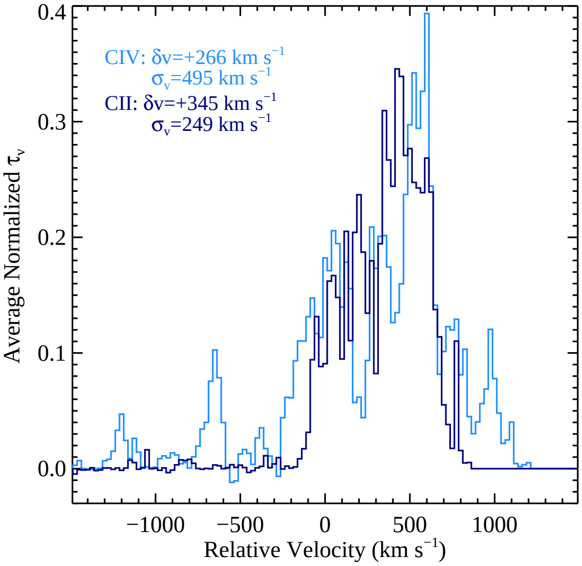

Figure 2.10 Average optical depth profiles of the QPQ8 sample, generated from the ensemble with each normalized to a peak optical depth of 1. These profiles stress the large velocity widths of the gas and also a peculiar bias toward positive velocity relative to systemic.

consider it improbable that the velocity widths we have observed are entirely virialized motions, and thus likely require non-gravitational kinematics i.e. outflows. Note that satellite galaxies within the halo should follow the potential and have a similar line-of-sight velocity dispersion. If galaxies clustered to the quasar host on larger scales also contribute to the observed velocity widths, the widths will partly represent Hubble flow of non-collapsed material. This scenario is rather unlikely, however, and the probability of intercepting a random optically thick absorber is only ≈ 4%, and clustering would only increase that to 24% according to QPQ6 (also see the discussion in Johnson et al. (2015)). We eagerly await advances in hydrodynamic simulations of massive $z \sim 2$ galaxies to explore these scenarios. The greatest challenge may for such feedback to manifest itself as cool, optically thick gas on CGM scales (Faucher-Giguère & Quataert 2012). Although Faucher-Giguère et al. (2016) are able to reproduce the high covering fraction of optically thick gas, their velocity fields are not extreme enough.

Recently, Johnson et al. (2015) have studied the CGM surrounding $z \sim 1$ quasars using QPQ techniques, and reported that 40% of the Mg II absorption occurs at radial velocities exceeding the expected average virial velocity $300\,\mathrm{km\ s^{-1}}$, which they interpret as quasar-driven outflows. For the QPQ8 sample, we found four out of seven C II systems and eight out of 10 C IV systems exhibit $\bar{\delta v}$ exceeding the one-dimensional virial velocity (see Figure 2.9). To allow a one-to-one comparison between our results and Johnson et al. (2015), we state that two out of seven C II systems and six out of 10 C IV systems exhibit $\bar{\delta v}$ exceeding 300 $\mathrm{km\,s^{-1}}$. This is consistent with Johnson et al. (2015), especially considering the higher random probability for C IV absorbers.

However, we caution that the mere presence of a few large kinematic offsets cannot be used to make the case against gravitational motions, unless the shift is of order $\sim$ 1000 $\mathrm{km\,s^{-1}}$, such as for the J1144+0959 absorption system of QPQ8. Clustering constrains only the average mass of the dark matter halos occupied by quasars, and not the distribution function. The distribution of halo mass occupation could be very broad or have significant tails, both of which could both give rise to occasional large velocity shifts, which would not require non-gravitational kinematics. (On a side note, despite the large velocity shift of the J1144+0959 absorption system from $z_{\rm fg}$, in Appendix C we demonstrated that it is likely the gas is physically associated with the quasar. For random incidence, the probability of finding one such strong C IV absorber is only 3%, with an even smaller probability for a C II absorber. Clustering would at most quadrupole this estimate.)

Moreover, the [O III] emission occasionally exhibits a significant blue-shifted tail relative to the systemic value defined by [O II] (see Figure 2.2). Systematic shifts from redshift errors of the order of $200\,\mathrm{km\,s^{-1}}$ are occasionally expected (Boroson 2005). A second caveat is that we used a mixture of [O III] and Mg II systemic redshifts, the latter being less accurate.

Now consider the putative bias to positive velocities that is apparent in Figure 2.10. Because the sightlines penetrate the entire halo, there is an inherent symmetry to the experiment. Both random velocity fields (e.g. random sampling of a virialized ensemble of CGM gas) and coherent velocity fields (e.g. outflow) will therefore yield symmetric absorption about $v = 0\,\mathrm{km\ s^{-1}}$. If the apparent asymmetry in Figure 2.10 is confirmed with a larger sample, one may require a non-dynamical process to provide the asymmetry. One possibility is an asymmetric radiation field that preferentially ionizes the gas moving toward the observer, i.e. where the quasar is known to shine. The quasar is obscured in the direction pointing away from us, and the gas observed in absorption lies preferentially behind the quasar and is shadowed. One may either interpret the redshift as an organized velocity field of flow away from the galaxy or interpret the velocity as a proxy for distance along the line of sight, as it would be if the material were in the Hubble flow and hence this asymmetry were to arise from a transverse proximity effect. There is no known case of a quasar shining only toward us, however. Another explanation is that, given the finite lifetime of quasar episodes, light from the background quasar may arrive at absorbers behind the foreground quasar before the ionizing radiation from the foreground quasar arrives. On the other hand, light from the background quasar will need to travel larger distances to reach the absorbers in front of the foreground quasar and will hence allow more time for the foreground quasar's radiation to reach and ionize them (see Figure 8 of Kirkman & Tytler 2008). We note, however, that Shen & Ho (2014) and Shen et al. (2016b) found a correlation between the fraction of total [O III] flux that is in the blueshifted wing and quasar luminosity. The putative redshift of absorbing components relative to the systemic value is subject to errors in redshift determination. We defer a more elaborated discussion to future papers that will focus on the kinematics. We are assembling a much larger sample of pairs with precise redshift measurements to better resolve this kinematic signature, using metal absorption lines to study on gas on CGM scales (QPQ9) and H I to probe gas on larger scales in the Lyα forest (Hennawi et al. 2017, in preparation).

2.4.2 Chemical Abundances

The frequent detection of metal line absorption in the CGM surrounding quasars, even at low spectral resolution (QPQ5, QPQ7), implies a significant enrichment of the gas in heavy elements. Quantitative estimates for the metallicity, however, require an assessment of the ionization state because the observed atoms in a given ionization state may comprise only a small fraction of the total hydrogen and metal column densities. Furthermore, high spectral resolution is necessary to precisely estimate the column densities and to assess line saturation. With the majority of the QPQ8 sample, we satisfy both of these requirements and may constrain the chemical abundances for a set of elements.

Consider first an estimate for the metallicity [M/H] of each pair in the QPQ8 sample, i.e. an assessment of the heavy element enrichment for the gas comprising the CGM. In what follows, we focus on the cool gas by emphasizing the subsystems that dominate the H I absorption in each pair. While the more highly ionized subsystems may have a large total column $N_{\rm H}$ (e.g. Crighton et al. 2013), these components are subject to greater uncertainties in the ionization modeling and may better track a more highly ionized phase that is physically distinct from the cool CGM. Therefore, we report average abundances by weighting the results of each subsystem by our $N_{\rm HI}$ estimate instead of $N_{\rm H}$. We have calculated [M/H] values weighted by $N_{\rm H}$ instead of $N_{\rm NHI}$, and found very similar values for each absorption system.

Although we have constrained ionization models for the majority of our sample, we emphasize that the data exhibit positive detections of the O I $\lambda1302$ transition for seven of the 14 pairs. In these cases, we may estimate [M/H] directly from the measured $\rm O^0/H^0$ ratio, i.e. $[{\rm O/H}] = \log N({\rm O}^0) - \log N_{\rm HI} - \epsilon_{\rm O} + 12$, where $\epsilon_{\rm O}$ is the solar abundance of oxygen on a logarithmic scale, with the expectation that ionization corrections are small. This assertion follows from the very similar ionization potentials of these atoms and the charge exchange reactions that couple their ionization for a range of physical conditions. When $N_{\rm HI} < 10^{19}\,{\rm cm}^{-2}$ or

$\log U > -2$, however, the O^0/H^0 ratio may underestimate [O/H], especially in the presence of a hard radiation field (e.g., QPQ3). In this respect, [O/H] estimated without any ionization correction provides a conservative lower bound to [M/H]. We are further motivated to focus first on oxygen because this element frequently dominates by mass and number among the heavy elements.

Roughly half of the systems showing O I detections have saturated profiles that yield only lower limits to [O/H]. For these cases we set an additional upper bound to [M/H] from our analysis of [Si/H]. We set the upper bound to [M/H] from the Si^+/H^0 measurements incremented by the 2σ uncertainty in the estimated ionization corrections. For systems where Si II absorption occurs in multiple subsystems, we adopt the $N_{\rm HI}$-weighted [Si/H] value to emphasize the cool gas that is expected to dominate the H I absorption. We found that [O/H] is often larger than [Si/H], and for cases where the [Si/H] value exceeds the lower limit from [O/H] we adopted the former. In one other case where the [O/H] estimate requires a large ionization correction, J1144+0959 (see below and Appendix C), [Si/H] is adopted for the metallicity estimate.

The resulting distribution of [M/H] for these seven systems, all of which have $N_{\rm HI} > 10^{18}\,{\rm cm}^{-2}$, is presented in Figure 2.11. All of the measurements exceed 1/10 solar and the median metallicity is -0.60 dex. This is a conservative value because three of the measurements are formally lower limits and because ionization corrections to O^0/H^0 would only increase [M/H]. Furthermore, the $N_{\rm HI}$ values estimated for these systems are more tightly bounded at the upper end by the absence of damping wings, and lower $N_{\rm HI}$ values would yield even higher [M/H]. We conclude that the cool CGM surrounding massive $z \sim 2$ galaxies hosting quasars has a median [M/H] of at least 1/3 solar.

There are four highly ionized systems at $R_\perp > 160$ kpc that offer estimates of the enrichment of the extended CGM from analysis of Si^{2+} (J0932+0925) or Si^{3+} (J0225+0048, J1026+4614, J1038+5027). In two of these cases, the estimates have uncertainties exceeding 1.0 dex because of poor constraints on the ionization state

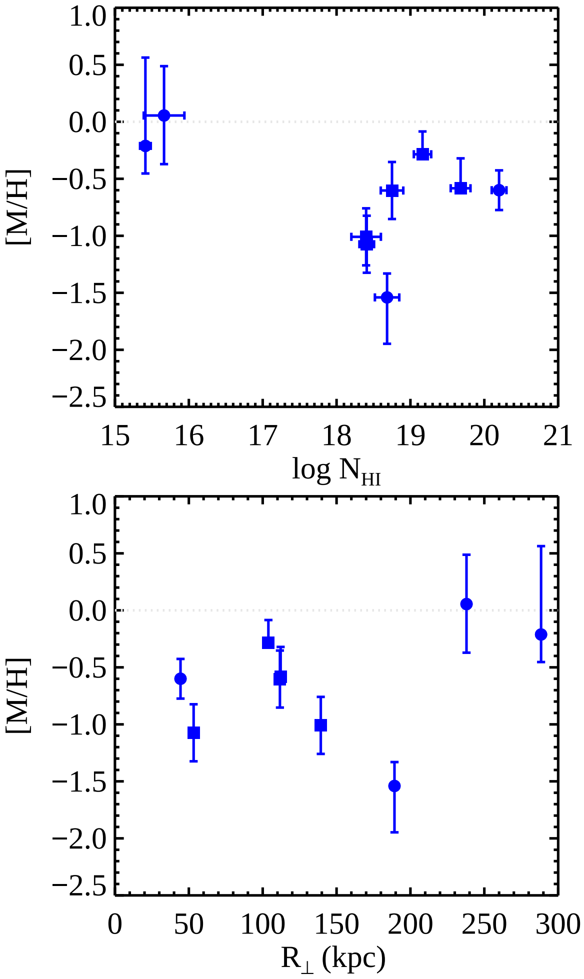

Figure 2.11 All metallicity estimates for the cool gas of the full sample, estimated from the O I, Si II, Si III or Si IV columns with ionization corrections from Cloudy. Estimations from O I are plotted with squares and estimations from Si ions are plotted with circles. All measurements exceed 1/10 solar and the median [M/H]$= -0.60$ dex. The measurements exhibit no correlation with $N_{\rm HI}$ or $R_{\perp}$. Significant enrichment exists even beyond the estimated virial radius of the host halos at $\approx$ 160 kpc. Note that in the [M/H] versus $R_{\perp}$ subplot there are two almost overlapping points at $R_{\perp} = 112$ kpc.

Table 2.6. Chemical Abundances

Quasar Pair	$\log N_{\rm HI}/{\rm cm}^{-2}$	[M/H]	[O/H]^a	[Si/H]^a	[Fe/H]^a	[C/H]^a	Comment
J0225+0048	18.9	$-1.5^{+1.0\,g}_{-1.0}$		$-1.5^{+1.0\,k}_{-1.0}$		$-2.8^{+9.8\,k}_{-1.1}$	$N_{\rm HI}$ very uncertain.
J0341+0000	16.6						No metals detected.
J0409-0411	14.2						No metals detected.
J0853-0011	18.8	$-0.6^{+0.2\,b}_{-0.2}$	$-0.6^{+0.2\,h}_{-0.2}$	$-1.0^{+0.3\,i}_{-0.6}$	$-1.4^{+0.2\,i}_{-0.6}$	$> -1.4^{i}$	
J0932+0925	15.7	$0.1^{+0.4\,f}_{-0.4}$		$0.1^{+0.4\,j}_{-0.4}$		$-0.0^{+0.7\,i}_{-0.8}$	
J1026+4614	15.4	$-0.2^{+0.8\,g}_{-0.2}$		$-0.2^{+0.8\,k}_{-0.2}$		$-0.5^{+0.5\,k}_{-0.4}$	
J1038+5027	16.9	$-1.5^{+0.8\,g}_{-0.5}$		$-1.5^{+0.8\,k}_{-0.5}$		$-1.6^{+0.9\,k}_{-0.7}$	U value very uncertain.
J1144+0959	18.7	$-1.5^{+0.2\,e}_{-0.4}$	$-1.9^{+0.2\,h}_{-0.2}$	$-1.5^{+0.2\,i}_{-0.4}$	$-0.3^{+0.9\,i}_{-0.6}$	$> -2.1^{i}$	
J1145+0322	18.4	$-1.0^{+0.2\,b}_{-0.2}$	$-1.0^{+0.2\,h}_{-0.2}$	$-1.1^{+0.4\,i}_{-0.4}$	$-0.8^{+0.6\,i}_{-0.4}$	$> -1.2^{i}$	
J1204+0221	19.7	$-0.6^{+0.3\,c}$	$> -0.6^{h}$	$> -0.7^{i}$	$-1.3^{+0.2\,i}_{-0.2}$	$> -1.0^{i}$	
J1420+1603	19.2	$-0.3^{+0.2\,c}$	$> -0.3^{h}$	$-1.0^{+0.4\,i}_{-0.4}$	$-0.9^{+0.4\,i}_{-0.4}$	$> -0.7^{i}$	
J1427-0121	18.4	$-1.1^{+0.2\,b}_{-0.2}$	$-1.1^{+0.2\,h}_{-0.2}$	$-2.1^{+0.2\,i}_{-1.3}$		$-1.7^{+0.2\,i}_{-1.4}$	
J1553+1921	20.2	$-0.6^{+0.2\,e}_{-0.2}$	$> -1.8^{h}$	$-0.6^{+0.2\,i}_{-0.2}$	$-1.7^{+0.1\,i}_{-0.1}$	$> 0.2^{i}$	
J1627+4605	16.9						Only C IV detected.

[a] Errors in abundances are propagated from errors in HI and metal ion column densities and errors in ionization parameter values.

[b] Adopted [O/H] from OI/HI values.

[c] Adopted [O/H] from OI/HI as lower limit, capped by [Si/H] measurement. See the main text for details.

[d] Adopted [O/H] lower limit. No QPQ8 systems match this case.

[e] Adopted [Si/H] from SiII/HI values with ionization corrections, including cases where [Si/H] > [O/H] lower limit. See the text.

[f] Adopted [Si/H] from SiIII/HI values with ionization corrections.

[g] Adopted [Si/H] from SiIV/HI values with ionization corrections.

[h] Using OI/HI as a proxy.

[i] Measured from the first ionization state of the element, with ionization corrections applied.

[j] Measured from the second ionization state of the element, with ionization corrections applied.

[k] Measured from the third ionization state of the element, with ionization corrections applied.

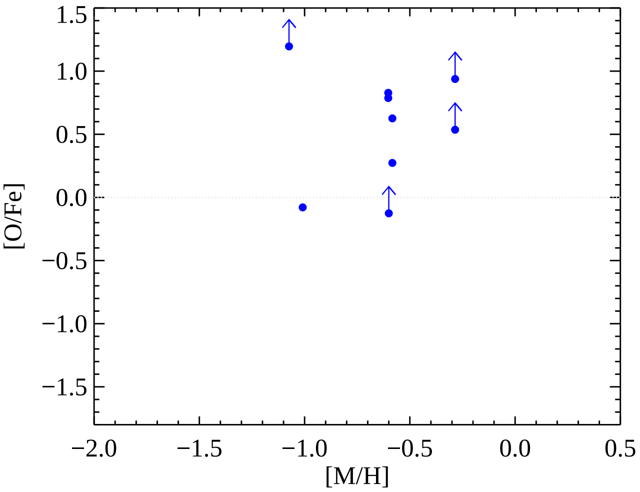

Figure 2.12 [O/Fe] estimates after adopting the ionization corrections to O^0/Fe^+. Nearly all measurements indicate supersolar O/Fe ratio, implying a significant fraction of the CGM surrounding quasars must have enhanced α/Fe abundance. Our findings suggest a star formation history similar to elliptical galaxies and a starburst that lasted less than 1 Gyr.

and/or $N_{\rm HI}$. These are not considered further. One other highly ionized system at $R_\perp > 160$ kpc (J1627+4605) exhibits only C^{3+} and is also not considered further. Lastly, two systems exhibit no positive detection of heavy elements (J0341+0000, J0409−0411). While this could reflect a very metal poor gas, the observed H I absorption is also very weak ($N_{\rm HI} < 10^{15}\,{\rm cm}^{-2}$), and the absence of heavy elements may simply reflect the absence of a substantial cool CGM along those sightlines.

Figure 2.11 shows all of these [M/H] estimates for the cool gas of the full QPQ8 sample, and Table 2.6 lists their values. The measurements exhibit no strong correlation with H I column density or impact parameter. Indeed, there is evidence for significant enrichment of the gas even beyond the estimated virial radius of the halos hosting quasars. In QPQ7, we conservatively estimated a gas minimum metallicity of 1/10 solar for the CGM and inferred metal masses $> 10^7$ $M_\odot$. In QPQ5, we estimated a maximum metallicity of 1/2 solar and inferred an upper bound on metal masses $< 10^9$ $M_\odot$. The results presented here indicate metallicities that are several times higher. With the Si measurements scaled to O assuming solar relative abundance, we derive a median metal column density of $10^{16.7}\,\mathrm{cm}^{-2}$ for the seven sightlines within 200 kpc. This corresponds to a total oxygen mass in the cool CGM of $M_{\rm O}^{\rm CGM} \approx 4.9 \times 10^8$ $\mathrm{M}_\odot\,(R_\perp/160\,\mathrm{kpc})^2$. Furthermore, assuming that oxygen accounts for 44% of the metal mass (Asplund et al. 2009), we refined our mass estimate to be $M_{\rm metal}^{\rm CGM} = 1.1 \times 10^9$ $\mathrm{M}_\odot\,(R_\perp/160\,\mathrm{kpc})^2$. Theoretical calculations of yields from nucleosynthesis in core-collapse supernovae (Nomoto et al. 2006; Sukhbold et al. 2016) predict an oxygen yield mass fraction of 0.008, scaled to a Kroupa initial mass function. Thus, the total stellar mass that must have formed to synthesize all the oxygen in the cool CGM, not accounting for oxygen locked up in stellar content, in the ISM, or in the warm-hot/hot-phase CGM, has to be $M_* > 6.1 \times 10^{10}$ $\mathrm{M}_\odot\,(R_\perp/160\,\mathrm{kpc})^2$. To form this stellar mass by $z = 2.4$, the median $z_{\rm fg}$ of the QPQ8 sample, the average star formation rate required is > 34 $\mathrm{M}_\odot\,\mathrm{yr}^{-1}$ if the galaxies first formed at $z \sim 6$. From halo abundance matching techniques (Behroozi et al. 2013), the typical stellar mass of a host galaxy of the QPQ8 sample is $M_{\rm gal} = (6 \pm 3) \times 10^{10}$ $\mathrm{M}_\odot$. Whitaker et al. (2014) gives the star-formation rate of the star forming sequence at $z \sim 2$–3 at this galaxy mass to be 100 $\mathrm{M}_\odot\,\mathrm{yr}^{-1}$. Our estimate of the minimum average star formation rate required, and hence the total oxygen mass in the cool CGM, is consistent with the instantaneous total star formation rate inferred from these scaling relations.

We have also examined the abundance ratios of a subset of the elements, restricting this analysis to low ions to minimize the effects of ionization. We focus on O/Fe, which is a chemical signature of the supernovae that have enriched the gas. High values are indicative of massive stellar nucleosynthesis, i.e. core-collapse supernovae, whereas low values imply substantial enrichment by Type Ia supernovae (SNe Ia)(e.g., Tinsley 1979).

Figure 2.12 presents [O/Fe] estimates after adopting the ionization corrections from our favored models against the $N_{\rm HI}$ measurements. Nearly all of the measurements indicate a supersolar O/Fe ratio, implying that a significant fraction of the CGM surrounding quasars must have an enhanced α/Fe abundance. The obvious exception is subsystem F from the J1144+0959 pair. Perhaps not coincidentally, this subsystem has the highest estimated U parameter of those that exhibit O or Fe, and therefore has the largest ionization correction for $\{O^0/Fe^+\}$. The corrected [O/Fe] value is still subsolar, although we caution that the uncertainty is many tenths dex given the high U value. Furthermore, the [O/Fe] values from QPQ8 show a large dispersion spanning two orders of magnitude.

In summary, the cool gas surrounding $z \sim 2$ massive galaxies hosting quasars to ≈ 200 kpc is highly enriched and α-enhanced. This implies that the gas expelled from these galaxies (and their progenitors) was enriched primarily by core-collapse supernovae. Furthermore, if supernovae explosions are the principal factor in transporting metals to the CGM, we may speculate that core-collapse supernovae dominate in high$-z$ massive galaxies hosting quasars.

The high [α/Fe] enhancement suggests a star formation history similar to elliptical galaxies: (e.g. Matteucci 1994; Conroy et al. 2014), which these quasar host galaxies are expected to evolve into. Currently there are three competing models that explain [α/Fe] enhancement in the *stellar* content of elliptical galaxies (1) selective loss of Fe via galactic winds (Trager et al. 2000); (2) a short starburst that ceased before Fe produced from SNe Ia became available for incorporation into new stars; and (3) a variable initial mass function flattened at the high-mass end (Thomas 1999). Our finding that the CGM shows a high [α/Fe] enhancement strongly disfavors the scenario where more Fe than α elements is selectively ejected through outflows. It is more likely that the supersolar α/Fe ratios reflect an intrinsic nucleosynthetic enhancement. This conclusion is further strengthened by X-ray observations of the hot interstellar medium of early-type galaxies (Loewenstein & Davis 2010, 2012; Konami et al. 2014) and the hot intracluster medium (Mushotzky et al. 1996; Sato et al. 2007) where enhanced α/Fe ratios are similarly found (but see Simionescu et al. 2015). Furthermore, if the initial mass function is not flatter, the starburst-driven galactic-scale winds must occur before the Fe production from SNe Ia starts to become important; hence we expect the duration of starburst lasts less than 1 Gyr. In turn this implies a minimum star formation rate > 55 $\mathrm{M}_{\odot}$ yr^{-1} based on the inferred total stellar mass formed for synthesizing all oxygen in the cool CGM.

2.4.3 Surface Density Profiles

Figure 2.13 presents scatter plots of the H I column density measurements against projected quasar pair separation $R_{\perp}$ calculated at z_{fg}. Figure 2.14 presents the same for C II column density. Both ions exhibit a decline in surface density with increasing $R_{\perp}$. Statistically, a Kendalls's tau test gives a 99.8% probability that the null hypothesis of no correlation between N_{HI} and $R_{\perp}$ is ruled out. A similar test gives a 98.7% probability that the null hypothesis of no correlation between N_{CII} and $R_{\perp}$ is ruled out, and we expect the correlation to be stronger because the N_{CII} absorptions detected at small $R_{\perp}$ are saturated and N_{CII} is not detected at 3σ confidence at large $R_{\perp}$. The observed low ion absorption is thus tracing the CGM gas of the foreground quasar. We further note that strong H I absorption exists even beyond the estimated virial radius of $\approx 160\,\mathrm{kpc}$.

For comparison, in Figure 2.13 we also plot the work of Simcoe et al. (2006),Rudie et al. (2012), and Crighton et al. (2013, 2015) for N_{HI} as a function of $R_{\perp}$ in the CGM of $z \sim 2$–3 galaxies, in which $R_{\perp}$ refers to the transverse, physical distance. Their work uses background quasars as sightlines to probe the CGM of foreground galaxies. Their galaxies typically have $M_{*} \sim 1 \times 10^{10}$ $\mathrm{M}_{\odot}$, which characterizes the typical stellar mass in star-forming galaxies at $z \sim 2$–3, while the typical host galaxy of the QPQ8 sample inferred from halo abundance matching has $M_{*} \sim 6 \times 10^{10}$ $\mathrm{M}_{\odot}$, i.e. it is much more massive. At $R_{\perp} \approx 200$–300 kpc, the QPQ8 N_{HI} values smoothly join those measured for the more typical $z \sim 2$–3 star-forming galaxy population, which are still significantly enhanced compared to the IGM absorption at $\gtrsim 300$ kpc. At $R_{\perp} \lesssim 200$ kpc, we find that the N_{HI} values of the QPQ8 sample are significantly larger that those of the coeval galaxies, as

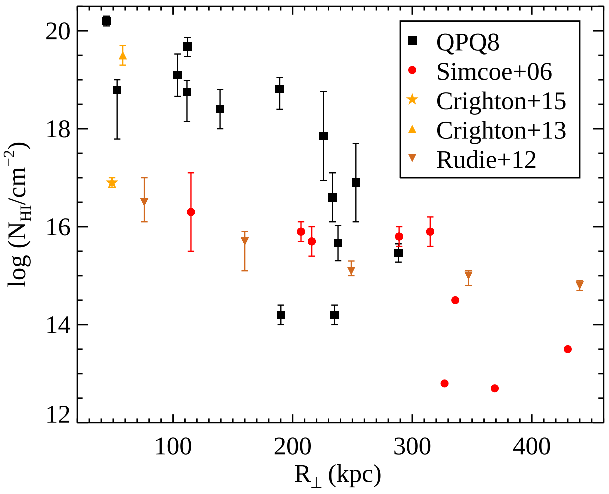

Figure 2.13 Scatter plots of $N_{\rm HI}$ measurements against projected quasar pair separation calculated at $z_{\rm fg}$. The H I exhibits a statistically significant decline in surface density with $R_\perp$. Strong H I absorption exists even beyond the estimated virial radius of $\approx$ 160 kpc. For comparison we also plot CGM $N_{\rm HI}$ measurements of $z \sim$ 2–3 galaxies from the literature as a function of projected distance from the galaxies. At $R_\perp \leq$ 200 kpc, the $N_{\rm HI}$ values of QPQ8 dominate those of coeval galaxies.

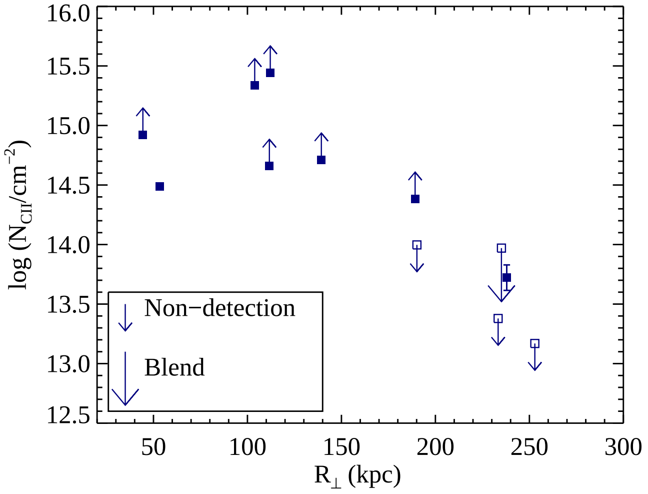

Figure 2.14 Scatter plots of $N_{\rm CII}$ measurements against $R_\perp$. Similar to H I, the C II ion exhibits a statistically significant decline in surface density with $R_\perp$. Theobserved low ion absorption thus traces the CGM gas of the foreground quasar.

inferred previously from measurements of equivalent width (QPQ5, QPQ6).

We calculated the H I mass in the cool CGM by considering the $R_\perp$ values as annular bins. We calculated the mass in the ith annulus from $M_i = N_{\rm HI}(R_i) m_{\rm H} \pi (R_i^2 - R_{i-1}^2)$ and summed up the mass in all annuli. The total H I within 160 kpc is then found to be $M_{\rm HI}^{\rm CGM} = 1.3 \times 10^{10}$ M$_\odot$. Even without any ionization correction, we infer that the baryonic mass of the cool CGM approaches the stellar mass. In a highly clustered environment, the observed gas could be contributed by the CGM of neighboring gaalxies. In this regard, the H I mass estimate can be considered an upper limit.

Concerning the C II ion, the absorption within $R_\perp < 200$ kpc is strong and saturated, with a median $N_{\rm CII} > 14.7$ cm^{-2}, indicating a substantial metal mass. At $R_\perp > 200$ kpc, we have one solid detection of C II in the J0932+0925 system, two non-detections in the J1038+5027 system and the J1627+4605 system shown as 3-σ upper limits in Figure 2.14, and one system J0409$-$0411 whose C II is blended with unrelated intergalactic absorption, depicted by a large downward arrow. Our results quantitatively assert the conclusion of QPQ7 that the gas surrounding massive, $z \sim 2$ galaxies hosting quasars represents the pinnacle of the cool CGM, in terms of the neutral hydrogen mass and the enrichment.

We detect cool enriched gas transverse to the sightline to the foreground quasars to at least $\approx$ 200 kpc. Our results indicate the quasar plays a minor role in producing the cool CGM, and our argument is as follows. Observations of spatial clustering of quasars (Haiman & Hui 2001; Martini & Weinberg 2001; Martini 2004), observations of the transverse proximity effect in He II (Jakobsen et al. 2003), as well as simulations of galaxy mergers that include supermassive black holes (Hopkins et al. 2005), all constrain the quasar lifetime to be 10^6–10^8 yr, with a preference for 10^7 yr. If the velocities represent outflows, given that the line-of-sight velocity dispersion is 249 km s^{-1} in C II and 495 km s^{-1} in C IV, as discussed in Section 2.4.1, then even if the observed quasar episode has been active for 10^8 yr and accelerate material to 500 km s^{-1}, this gas would only reach 50 kpc.

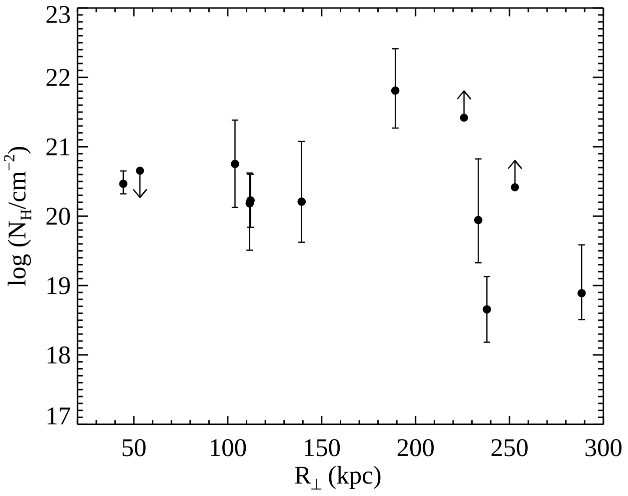

Figure 2.15 The total H column from ionization state modeling as a function of $R_\perp$. We see little evolution in N_H up to $\approx$ 200 kpc, as both N_HI and the neutral fraction x_HI anticorrelate with $R_\perp$. The median is $N_\mathrm{H} = 10^{20.5}$ cm^{-2}.

It is unlikely that the observed quasar episode alone could transport all of this cool material from the interstellar medium of the galaxies. Furthermore, we found no statistically significant trend between C II column density and quasar luminosity L_bol or the UV enhancement factor g_UV, contrary to the claims in Johnson et al. (2015) where they investigated Mg II in $z \sim 1$ quasar CGMs. We caution the readers, however, that the mean L_bol of QPQ8 is $10^{46.4}$ erg s^{-1}, which is nearly an order of magnitude higher than the mean L_bol of the sample of Johnson et al. (2015) at $10^{45.5}$ erg s^{-1}.

As described in Section 2.3.3, we modeled the ionization state and calculated N_H for each absorption system. In Figure 2.15 we plot N_H as a function of $R_\perp$. Consistent with expectation, we do not observe any significant variation of N_H with $R_\perp$ up to $\approx 200\,\mathrm{kpc}$, as both N_HI and the neutral fraction x_HI anticorrelate with $R_\perp$.

Using the median $N_\mathrm{H} = 10^{20.5}\,\mathrm{cm}^{-2}$ and the median [M/H] $= -0.6$ (Figure 2.11) within 200 kpc, we constructed cumulative mass profiles of total H and metals in the cool CGM, and the results are plotted in Figure 2.16. For reference, we also included the expected baryonic mass projected profile of an NFW halo with concentration parameter $c = 4$ (Navarro et al. 1997) and dark matter mass $M_{\rm DM} = 10^{12.5}\,{\rm M}_{\odot}\,(R_{\perp}/160~{\rm kpc})^2$. We assumed the cosmic baryon fraction 0.17. We also plotted the typical host galaxy mass of the QPQ8 sample using halo abundance matching techniques (Behroozi et al. 2013) and assuming a 50% gas fraction, as well as the range of supermassive black hole mass of the QPQ8 sample, calculated from the bolometric luminosity of the quasars and assuming an Eddington ratio $f_{\rm Edd} = 0.1$. We estimated the total mass of the cool CGM as $M_{\rm cool}^{\rm CGM}(R_{\perp}) \approx 1.9 \times 10^{11}~{\rm M}_{\odot}~(R_{\perp}/160~{\rm kpc})^2$. Since the median $N_{\rm H}$ of the sample is not sensitive to one system with the highest $N_{\rm H}$, namely J1144+0959, our estimate of the cool CGM mass is representative of the sample. In QPQ7 we estimated an infall time $\tau_{\rm infall} \lesssim 1$ Gyr. The corresponding inflow rate of cool gas $M_{\rm cool}^{\rm CGM}/\tau_{\rm infall}$ exceeds 100 $\rm M_{\odot}\,yr^{-1}$. This is comparable to the star formation rate of massive star-forming galaxies at $z \sim 2$, and is enough to fuel star formation for at least 1 Gyr. The QPQ8 results further strengthen the conclusion of QPQ3 and QPQ7 that quasars are unlikely to quench star formation at $z \sim 2$.

It can be seen in Figure 2.16 that at the virial radius the cool gas fraction accounts for only $\approx 1/3$ of the total expected baryonic mass. Together with the galaxy's stellar and gas mass, they account for $\approx 56\%$ of the total baryonic budget. Modern X-ray observations of the hot intracluster medium at $z \gtrsim 1$ (Andreon 2012; Baldi et al. 2012) report metallicities $\approx 1/3$ solar, which is consistent with the median $[{\rm M/H}] = -0.6$ dex found for the cool CGM in this work. If we assume that $[{\rm M/H}] = -0.6$ is a good representation of the metallicity of the cool and the hot-phase CGM, then similarly to the total H, at the virial radius the cool CGM accounts for only 1/3 of the total expected metal mass. A massive reservoir of warm/hot, enriched gas within the QPQ halos is thus required to complete the baryonic mass budget. Such warm/hot intracluster medium is predicted to be already fully in place at $z \sim 2$ in massive halos (e.g. Fumagalli et al. 2014).

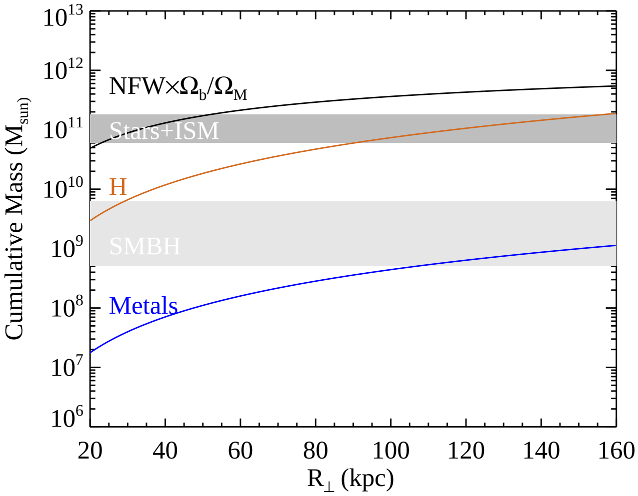

Figure 2.16 Using the median $N_{\rm H}$ and the median [M/H] within 200 kpc, we constructed cumulative mass profiles of total H and metals in the cool CGM. For reference we also included the expected baryonic mass projected profile of an NFW halo with $c = 4$ and dark matter mass $M_{\rm DM} = 10^{12.5}\,{\rm M}_\odot\ (R_\perp/160\,{\rm kpc})^2$. We also plotted the typical host galaxy mass, as well as the range of supermassive black hole mass of the QPQ8 sample. We estimated the total mass of the cool CGM as $M_{\rm cool}^{\rm CGM} \approx 1.9 \times 10^{11}\ {\rm M}_\odot\ (R_\perp/160\ {\rm kpc})^2$. This accounts for 1/3 of the total expected baryonic mass.

2.4.4 Volume Density and Linear Size of the Absorbers

From our analysis, there are two standard methods for assessing the volume density $n_{\rm H}$ of the gas and, in turn, offering an assessment of the linear scale ℓ of the absorption system. One approach is to assume an intensity for the incident radiation field intensity J_ν and then convert the estimated ionization parameter U into an estimate of $n_{\rm H}$. The uncertainties in this analysis are large: we have no direct constraint on J_ν, the error in U is substantial, and systematic uncertainties in the photoionization modeling influence this treatment. Therefore, we proceed in a conservative fashion.

For J_ν, we consider two limits: (1) the gas is illuminated by only the EUVB, where we adopt the spectral energy distribution of the cosmic ultraviolet background normalized to the estimate of Faucher-Giguère et al. (2008) for the effective IGM Lyα opacity; (2) the gas is fully illuminated by the foreground quasar, which shines isotropically, and the gas is at a distance r equal to the impact parameter $R_\perp$. The first limit sets a lower bound to J_ν and therefore the density while the latter sets an upper limit to $n_{\rm H}$. For the EUVB case, we would require $n_{\rm H} \approx 10^{-3}\,{\rm cm}^{-3}$. This is a somewhat low value for overdense and optically thick gas, but is comparable to predictions from simulations (Rosdahl & Blaizot 2012). A Lyα fluorescence analysis (Arrigoni Battaia et al. 2016) suggests $n_{\rm H} \approx 0.6 \times 10^{-2}$ cm^{-3}, which is not that far from our result given the uncertainties. Furthermore, the resultant length scale $\ell \equiv N_{\rm H}/n_{\rm H}$ would exceed 100 kpc per cloud for the typical $N_{\rm H}^{\rm QPQ8} \approx 10^{20.5}$ cm^{-2}. Although not strictly ruled out for the majority of our sample (see below), we suspect that the densities are significantly higher and that ℓ is correspondingly smaller. If the quasar emits isotropically and $r \approx R_\perp$, then the implied densities are $n_{\rm H} \approx 1 - 10\,{\rm cm}^{-3}$. Such values are characteristic of the diffuse interstellar medium of galaxies. In this extreme, we recover $\ell \approx 1 - 10\,{\rm pc}$, which has been previously reported for some absorption systems (Sargent et al. 1979; Simcoe et al. 2006) and yet may be considered extreme. In another study, metal-enriched gas clumps in the circumgalactic medium at $z \sim 2.5$ are found to have sizes of 100–500 pc (Crighton et al. 2015).

An independent assessment of the density may be obtained from analysis of the fine-structure absorption of C^+ and Si^+ (e.g., Prochaska 1999; Silva & Viegas 2002, QPQ3). Under the assumption that electron collisions dominate the excitation of these ions in our photoionized gas, the ratio of the excited state to the ground state yields a precise estimate for n_e. We have previously assessed in QPQ3 whether the gas could be excited indirectly by UV pumping (e.g. Prochaska et al. 2006), and find that the quasars are too faint. From the QPQ8 data set, we report two positive detections and several upper limits of C II* $\lambda 1335$ absorption. Following the methodology in QPQ3, we assumed an electron gas temperature of 20,000 K and obtained $n_{\rm e} = \frac{106}{2(N({\rm C}^+_{J=1/2})/N({\rm C}^+_{J=3/2}))-1}$, where $J = 1/2$ represents the ground state and $J = 3/2$ is the first excited level. In Table 2.5 we present the resultant estimates of $n_{\rm e}$ and the corresponding linear size per cloud $\ell = N_{\rm H}/n_{\rm H}$, where $n_{\rm H} = n_e/(1 - x_{\rm HI})$, not compensating for the contribution of ionized helium to electron density. For the positive detections, we find $n_e > 10\,{\rm cm}^{-3}$. For subsystem F of J1420+1603FG, n_e even exceeds the electron density expected for isotropic quasar illumination, $n_{\rm QSO}$ (Section 2.3.3), suggestive of local sources of radiation.

2.4.5 Peculiarities of the Quasar CGM

The environments of $z \sim 2$ quasars must be considered extreme compared with coeval Lyman break galaxies, at least in terms of overdensity and possibly an elevated, local radiation field. In this respect, the high metallicities, large CGM gas masses, and complex kinematics may follow naturally. As such, we are further motivated to search for peculiar features in the absorption line data that occur rarely, if at all, along random sightlines. We now summarize a series of examples that on their own are remarkable and together paint a highly unusual picture of the $z \sim 2$ universe.

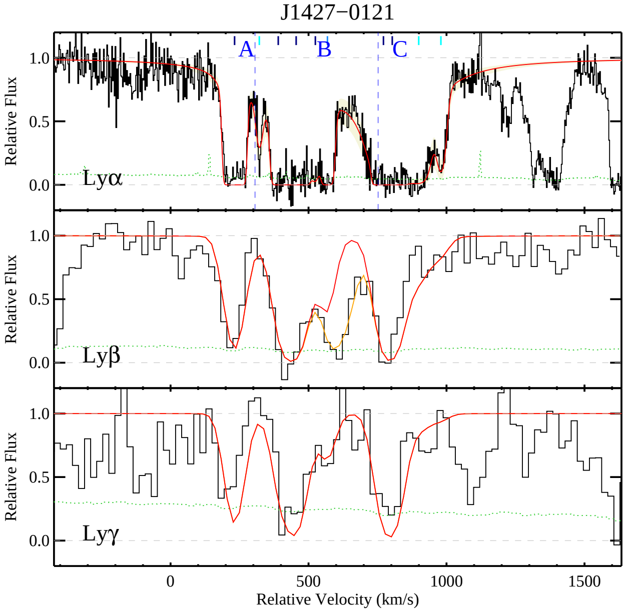

Figure 2.17 H I Lyman series absorption profiles for J1427−0121. The black histograms show the Lyman series identified in the J1427−0121BG spectrum at velocities consistent with J1427−0121FG. The navy ticks mark the centroid redshifts for H I components traced by low metal ions. The cyan ticks mark H I components not associated with metal ions. The red curve is the Voigt profile modeling fit of summing up all H I components associated with J1427−0121FG. The orange curve is the modeling fit including Lyα forest contamination. The positive flux at Lyα suggests $N_{\rm HI} < 10^{14}$ cm^{-2} whereas the positive detections of low ions and the high opacities at Lyβ and Lyγ indicate $N_{\rm HI} \gg 10^{14}$ cm^{-2}. We suspect that the flux at Lyα is unresolved Lyα emission as predicted for gas illuminated by the ionizing flux of a nearby quasar. The green histogram presents the 1σ noise in the normalized flux.

2.4.5.1 Evidence for Elevated Radiation Field

The most extreme case, in our opinion, is the putative Lyα emission in subsystem A of J1427$-$0121FG. As shown in Figure 2.17, the positive flux at Lyα suggests $N_{\rm HI} < 10^{14}\,{\rm cm^{-2}}$ whereas the positive detections of low ions and the high opacities at Lyβ and Lyγ indicate $N_{\rm HI} \gg 10^{14}\,{\rm cm^{-2}}$. Although metal-bearing systems with $N_{\rm HI} \sim 10^{14}\,{\rm cm^{-2}}$ have been reported previously (e.g., Boksenberg & Sargent 2015), these are very rare and are generally dominated by C IV and O VI absorption (Simcoe et al. 2004). We strongly suspect that the flux at Lyα is unresolved Lyα emission as predicted for gas illuminated by the ionizing flux of a nearby quasar (e.g., Hennawi & Prochaska 2013; Cantalupo et al. 2014; Hennawi et al. 2015). In Figure 5 of QPQ4, we showed Gemini spectrum of the J1427$-$0121 pair after subtraction of the point-spread function and there is no revealing residual Lyα emission to the sensitivity limit ${\rm SB}_{1\sigma} = 0.14 \times 10^{-17}\,{\rm erg\,s^{-1}\,cm^{-2}\,arcsec^{-2}}$. Thus this emission is spatially unresolved, i.e. it is consistent with the point spread function of the foreground quasar. This phenomenon, however, is rare in our quasar pair sample (QPQ4) and we identify no other example in the eight cases from QPQ8 where we have coverage of Lyβ or higher-order Lyman series lines.

To estimate the Lyα flux more accurately we prefer a lower dispersion spectrum than our follow-up spectra with echelle/echellette resolution. Based on the SDSS spectrum continuum, we estimated the Lyα flux $F_{\rm Ly\alpha} = 1.5 \times 10^{-17}\,{\rm erg\,s^{-1}\,cm^{-2}}$. Since the size of the emitting cloud has to be smaller than the typical seeing disk of $1''$, the Lyα surface brightness is ${\rm SB}_{\rm Ly\alpha} > 1.5 \times 10^{-17}\,{\rm erg\,s^{-1}\,cm^{-2}\,arcsec^{-2}}$. If the absorber is optically thin, we may estimate the surface brightness of subsystem A following the formalism of QPQ4. Specifically, we assumed a volume density that is the same as that of subsystem C, which is calculated to be $n_{\rm H} = 16\,{\rm cm^{-3}}$ from the $N_{\rm CII}/N_{\rm CII*}$ ratio. We adopted the $N_{\rm H}$ value from photoionization modeling. The expected ${\rm SB}_{\rm Ly\alpha} \approx 3.3 \times 10^{-17}$ erg s^{-1} cm^{-2} arcsec^{-2}. If the absorber is optically thick, the formalism of QPQ4 then gives ${\rm SB}_{\rm Ly\alpha} \approx$

9.5×10^{-17} erg $\mathrm{s^{-1}}$ $\mathrm{cm^{-2}}$ $\mathrm{arcsec^{-2}}$. Since the measured Lyα flux corresponds to lower Lyα surface brightness, the characteristic angular size of the absorber should be smaller than the typical seeing disk of $1''$, corresponding to < 8 kpc. Furthermore, again following the formalism of QPQ4, should this absorber be optically thin, this level of Lyα fluorescence would imply $N_{\rm HI} = 1.1 \times 10^{17}\,\mathrm{cm^{-2}}$, and hence the optically thin assumption breaks down. The absorber probably lies in the transition from the optically thin to the optically thick limit. Alternatively, Lyα emission can result from collisional excitation. In the absence of significant metal enrichment, collisionally excited Lyα emission is the primary coolant for gas at $T \sim 10^4\,\mathrm{K}$. Collisional excitation of neutral hydrogen requires a non-negligible neutral fraction, and the resulting surface brightness is exponentially sensitive to gas temperature via the collisional excitation rate coefficient $q_{\rm 1s \rightarrow 2p}\,(T)$. Thus the electron density estimated will be uncertain by orders of magnitude. However, we expect that recombination dominates cooling radiation. Hennawi et al. (2015) reports that the Lyα emission from collisional excitation is at most 20% of the Lyα emission from recombination, for the nebula illuminated by a quasar quartet discovered by them.

In previous works (QPQ2, QPQ4, QPQ6), we have argued that quasars emit anisotropically owing to the high incidence of optically thick, cool gas in the transverse direction relative to that observed along the direct sightline. With the high fidelity of our QPQ8 sample, we may search for more subtle signatures in which at least a portion of the transverse sightline is illuminated by a luminous and hard radiation field. One such signature would be the N V doublet $\lambda\lambda 1238, 1242$, which may also trace a distinct warm-hot phase. With an ionization potential of 5.5 Ryd, production of the $\mathrm{N^{4+}}$ ion requires a gas with $T \gtrsim 10^5\,\mathrm{K}$ for collisional ionization or a high intensity of extreme UV photons. Indeed, N V is very rarely detected in random, intervening systems along quasar sightlines (Fox et al. 2009) or even in the CGM of Lyman break galaxies (Turner et al. 2014), but it is more frequently detected in gas associated with the quasar itself. For each pair in the

QPQ8 sample, we have coverage of the N V doublet but these lines are free of the Lyα forest in only three cases. Of these, we report one positive detection (J1026+4614). Our photoionization model for this gas yields $\log U \approx -1.9$ dex (see Appendix C). To achieve this U value with the EUVB, one would require a very low gas density $n_{\rm H} \approx 10^{-4}\,{\rm cm}^{-3}$ and an absorber size $\ell = N_{\rm H}/n_{\rm H} \approx$ 13 kpc. Given the rarity of N V detections along random quasar sightlines, we contend that this gas is illuminated by the foreground quasar, although the flux need not be as bright as that observed along our sightline, or the flux may also exhibit temporal variability. The absence of N V in the other two pairs with coverage outside the Lyα forest and the four cases with minimal IGM blending suggests that only small portions of the transverse sightlines are illuminated. This conclusion is tempered by the possible underabundance of N, but large deviations from solar relative abundances tend to occur in gas with metallicities much lower than those estimated for this CGM (e.g. Henry et al. 2000). Taking the median values of $[{\rm M/H}] = -0.6$ and $N_{\rm H} = 10^{20.5}\,{\rm cm}^{-2}$, using Cloudy we estimated $N_{\rm NV} =$ $10^{9.3}$–$10^{14.7}$ ${\rm cm}^{-2}$ for the QPQ8 systems, varying $\log U$ from -4 to -2. Hence only for high values of the U parameter will N V become strong enough to detect in most of our echellette-resolution data, whose detection limit is on average $N_{\rm HV} <$ $10^{13.6}$ ${\rm cm}^{-2}$. Another doublet that may trace a quasar-illuminated gas or a distinct warm-hot phase is the O VI doublet $\lambda\lambda 1031, 1037$. However, in the QPQ8 data we are unable resolve this doublet from coincident absorption in the Lyα forest.

The subsystem F of J1144+0959FG exhibits significant low ion absorption, e.g. O I and Fe II, and has an estimated $N_{\rm HI} \approx 10^{18}\,{\rm cm}^{-2}$. These properties characterize an optically thick, partially ionized Lyman limit system. The very strong medium and high ions, however, yield an ionization parameter $\log U \approx -2$, giving a neutral fraction of $x_{\rm HI} \approx 10^{-3}$ and a total $N_{\rm H} \approx 10^{21}\,{\rm cm}^{-2}$. If the volume density is close to the rough upper bound $n_{\rm QSO} = 10^{-0.3}$ ${\rm cm}^{-3}$, then together these suggest an elevated radiation field.

Given the rarity of such phenomena along random quasar sightlines, we may hypothesize that where one observes similar cases an AGN may be present or recently was shining (Oppenheimer & Schaye 2013). In this study, evidence for an elevated radiation field is found for only two out of 14 quasar environments studied. We do not believe that the quasar CGM is qualitatively peculiar relative to other massive galaxies, but to date QPQ is the only statistical sample to characterize the physical properties of the CGM of massive galaxies at $z \sim 2$. For the typical bolometric luminosities of these quasars, observations imply star formation rates comparable to inactive star-forming galaxies of similar masses (e.g. Rosario et al. 2013).

Farina et al. (2013) studied a mass-controlled sample and found that, if the mass of the galaxies is taken into account as an additional parameter that influences the extent of the gaseous halos, then the distribution of Mg II absorbers around quasars is consistent with that for normal galaxies.

2.4.5.2 Evidence for Elevated Volume Density

In Section 2.4.4, we assessed the density of the gas through analysis of C II* λ1335 absorption and reported two positive detections. Among these, subsystem F of J1420+1603FG has a C II* λ1335 optical depth exceeding 0.8 at its peak and a ratio of excited to ground state of ≈ 1.1. To our knowledge, this exceeds any such measurement along an extragalactic sightline including gamma-ray bursts (Prochaska et al. 2006), whose gas is radiatively excited. In turn, this requires an electron density $n_{\rm e} = 10^{2.2}\,{\rm cm}^{-3}$, which defies conventional wisdom for diffuse CGM gas (Werk et al. 2014). Similar inferences, however, have been drawn from the Lyα nebulae surrounding $z \sim 2$ quasars (Cantalupo et al. 2014; Arrigoni Battaia et al. 2015a,b; Hennawi et al. 2015) and the extended narrow emission line regions and nebulae of other AGNs and radio galaxies (Stockton et al. 2002; Dey et al. 2005; Fu & Stockton 2007; Humphrey et al. 2007). Given that the inferred absorption pathlength is $\ell \lesssim 1$ pc, one must invoke a large population of such clouds to explain our intersecting even one given $(\ell/R_\perp)^2 < 10^{-10}$. Furthermore, small and dense clumps will be disrupted by hydrodynamic instabilities as they move through a hotter CGM phase, unless the pressure of the hot plasma is able to confine the compact clumps (Arrigoni Battaia et al. 2015a; Crighton et al. 2015). Furthermore, such a small cloud is representative of the dense knots inside giant molecular clouds. However, the absence of Lyman–Werner bands implies $N_{\mathrm{H}_2} < 10^{18}$ cm^{-2}.

2.5 Summary and Future Outlook

In the "QPQ" series of papers, we have introduced a novel technique to study the CGM surrounding quasar host galaxies, which provides clues to the physics of massive galaxy formation and the nature of quasar feedback. We mined the existing quasar catalogs for closely projected, physically unassociated quasar pairs and confirmed them with follow-up spectroscopy. From a total of $\approx$ 700 confirmed pairs, we selected 14 pairs with projected separations $<$ 300 kpc and data with high dispersion and high S/N, to study the CGM surrounding quasars at $z\sim$2–3. We analyzed the velocity fields of the absorbing gas, the H I and metal ion column densities, and the ionization state characterized by the ionization parameter U. These analyses constrain the physical state of the cool gas near the foreground quasars, including its kinematics, chemical abundance patterns, surface density profiles, volume density, size of the absorbers, and the intensity of the impinging radiation field. These analyses also test for the presence of a hotter phase of the CGM. Our key findings are as follows.

Model-independent Constraints:

1. The low (e.g. C II) and high (e.g. C IV) ions roughly trace each other in velocity structure. The velocity widths exceed all previous measurements of gas surrounding any galaxy populations, with a RMS $\sigma_v = 495\,\mathrm{km\,s^{-1}}$ for C IV and $\sigma_v = 249\,\mathrm{km\,s^{-1}}$ for C II . The velocity centroids of the absorption profiles are frequently biased to positive (redshifted) velocities

from the systemic redshift of the foreground quasars.

2. The surface density of H I and low metal ions (traced by C II) declines with $R_\perp$. H I absorption is strong even beyond the estimated virial radius. The H I column densities are significantly larger than those of coeval galaxies.

3. In one case, subsystem A of J1427−0121FG, we suspect the presence of unresolved Lyα emission, a prediction for gas illuminated by the foreground quasar. In another case, J1026+4614, we detected N V absorption and we contend that the gas is at least partially illuminated by the foreground quasar. The non-detection of N V in all other absorption systems, however, suggests that only small portions of the transverse sightlines are illuminated and the flux need not be as high as along the line of sight.

Model-dependent Constraints:

1. The ionization parameter U positively correlates with projected distance from the foreground quasar. This runs contrary to expectation should the foreground quasar dominate the ionizing radiation field.

2. The CGM is significantly enriched even beyond the estimated virial radius of the host dark matter halos ($\approx$ 160 kpc). Within $R_\perp \approx 200$ kpc, the median metallicity is $[\mathrm{M/H}] = -0.6\,\mathrm{dex}$.

3. The O/Fe ratio is supersolar in nearly all measurements. A significant fraction of the CGM must have an enhanced α/Fe abundance, suggestive of a star formation history similar to massive ellipticals with a short starburst duration.

4. We did not find any evolution in the total H column up to $R_\perp \approx 200$ kpc, consistent with the finding that both the H I column and the neutral gas fraction decline with $R_\perp$. The median total H column is $N_\mathrm{H} \approx 10^{20.5}$ cm^{-2}.

5. Within the estimated virial radius, we found that the total mass of the cool-phase CGM is substantial: $M_{\rm cool}^{\rm CGM} \approx 1.5 \times 10^{11}$ $\rm M_\odot$ $(R_\perp/160~{\rm kpc})^2$. This accounts for 1/3 of the dark halo baryonic budget.

6. For two absorption subsystems with positive detection of the C II* fine-structure line, we estimated the electron volume density and the corresponding linear size per cloud, and found $n_e > 10$ cm^{-3}. In one case, subsystem F of J1420+1603FG, the C II* to C II column ratio exceeds any previous measurement along extragalactic sightlines. The implied $n_e = 10^{2.2}$ cm^{-3} even defies conventional wisdom that the CGM is primarily diffuse.

Below we list several directions of future inquiry.

1. Assemble a larger sample of quasar pairs with precise redshift measurements to better quantify any anisotropy in the velocity fields of metal ions on the CGM scale (QPQ9), and H I on larger scales (J. F. Hennawi et al. 2017, in preparation).

2. Model the transverse proximity effect out to large scales to determine the average opening angle or variability timescale of the quasar radiation, which would help in the interpretation of the CGM measurements, in particular how often these CGM absorbers are expected to be illuminated.

3. Cosmological simulations of galaxy formation that include feedback from AGNs and/or winds powered by star formation to determine whether they can reproduce the observed cool and often optically thick quasar CGM.

4. Use projected submillimeter galaxy-quasar pairs to study the CGM surrounding submillimeter galaxies, whose clustering strength is comparable to quasars. This will help isolate the impact of quasar feedback on the CGM.

5. Narrow-band (Cantalupo et al. 2014) and integral field (Martin et al. 2014) imaging of the CGM.

2.6 Acknowledgements

We thank the anonymous referee for a careful review and help in consolidating the findings. J.X.P. and M.W.L. acknowledge support from the National Science Foundation (NSF) grants AST-1010004, AST-1109452, AST-1109447, and AST-1412981. We acknowledge the contributions of Sara Ellison, Crystal Martin, and George Djorgovski in obtaining the ESI spectra analyzed in this manuscript. We thank Ryan Cooke for his software ALIS to model Voigt profiles and technical support. We thank Guillermo Barro for technical support for the MOSFIRE data reduction pipeline. We thank George Becker for helpful advices on X-SHOOTER data reduction. We thank Camille Leibler for valuable comments on chemical enrichment patterns. We thank Justin Brown for comments on supernova nucleosynthesis yields. We thank John O'Meara for sharing his metal-enriched IGM absorption data. We thank Emanuele P. Farina for a thorough examination of the manuscript. M.W.L. thanks Sprite Chu for professional computing support.

Much of the data presented herein were obtained at the W. M. Keck Observatory, which is operated as a scientific partnership among the California Institute of Technology, the University of California, and the National Aeronautics and Space Administration. The Observatory was made possible by the generous financial support of the W. M. Keck Foundation.

Some of the data herein were obtained at the Gemini Observatory, which is operated by the Association of Universities for Research in Astronomy, Inc., under a cooperative agreement with the NSF on behalf of the Gemini partnership: the NSF (United States), the Science and Technology Facilities Council (United Kingdom), the National Research Council (Canada), CONICYT (Chile), the Australian Research Council (Australia), Ministério da Ciência, Tecnologia e Inovação (Brazil) and Ministerio de Ciencia, Tecnología e Innovación Productiva (Argentina).

The authors wish to recognize and acknowledge the very significant cultural role and reverence that the summit of Mauna Kea has always had within the

indigenous Hawaiian community. We are most fortunate to have the opportunity to conduct observations from this mountain.

Some of the data were obtained with the 6.5 m Magellan Telescopes located at Las Campanas Observatory, Chile.

Some of the data were obtained with the European Southern Observatory Very Large Telescope under program ID 087.A-0610(A).

2.7 Appendix A: Treatment of C IV in Kinematic Analysis

For C IV $\lambda1548$, we required a special treatment for the absorption systems where the velocity width exceeds the doublet separation $c\Delta\lambda/\lambda \approx 500\,\mathrm{km\ s^{-1}}$. In these cases the optical depth profiles overlap and we made the following modifications to estimate Δv_{90} and $\bar{\delta v}$. Specifically we examined the optical depth profile of the entire doublet and boosted the opacity by 1.5 in the region of overlap and by 2 at velocities where only absorption by C IV $\lambda1550$ is present. These factors account for the 2:1 ratio in the oscillator strengths of the two transitions. We then calculated Δv_{90} and $\bar{\delta v}$ from the optical depth profile of the full doublet and offset the derived quantities by the doublet separation.

2.8 Appendix B: Robustness of Column Density Measurements

We examined the effect of saturated narrow features appearing unsaturated in low-resolution spectra, which would result in underestimated ion column densities. The chapter conservatively reports lower limits for cases where the normalized flux goes below 0.4. In this chapter we use echelle spectra to analyze the metal absorption subsystems of J1144+0959, J1204+0221, and J1427−0121.

We have obtained echellette spectra of them using MagE. Figure 2.18 plots the column densities of the metal absorption subsystems measured from echellette spectra versus echelle spectra, where the normalized flux is greater than 0.4 in the echellette spectra. The data points include all metal ions such as C^+, C^3+, O^0, etc and do not differentiate them. For an ion species where multiple transitions are available for measurement, the column density reported is the mean of the measurements weighted by inverse variance. The data points in Figure 2.18 are color coded to indicate those with more than one transition analyzed. We do not see any systematic bias in measurement using strong versus weak lines.

The data points show an increased scatter with decreasing column density. This is what we would expect intuitively, because the relative error in weaker absorption is larger. The linear best fit is very close to the $y = x$ line, and there is only one data point that deviates more than 3σ from the $y = x$ line. If we force the linear best fit to pass through the origin, which would be the case were S/N infinite, then the slope equals 1.00. Figure 2.18 shows both data points that lie above the $y = x$ line and data points that lie below it. The overall mean agreement demonstrates that our criterion on the minimum normalized flux for reporting lower limits captures the saturated components well. Moreover, there is also no evidence of systematic bias to higher column density measurements from echellette spectra that may originate from unresolved contamination from neighboring absorption features.

We also fitted Voigt profiles to unsaturated metal absorption components in the echelle spectrum of J1427−0121, and summed the total column densities in each subsystem. Our aim was only to verify that Voigt profile fitting and AODM give the same column densities. For the χ^2 minimization process, we set the Doppler b values to be 5 $\mathrm{km\,s^{-1}}$ minimum as determined by the resolution limit, although the model preferred lower values for a few components. Conventionally, the minimum b value is 8 km $\mathrm{s^{-1}}$ due to turbulence, and contributions from turbulence dominate over thermal broadening. This is just as expected for an instrumental resolution high enough to resolve the lines.

We have defined absorption subsystems as those separated in distinct velocity intervails, with no obvious ionization gradient within. The three echelle sightlines also allow us to examine any remaining ionization gradient within a subsystem. We considered the J1427−0121 sightline. We performed a component-by-component photoionization modeling for its subsystem C, and omitted its subsystems A and B for that analysis. There is residual Lyα emission at the absorption trough of subsystem A, which makes it difficult to deblend the two absorption components in H I at velocities defined by the metal ions. The three components of subsystem B that contain low ions are all weak absorption, which makes it difficult to analyze them separately. Subsystem C contains two components and we found $\log U < -3.6$ and $\log U < -3.4$ respectively. In the ionization modeling treatment in this study, we adopted $\log U < -3.4^{+0.3}$ for subsystem C. We conclude that measuring column densities using AODM is robust to within the uncertainties allowed for ionization modeling-dependent analysis.

2.9 Appendix C: Notes on Individual Pairs

We present a detailed description, including figures and tables, for the absorption associated with each of the foreground quasars in the QPQ8 sample. See Section 3.3 for a description of the techniques employed in the analysis. In Table 2.21, we present the H I column density measurements of each absorption subsystem.

J0225+0048—Figure 2.19 reveals absorption for this pair in roughly three distinct velocity intervals spanning a total of $\Delta v \approx 1000\,\mathrm{km\,s^{-1}}$. We define three subsystems based on the strong features in the H I Lyman series absorption. We present the ionic column densities measured with the AODM in Table 2.7. Absorption from high ions $\mathrm{Si^{3+}}$ and $\mathrm{C^{3+}}$ is strong in subsystems A and B and moderate in subsystem C. No low ion transitions are detected for any of the

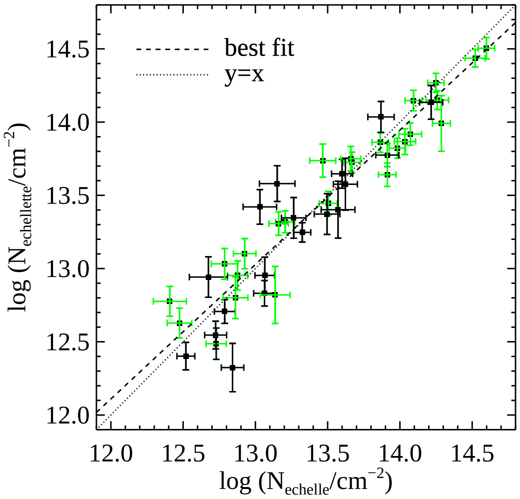

Figure 2.18 Column densities of ions of the subsystems of J1144+0959, J1204+0221, and J1427−0121, measured from echellette spectra vs. echelle spectra, where the normalized flux is greater than 0.4 in the echellette spectra. Error bars colored in green indicate that multiple transitions of the same species are available for measurement. The plot shows that our criterion of normalized flux going below 0.4 for reporting lower limits captures saturated components well.

subsystems, indicating a highly ionized gas. Regarding the $N_{\rm HI}$ analysis, we have limited constraints given that the echellette-resolution data covers only the Lyα transition. There is no indication of damping wings and the lines are saturated, i.e. on the flat portion of the curve of growth. We also present the lower dispersion GMOS spectrum that covers Lyβ. The gas shows absorption separated in roughly three distinct velocity intervals. If we assume minimum Doppler $b_{\rm A,B,C}$ values of 15 km s^{-1}, the lack of strong damping wings in all three subsystems yields strict upper limits of $N_{\rm HI}^{\rm A} < 10^{18.6}$ cm^{-2}, $N_{\rm HI}^{\rm B} < 10^{18.7}$ cm^{-2}, and $N_{\rm HI}^{\rm C} < 10^{18.5}$ cm^{-2}. If we assume maximum Doppler $b_{\rm A,B,C}$ values of 60 km s^{-1} and single components, the equivalent widths demand $N_{\rm HI}^{\rm A} > 10^{15.6}$ cm^{-2}, $N_{\rm HI}^{\rm B} > 10^{16.1}$ cm^{-2} and $N_{\rm HI}^{\rm C} > 10^{16.0}$ cm^{-2}. We fitted these data with the ALIS software package assuming seven components (see Table 2.21), with redshifts set by the metal line absorption. We find solutions with nearly equivalent χ^2 that range from $N_{\rm HI} = 10^{16.4}\,{\rm cm}^{-2}$ to $10^{18.9}\,{\rm cm}^{-2}$. We adopted approximately the central $N_{\rm HI}$ values in this range and a correspondingly large uncertainty for each subsystem. Because no low ion states are detected, the ionic ratios Si^{+}/Si^{3+} and C^{+}/C^{3+} impose lower limits on U. Our ionization modeling yields $\log U_{\rm A} > -2.4$, $\log U_{\rm B} > -2.3$, and $\log U_{\rm C} > -2.6$. To further constrain U we also considered the Si^{3+}/C^{3+} ratios. They imply yet higher U values, provided the relative abundances are roughly solar. These U values suggest that either the radiation field is much stronger than the EUVB and the foreground quasar is shining on the gas, or that $n_{\rm H} \ll 0.1$ cm^{-3}.

J0341+0000—Within ±1000 km s^{-1} of $z_{\rm fg}$ we identify no system with a rest equivalent width for Lyα exceeding 0.3 Å. We present AODM measurements of the upper limits to any associated metal ion columns in Table 2.8. Associating the strongest absorption line to the quasar at $z = 2.1286$ (Figure 2.20), we measured $N_{\rm HI} = 10^{14.2\pm0.2}$ cm^{-2} from a fit to the data. Although there is uncertainty dominated by possible line saturation, we strictly constrain $N_{\rm HI} < 10^{14.4}$ cm^{-2} assuming $b > 15$ km s^{-1}.

With the absence of metal line detections, we have no constraints on the ionization state of the gas. The low N_{HI} column, however, implies a highly ionized medium. Together the data suggests either an extreme ionization state, low metallicity, or little gas along the sightline.

J0409-0411—Similar to J0341+0000, this system shows no Lyα line with a peak optical depth greater than 2 within $1000\,\mathrm{km\,s^{-1}}$ of z_{fg} (Figure 2.21). We present AODM measurements of the upper limits to any associated metal ion columns in Table 2.9. The strongest Lyα line at $z = 1.7027$ has an equivalent width $W_{\mathrm{Ly\alpha}} = 0.45 \pm 0.04\,\text{Å}$. A line profile analysis gives $N_{\mathrm{HI}} = 10^{14.2\pm0.2}$ cm^{-2} for the complex with the uncertainty dominated by possible line saturation.

With the absence of metal line detections, we have no constraints on the ionization state of the gas. The low N_{HI}column, however, implies a highly ionized medium.

J0853-0011—The ions show absorption in roughly three distinct velocity intervals spanning a total of $\Delta v \approx 650$ km s^{-1} (Figure 2.22). We define three subsystems across the complex. We present the ionic column densities measured with AODM in Table 2.10. One notes moderate absorption in subsystem A and strong absorption in subsystems B and C from a series of low ions, including O^0, Si^+, C^+, Fe^+ and Al^+. Subsystems B and C are characteristic of Lyman limit systems where the large H I opacity self-shields gas from local or background UV sources (e.g. Prochaska et al. 2015). Elements therefore occupy the first ionization state with an ionization potential greater than 1 Ryd. Furthermore, there is only weak Si IV and C IV absorption. Altogether the data suggest an optically thick gas.

The Lyβ, Lyγ and Lyδ profiles show absorptions in three distinct velocity intervals corresponding to the three subsystems. The absence of strong damping wings in the the Lyα absorption profiles demands $N_{\mathrm{HI}}^{\mathrm{A}} < 10^{18.0}$ cm^{-2}, $N_{\mathrm{HI}}^{\mathrm{B}} < 10^{18.8}$ cm^{-2} and $N_{\mathrm{HI}}^{\mathrm{C}} < 10^{18.4}$ cm^{-2}. Assuming maximum $b_{\mathrm{A,B,C}}$ values of 60 km s^{-1} and absorption dominated by single components, as implied by the H I and metal line profiles, the measured equivalent widths imply $N_{\mathrm{HI}}^{\mathrm{A}} > 10^{14.8}$ cm^{-2}, $N_{\mathrm{HI}}^{\mathrm{B}} >$

$10^{16.0}$ cm^{-2} and $N_{\rm HI}^{\rm C} > 10^{15.2}$ cm^{-2}. The asymmetric Lyα absorption profile of subsystem B implies modest blending with a weak H I component. The Lyγ profile is blended with an unrelated H I component of $N_{\rm HI} \approx 10^{14.8}$ cm^{-2} at $z \approx 1.7211$. We adopt $N_{\rm HI}^{\rm A} = 10^{16.8 \pm 0.6}$ cm^{-2}, $N_{\rm HI}^{\rm B} = 10^{18.6^{+0.2}_{-0.6}}$ cm^{-2} and $N_{\rm HI}^{\rm C} = 10^{18.2^{+0.3}_{-0.6}}$ cm^{-2}, where the error in $N_{\rm HI}$ is dominated by Lyα forest contamination and line saturation.

Multiple ionization states of the same element, Fe^{+}/Fe^{2+}, Si^{+}/Si^{3+}, Al^{+}/Al^{2+} and C^{+}/C^{3+}, provide observational constraints on U. The gas shows systematically stronger low ion absorption and correspondingly lower U values, $\log U < -3$, than the majority of the QPQ8 sample. We adopt $\log U_{\rm A} = -3.2$, $\log U_{\rm B} = -3.4$, and $\log U_{\rm C} = -3.1$, giving $x_{\rm HI,A} = 0.01$, $x_{\rm HI,B} = 0.08$, and $x_{\rm HI,C} = 0.02$, and $N_{\rm H}^{\rm A} = 10^{18.9}\,{\rm cm}^{-2}$, $N_{\rm H}^{\rm B} = 10^{19.7}\,{\rm cm}^{-2}$, and $N_{\rm H}^{\rm C} = 10^{20.0}\,{\rm cm}^{-2}$.

J0932+0925—The ions show absorption in roughly three distinct velocity intervals spanning a total of $\Delta v \approx 1200\,{\rm km\,s^{-1}}$ (Figure 2.23) that demarcate three subsystems. We present the ionic column densities measured with AODM in Table 2.11. One notes strong C IV absorption in subsystem B and moderate C IV absorption in subsystems A and C. C II absorption is weak in subsystem A and absent in subsystems B and C. The intermediate ion Si III λ1206 transition is located in a relatively clean region of the Lyα forest. Qualitatively the data indicates a highly ionized gas.

Only the Lyα and the Lyβ absorption profiles have sufficient S/N for analysis. The stronger absorption features of subsystems A and B are well constrained by both the Lyα and the Lyβ profiles. Subsystem C and the weaker components of subsystems A and B which have their Lyβ profiles blended with Lyα forest lines, all have $N_{\rm HI}$ values on the linear part of the curve of growth. For the strongest component in subsystem A, the measured equivalent width constrains $10^{14.5}$ cm^{-2} $< N_{\rm HI}^{\rm A} < 10^{17.5}\,{\rm cm}^{-2}$ assuming that b_A lies in the range 15–60 km s^{-1}. The strongest absorption feature of subsystem B is asymmetric in Lyα and Lyβ, suggesting that it contains two H I components, as modeled. Our best-fit solution gives a total $N_{\rm HI}^{\rm B} = 10^{15.1^{+0.3}_{-0.3}}$ cm^{-2}, where the errors are dominated by uncertainty in continuum placement and Lyα forest line blending. The $N_{\rm HI}$ values for subsystem C are well constrained by the unsaturated Lyαprofile.

This system has Si^{2+} and Si^{3+} detections, which constrain the U value for the three subsystems. These are also consistent with the constraints derived from C^{+}/C^{3+}.

J1026+4614—The ions show absorption in two velocity intervals spanning a total of $\Delta v \approx 240$ km s^{-1} (Figure 2.24). We present the ionic column densities in Table 2.12. This is the only member of the QPQ8 sample with strong absorption from the N V doublet, although we also note that it is also one of the few where those transitions lie outside the Lyα forest. Together with the lack of low ions, the data suggest the ionization state of the gas is extreme. It is peculiar that in subsystem A the lines of the seemingly unsaturated C IV doublet $\lambda\lambda1548$, 1550 have similar optical depth, i.e., inconsistent with the oscillator strength ratio of 2 to 1. We suspect hidden saturation because there is no evidence for partial covering in the other observed doublets, and treat the C IV $\lambda1548$ measurement as a lower limit. Figure 2.24 presents the the Lyα, Lyβ, Lyγ and Lyδ profiles of this absorption system.

All of the components become unsaturated by Lyγ and therefore yield precise measurements for the column densities. The Lyβ absorption profile is blended with two Lyα forest lines of respectively $N_{\rm HI} \approx 10^{14.7}$ cm^{-2} and $N_{\rm HI} \approx 10^{15.3}$ cm^{-2} located at respectively $z \approx 2.6658$ and $z \approx 2.6669$. The Lyγ absorption profile is blended with a Lyα forest line of $N_{\rm HI} \approx 10^{14.2}$ cm^{-2} at $z \approx 2.4773$. The Lyδ absorption profile is blended with a Lyα forest line of $N_{\rm HI} \approx 10^{15.8}$ cm^{-2} at $z \approx 2.3951$. Modeling these blends together with the Lyman series absorption, we recovered a best-fit solution with $N_{\rm HI}^{\rm A} = 10^{15.4\pm0.2}$ cm^{-2} and $N_{\rm HI}^{\rm B} = 10^{14.6\pm0.1}$ cm^{-2}. The errors are dominated by continuum placement at the higher Lyman series lines.

The non-detection of lower ionization states in subsystem A constrain $\log U >$

-2.3. If we assume relative solar abundances, the measured $\mathrm{Si}^{3+}/\mathrm{N}^{4+}$ ratio implies $\log U \approx -1.9$. We adopt a larger uncertainty toward higher U values to account for non-solar abundances. Our model for subsystem B, which does not show N V absorption, has a lower U value consistent with the various constraints. We adopt a larger uncertainty for higher U values to allow for an enhanced intrinsic Si/C abundance ratio.

J1038+5027—The ions show absorption spanning a total of $\Delta v \approx 260\,\mathrm{km\,s^{-1}}$ (Figure 2.25). We present the ionic column densities in Table 2.13. There is strong C IV absorption and moderate Si IV absorption, together with weak low ions suggesting a highly ionized gas.

We present the Lyα profile of this absorption system. The Lyβ profile is blended with a strong absorption system and is not useful for N_{HI} modeling. The asymmetric Lyα profile is well modeled by least two H I components, with the weaker one unsaturated at Lyβ. The lack of obvious damping wings restricts $N_{\mathrm{HI}} < 10^{18.4}\,\mathrm{cm^{-2}}$. Assuming a maximum b-value of $60\,\mathrm{km\,s^{-1}}$, the Lyα equivalent width requires $N_{\mathrm{HI}} > 10^{15.3}\,\mathrm{cm^{-2}}$. We adopt a total $N_{\mathrm{HI}} = 10^{16.6\pm0.5}\,\mathrm{cm^{-2}}$, where the large errors are due to line saturation.

The $\mathrm{Si}^{+}/\mathrm{Si}^{3+}$ and $\mathrm{C}^{+}/\mathrm{C}^{3+}$ ratios place lower limits on U. To better constrain the U value, we also consider the $\mathrm{Si}^{+}/\mathrm{C}^{3+}$ ratio under the assumption of solar relative abundances. Adopting $\log U = -2.2$, we recovered $x_{\mathrm{HI}} = 0.0005$, corresponding to $N_{\mathrm{H}} = 19.9\,\mathrm{cm^{-2}}$.

J1144+0959— This very complex absorption system exhibits a velocity spread of nearly 2000 $\mathrm{km\,s^{-1}}$ (Figure 2.26), which we divide into six subsystems. We present the ionic column densities in Table 2.14. Given the large velocity separation of the subsystems, we examined the possibility that some of the gas is unassociated with the foreground quasar. The total equivalent width of C IV 1548 of subsystems A, B, C, and D, $W_{1548} = 0.86\,\text{Å}$, is large. The C IV survey conducted by Cooksey et al. (2013) reported the incidence of strong C IV absorbers of equivalent width > 0.6 Å at $z \approx 2.97$ to be $\frac{dN_{\mathrm{CIV}}^{>0.6\mathring{\mathrm{A}}}}{dz} = 0.83$. Thus in a ±1500 $\mathrm{km\,s^{-1}}$

window around $z \approx 2.97$, the probability of finding at least one strong C IV absorber is 3%. According to the QSO-C IV clustering analysis in QPQ7 and Vikas et al. (2013), clustering would at most quadrupole this probability. We consider it unlikely that subsystems A, B, C, and D are not physically associated with the foreground quasar. We note further that the positive detections of C II $\lambda1334$ and Al II $\lambda1670$, which have an even a smaller random incidence, strongly imply the physical association of all the gas to the environment of J1144+0959FG.

Subsystem A shows strong C IV, strong C III absorption in an apparently clean region of the Lyα forest, and the absence of low ion absorption. Subsystem B shows moderate absorption from C^+ and strong absorption from C^{3+} and Si^{3+}. Subsystem C shows moderate absorption from C^+ and weak absorption from C^{3+} and Si^{3+}. Subsystem D shows moderate absorption from C^+ and moderate absorption from C^{3+} and Si^{3+}. As a group subsystems A, B, C, and D trace a highly ionized gas. Subsystem E shows moderate absorption from high ions C^{3+} and Si^{3+} and no corresponding low ion absorption. Lastly, subsystem F shows strong absorption from high ions C^{3+} and Si^{3+} and strong absorption from low ions O^0, C^+, Si^+, Al^+ and Fe^+.

We present the Lyα, Lyβ, and Lyγ velocity profiles of this complex absorption system. The data also cover Lyδ, but the majority of the complex is blended strongly with a damped Lyα system with $N_{\rm HI} \approx 10^{20.3}$ cm^{-2} at $z \approx 2.0933$. Two groups of absorbers with associated metal lines separated by $\sim 1000\,{\rm km\,s^{-1}}$ are found in a $\pm1500\,{\rm km\,s^{-1}}$ window around $z_{\rm fg}$. Subsystem A has four weak components, among which two are associated with high ion absorption, e.g. C IV, and possibly O VI. Its total $N_{\rm HI}^{\rm A} = 10^{13.5\pm0.2}\,{\rm cm^{-2}}$ is well constrained. In the Lyman series, subsystems B and C are blended together, but their centroid velocities can be precisely constrained by the unblended absorption profiles of low ions. The absence of strong Lyα damping wings demands a total $N_{\rm HI}^{\rm B+C} < 10^{18.7}\,{\rm cm^{-2}}$. Assuming a maximum $b_{\rm B,C}$ value of 60 km s^{-1}, the large Lyα equivalent width demands a total $N_{\rm HI}^{\rm B+C} > 10^{16.1}$ cm^{-2}. Our best-fit solution gives $N_{\rm HI}^{\rm B} = 10^{18.1^{+0.2}_{-0.4}}$ cm^{-2} and

$N_{\rm HI}^{\rm C} = 10^{18.3^{+0.2}_{-0.4}}$ cm^{-2}, where the errors are dominated by line blending and line saturation. Subsystem D shows multiple components, one associated with ions and three weaker components that lack any metal ion detection. For the stronger component, the lack of strong Lyα damping wings demands a total $N_{\rm HI}^{\rm D} < 10^{19.2}$ cm^{-2}, while the large Lyα equivalent width requires $N_{\rm HI}^{\rm D} > 10^{15.6}$ cm^{-2}, assuming $b_{\rm D} < 60$ km s^{-1}. The three weaker components at $v \approx -700$ km s^{-1} have Lyα and Lyβ equivalent widths that lie on the linear part of the curve of growth and hence are tightly constrained. Summing up the four components, our best-fit solution gives a total $N_{\rm HI}^{\rm D} = 10^{17.9\pm0.5}$ cm^{-2}, where the errors are dominated by line blending and saturation. For subsystem E, the unsaturated Lyman lines yield a precise constraint of $N_{\rm HI}^{\rm E} = 10^{15.6\pm0.2}$ cm^{-2}. Subsystem F contains two components associated with metal absorption and one component that is not associated with metals. The lack of strong Lyα damping wings restricts $N_{\rm HI}^{\rm F} < 10^{18.5}$ cm^{-2}, while the large Lyα equivalent width demands a total $N_{\rm HI}^{\rm F} > 10^{16.1}$ cm^{-2}. Our best-fit solution gives a total $N_{\rm HI}^{\rm F} = 10^{18.4^{+0.2}_{-0.4}}$ cm^{-2}, where the errors are dominated by blending in the Lyα, Lyβ and Lyγ profiles and line saturation. Altogether, we adopt $N_{\rm HI}^{\rm total} = 10^{18.8^{+0.2}_{-0.4}}$ cm^{-2} with the upper bound a strict limit given the absence of Lyαdamping wings.

For subsystem A, the $\rm C^+/C^{3+}$ and $\rm C^{2+}/C^{3+}$ ratios constrain $-2.2 < \log U_{\rm A} < -1.5$. We expect the U value to lie closer to the upper value because C III is only mildly saturated and the $\rm Si^{3+}/C^{3+}$ ratio is consistent with this estimate. For subsystems B and C, the observed $\rm Si^+/Si^{3+}$ ratios put $U_{\rm B,C}$ at a different value than $\rm C^+/C^{3+}$ does, indicating a multiphase absorber. We give stronger weight to the constraint from $\rm Si^+/Si^{3+}$ regarding the lower ionization gas phase. For subsystem D, the observed $\rm Si^+/Si^{3+}$ and $\rm C^+/C^{3+}$ ratios constrain $U_{\rm D}$ well. For subsystem E, the observed $\rm C^+/C^{3+}$ ratio gives a precise value for $U_{\rm E}$ that is fully consistent with the observed $\rm Si^+/Si^{3+}$ and $\rm Al^+/Al^{2+}$ ratios. Subsystem F exhibits positive detections from a wide range of ions. Despite the significant low ion absorption, the measurements imply a highly ionized system. This is argued from the $\mathrm{Si}^+/\mathrm{Si}^{3+}$, $\mathrm{Al}^+/\mathrm{Al}^{2+}$, and $\mathrm{C}^+/\mathrm{C}^{3+}$ ratios. It is further implied by the very low $\mathrm{O}^0/\mathrm{Fe}^+$ ratio, as discussed in Section 2.4.2. Unfortunately none of these is highly constraining because a number of the measurements are formally lower limits. Adopting the C^+, C^{3+}, and Si^{3+} values as measurements instead of limits, their measured ratios suggest $\log U_\mathrm{F} \approx -2$. We adopt this value and a large uncertainty.

J1145+0322—The ions show absorption spanning a total of $\Delta v \approx 300\,\mathrm{km\,s^{-1}}$ (Figure 2.27). We present the ionic column densities in Table 2.15. Absorption from low ions is strong for C^+, Si^+, Al^+ and Mg^+ and moderate for Fe^+ and Mg^0. There is also strong absorption from high ions Si^{3+} and C^{3+}. Together the data suggest a partially ionized gas characteristic of Lyman limit systems.

Figure 2.27 presents the Magellan/MagE spectrum at Lyα. Given the relatively low S/N of these data, we also included a lower-resolution Keck/LRIS spectrum in the profile fits. The dominant absorber is asymmetric, suggesting blending with a weaker, unresolved component. The absorption at $v \approx +500\,\mathrm{km\,s^{-1}}$ is not associated with any metal ion detection. Assuming a single component with a b value ranging from 15 to $60\,\mathrm{km\,s^{-1}}$, the large Lyα equivalent width and the lack of strong damping wings together restrict the range of N_HI to be $10^{18.0}$–$10^{18.6}$ $\mathrm{cm^{-2}}$. Our best-fit solution gives a total $N_\mathrm{HI} = 10^{18.4\pm0.4}$ $\mathrm{cm^{-2}}$, where the errors are dominated by the lack of higher Lyman series lines.

The high $\mathrm{Si}^+/\mathrm{Si}^{3+}$ ratio suggests a lower ionization state with $\log U \approx -3$. On the other hand, the $\mathrm{Al}^+/\mathrm{Al}^{3+}$ and highly saturated C IV doublet impliy higher U values. These conflicting constraints suggest that the profile is a blend of material with varying ionization state, although there is no obvious evidence for such a blend in the line profiles. We proceeded by adopting $\log U = -2.9$ with a larger uncertainty toward higher values.

J1204+0221—As reported previously in QPQ3, the ions show absorption spanning a total of $\Delta v \approx 760$ km $\mathrm{s^{-1}}$ (Figure 2.28, or see Figure 3 of QPQ3) that we separate into three subsystems. We present ionic column densities in Table 2.16. We refer the reader to QPQ3 for details on the H I and photoionization modeling.

Summarizing the previous findings, there is absorption from a series of low ions O^0, C^+, Si^+, N^0 , N^+, Al^+ and Fe+, characteristic of optically thick absorbers. Weak Si IV and C IV absorption indicates that the ionization state of the gas is not extreme. The absence of strong N V and O VI limits the flux of photons with energies $h\nu \gtrsim 4$ Ryd and rules out a collisionally ionized gas with $T \approx 10^5\,\mathrm{K}$. The strong N II absorption traces the N I profile for subsystems A and C, but the ionic ratio N^+/N^0 varies significantly across subsystem B. In QPQ3, the N II column density of subsystem A is obtained by Voigt profile modeling, while in this study it is obtained by AODM. In our AODM treatment, if a line is resolved, as in the case for this echelle sightline, we consider a component to be saturated if the minimum of the absorption trough is below 0.5 times the 1σ error. Hence, while a good measurement for the N II column density is reported in QPQ3, a lower limit is reported in QPQ8 for consistency across the whole sample.

We present the Lyα and Lyβ profiles of this absorption system and reproduce the results shown in Figure 2 of QPQ3. For subsystems A and C, the absence of strong Lyα damping wings restricts $N_{\rm HI}^{\rm A,C} < 10^{19}\,\mathrm{cm^{-2}}$, while the Ly$\beta$ profile demands $b_{\rm A,C} < 25\,\mathrm{km\,s^{-1}}$. Our best estimates give $N_{\rm HI}^{\rm A,C} = 10^{18.6\pm0.4}\,\mathrm{cm^{-2}}$. With the constraints on subsystems A and C, we estimated $N_{\rm HI}^{\rm B} = 10^{19.6\pm0.2}\,\mathrm{cm^{-2}}$, which is insensitive to the $b_{\rm B}$ value.

In QPQ3, we adopted $\log U \lesssim -3$ for all three subsystems. We have revised our estimate in this study. This absorption system shows a varying U parameter. For subsystems A and C, the observed Fe^+/Fe^{2+} ratio requires a lower U parameter than other ionic ratios. Nonetheless the Si^+/Si^{3+}, Al^+/Al^{2+}, N^0/N^+ and C^+/C^{3+} ratios are roughly consistent with a single U value for each of subsystems A and C. For subsystem B, due to the high $N_{\rm HI}$ column, the ionic ratios predicted by Cloudy are rather insensitive to U. Apart from the Si^+/Si^{3+} ratio, other ionic ratios are roughly consistent with a single U. There is compelling evidence that the foreground quasar is not shining on the gas for any reasonable gas density. The observed ionic ratios are also consistent with the EUVB being dominant if $n_{\rm H} \lesssim$

10^{-3} cm^{-3}. Detailed component-by-component fitting of the echelle spectrum reveals that the low and high ions do not have the same velocity structure. The low-to-high ion ratios, in particular C^+/C^{3+}, should therefore be considered lower limits for the low ionization phase. We adopted $\log U_{\rm A} = -3.3$, $\log U_{\rm B} = -3.6$ and $\log U_{\rm C} = -3.6$.

J1420+1603—The ions show complex absorption in a series of components spanning $\Delta v \approx 1350\,{\rm km\,s^{-1}}$ (Figure 2.29) that we separate into six subsystems. We present ionic column densities in Table 2.17. There is strong absorption throughout the interval from low ions, e.g., O^0, Si^+, C^+, Al^+, Fe^+,Mg^+ and Mg^0. The absorption consistent with C II* $\lambda1335$ from subsystem F cannot be associated to the C II $\lambda1334$ transition at another velocity. Together with modest absorption from high ions Si^{3+} and C^{3+}, the data suggest a partially ionized gas. The spectral resolution of FWHM $\approx 51\,{\rm km\,s^{-1}}$ implies that C II $\lambda1334$ and C IV $\lambda1548$ are heavily saturated in subsystems D and E. This system is one of the few cases where the N V doublet lies redward of the background quasar's Lyα forest. We report no positive detections in any of the subsystems.

Our data cover only the Lyα transition of this complex absorption system. The high S/N spectrum exhibits no evidence for strong damping wings, which constrains the total $N_{\rm HI} < 10^{19}\,{\rm cm^{-2}}$ assuming that the majority of H I gas traces the low ion metal absorption. Tighter limits may be placed on the subsystems at the ends of the interval, i.e., for subsystems A and F, $N_{\rm HI}^{\rm A,F} < 10^{18.5}\,{\rm cm^{-2}}$. The large Ly$\alpha$ equivalent widths for subsystems D and E imply $N_{\rm HI} > 10^{18}\,{\rm cm^{-2}}$ for $b_{\rm D,E} < 60\,{\rm km\,s^{-1}}$ provided line blending is not severe. We took the best estimates from ALIS and adopted a 0.4 dex uncertainty.

With the exception of the weakly absorbing subsystem A, we found that the gas throughout the system is consistent with a single ionization parameter of $\log U \approx -3$. Subsystems B, C, D, E, and F have a series of observed ionic ratios that together impose tight and consistent constraints on U. The relatively low U value reflects the strong low ion absorption observed throughout the complex.

The U parameter for subsystem A is not as well constrained, but a higher value is preferred.

J1427-0121—The ions show absorption in roughly three distinct velocity intervals spanning a total of $\Delta v \approx 670\,\mathrm{km\,s^{-1}}$ (Figure 2.30) that we divide into three subsystems. We present the ionic column densities in Table 2.18. Low ions are detected throughout the complex, including moderate absorption from O I λ1302 in subsystem C. In addition, weak C II* λ1335 absorption is detected in one of the components, implying a relatively dense gas. High ion absorption from C^{3+} and Si^{3+} is detected in subsystems A and B and remarkably absent in subsystem C. The C II, Si II and Si IV profiles are similar throughout the complex, whereas the C IV profile differs from the low ions in subsystem B. This suggests a contribution to C IV absorption from a different phase along the sightline.

We present the Lyα, Lyβ, and Lyγ transitions of this absorption system measured using Magellan/MIKE and Magellan/MagE. These data offer a terrific puzzle: the Lyα profile of subsystem A, and to a lesser extent subsystem B, is unsaturated despite the presence of strong low ion absorption and strong Lyβ and Lyγ absorption in the lower-resolution MagE data. In turn, the Lyα profile would require $N_{\rm HI} < 10^{14.5}$ cm^{-2} while the higher-order lines demand much larger $N_{\rm HI}$ values. We identify three scenarios that could resolve this apparent conundrum: (i) the gas is optically thin at Lyα, which represents the first such case reported with corresponding C II and Si II absorption, and the absorption at Lyβ and Lyγ is unrelated IGM absorption; (ii) we have performed poor sky subtraction at these wavelengths; (iii) there is unresolved Lyα emission that is 'filling in' the Lyα absorption (e.g. from fluorescence of the quasar ionizing flux Hennawi et al. 2009; Cantalupo et al. 2012; Hennawi & Prochaska 2013; Finley et al. 2013; Cai et al. 2014). Of these three, the second is the least extraordinary. We have carefully inspected the data reduction process for this spectrum and cannot identify any error, and we further note that other lines close by in wavelength, e.g. subsystem C, exhibit complete absorption. We consider the first option to the be the most improbable and therefore proceeded by fitting the Lyman series lines with a revised zero level that gives complete absorption at Lyα. At present, we interpret the non-zero flux as unresolved Lyα emission along the sightline. We estimated a total $N_{\rm HI}^{\rm A} = 10^{17.3^{+0.5}_{-1.0}}$ cm^{-2}, a total $N_{\rm HI}^{\rm B} = 10^{18.3^{+0.2}_{-1.0}}$ cm^{-2} and a total $N_{\rm HI}^{\rm C} = 10^{18.6^{+0.2}_{-1.0}}$ cm^{-2}, where the errors are dominated by blending of the absorption profiles and degeneracy between $N_{\rm HI}$ and b values.

Because the C IV profile does not closely track other ions, including Si IV, we give stronger weight to the Si^{+}/Si^{3+} ratio for constraining the U parameter. This approach is further supported by the observed C^{+}/Si^{3+} ratio. The only significant ionization gradient within a subsystem is in C IV, hence we consider the C IV column densities measured as upper limits when we perform ionization modeling. The gas in subsystems A and B, which exhibit high ions, is well modeled by $\log U = -3.1$ and -2.6 respectively. The absence of high ion absorption in subsystem C together with stronger low ion absorption requires a much lower U value. We adopted $\log U < -3.4$. Subsystem C shows C II* which allows us to constrain its electron density $n_e = 16\,{\rm cm}^{-3}$, as discussed in Section 2.4.4. This n_e implies that the gas receives an ionizing flux that is ≈ 0.25 of that expected should the quasar shine isotropically. Should the gas be illuminated only by the EUVB, the n_e would imply log $U = -7.1$.

J1553+1921—The ions show absorption spanning a total of $\Delta v \approx 500\,{\rm km\,s^{-1}}$, with the majority of low ion absorption confined to $\approx 100\,{\rm km\ s^{-1}}$ (Figure 2.31). We present the ionic column densities in Table 2.19. This is a damped Lyα system and we observe strong absorption from low ion transitions of O^{0}, Si^{+}, C^{+}, Fe^{+}, Al^{+}, Mg^{+}, and Mg^{0}. Interestingly, we find corresponding high ion absorption at the same velocities.

The Lyα profile shows strong damping wings that constrain $N_{\rm HI}$ to be $10^{20.2\pm0.1}$ cm^{-2}, insensitive to the Doppler b. The line centroid of Lyα is consistent with the peak optical depth of the low ion transitions.

The observed Si^{+}/Si^{3+} ratio suggests $\log U \approx -3.2$, if these ions trace the same phase of gas. In damped Lyα systems this is rarely the case (e.g. Wolfe & Prochaska 2000), but we do find close kinematic alignment between the Si II and Si IV transitions, and the absorption profiles are all narrow. This $\log U$ value is also consistent with the upper limits placed by the observed C^+/C^{3+} and Al^+/Al^{2+} ratios. Since the absorption at C II λ1334 is strongly saturated, the upper limit given by C^+/C^{3+} is a generous limit even if some of the C^{3+} comes from another phase of gas. We adopted $\log U = -3.2$ and allow for much lower values. At this U value, the neutral fraction is approximately 50%.

J1627+4605—Only moderate absorption from C^{3+} is detected in the system we associated with J1627+4605FG. This gas spans a velocity interval of $\Delta v \approx 150\,\mathrm{km\,s^{-1}}$ (Figure 2.32). We present the ionic column densities in Table 2.20. Together with an absence of any low ions, the data suggest a highly ionized gas.

We present the Lyα and Lyβ velocity profiles of this system. Higher-order lines are compromised by a Lyman limit system at lower redshift. Restricting to b-values ranging from 15–60 km s^{-1}, the Lyα equivalent width and the lack of Lyα damping wings of the dominant absorber require $10^{15.1}$ cm^{-2} $< N_{\mathrm{HI}} < 10^{18.0}$ cm^{-2}. There are three additional weak absorbers included in our model. We recovered $N_{\mathrm{HI}} = 10^{16.9}\,\mathrm{cm^{-2}}$ as the best-fitted value and adopted a large uncertainty of 0.8 dex owing to line saturation.

C^{3+} is the only ion detected and our ionization constraints include limits to C^+/C^{3+} and Si^{3+}/C^{3+}. These require $\log U$ greater than -2.5 and -2.2 respectively. We adopted $\log U = -2.0$ with a large uncertainty for higher values.

Figure 2.19 Combined figure for the J0225+0048 pair. (Left) Metal line transitions from the absorbers identified at velocities consistent with $z_{\rm fg} = 2.7265$. Absorptions well separated in distinct velocity intervals are designated as subsystems A, B, C, etc. and marked by the vertical dashed lines in the upper panels. Absorptions that are unrelated to the foreground quasar, e.g. blends in the Lyα forest, are presented as dashed, gray lines. The green histograms show the 1σ noise in the normalized flux. (Top right) Lyman series absorption profiles identified in the background quasar spectrum at velocities consistent with the foreground quasar of each projected pair. The green histograms show the 1σ noise in the normalized flux. The relative velocity $v = 0\,{\rm km\,s^{-1}}$ corresponds to the redshift of the foreground quasar. For each system we performed Voigt profile modeling with χ^2 minimization. We introduced H I components centered at relative velocities traced by the peak optical depths of the associated metal ion absorptions. The navy ticks mark the centroid redshifts for components traced by low ions, while the blue ticks mark the centroids for components traced by high ions. H I components not associated with any metal ions are marked with cyan ticks. Additional H I components introduced to model Lyα forest blending are omitted in the tick marks. The red curve is the convolved fit of all H I components associated with the foreground quasar, and the beige shades mark the estimated $\pm 1\sigma$ errors in H I column densities.The orange curve is the convolved fit of all H I components associated with the foreground quasar and the Lyα forest contaminations, if any. (Bottom right) Cloudy modeling of the ionization parameter U for each of the 12 quasar-associated absorption systems where metal ion column measurements are available. Solid curves show predicted ionic ratios as a function of U for a series of ion pairs. Overplotted on the curves are observational constraints of the subsystems, indicated by solid boxes, whose edges are the 1σ uncertainties, or indicated by arrows for lower and upper limits. The observations indicate a varying U.

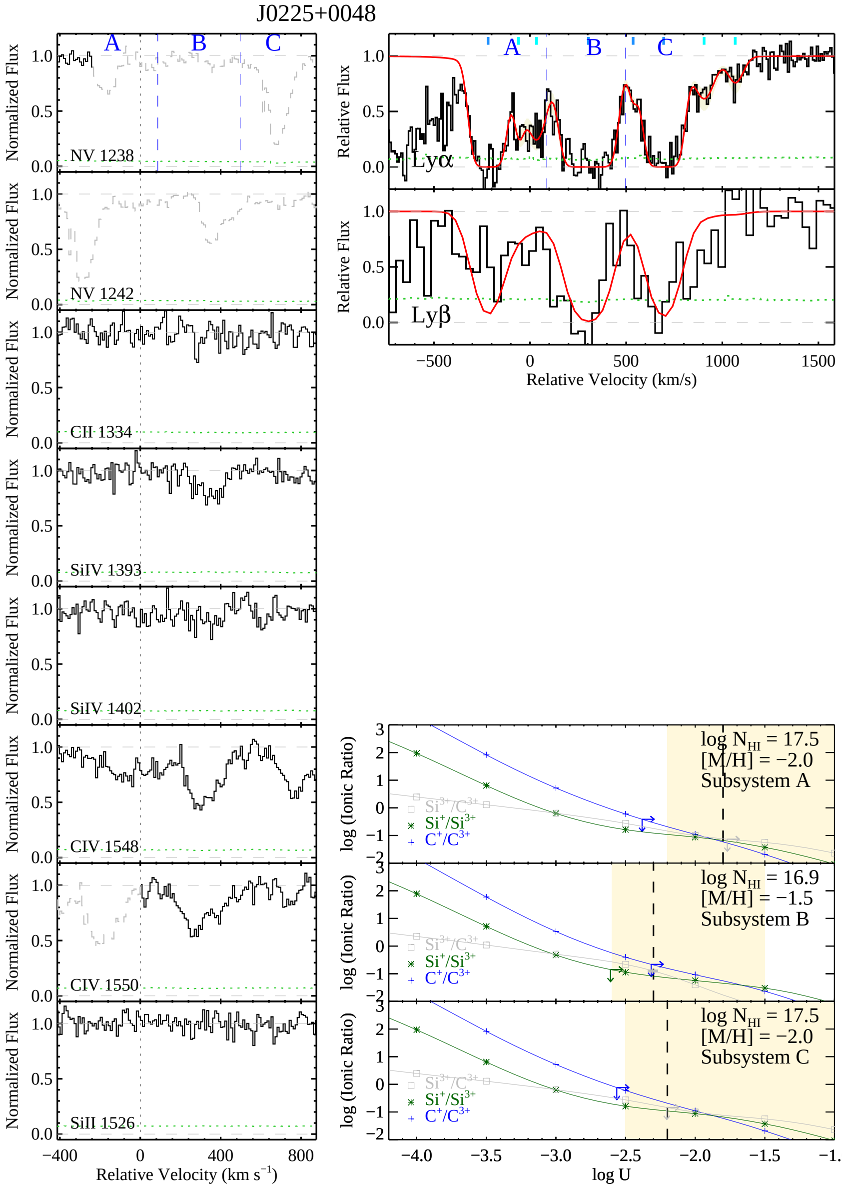
J0225+0048
A
B
C
NV 1238
NV 1242
CII 1334
SiIV 1393
SiIV 1402
CIV 1548
CIV 1550
SiII 1526
Normalized Flux
0.0
0.5
1.0
−400
0
400
800
Relative Velocity (km s^{-1})
Lyα
Lyβ
Relative Flux
−500
0
500
1000
1500
Relative Velocity (km/s)
log N_{HI} = 17.5
[M/H] = −2.0
Subsystem A
log N_{HI} = 16.9
[M/H] = −1.5
Subsystem B
log N_{HI} = 17.5
[M/H] = −2.0
Subsystem C
Si^{3+}/C^{3+}
Si^{+}/Si^{3+}
C^{+}/C^{3+}
log (Ionic Ratio)
−4.0
−3.5
−3.0
−2.5
−2.0
−1.5
−1.0
log U

Figure 2.19

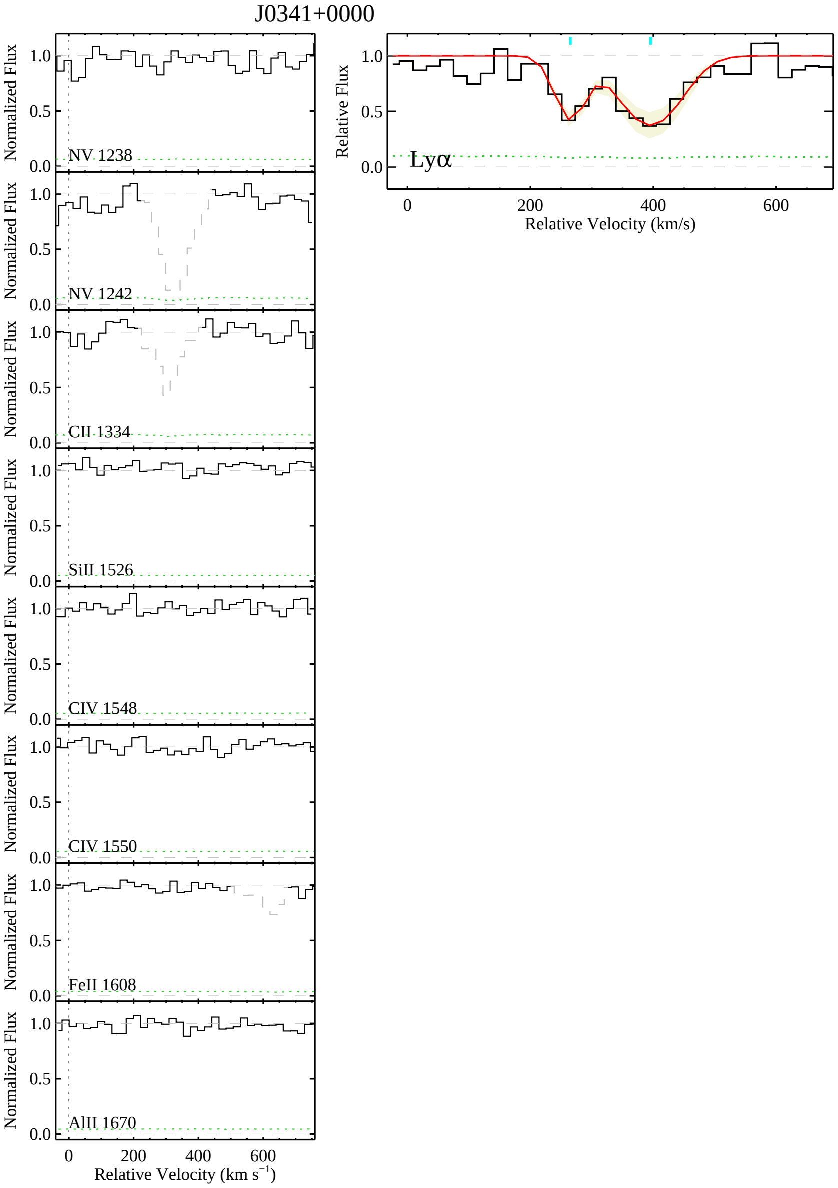

Figure 2.20 Similar to Figure 2.19 but for J0341+0000 at $z_{\rm fg} = 2.1233$.

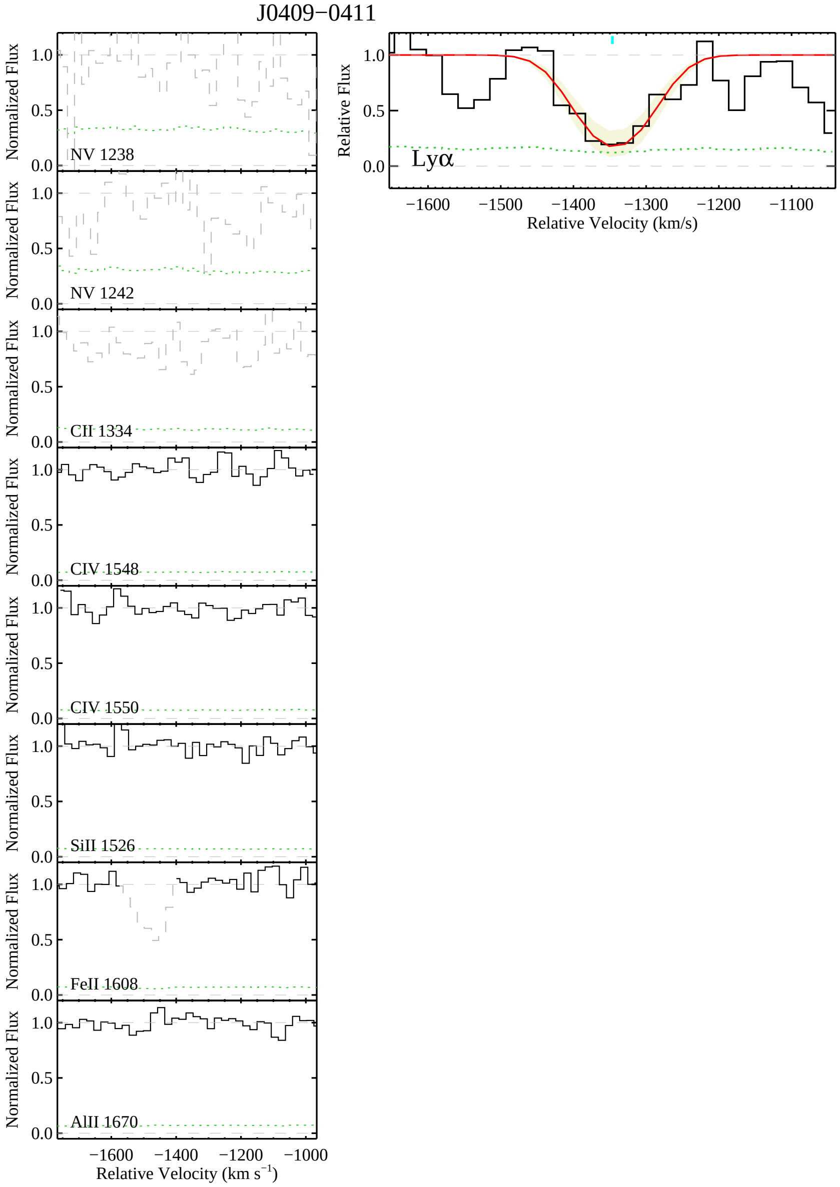

Figure 2.21 Similar to Figure 2.19 but for J0409−0411 at $z_{\rm fg} = 1.7155$.

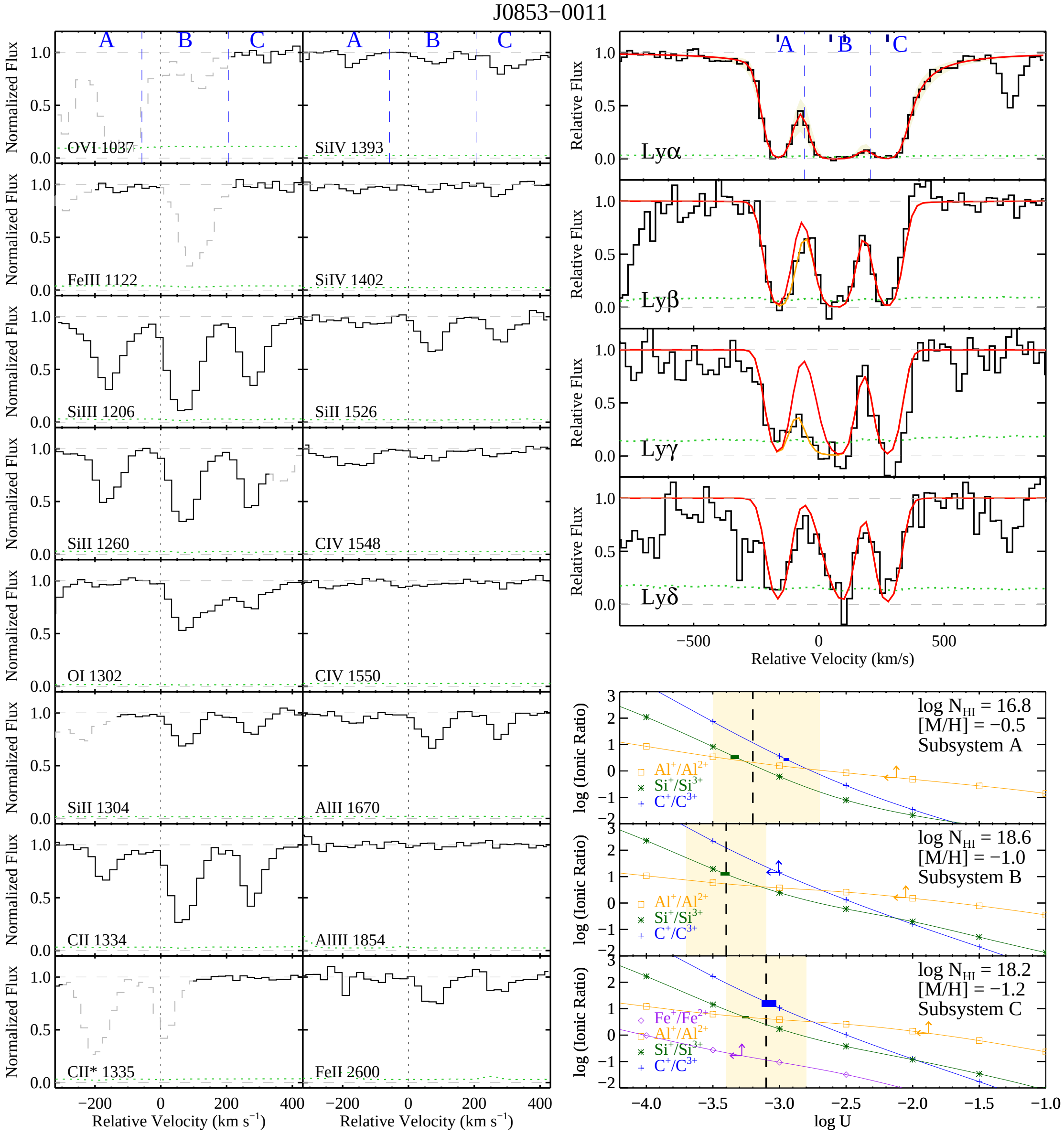

Figure 2.22 Similar to Figure 2.19 but for J0853−0011 at $z_{\rm fg} = 2.4014$.

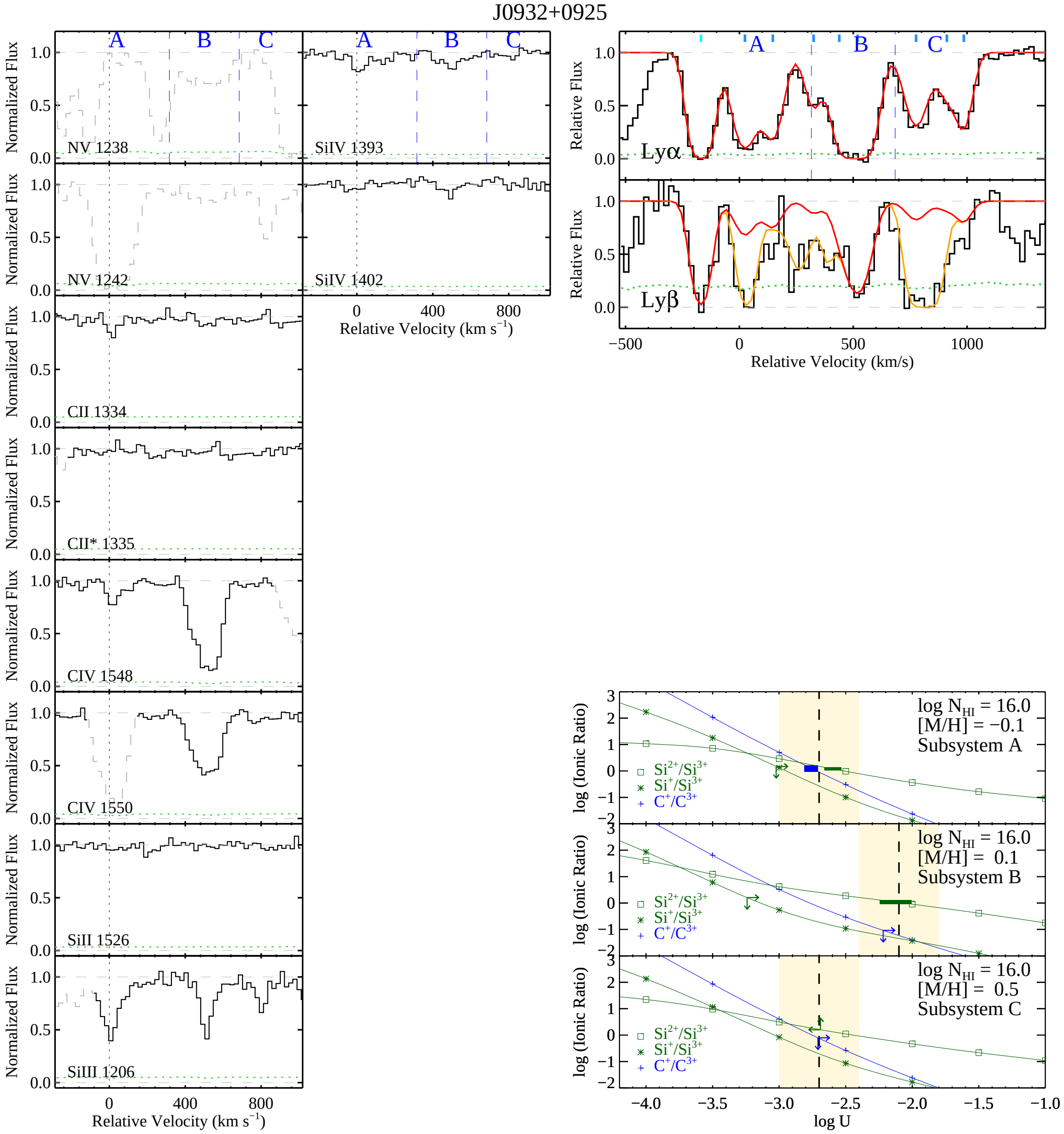

Figure 2.23 Similar to Figure 2.19 but for J0932+0925 at $z_{\rm fg} = 2.4170$.

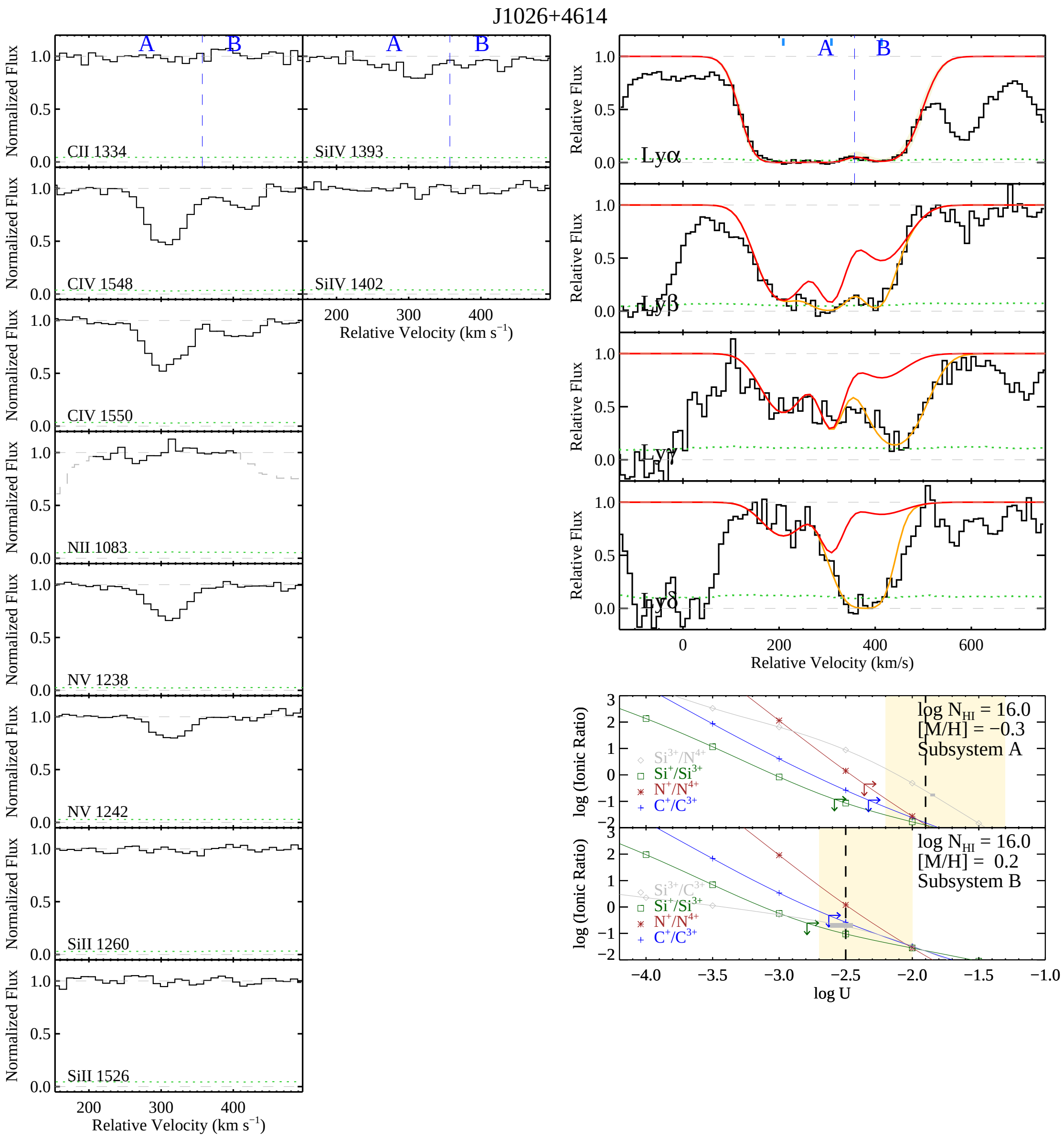

Figure 2.24 Similar to Figure 2.19 but for J1026+4614 at $z_{\rm fg} = 3.3401$.

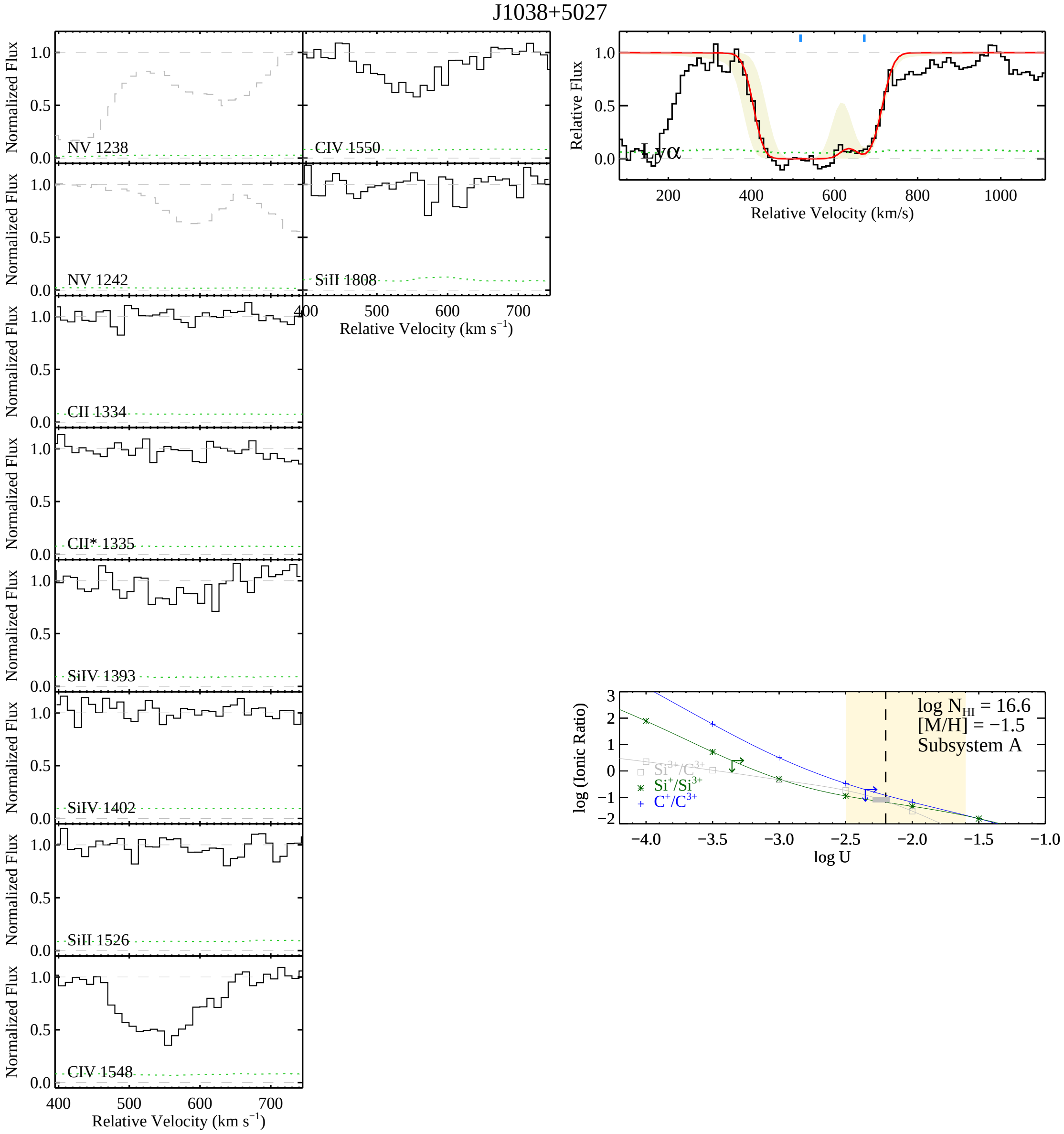

Figure 2.25 Similar to Figure 2.19 but for J1038+5027 at $z_{\rm fg} = 3.1322$.

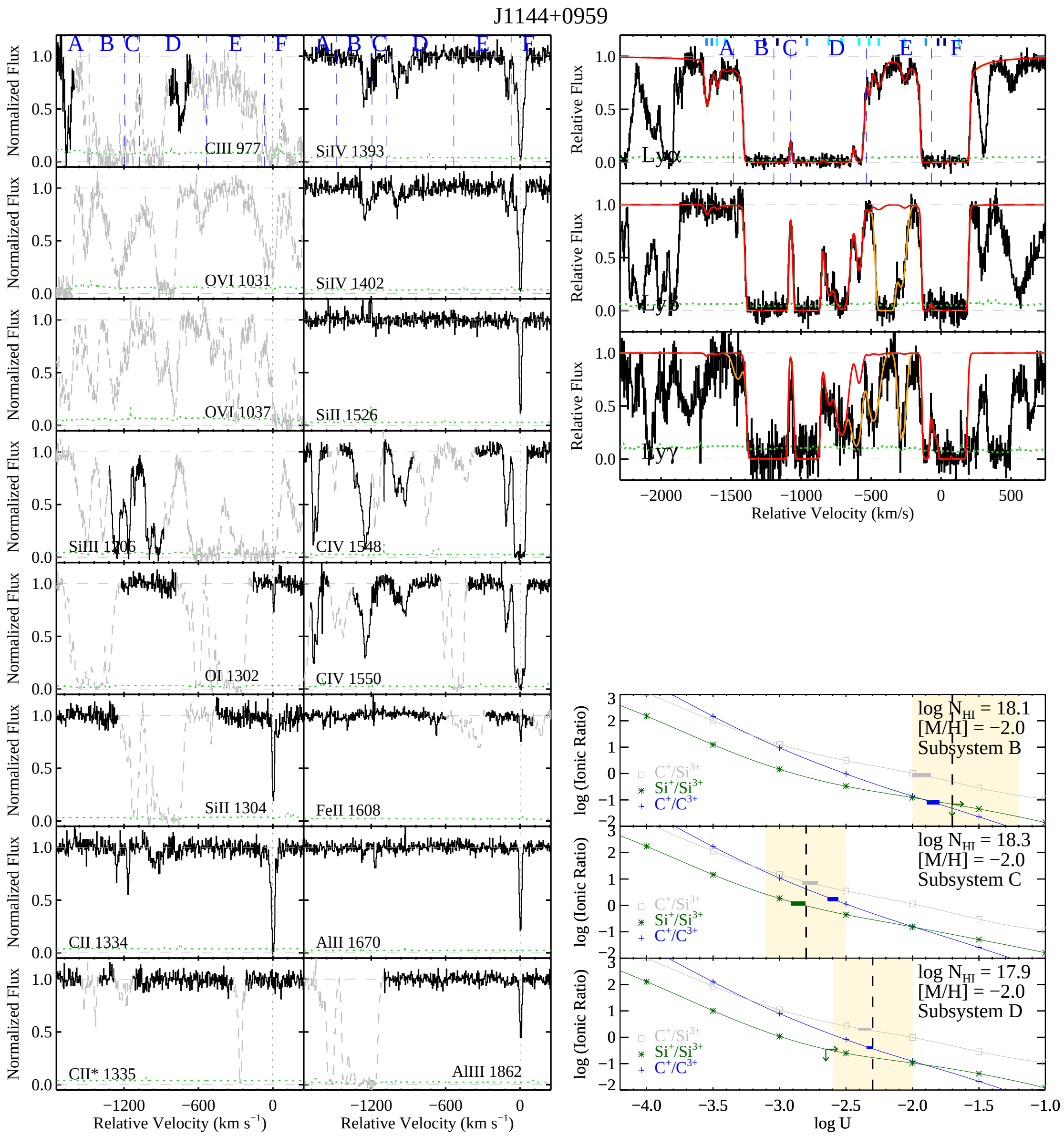

Figure 2.26 Similar to Figure 2.19 but for J1144+0959 at $z_{\rm fg} = 2.9731$.

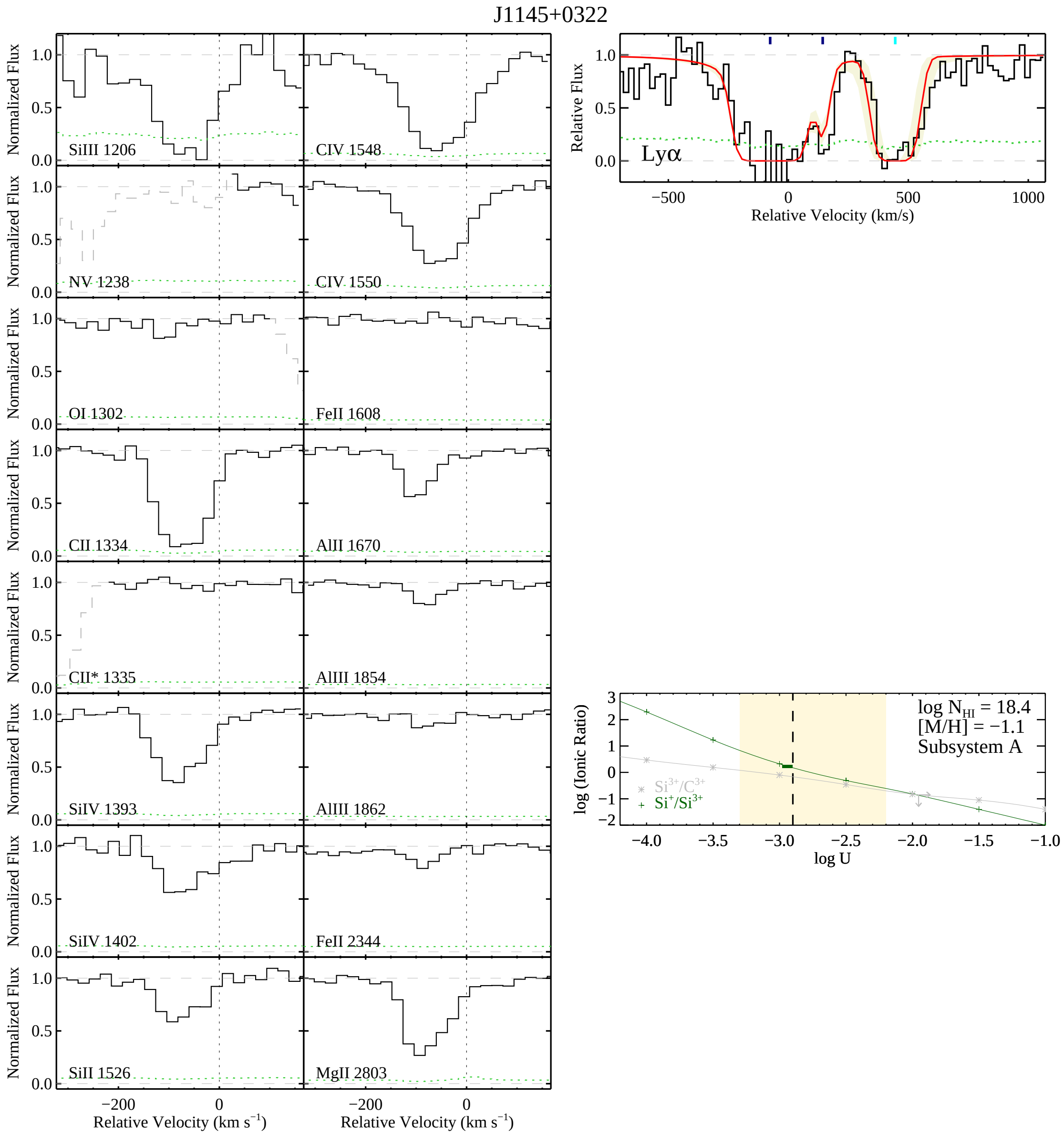

Figure 2.27 Similar to Figure 2.19 but for J1145+0322 at $z_{\rm fg} = 1.7652$.

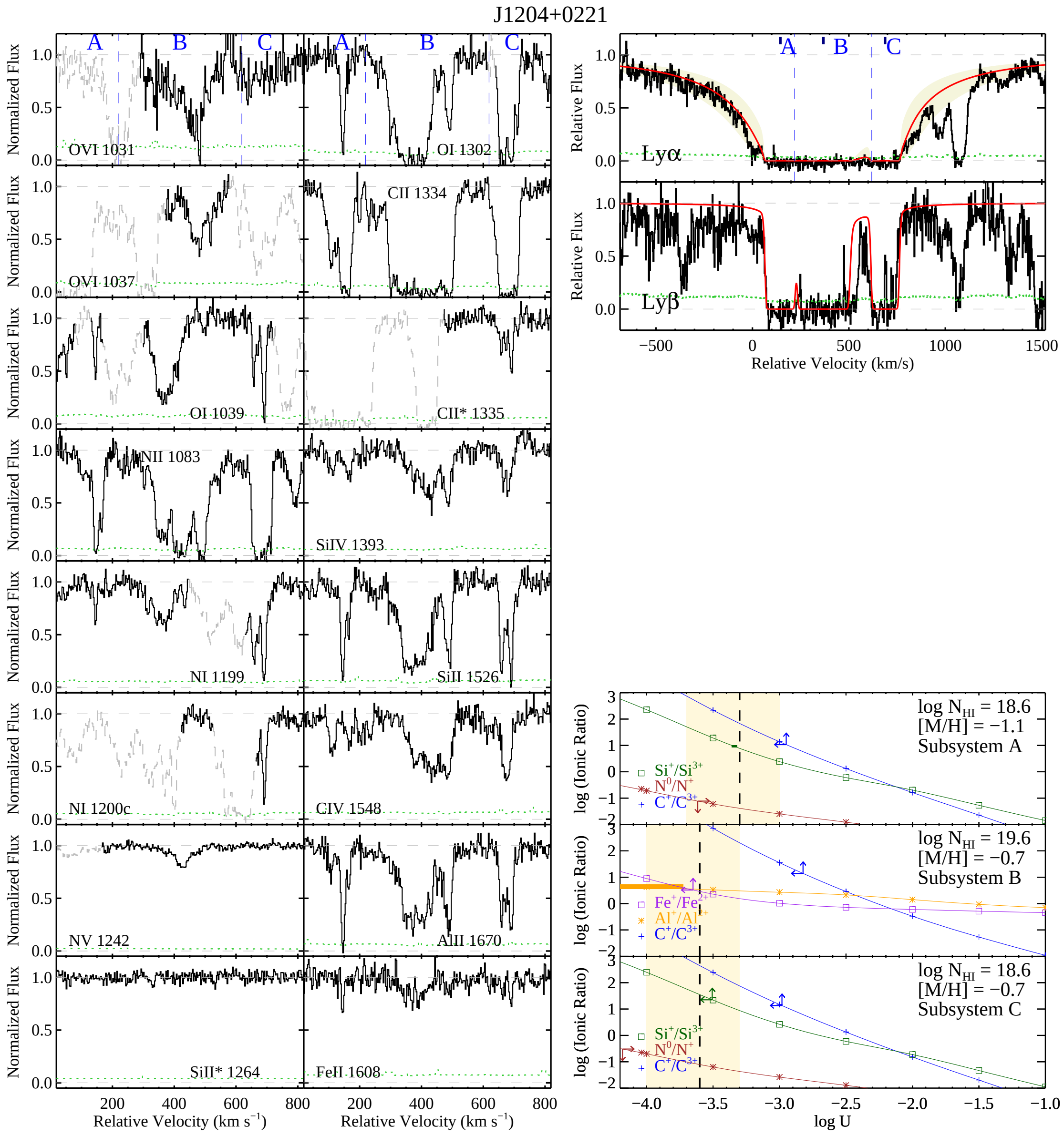

Figure 2.28 Similar to Figure 2.19 but for J1204+0221 at $z_{\rm fg} = 2.4358$.

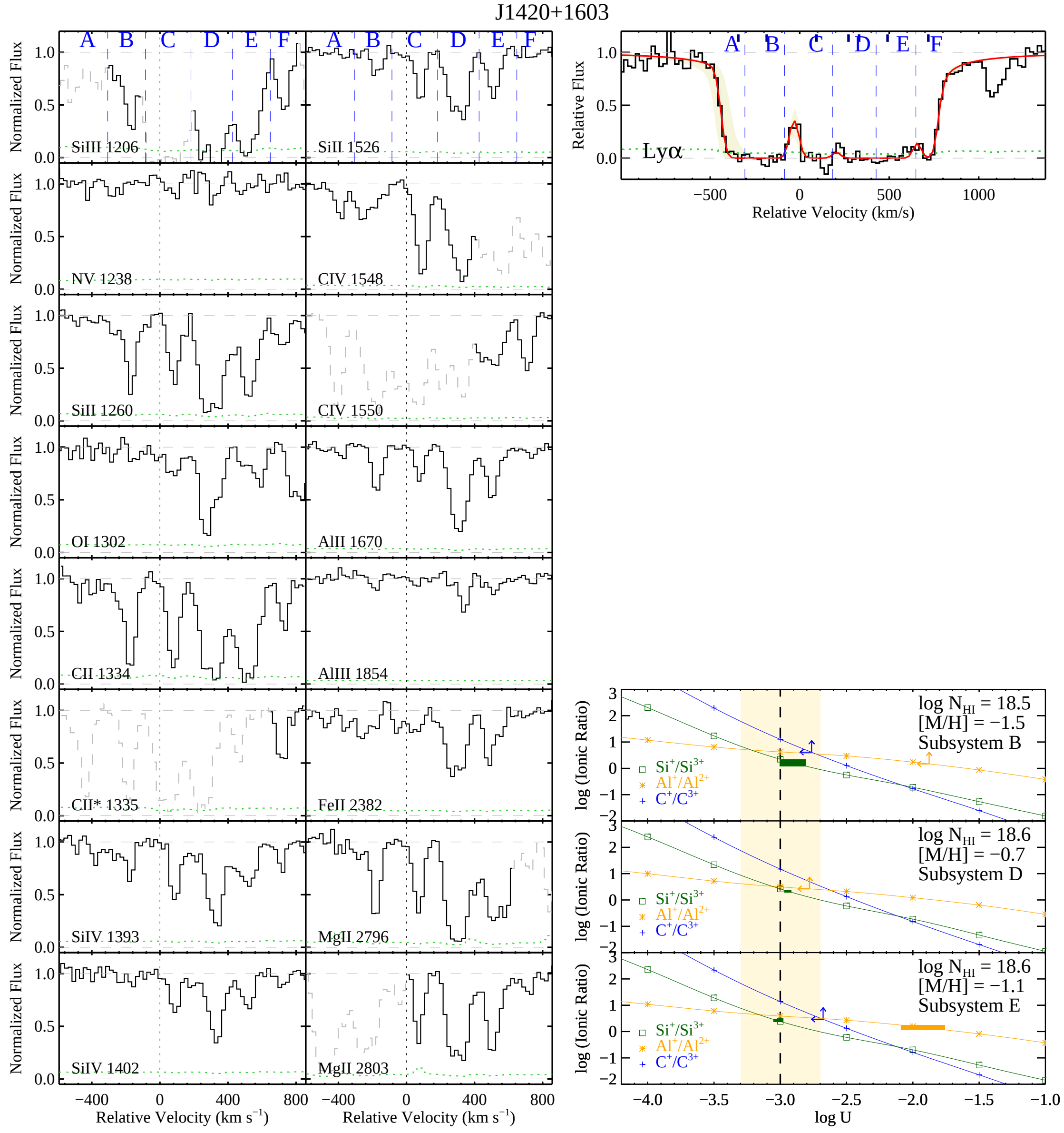

Figure 2.29 Similar to Figure 2.19 but for J1420+1603 at $z_{\rm fg} = 2.0197$.

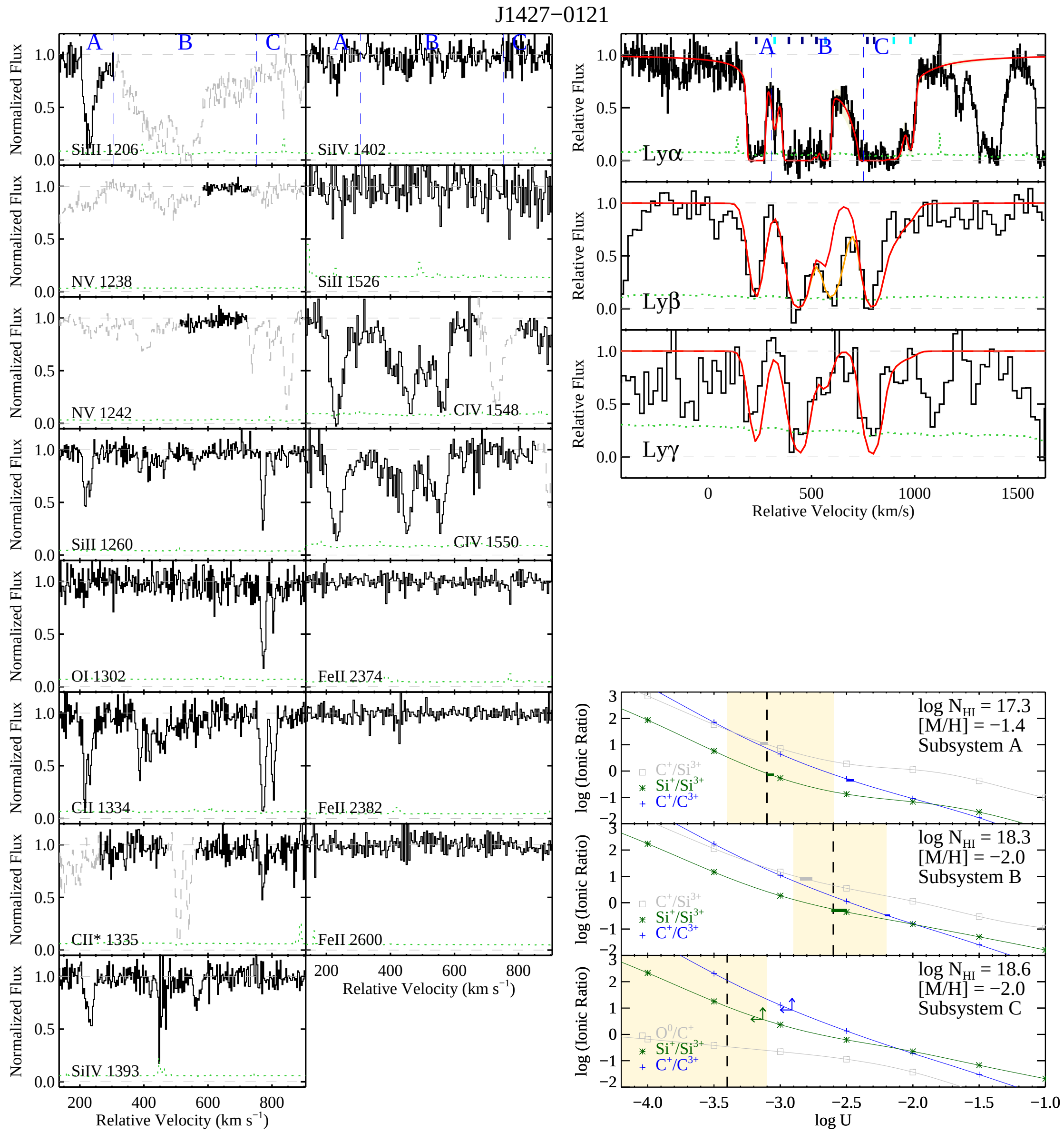

Figure 2.30 Similar to Figure 2.19 but for J1427−0121 at $z_{\rm fg} = 2.2736$.

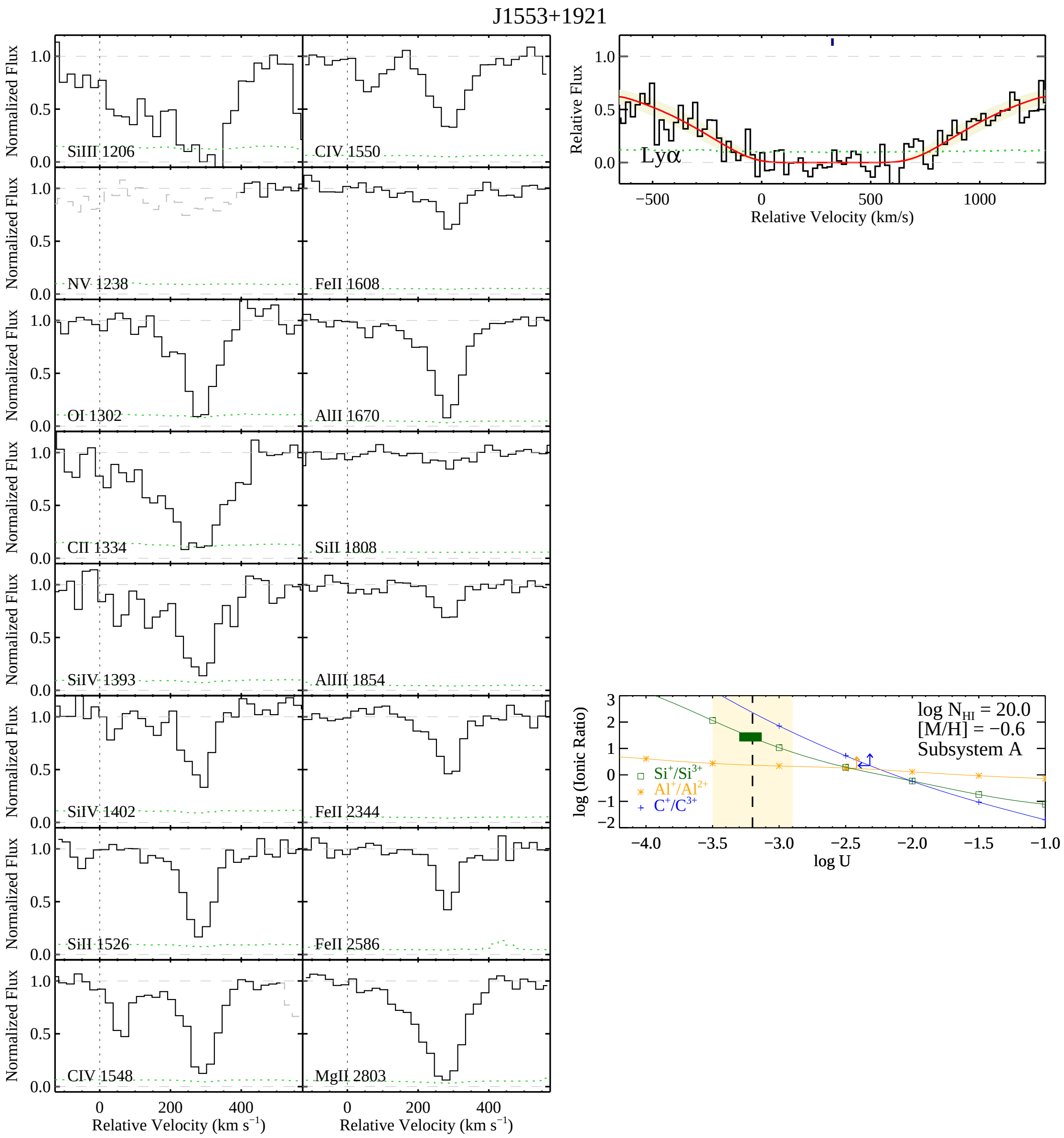

Figure 2.31 Similar to Figure 2.19 but for J1553+1921 at $z_{\rm fg} = 2.0098$.

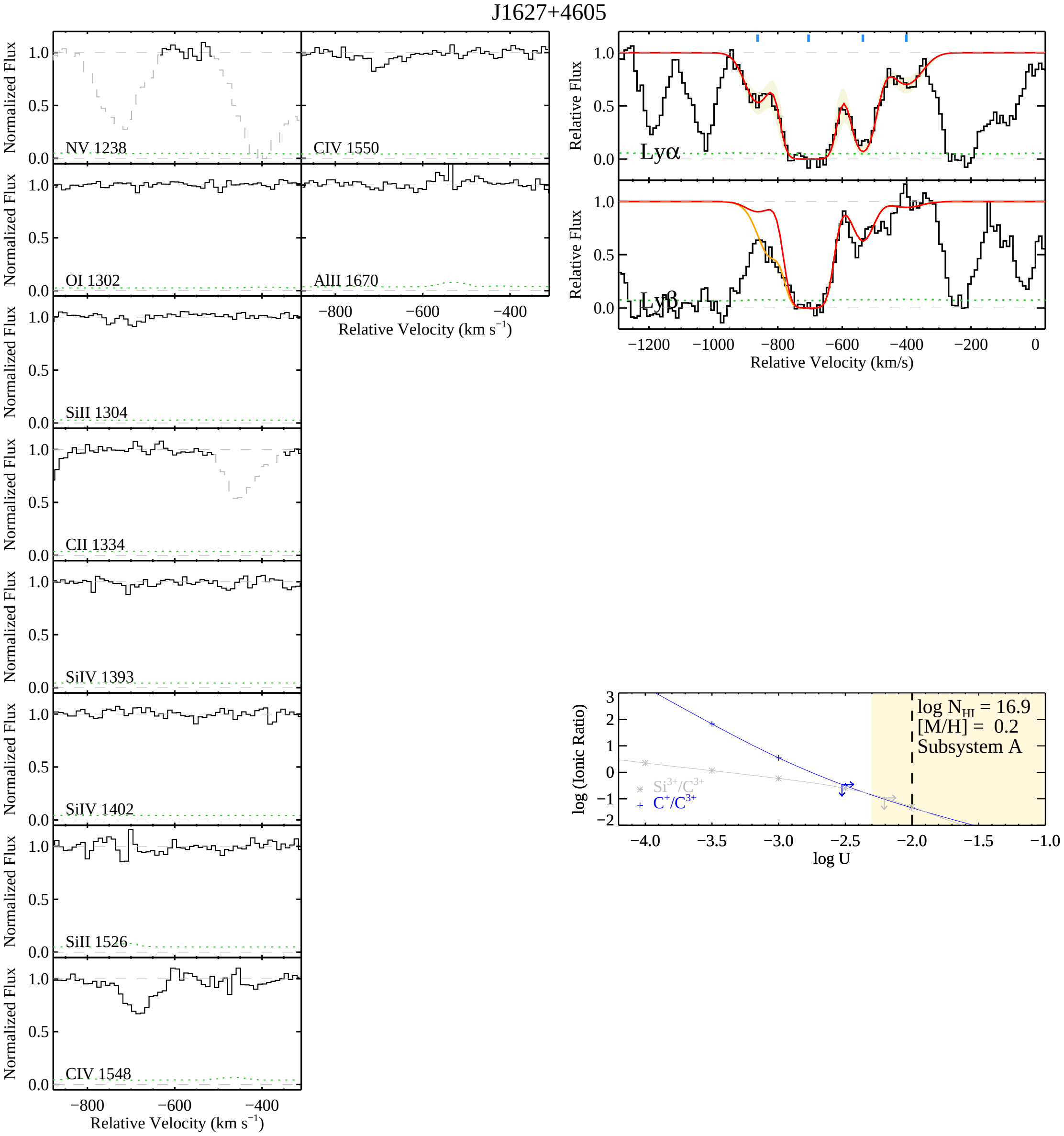

Figure 2.32 Similar to Figure 2.19 but for J1627+4605 at $z_{\rm fg} = 3.8137$.

Table 2.7. Ionic Column Densities for J0225+0048FG

Ion	$\lambda_{\rm rest}$ (Å)	$v^{a}_{\rm int}$ (km s^{-1})	log $N_{\rm AODM}$	Rest EW (Å)
		A		
C II			< 13.66	
	1334.5323	$[-363, 88]$	< 13.66	0.000 ± 0.030
C II*			< 13.70	
	1335.7077	$[-363, 88]$	< 13.70	0.005 ± 0.030
C IV			14.07 ± 0.03	
	1548.1950	$[-363, 88]$	14.07 ± 0.03	0.419 ± 0.025
Si II			< 12.55	
	1260.4221	$[-363, 88]$	< 12.55	0.028 ± 0.016
	1526.7066	$[-363, 88]$	< 13.45	-0.028 ± 0.025
Si IV			< 12.94	
	1393.7550	$[-363, 88]$	< 12.94	0.038 ± 0.026
	1402.7700	$[-363, 88]$	< 13.29	0.080 ± 0.025
		B		
C II			< 13.62	
	1334.5323	$[88, 498]$	< 13.62	0.024 ± 0.027
C II*			< 13.67	
	1335.7077	$[88, 498]$	< 13.67	0.065 ± 0.027
C IV			14.28 ± 0.03	
	1548.1950	$[88, 498]$	14.28 ± 0.03	0.609 ± 0.023
Si II			< 12.54	
	1260.4221	$[88, 498]$	< 12.54	0.036 ± 0.016
	1526.7066	$[88, 498]$	< 13.44	0.004 ± 0.024
Si IV			13.39 ± 0.05	
	1393.7550	$[88, 498]$	13.36 ± 0.06	0.184 ± 0.024
	1402.7700	$[88, 498]$	13.47 ± 0.08	0.121 ± 0.024
		C		
C II			< 13.58	
	1334.5323	$[498, 827]$	< 13.58	0.042 ± 0.024
C II*			< 13.63	

Table 2.7 (cont'd)

Ion	$\lambda_{\rm rest}$ (Å)	$v^a_{\rm int}$ (km s^{-1})	$\log N_{\rm AODM}$	Rest EW (Å)
	1335.7077	$[498, 827]$	< 13.63	0.028 ± 0.025
C IV			13.69 ± 0.10	
	1550.7700	$[498, 827]$	13.69 ± 0.10	0.091 ± 0.022
Si II			< 12.48	
	1260.4221	$[498, 827]$	< 12.48	-0.016 ± 0.014
	1526.7066	$[498, 827]$	< 13.40	0.032 ± 0.021
Si IV			< 12.86	
	1393.7550	$[498, 827]$	< 12.86	0.032 ± 0.021
	1402.7700	$[498, 827]$	< 13.17	0.041 ± 0.022

[a] Velocity interval for the AODM column density measurement. Velocities are relative to the redshift of the foreground quasar J0225+0048FG, $z_{\rm fg} = 2.7265$.

Table 2.8. Ionic Column Densities for J0341+0000FG

Ion	$\lambda_{\rm rest}$ (Å)	$v^a_{\rm int}$ (km s^{-1})	$\log N_{\rm AODM}$	Rest EW (Å)
		A		
C II			< 14.00	
	1334.5323	$[120, 470]$	< 14.00	0.146 ± 0.028
C II*			< 13.69	
	1335.7077	$[120, 470]$	< 13.69	0.006 ± 0.029
C IV			< 13.28	
	1548.1950	$[120, 470]$	< 13.28	-0.003 ± 0.026
	1550.7700	$[120, 470]$	< 13.59	0.029 ± 0.026
N V			< 13.54	
	1238.8210	$[120, 470]$	< 13.54	0.038 ± 0.024
Al II			< 12.18	
	1670.7874	$[120, 470]$	< 12.18	0.031 ± 0.023
Si II			< 13.42	
	1526.7066	$[120, 470]$	< 13.42	-0.033 ± 0.023
Fe II			< 13.62	
	1608.4511	$[120, 470]$	< 13.62	0.035 ± 0.018

[a] Velocity interval for the AODM column density measurement. Velocities are relative to the redshift of the foreground quasar J0341+0000FG, $z_{\rm fg} = 2.1233$.

Table 2.9. Ionic Column Densities for J0409−0411FG

Ion	$\lambda_{\rm rest}$ (Å)	$v_{\rm int}^{a}$ (km s^{-1})	$\log N_{\rm AODM}$	Rest EW (Å)
		A		
C II			< 13.97	
	1334.5323	$[-1458, -1238]$	< 13.97	0.156 ± 0.038
C IV			< 13.31	
	1548.1950	$[-1458, -1238]$	< 13.31	-0.033 ± 0.028
	1550.7700	$[-1458, -1238]$	< 13.64	0.024 ± 0.029
Al II			< 12.26	
	1670.7874	$[-1458, -1238]$	< 12.26	-0.050 ± 0.029
Si II			< 13.48	
	1526.7066	$[-1458, -1238]$	< 13.48	-0.005 ± 0.026
Fe II			< 14.12	
	1608.4511	$[-1458, -1238]$	< 14.12	0.128 ± 0.027

[a] Velocity interval for the AODM column density measurement. Velocities are relative to the redshift of the foreground quasar J0409-0411FG, $z_{\rm fg} = 1.7155$.

Table 2.10. Ionic Column Densities for J0853−0011FG

Ion	$\lambda_{\rm rest}$ (Å)	$v^a_{\rm int}$ (km s^{-1})	$\log N_{\rm AODM}$	Rest EW (Å)
A				
C II			13.89 ± 0.03	
	1334.5323	$[-271, -51]$	13.89 ± 0.03	0.139 ± 0.010
C IV			13.45 ± 0.04	
	1548.1950	$[-271, -51]$	13.49 ± 0.04	0.118 ± 0.010
	1550.7700	$[-271, -51]$	13.26 ± 0.13	0.035 ± 0.010
N V			< 13.90	
	1242.8040	$[-271, -51]$	< 13.90	0.080 ± 0.010
O I			< 13.36	
	1302.1685	$[-271, -51]$	< 13.36	0.016 ± 0.006
Al II			12.08 ± 0.07	
	1670.7874	$[-271, -51]$	12.08 ± 0.07	0.053 ± 0.008
Al III			< 12.33	
	1854.7164	$[-271, -51]$	< 12.33	0.005 ± 0.012
	1862.7895	$[-271, -51]$	< 12.69	0.039 ± 0.013
Si II			13.26 ± 0.03	
	1193.2897	$[-271, -51]$	13.25 ± 0.04	0.101 ± 0.010
	1260.4221	$[-271, -51]$	13.25 ± 0.03	0.201 ± 0.008
	1526.7066	$[-271, -51]$	13.37 ± 0.06	0.060 ± 0.009
	1808.0130	$[-271, -51]$	< 14.76	0.036 ± 0.010
Si III			> 13.30	
	1206.5000	$[-271, -51]$	> 13.30	0.315 ± 0.008
Si IV			12.72 ± 0.07	
	1393.7550	$[-271, -51]$	12.63 ± 0.10	0.037 ± 0.009
	1402.7700	$[-271, -51]$	12.94 ± 0.09	0.039 ± 0.008
Fe II			< 12.67	
	1608.4511	$[-271, -51]$	< 13.29	-0.006 ± 0.009
	2344.2140	$[-271, -51]$	< 13.22	0.004 ± 0.030
	2374.4612	$[-271, -51]$	< 13.64	0.013 ± 0.023
	2382.7650	$[-271, -51]$	< 12.67	-0.012 ± 0.026
	2586.6500	$[-271, -51]$	< 13.33	0.084 ± 0.026
	2600.1729	$[-271, -51]$	< 12.88	0.013 ± 0.035
Fe III			< 13.90	
	1122.5260	$[-271, -51]$	< 13.90	0.046 ± 0.011

Table 2.10 (cont'd)

Ion	$\lambda_{\rm rest}$ (Å)	$v_{\rm int}^{a}$ (km s^{-1})	$\log N_{\rm AODM}$	Rest EW (Å)
		B		
C II			> 14.40	
	1334.5323	$[-51, 209]$	> 14.40	0.345 ± 0.011
C IV			13.24 ± 0.06	
	1548.1950	$[-51, 209]$	13.21 ± 0.07	0.064 ± 0.011
	1550.7700	$[-51, 209]$	13.35 ± 0.11	0.044 ± 0.011
N V			< 14.07	
	1242.8040	$[-51, 209]$	< 14.07	0.119 ± 0.011
O I			14.68 ± 0.03	
	1302.1685	$[-51, 209]$	14.68 ± 0.03	0.287 ± 0.005
Al II			12.58 ± 0.03	
	1670.7874	$[-51, 209]$	12.58 ± 0.03	0.156 ± 0.009
Al III			< 12.38	
	1854.7164	$[-51, 209]$	< 12.37	0.000 ± 0.013
	1862.7895	$[-51, 209]$	< 12.78	0.049 ± 0.013
Si II			13.91 ± 0.03	
	1193.2897	$[-51, 209]$	> 13.79	0.278 ± 0.010
	1260.4221	$[-51, 209]$	> 13.49	0.304 ± 0.008
	1304.3702	$[-51, 209]$	14.02 ± 0.03	0.132 ± 0.006
	1526.7066	$[-51, 209]$	13.82 ± 0.03	0.152 ± 0.009
	1808.0130	$[-51, 209]$	< 14.79	0.038 ± 0.010
Si III			> 13.58	
	1206.5000	$[-51, 209]$	> 13.58	0.443 ± 0.009
Si IV			12.81 ± 0.06	
	1393.7550	$[-51, 209]$	12.81 ± 0.07	0.056 ± 0.009
	1402.7700	$[-51, 209]$	12.80 ± 0.14	0.028 ± 0.009
Fe II			13.10 ± 0.04	
	1608.4511	$[-51, 209]$	< 13.31	0.025 ± 0.009
	2344.2140	$[-51, 209]$	13.21 ± 0.11	0.083 ± 0.022
	2374.4612	$[-51, 209]$	< 13.69	0.018 ± 0.026
	2382.7650	$[-51, 209]$	13.01 ± 0.08	0.129 ± 0.028
	2586.6500	$[-51, 209]$	13.31 ± 0.11	0.079 ± 0.020
	2600.1729	$[-51, 209]$	13.12 ± 0.05	0.166 ± 0.022

Table 2.10 (cont'd)

Ion	$\lambda_{\rm rest}$ (Å)	$v_{\rm int}^{a}$ (km s^{-1})	$\log N_{\rm AODM}$	Rest EW (Å)
C				
C II			14.10 ± 0.03	
	1334.5323	$[209, 379]$	14.10 ± 0.03	0.195 ± 0.009
C II*			< 13.24	
	1335.7077	$[209, 379]$	< 13.24	0.011 ± 0.010
C IV			12.90 ± 0.12	
	1548.1950	$[209, 379]$	12.90 ± 0.12	0.031 ± 0.009
	1550.7700	$[209, 379]$	< 13.16	0.019 ± 0.009
N V			< 13.88	
	1242.8040	$[209, 379]$	< 13.88	0.076 ± 0.009
O I			14.31 ± 0.03	
	1302.1685	$[209, 379]$	14.31 ± 0.03	0.135 ± 0.005
O VI			< 14.07	
	1037.6167	$[209, 379]$	< 14.07	0.014 ± 0.024
Al II			12.34 ± 0.04	
	1670.7874	$[209, 379]$	12.34 ± 0.04	0.092 ± 0.008
Al III			< 12.27	
	1854.7164	$[209, 379]$	< 12.27	-0.006 ± 0.010
	1862.7895	$[209, 379]$	< 12.57	0.010 ± 0.010
Si II			13.65 ± 0.03	
	1193.2897	$[213, 379]$	> 13.43	0.139 ± 0.008
	1304.3702	$[209, 379]$	13.70 ± 0.03	0.065 ± 0.005
	1526.7066	$[209, 379]$	13.59 ± 0.04	0.093 ± 0.009
	1808.0130	$[209, 379]$	< 14.61	0.005 ± 0.008
Si III			> 13.18	
	1206.5000	$[213, 379]$	> 13.18	0.232 ± 0.007
Si IV			12.97 ± 0.04	
	1393.7550	$[209, 379]$	13.02 ± 0.04	0.089 ± 0.007
	1402.7700	$[209, 379]$	12.71 ± 0.14	0.022 ± 0.007
Fe II			12.90 ± 0.06	
	1608.4511	$[209, 379]$	< 13.21	0.017 ± 0.007
	2344.2140	$[209, 379]$	13.27 ± 0.11	0.096 ± 0.025
	2374.4612	$[209, 379]$	< 13.60	0.020 ± 0.020
	2382.7650	$[209, 379]$	12.94 ± 0.08	0.126 ± 0.023
	2586.6500	$[209, 379]$	< 13.10	0.032 ± 0.017

Table 2.10 (cont'd)

Ion	$\lambda_{\rm rest}$ (Å)	$v_{\rm int}^{a}$ (km s^{-1})	$\log N_{\rm AODM}$	Rest EW (Å)
	2600.1729	$[209, 379]$	12.75 ± 0.13	0.075 ± 0.023
Fe III			< 13.68	
	1122.5260	$[209, 379]$	< 13.68	0.006 ± 0.009

[a] Velocity interval for the AODM column density measurement. Velocities are relative to the redshift of the foreground quasar J0853-0011FG, $z_{\rm fg} = 2.4014$.

Table 2.11. Ionic Column Densities for J0932+0925FG

Ion	$\lambda_{\rm rest}$ (Å)	$v_{\rm int}^{a}$ (km s^{-1})	$\log N_{\rm AODM}$	Rest EW (Å)
		A		
C II			13.72 ± 0.11	
	1334.5323	$[-237, 316]$	13.72 ± 0.11	0.100 ± 0.025
C II*			< 13.62	
	1335.7077	$[-190, 316]$	< 13.62	0.069 ± 0.025
C IV			13.62 ± 0.06	
	1548.1950	$[-237, 316]$	13.62 ± 0.06	0.159 ± 0.023
	1550.7700	$[-237, 316]$	< 14.83	0.786 ± 0.022
N V			< 15.36	
	1242.8040	$[-237, 316]$	< 15.36	1.004 ± 0.026
Al II			< 12.07	
	1670.7874	$[-237, 316]$	< 12.07	0.005 ± 0.018
Al III			< 12.61	
	1854.7164	$[-237, 316]$	< 12.61	-0.005 ± 0.022
	1862.7895	$[-237, 316]$	< 13.05	0.072 ± 0.030
Si II			< 13.40	
	1526.7066	$[-237, 316]$	< 13.40	0.063 ± 0.020
	1808.0130	$[-237, 316]$	< 14.94	0.013 ± 0.018
Si III			13.31 ± 0.03	
	1206.5000	$[-140, 316]$	13.31 ± 0.03	0.350 ± 0.020
Si IV			13.23 ± 0.05	
	1393.7550	$[-237, 316]$	13.23 ± 0.05	0.145 ± 0.018
	1402.7700	$[-237, 316]$	< 13.09	0.002 ± 0.019
Fe II			< 13.04	
	1608.4511	$[-237, 316]$	< 14.22	0.210 ± 0.018
	2344.2140	$[-237, 316]$	< 13.47	0.156 ± 0.040
	2374.4612	$[-237, 316]$	< 14.16	0.215 ± 0.046
	2382.7650	$[-237, 316]$	< 13.04	0.167 ± 0.054
	2586.6500	$[-237, 316]$	< 13.56	0.061 ± 0.049
	2600.1729	$[-237, 316]$	< 13.13	0.128 ± 0.056
		B		
C II			< 13.52	

Table 2.11 (cont'd)

Ion	$\lambda_{\rm rest}$ (Å)	$v_{\rm int}^{a}$ (km s^{-1})	log $N_{\rm AODM}$	Rest EW (Å)
	1334.5323	[316, 684]	< 13.52	0.048 ± 0.022
C II*			< 13.57	
	1335.7077	[316, 684]	< 13.57	0.059 ± 0.022
C IV			14.56 ± 0.03	
	1548.1950	[316, 684]	> 14.52	0.755 ± 0.017
	1550.7700	[316, 684]	14.56 ± 0.03	0.537 ± 0.018
N V			< 14.25	
	1242.8040	[316, 684]	< 14.25	0.178 ± 0.024
Al II			< 11.98	
	1670.7874	[316, 684]	< 11.98	-0.003 ± 0.015
Al III			< 12.54	
	1854.7164	[316, 684]	< 12.54	0.014 ± 0.019
	1862.7895	[316, 684]	< 12.87	0.012 ± 0.020
Si II			< 13.27	
	1526.7066	[316, 684]	< 13.27	-0.002 ± 0.016
	1808.0130	[316, 684]	< 14.85	0.008 ± 0.015
Si III			13.10 ± 0.04	
	1206.5000	[316, 684]	13.10 ± 0.04	0.212 ± 0.019
Si IV			13.06 ± 0.07	
	1393.7550	[316, 684]	13.06 ± 0.07	0.098 ± 0.015
	1402.7700	[316, 684]	< 13.01	0.008 ± 0.016
Fe II			< 12.90	
	1608.4511	[316, 684]	< 13.91	0.104 ± 0.015
	2344.2140	[316, 684]	< 13.35	0.021 ± 0.041
	2374.4612	[316, 684]	< 13.90	0.080 ± 0.041
	2382.7650	[316, 684]	< 13.09	0.184 ± 0.042
	2586.6500	[316, 684]	< 13.41	0.030 ± 0.035
	2600.1729	[316, 684]	< 12.90	-0.005 ± 0.039
		C		
C II			< 13.50	
	1334.5323	[685, 1018]	< 13.50	0.057 ± 0.021
C II*			< 13.55	
	1335.7077	[685, 1018]	< 13.55	0.038 ± 0.021
C IV			13.61 ± 0.11	

Table 2.11 (cont'd)

Ion	$\lambda_{\rm rest}$ (Å)	$v_{\rm int}^{a}$ (km s^{-1})	$\log N_{\rm AODM}$	Rest EW (Å)
	1548.1950	$[685, 1018]$	> 14.07	0.355 ± 0.018
	1550.7700	$[685, 1018]$	13.61 ± 0.11	0.079 ± 0.020
N V			< 14.53	
	1242.8040	$[685, 1018]$	< 14.53	0.299 ± 0.022
Al II			12.09 ± 0.11	
	1670.7874	$[685, 1018]$	12.09 ± 0.11	0.055 ± 0.015
Al III			< 12.56	
	1854.7164	$[685, 1018]$	< 12.56	0.050 ± 0.019
	1862.7895	$[685, 1018]$	< 12.86	0.022 ± 0.020
Si II			< 13.26	
	1526.7066	$[685, 1018]$	< 13.26	0.016 ± 0.016
	1808.0130	$[685, 1018]$	< 15.00	0.062 ± 0.014
Si III			12.89 ± 0.05	
	1206.5000	$[685, 1018]$	12.89 ± 0.05	0.150 ± 0.018
Si IV			< 12.69	
	1393.7550	$[685, 1018]$	< 12.69	0.018 ± 0.015
	1402.7700	$[685, 1018]$	< 12.99	0.000 ± 0.015
Fe II			< 12.90	
	1608.4511	$[685, 1018]$	< 14.18	0.183 ± 0.013
	2344.2140	$[685, 1018]$	< 13.25	0.002 ± 0.033
	2374.4612	$[685, 1018]$	< 13.91	0.028 ± 0.042
	2382.7650	$[685, 1018]$	< 13.27	0.269 ± 0.040
	2586.6500	$[685, 1018]$	< 13.35	0.006 ± 0.030
	2600.1729	$[685, 1018]$	< 12.90	0.087 ± 0.038

[a] Velocity interval for the AODM column density measurement. Velocities are relative to the redshift of the foreground quasar J0932+0925FG, $z_{\rm fg} = 2.4170$.

Table 2.12. Ionic Column Densities for J1026+4614FG

Ion	$\lambda_{\rm rest}$ (Å)	$v_{\rm int}^{a}$ (km s^{-1})	$\log N_{\rm AODM}$	Rest EW (Å)
		A		
C II			< 13.02	
	1334.5323	$[240, 360]$	< 13.02	0.008 ± 0.007
C II*			< 13.06	
	1335.7077	$[240, 360]$	< 13.06	-0.016 ± 0.007
C IV			13.98 ± 0.03	
	1548.1950	$[240, 360]$	> 13.76	0.182 ± 0.006
	1550.7700	$[240, 360]$	13.98 ± 0.03	0.156 ± 0.006
N II			< 13.32	
	1083.9900	$[240, 360]$	< 13.32	0.001 ± 0.007
N V			13.67 ± 0.03	
	1238.8210	$[240, 360]$	13.66 ± 0.03	0.086 ± 0.004
	1242.8040	$[240, 360]$	13.70 ± 0.04	0.049 ± 0.004
Si II			< 11.98	
	1260.4221	$[240, 360]$	< 11.99	0.007 ± 0.005
	1526.7066	$[240, 360]$	< 12.97	-0.002 ± 0.008
Si IV			12.91 ± 0.05	
	1393.7550	$[240, 360]$	12.91 ± 0.05	0.068 ± 0.007
	1402.7700	$[240, 360]$	< 12.64	0.005 ± 0.007
		B		
C II			< 12.95	
	1334.5323	$[357, 446]$	< 12.96	-0.009 ± 0.006
C II*			< 13.01	
	1335.7077	$[357, 446]$	< 13.01	-0.004 ± 0.006
C IV			13.27 ± 0.03	
	1548.1950	$[357, 446]$	13.21 ± 0.04	0.060 ± 0.005
	1550.7700	$[357, 446]$	13.46 ± 0.05	0.055 ± 0.005
N V			< 12.67	
	1238.8210	$[357, 446]$	< 12.67	0.005 ± 0.003
	1242.8040	$[357, 446]$	< 13.03	0.004 ± 0.004
Si II			< 11.96	
	1260.4221	$[357, 446]$	< 11.96	0.001 ± 0.004

Table 2.12 (cont'd)

Ion	$\lambda_{\rm rest}$ (Å)	$v^{a}_{\rm int}$ (km s^{-1})	$\log N_{\rm AODM}$	Rest EW (Å)
	1526.7066	$[357, 446]$	< 12.92	0.001 ± 0.007
Si IV			12.57 ± 0.08	
	1393.7550	$[357, 446]$	12.57 ± 0.08	0.032 ± 0.006
	1402.7700	$[357, 446]$	< 12.59	0.009 ± 0.006

[a] Velocity interval for the AODM column density measurement. Velocities are relative to the redshift of the foreground quasar J1026+4614FG, $z_{\rm fg} = 3.3401$.

Table 2.13. Ionic Column Densities for J1038+5027FG

Ion	$\lambda_{\rm rest}$ (Å)	$v^{a}_{\rm int}$ (km s^{-1})	$\log N_{\rm AODM}$	Rest EW (Å)
		A		
C II			< 13.38	
	1334.5323	$[466, 676]$	< 13.38	-0.011 ± 0.016
C II*			< 13.35	
	1335.7077	$[536, 676]$	< 13.35	0.016 ± 0.013
C IV			14.08 ± 0.03	
	1548.1950	$[466, 676]$	14.08 ± 0.03	0.364 ± 0.019
	1550.7700	$[466, 676]$	14.09 ± 0.04	0.211 ± 0.019
Si II			< 13.39	
	1526.7066	$[466, 676]$	< 13.39	0.029 ± 0.021
	1808.0130	$[466, 676]$	< 15.17	0.044 ± 0.029
Si IV			13.00 ± 0.10	
	1393.7550	$[466, 676]$	13.00 ± 0.10	0.079 ± 0.019
	1402.7700	$[466, 676]$	< 13.13	-0.023 ± 0.021

[a] Velocity interval for the AODM column density measurement. Velocities are relative to the redshift of the foreground quasar J1038+5027FG, $z_{\rm fg} = 3.1323$.

Table 2.14. Ionic Column Densities for J1144+0959FG

Ion	$\lambda_{\rm rest}$ (Å)	$v^{a}_{\rm int}$ (km s^{-1})	log $N_{\rm AODM}$	Rest EW (Å)
		A		
C II			< 12.72	
	1334.5323	$[-1690, -1605]$	< 12.72	-0.004 ± 0.004
C III			> 13.66	
	977.0200	$[-1690, -1605]$	> 13.66	0.157 ± 0.005
C IV			13.98 ± 0.03	
	1548.1950	$[-1690, -1605]$	13.92 ± 0.03	0.196 ± 0.002
	1550.7700	$[-1690, -1605]$	14.09 ± 0.03	0.169 ± 0.003
Si II			< 12.53	
	1526.7066	$[-1690, -1605]$	< 12.53	0.007 ± 0.003
Si IV			< 12.08	
	1393.7550	$[-1690, -1605]$	< 12.08	-0.002 ± 0.004
	1402.7700	$[-1690, -1605]$	< 12.31	0.002 ± 0.003
		B		
C II			13.15 ± 0.07	
	1334.5323	$[-1352, -1192]$	13.15 ± 0.07	0.025 ± 0.005
C IV			14.25 ± 0.03	
	1548.1950	$[-1352, -1192]$	> 14.24	0.411 ± 0.003
	1550.7700	$[-1352, -1192]$	14.25 ± 0.03	0.267 ± 0.004
Si II			< 12.04	
	1260.4221	$[-1352, -1192]$	< 12.04	0.006 ± 0.005
	1526.7066	$[-1352, -1192]$	< 12.92	-0.046 ± 0.009
Si III			< 13.54	
	1206.5000	$[-1317, -1192]$	< 13.54	0.347 ± 0.003
Si IV			13.21 ± 0.03	
	1393.7550	$[-1352, -1192]$	13.20 ± 0.03	0.119 ± 0.005
	1402.7700	$[-1352, -1192]$	13.21 ± 0.03	0.065 ± 0.005
		C		
C II			13.27 ± 0.04	
	1334.5323	$[-1192, -1142]$	13.27 ± 0.04	0.030 ± 0.003

Table 2.14 (cont'd)

Ion	$\lambda_{\rm rest}$ (Å)	$v^a_{\rm int}$ (km s^{-1})	log $N_{\rm AODM}$	Rest EW (Å)
C IV			13.03 ± 0.07	
	1550.7700	$[-1192, -1142]$	13.03 ± 0.07	0.020 ± 0.003
Si II			12.48 ± 0.04	
	1260.4221	$[-1192, -1142]$	12.48 ± 0.04	0.033 ± 0.003
	1526.7066	$[-1192, -1142]$	< 12.60	0.009 ± 0.004
Si III			< 13.14	
	1206.5000	$[-1192, -1142]$	< 13.14	0.147 ± 0.002
Si IV			12.41 ± 0.06	
	1393.7550	$[-1192, -1142]$	12.44 ± 0.08	0.021 ± 0.004
	1402.7700	$[-1192, -1142]$	12.37 ± 0.10	0.010 ± 0.002
		D		
C II			13.47 ± 0.04	
	1334.5323	$[-1070, -870]$	13.47 ± 0.04	0.053 ± 0.005
C II*			< 12.97	
	1335.7077	$[-1070, -870]$	< 12.97	0.010 ± 0.005
C IV			13.86 ± 0.03	
	1548.1950	$[-1070, -870]$	13.88 ± 0.03	0.248 ± 0.004
	1550.7700	$[-1070, -870]$	13.82 ± 0.03	0.121 ± 0.004
Si II			< 12.71	
	1526.7066	$[-1070, -870]$	< 12.71	0.007 ± 0.004
Si IV			13.16 ± 0.03	
	1393.7550	$[-1070, -870]$	13.17 ± 0.03	0.118 ± 0.005
	1402.7700	$[-1070, -870]$	13.14 ± 0.03	0.058 ± 0.005
		E		
C II			12.84 ± 0.10	
	1334.5323	$[-145, -70]$	12.84 ± 0.10	0.013 ± 0.003
C IV			13.67 ± 0.03	
	1548.1950	$[-145, -70]$	13.66 ± 0.03	0.130 ± 0.002
	1550.7700	$[-145, -70]$	13.70 ± 0.03	0.083 ± 0.002
Al II			11.24 ± 0.14	
	1670.7874	$[-145, -70]$	11.24 ± 0.14	0.008 ± 0.002
Al III			< 12.21	

Table 2.14 (cont'd)

Ion	$\lambda_{\rm rest}$ (Å)	$v_{\rm int}^{a}$ (km s^{-1})	$\log N_{\rm AODM}$	Rest EW (Å)
	1862.7895	$[-145, -70]$	< 12.21	0.013 ± 0.003
Si II			< 12.51	
	1526.7066	$[-145, -70]$	< 12.51	-0.002 ± 0.003
Si IV			12.88 ± 0.03	
	1393.7550	$[-145, -70]$	12.88 ± 0.03	0.058 ± 0.003
	1402.7700	$[-145, -70]$	12.88 ± 0.04	0.031 ± 0.003
Fe II			< 12.65	
	1608.4511	$[-145, -70]$	< 12.65	0.005 ± 0.002
		F		
C II			> 14.24	
	1334.5323	$[-73, 62]$	> 14.24	0.168 ± 0.004
C II*			< 12.86	
	1335.7077	$[-73, 62]$	< 12.86	0.009 ± 0.004
C IV			> 14.73	
	1548.1950	$[-73, 62]$	> 14.55	0.519 ± 0.003
	1550.7700	$[-73, 62]$	> 14.73	0.456 ± 0.002
O I			13.16 ± 0.13	
	1302.1685	$[-73, 22]$	13.16 ± 0.13	0.009 ± 0.003
Al II			12.52 ± 0.03	
	1670.7874	$[-73, 62]$	12.52 ± 0.03	0.094 ± 0.003
Al III			13.06 ± 0.03	
	1862.7895	$[-73, 62]$	13.07 ± 0.03	0.073 ± 0.004
Si II			13.91 ± 0.03	
	1190.4158	$[-23, 62]$	> 13.81	0.096 ± 0.003
	1260.4221	$[-48, 57]$	> 13.41	0.174 ± 0.003
	1304.3702	$[-73, 62]$	14.03 ± 0.03	0.101 ± 0.004
	1526.7066	$[-73, 62]$	13.85 ± 0.03	0.100 ± 0.004
	1808.0130	$[-73, 62]$	< 15.00	0.048 ± 0.004
Si IV			> 13.92	
	1393.7550	$[-73, 62]$	> 13.74	0.255 ± 0.004
	1402.7700	$[-73, 62]$	> 13.92	0.196 ± 0.004
Fe II			13.25 ± 0.05	
	1608.4511	$[-73, 22]$	13.25 ± 0.05	0.021 ± 0.002

[a] Velocity interval for the AODM column density measurement. Velocities are relative to the redshift of the foreground quasar J1144+0959FG, $z_{\rm fg} = 2.9731$.

Table 2.15. Ionic Column Densities for J1145+0322FG

Ion	$\lambda_{\rm rest}$ (Å)	$v_{\rm int}^{a}$ (km s^{-1})	$\log N_{\rm AODM}$	Rest EW (Å)
		A		
C II			> 14.71	
	1334.5323	$[-278, 122]$	> 14.71	0.504 ± 0.022
C II*			< 13.61	
	1335.7077	$[-258, 122]$	< 13.61	0.055 ± 0.024
C IV			> 14.59	
	1548.1950	$[-278, 122]$	> 14.55	0.777 ± 0.028
	1550.7700	$[-278, 122]$	> 14.59	0.523 ± 0.029
O I			14.08 ± 0.14	
	1302.1685	$[-278, 72]$	14.08 ± 0.14	0.083 ± 0.027
Mg I			< 11.98	
	2852.9642	$[-278, 122]$	< 11.98	0.077 ± 0.041
Mg II			> 13.72	
	2796.3520	$[-278, 122]$	> 13.53	0.859 ± 0.029
	2803.5310	$[-278, 122]$	> 13.72	0.758 ± 0.034
Al II			12.73 ± 0.05	
	1670.7874	$[-278, 122]$	12.73 ± 0.05	0.204 ± 0.023
Al III			12.92 ± 0.06	
	1854.7164	$[-278, 122]$	12.90 ± 0.07	0.120 ± 0.019
	1862.7895	$[-278, 122]$	13.00 ± 0.11	0.078 ± 0.020
Si II			13.97 ± 0.05	
	1190.4158	$[-278, 122]$	< 14.19	0.371 ± 0.069
	1260.4221	$[-278, 122]$	> 13.82	0.496 ± 0.043
	1304.3702	$[-278, 122]$	< 14.41	0.315 ± 0.025
	1526.7066	$[-278, 122]$	13.97 ± 0.05	0.201 ± 0.025
Si III			> 13.77	
	1206.5000	$[-278, 122]$	> 13.77	0.602 ± 0.092
Si IV			13.74 ± 0.03	
	1393.7550	$[-278, 122]$	13.70 ± 0.03	0.320 ± 0.025
	1402.7700	$[-278, 122]$	13.84 ± 0.04	0.256 ± 0.024
Fe II			13.53 ± 0.09	
	1608.4511	$[-278, 122]$	< 13.69	0.045 ± 0.021
	2344.2140	$[-278, 122]$	13.53 ± 0.09	0.178 ± 0.039
	2374.4612	$[-278, 122]$	< 13.84	0.043 ± 0.036

Table 2.15 (cont'd)

Ion	$\lambda_{\rm rest}$ (Å)	$v^{a}_{\rm int}$ (km s^{-1})	$\log N_{\rm AODM}$	Rest EW (Å)
	2586.6500	$[-278, 122]$	< 13.68	0.189 ± 0.036

[a] Velocity interval for the AODM column density measurement. Velocities are relative to the redshift of the foreground quasar J1145+0322FG, $z_{\rm fg} = 1.7652$.

Table 2.16. Ionic Column Densities for J1204+0221FG

Ion	$\lambda_{\rm rest}$ (Å)	$v^{a}_{\rm int}$ (km s^{-1})	$\log N_{\rm AODM}$	Rest EW (Å)
A				
C II			> 14.63	
	1036.3367	$[57, 207]$	> 14.63	0.248 ± 0.009
	1334.5323	$[77, 247]$	> 14.58	0.363 ± 0.005
C IV			13.60 ± 0.03	
	1548.1950	$[77, 247]$	13.60 ± 0.03	0.141 ± 0.007
N I			13.34 ± 0.05	
	1199.5496	$[107, 207]$	13.33 ± 0.05	0.032 ± 0.004
N II			> 14.45	
	1083.9900	$[77, 247]$	> 14.45	0.166 ± 0.005
N V			< 13.10	
	1242.8040	$[107, 187]$	< 13.10	0.013 ± 0.001
O I			14.36 ± 0.04	
	1039.2304	$[107, 167]$	14.55 ± 0.06	0.023 ± 0.004
	1302.1685	$[77, 247]$	14.32 ± 0.05	0.081 ± 0.007
O VI			< 13.67	
	1031.9261	$[87, 167]$	< 13.67	0.050 ± 0.006
Al II			> 12.74	
	1670.7874	$[87, 207]$	> 12.74	0.151 ± 0.006
Al III			< 12.41	
	1854.7164	$[87, 207]$	< 12.41	0.038 ± 0.011
Si II			13.89 ± 0.03	
	1190.4158	$[87, 207]$	> 13.88	0.139 ± 0.004
	1260.4221	$[57, 217]$	> 13.60	0.262 ± 0.003
	1526.7066	$[107, 207]$	13.89 ± 0.03	0.116 ± 0.005
Si II*			< 11.93	
	1264.7377	$[57, 217]$	< 11.93	0.007 ± 0.004
Si III			> 13.66	
	1206.5000	$[57, 237]$	> 13.66	0.441 ± 0.004
Si IV			12.93 ± 0.03	
	1393.7550	$[77, 207]$	12.90 ± 0.03	0.065 ± 0.005
	1402.7700	$[77, 207]$	13.03 ± 0.05	0.046 ± 0.005
Fe II			13.34 ± 0.10	
	1608.4511	$[107, 187]$	13.34 ± 0.10	0.025 ± 0.006

Table 2.16 (cont'd)

Ion	$\lambda_{\rm rest}$ (Å)	$v^a_{\rm int}$ (km s^{-1})	log $N_{\rm AODM}$	Rest EW (Å)
Fe III			< 13.37	
	1122.5260	$[87, 187]$	< 13.37	-0.000 ± 0.005
B				
C II			> 15.24	
	1036.3367	$[269, 519]$	> 15.24	0.779 ± 0.008
	1334.5323	$[309, 519]$	> 15.10	0.889 ± 0.004
C IV			14.09 ± 0.03	
	1548.1950	$[309, 519]$	14.11 ± 0.03	0.382 ± 0.007
	1550.7700	$[309, 519]$	14.06 ± 0.03	0.195 ± 0.008
N I			> 14.01	
	1199.5496	$[269, 449]$	> 14.01	0.143 ± 0.005
N II			> 15.10	
	1083.9900	$[269, 519]$	> 15.10	0.589 ± 0.005
N V			< 13.81	
	1242.8040	$[309, 519]$	< 13.81	0.065 ± 0.002
O I			15.61 ± 0.03	
	1039.2304	$[309, 519]$	15.61 ± 0.03	0.225 ± 0.006
	1302.1685	$[269, 529]$	> 15.35	0.692 ± 0.007
O VI			< 14.58	
	1031.9261	$[309, 519]$	< 14.58	0.308 ± 0.010
Al II			13.32 ± 0.03	
	1670.7874	$[269, 519]$	13.32 ± 0.03	0.619 ± 0.009
Al III			12.68 ± 0.08	
	1854.7164	$[369, 519]$	12.68 ± 0.08	0.068 ± 0.014
Si II			14.60 ± 0.03	
	1304.3702	$[269, 519]$	14.64 ± 0.03	0.416 ± 0.009
	1526.7066	$[269, 519]$	14.58 ± 0.03	0.582 ± 0.008
	1808.0130	$[319, 419]$	< 14.65	0.005 ± 0.009
Si II*			< 12.04	
	1264.7377	$[269, 529]$	< 12.04	-0.002 ± 0.005
Si III			> 14.02	
	1206.5000	$[269, 529]$	> 14.02	0.823 ± 0.004
Si IV			13.50 ± 0.03	
	1393.7550	$[309, 519]$	13.50 ± 0.03	0.234 ± 0.006

Table 2.16 (cont'd)

Ion	$\lambda_{\rm rest}$ (Å)	$v_{\rm int}^a$ (km s^{-1})	$\log N_{\rm AODM}$	Rest EW (Å)
	1402.7700	$[309, 519]$	13.50 ± 0.03	0.128 ± 0.007
Fe II			13.87 ± 0.04	
	1608.4511	$[319, 469]$	13.87 ± 0.04	0.088 ± 0.008
Fe III			< 13.35	
	1122.5260	$[319, 419]$	< 13.35	0.008 ± 0.004
			C	
C II			> 14.79	
	1036.3367	$[618, 718]$	> 14.79	0.281 ± 0.004
	1334.5323	$[588, 748]$	> 14.67	0.364 ± 0.004
C II*			13.62 ± 0.03	
	1335.7077	$[588, 748]$	13.62 ± 0.03	0.061 ± 0.005
C IV			13.66 ± 0.03	
	1548.1950	$[588, 748]$	13.71 ± 0.03	0.158 ± 0.007
	1550.7700	$[588, 748]$	13.48 ± 0.06	0.051 ± 0.008
N I			14.29 ± 0.03	
	1134.9803	$[638, 718]$	14.13 ± 0.04	0.049 ± 0.004
	1199.5496	$[618, 748]$	14.33 ± 0.03	0.213 ± 0.004
N II			> 14.80	
	1083.9900	$[618, 748]$	> 14.80	0.272 ± 0.004
N V			< 12.58	
	1242.8040	$[638, 738]$	< 12.58	-0.000 ± 0.001
O I			> 15.25	
	1039.2304	$[618, 718]$	> 15.25	0.088 ± 0.004
	1302.1685	$[588, 748]$	> 14.97	0.284 ± 0.007
O VI			< 13.70	
	1031.9261	$[698, 838]$	< 13.70	0.054 ± 0.009
Al II			12.79 ± 0.03	
	1670.7874	$[618, 738]$	12.79 ± 0.03	0.181 ± 0.007
Al III			< 12.28	
	1854.7164	$[668, 738]$	< 12.28	0.001 ± 0.010
Si II			> 14.14	
	1190.4158	$[618, 748]$	> 14.14	0.225 ± 0.004
	1526.7066	$[618, 738]$	> 14.08	0.170 ± 0.006
	1808.0130	$[618, 738]$	< 14.66	-0.012 ± 0.010

Table 2.16 (cont'd)

Ion	$\lambda_{\rm rest}$ (Å)	$v_{\rm int}^{a}$ (km s^{-1})	log $N_{\rm AODM}$	Rest EW (Å)
Si II*			< 11.82	
	1264.7377	[648, 748]	< 11.82	-0.002 ± 0.003
Si III			> 13.59	
	1206.5000	[648, 748]	> 13.59	0.339 ± 0.003
Si IV			12.79 ± 0.04	
	1393.7550	[618, 738]	12.74 ± 0.05	0.039 ± 0.006
	1402.7700	[618, 738]	12.90 ± 0.07	0.032 ± 0.005
Fe II			13.57 ± 0.07	
	1608.4511	[618, 738]	13.57 ± 0.07	0.045 ± 0.007
Fe III			< 13.37	
	1122.5260	[698, 798]	< 13.37	-0.001 ± 0.005

[a] Velocity interval for the AODM column density measurement. Velocities are relative to the redshift of the foreground quasar J1204+0221FG, $z_{\rm fg} = 2.4358$.

Table 2.17. Ionic Column Densities for J1420+1603FG

Ion	$\lambda_{\rm rest}$ (Å)	$v_{\rm int}^{a}$ (km s^{-1})	$\log N_{\rm AODM}$	Rest EW (Å)
		A		
C II			< 13.65	
	1334.5323	$[-543, -305]$	< 13.65	0.083 ± 0.027
C IV			13.63 ± 0.04	
	1548.1950	$[-543, -305]$	13.63 ± 0.04	0.155 ± 0.014
N V			< 13.56	
	1238.8210	$[-543, -305]$	< 13.56	0.008 ± 0.026
	1242.8040	$[-543, -305]$	< 13.92	0.011 ± 0.030
O I			< 14.01	
	1302.1685	$[-543, -305]$	< 14.01	0.032 ± 0.024
Mg I			< 11.84	
	2852.9642	$[-543, -305]$	< 11.83	0.028 ± 0.029
Mg II			< 12.61	
	2796.3520	$[-543, -305]$	< 12.61	0.029 ± 0.055
Al II			< 12.01	
	1670.7874	$[-543, -305]$	< 12.01	0.029 ± 0.016
Al III			< 12.45	
	1854.7164	$[-543, -305]$	< 12.45	-0.032 ± 0.016
	1862.7895	$[-543, -305]$	< 12.75	-0.043 ± 0.016
Si II			< 12.66	
	1260.4221	$[-543, -305]$	< 12.66	0.046 ± 0.021
	1526.7066	$[-543, -305]$	< 13.42	0.010 ± 0.023
Si IV			12.87 ± 0.14	
	1393.7550	$[-543, -305]$	12.87 ± 0.14	0.061 ± 0.020
	1402.7700	$[-543, -305]$	< 13.18	-0.016 ± 0.023
Fe II			< 12.81	
	1608.4511	$[-543, -305]$	< 13.56	0.002 ± 0.016
	2344.2140	$[-543, -305]$	< 13.37	0.125 ± 0.022
	2374.4612	$[-543, -305]$	< 13.74	0.031 ± 0.028
	2382.7650	$[-543, -305]$	< 13.08	0.178 ± 0.029
	2586.6500	$[-543, -305]$	< 13.37	-0.002 ± 0.031
	2600.1729	$[-543, -305]$	< 12.81	-0.025 ± 0.031
Fe III			< 14.60	
	1122.5260	$[-543, -305]$	< 14.60	0.035 ± 0.071

Table 2.17 (cont'd)

Ion	$\lambda_{\rm rest}$ (Å)	$v^a_{\rm int}$ (km s^{-1})	$\log N_{\rm AODM}$	Rest EW (Å)
		B		
C II			> 14.44	
	1334.5323	$[-305, -84]$	> 14.44	0.341 ± 0.023
C IV			< 13.83	
	1548.1950	$[-305, -84]$	< 13.83	0.239 ± 0.013
N V			< 13.60	
	1238.8210	$[-305, -84]$	< 13.60	0.031 ± 0.028
	1242.8040	$[-305, -84]$	< 13.91	-0.004 ± 0.029
O I			< 14.01	
	1302.1685	$[-305, -84]$	< 14.01	0.055 ± 0.024
Mg I			< 11.81	
	2852.9642	$[-305, -84]$	< 11.81	0.072 ± 0.027
Mg II			> 13.24	
	2796.3520	$[-305, -84]$	> 13.24	0.523 ± 0.030
Al II			12.60 ± 0.04	
	1670.7874	$[-305, -84]$	12.60 ± 0.04	0.152 ± 0.014
Al III			< 12.43	
	1854.7164	$[-305, -84]$	< 12.43	-0.003 ± 0.015
	1862.7895	$[-305, -84]$	< 12.73	-0.018 ± 0.015
Si II			13.49 ± 0.12	
	1260.4221	$[-305, -84]$	> 13.44	0.281 ± 0.018
	1526.7066	$[-305, -84]$	13.49 ± 0.12	0.073 ± 0.021
	1808.0130	$[-305, -84]$	< 14.94	-0.015 ± 0.018
Si III			> 13.31	
	1206.5000	$[-305, -124]$	> 13.31	0.302 ± 0.024
Si IV			13.27 ± 0.06	
	1393.7550	$[-305, -84]$	13.27 ± 0.06	0.149 ± 0.019
	1402.7700	$[-305, -84]$	< 13.18	0.032 ± 0.022
Fe II			< 12.79	
	1608.4511	$[-305, -84]$	< 13.54	-0.008 ± 0.016
	2344.2140	$[-305, -84]$	< 13.42	0.137 ± 0.021
	2374.4612	$[-305, -84]$	< 13.73	0.048 ± 0.027
	2382.7650	$[-305, -84]$	< 13.19	0.220 ± 0.028
	2586.6500	$[-305, -84]$	< 13.27	0.047 ± 0.025

Table 2.17 (cont'd)

Ion	$\lambda_{\rm rest}$ (Å)	$v^a_{\rm int}$ (km s^{-1})	$\log N_{\rm AODM}$	Rest EW (Å)
	2600.1729	$[-305, -84]$	< 12.79	0.072 ± 0.029
Fe III			< 14.54	
	1122.5260	$[-305, -84]$	< 14.54	0.010 ± 0.066
		C		
C II			> 14.44	
	1334.5323	$[-84, 183]$	> 14.44	0.328 ± 0.026
C IV			> 14.23	
	1548.1950	$[-84, 183]$	> 14.23	0.398 ± 0.013
N V			< 13.62	
	1238.8210	$[-84, 183]$	< 13.62	-0.016 ± 0.030
	1242.8040	$[-84, 183]$	< 13.95	0.021 ± 0.031
O I			14.38 ± 0.07	
	1302.1685	$[-84, 183]$	14.38 ± 0.07	0.159 ± 0.025
Mg I			< 11.90	
	2852.9642	$[-84, 183]$	< 11.90	0.070 ± 0.033
Mg II			> 13.51	
	2796.3520	$[-84, 183]$	> 13.16	0.435 ± 0.032
	2803.5310	$[-84, 183]$	> 13.51	0.525 ± 0.046
Al II			12.42 ± 0.06	
	1670.7874	$[-84, 183]$	12.42 ± 0.06	0.107 ± 0.015
Al III			< 12.47	
	1854.7164	$[-84, 183]$	< 12.47	0.010 ± 0.016
	1862.7895	$[-84, 183]$	< 12.77	-0.032 ± 0.016
Si II			13.87 ± 0.06	
	1260.4221	$[-84, 183]$	> 13.35	0.238 ± 0.020
	1526.7066	$[-84, 183]$	13.87 ± 0.06	0.160 ± 0.022
Si IV			13.57 ± 0.07	
	1393.7550	$[-84, 183]$	> 13.46	0.204 ± 0.021
	1402.7700	$[-84, 183]$	13.57 ± 0.07	0.147 ± 0.024
Fe II			< 12.94	
	1608.4511	$[-84, 183]$	< 13.58	-0.005 ± 0.017
	2344.2140	$[-84, 183]$	< 13.38	0.129 ± 0.024
	2374.4612	$[-84, 183]$	< 13.98	0.142 ± 0.030
	2382.7650	$[-84, 183]$	< 13.29	0.290 ± 0.030

Table 2.17 (cont'd)

Ion	$\lambda_{\rm rest}$ (Å)	$v^a_{\rm int}$ (km s^{-1})	$\log N_{\rm AODM}$	Rest EW (Å)
	2586.6500	$[-84, 183]$	< 13.37	0.004 ± 0.032
	2600.1729	$[-84, 183]$	< 12.94	0.040 ± 0.041
Fe III			< 14.60	
	1122.5260	$[-84, 183]$	< 14.60	0.017 ± 0.070
		D		
C II			> 14.91	
	1334.5323	$[184, 428]$	> 14.91	0.756 ± 0.020
C IV			> 14.57	
	1548.1950	$[184, 428]$	> 14.58	0.815 ± 0.010
N V			< 13.62	
	1238.8210	$[184, 428]$	< 13.62	-0.004 ± 0.029
	1242.8040	$[184, 428]$	< 13.94	0.021 ± 0.030
O I			> 15.01	
	1302.1685	$[184, 428]$	> 15.01	0.456 ± 0.022
Mg I			12.33 ± 0.07	
	2852.9642	$[184, 428]$	12.33 ± 0.07	0.255 ± 0.039
Mg II			> 13.97	
	2796.3520	$[184, 428]$	> 13.90	1.500 ± 0.033
	2803.5310	$[184, 428]$	> 13.97	1.149 ± 0.026
Al II			> 13.29	
	1670.7874	$[184, 428]$	> 13.29	0.557 ± 0.012
Al III			12.87 ± 0.06	
	1854.7164	$[184, 428]$	12.87 ± 0.06	0.103 ± 0.015
	1862.7895	$[184, 428]$	< 12.75	0.010 ± 0.015
Si II			14.35 ± 0.03	
	1260.4221	$[184, 428]$	> 14.00	0.673 ± 0.016
	1526.7066	$[184, 428]$	14.35 ± 0.03	0.423 ± 0.019
	1808.0130	$[184, 428]$	< 15.35	0.127 ± 0.018
Si III			> 14.03	
	1206.5000	$[184, 428]$	> 14.03	0.933 ± 0.021
Si IV			14.02 ± 0.03	
	1393.7550	$[184, 428]$	> 13.92	0.492 ± 0.019
	1402.7700	$[184, 428]$	14.02 ± 0.03	0.354 ± 0.021
Fe II			13.76 ± 0.03	

Table 2.17 (cont'd)

Ion	$\lambda_{\rm rest}$ (Å)	$v^{a}_{\rm int}$ (km s^{-1})	$\log N_{\rm AODM}$	Rest EW (Å)
	1608.4511	$[184, 428]$	13.73 ± 0.10	0.068 ± 0.016
	2344.2140	$[184, 428]$	13.85 ± 0.03	0.345 ± 0.022
	2374.4612	$[184, 428]$	< 14.40	0.356 ± 0.029
	2382.7650	$[184, 428]$	13.77 ± 0.03	0.692 ± 0.028
	2586.6500	$[184, 428]$	13.82 ± 0.05	0.240 ± 0.027
	2600.1729	$[184, 428]$	13.70 ± 0.03	0.544 ± 0.033
Fe III			< 14.59	
	1122.5260	$[184, 428]$	< 14.59	0.141 ± 0.063
			E	
C II			> 14.86	
	1334.5323	$[428, 650]$	> 14.86	0.650 ± 0.019
C IV			14.39 ± 0.03	
	1550.7700	$[428, 650]$	14.39 ± 0.03	0.391 ± 0.011
N V			< 13.61	
	1238.8210	$[428, 650]$	< 13.61	0.021 ± 0.028
	1242.8040	$[428, 650]$	< 13.90	0.011 ± 0.028
O I			< 14.44	
	1302.1685	$[428, 650]$	< 14.44	0.174 ± 0.024
Mg I			< 12.01	
	2852.9642	$[428, 650]$	< 12.01	0.115 ± 0.042
Mg II			> 13.70	
	2803.5310	$[428, 650]$	> 13.70	0.727 ± 0.026
Al II			12.82 ± 0.03	
	1670.7874	$[428, 650]$	12.83 ± 0.03	0.254 ± 0.013
Al III			12.67 ± 0.09	
	1854.7164	$[428, 650]$	12.67 ± 0.09	0.073 ± 0.015
	1862.7895	$[428, 650]$	< 12.73	0.008 ± 0.015
Si II			13.93 ± 0.04	
	1260.4221	$[428, 650]$	> 13.66	0.424 ± 0.017
	1304.3702	$[428, 650]$	14.15 ± 0.07	0.176 ± 0.025
	1526.7066	$[428, 650]$	13.89 ± 0.05	0.167 ± 0.019
	1808.0130	$[428, 650]$	< 14.91	-0.045 ± 0.018
Si III			> 13.84	
	1206.5000	$[428, 650]$	> 13.84	0.636 ± 0.022

Table 2.17 (cont'd)

Ion	$\lambda_{\rm rest}$ (Å)	$v_{\rm int}^{a}$ (km s^{-1})	$\log N_{\rm AODM}$	Rest EW (Å)
Si IV			13.52 ± 0.03	
	1393.7550	$[428, 650]$	13.51 ± 0.04	0.246 ± 0.019
	1402.7700	$[428, 650]$	13.57 ± 0.07	0.148 ± 0.023
Fe II			13.41 ± 0.03	
	1608.4511	$[428, 650]$	< 13.57	0.045 ± 0.016
	2344.2140	$[428, 650]$	13.45 ± 0.07	0.142 ± 0.022
	2374.4612	$[428, 650]$	< 13.98	0.139 ± 0.028
	2382.7650	$[428, 650]$	13.48 ± 0.03	0.390 ± 0.028
	2586.6500	$[428, 650]$	< 13.49	0.075 ± 0.037
	2600.1729	$[428, 650]$	13.29 ± 0.06	0.245 ± 0.030
Fe III			< 14.69	
	1122.5260	$[428, 650]$	< 14.69	0.200 ± 0.061
F				
C II			13.97 ± 0.06	
	1334.5323	$[651, 808]$	13.97 ± 0.06	0.154 ± 0.019
C II*			14.06 ± 0.05	
	1335.7077	$[651, 808]$	14.06 ± 0.05	0.164 ± 0.019
C IV			14.12 ± 0.03	
	1550.7700	$[651, 808]$	14.12 ± 0.03	0.208 ± 0.009
N V			< 13.53	
	1238.8210	$[651, 808]$	< 13.53	-0.009 ± 0.024
	1242.8040	$[651, 808]$	< 13.82	0.007 ± 0.023
O I			< 14.45	
	1302.1685	$[651, 808]$	< 14.45	0.160 ± 0.022
Mg I			< 11.95	
	2852.9642	$[651, 808]$	< 11.95	0.035 ± 0.038
Mg II			12.82 ± 0.04	
	2796.3520	$[651, 808]$	12.80 ± 0.05	0.242 ± 0.026
	2803.5310	$[651, 808]$	12.87 ± 0.07	0.146 ± 0.024
Al II			11.98 ± 0.12	
	1670.7874	$[651, 808]$	11.98 ± 0.12	0.043 ± 0.012
Al III			< 12.36	
	1854.7164	$[651, 808]$	< 12.36	-0.002 ± 0.013
	1862.7895	$[651, 808]$	< 12.68	-0.006 ± 0.013

Table 2.17 (cont'd)

Ion	$\lambda_{\rm rest}$ (Å)	$v_{\rm int}^a$ (km s^{-1})	$\log N_{\rm AODM}$	Rest EW (Å)
Si II			13.00 ± 0.06	
	1260.4221	$[651, 808]$	13.00 ± 0.06	0.126 ± 0.018
	1304.3702	$[651, 808]$	< 13.72	0.027 ± 0.024
	1526.7066	$[651, 808]$	< 13.28	0.018 ± 0.016
Si II*			< 12.62	
	1264.7377	$[651, 808]$	< 12.62	0.021 ± 0.017
Si III			13.04 ± 0.06	
	1206.5000	$[651, 808]$	13.04 ± 0.06	0.179 ± 0.021
Si IV			12.94 ± 0.11	
	1393.7550	$[651, 808]$	12.94 ± 0.11	0.070 ± 0.017
	1402.7700	$[651, 808]$	< 13.12	0.033 ± 0.019
Fe II			< 12.69	
	1608.4511	$[651, 808]$	< 13.49	-0.021 ± 0.014
	2344.2140	$[651, 808]$	< 13.02	0.010 ± 0.019
	2374.4612	$[651, 808]$	< 14.22	0.231 ± 0.023
	2382.7650	$[651, 808]$	< 12.69	0.040 ± 0.026
	2586.6500	$[651, 808]$	< 13.22	-0.008 ± 0.023
	2600.1729	$[651, 808]$	< 12.77	-0.017 ± 0.028
Fe III			< 14.56	
	1122.5260	$[651, 808]$	< 14.56	0.166 ± 0.048

[a] Velocity interval for the AODM column density measurement. Velocities are relative to the redshift of the foreground quasar J1420+1603FG, $z_{\rm fg} = 2.0197$.

Table 2.18. Ionic Column Densities for J1427−0121FG

Ion	$\lambda_{\rm rest}$ (Å)	$v_{\rm int}^{a}$ (km s^{-1})	$\log N_{\rm AODM}$	Rest EW (Å)
		A		
C II			13.91 ± 0.03	
	1334.5323	$[183, 313]$	13.91 ± 0.03	0.106 ± 0.006
C IV			14.26 ± 0.03	
	1548.1950	$[183, 313]$	> 14.12	0.280 ± 0.011
	1550.7700	$[183, 313]$	14.26 ± 0.03	0.236 ± 0.011
O I			< 13.42	
	1302.1685	$[183, 313]$	< 13.42	0.005 ± 0.006
Si II			12.73 ± 0.03	
	1260.4221	$[183, 313]$	12.72 ± 0.03	0.060 ± 0.004
Si III			13.06 ± 0.03	
	1206.5000	$[183, 313]$	13.06 ± 0.03	0.158 ± 0.006
Si IV			12.86 ± 0.04	
	1393.7550	$[183, 313]$	12.85 ± 0.04	0.052 ± 0.005
	1402.7700	$[183, 313]$	12.90 ± 0.08	0.031 ± 0.006
Fe II			< 12.24	
	2374.4612	$[183, 313]$	< 13.23	-0.000 ± 0.009
	2382.7650	$[183, 313]$	< 12.24	0.020 ± 0.009
	2600.1729	$[183, 313]$	< 12.37	0.014 ± 0.011
		B		
C II			14.03 ± 0.03	
	1334.5323	$[316, 684]$	14.04 ± 0.03	0.179 ± 0.010
C II*			< 12.99	
	1335.7077	$[364, 484]$	< 12.99	0.007 ± 0.006
C IV			14.52 ± 0.03	
	1548.1950	$[316, 684]$	> 14.44	0.674 ± 0.018
	1550.7700	$[316, 684]$	14.52 ± 0.03	0.480 ± 0.019
O I			< 13.40	
	1302.1685	$[364, 484]$	< 13.40	0.005 ± 0.006
Si II			12.84 ± 0.03	
	1260.4221	$[316, 684]$	12.84 ± 0.03	0.090 ± 0.006
Si IV			13.14 ± 0.05	

Table 2.18 (cont'd)

Ion	$\lambda_{\rm rest}$ (Å)	$v_{\rm int}^{a}$ (km s^{-1})	$\log N_{\rm AODM}$	Rest EW (Å)
	1393.7550	$[316, 684]$	13.12 ± 0.08	0.088 ± 0.010
	1402.7700	$[316, 684]$	13.16 ± 0.07	0.054 ± 0.010
Fe II			< 12.48	
	2374.4612	$[316, 684]$	< 13.48	-0.004 ± 0.016
	2382.7650	$[316, 684]$	< 12.48	0.019 ± 0.016
	2600.1729	$[316, 684]$	< 12.58	-0.022 ± 0.018
			C	
C II			14.07 ± 0.03	
	1334.5323	$[754, 834]$	14.07 ± 0.03	0.130 ± 0.004
C II*			13.50 ± 0.04	
	1335.7077	$[754, 834]$	13.50 ± 0.04	0.048 ± 0.004
C IV			< 13.15	
	1550.7700	$[754, 834]$	< 13.15	0.023 ± 0.009
O I			14.22 ± 0.03	
	1302.1685	$[754, 834]$	14.22 ± 0.03	0.080 ± 0.005
Si II			12.73 ± 0.03	
	1260.4221	$[754, 834]$	12.73 ± 0.03	0.054 ± 0.003
	1526.7066	$[754, 834]$	< 13.24	0.034 ± 0.013
Si IV			< 12.16	
	1393.7550	$[754, 834]$	< 12.16	0.007 ± 0.004
	1402.7700	$[754, 834]$	< 12.52	-0.004 ± 0.005
Fe II			< 12.10	
	2374.4612	$[754, 834]$	< 13.25	0.002 ± 0.009
	2382.7650	$[754, 834]$	< 12.10	0.009 ± 0.007
	2600.1729	$[754, 834]$	< 12.25	0.014 ± 0.008

[a] Velocity interval for the AODM column density measurement. Velocities are relative to the redshift of the foreground quasar J1427-0121FG, $z_{\rm fg} = 2.2736$.

Table 2.19. Ionic Column Densities for J1553+1921FG

Ion	$\lambda_{\rm rest}$ (Å)	$v_{\rm int}^{a}$ (km s^{-1})	$\log N_{\rm AODM}$	Rest EW (Å)
		A		
C II			> 14.92	
	1334.5323	$[-62, 535]$	> 14.92	0.950 ± 0.067
C II*			< 13.93	
	1335.7077	$[166, 535]$	< 13.93	-0.034 ± 0.052
C IV			14.57 ± 0.03	
	1548.1950	$[-62, 535]$	> 14.47	0.757 ± 0.036
	1550.7700	$[-62, 535]$	14.57 ± 0.03	0.566 ± 0.036
O I			> 15.05	
	1302.1685	$[-62, 535]$	> 15.05	0.436 ± 0.053
Mg I			12.46 ± 0.07	
	2852.9642	$[-62, 535]$	12.46 ± 0.07	0.320 ± 0.056
Mg II			> 14.09	
	2796.3520	$[-62, 535]$	> 13.94	1.953 ± 0.070
	2803.5310	$[-62, 535]$	> 14.09	1.405 ± 0.055
Al II			> 13.36	
	1670.7874	$[-62, 535]$	> 13.36	0.633 ± 0.031
Al III			13.11 ± 0.07	
	1854.7164	$[-62, 535]$	13.11 ± 0.07	0.188 ± 0.033
	1862.7895	$[-62, 535]$	< 13.08	0.075 ± 0.033
Si II			15.26 ± 0.14	
	1190.4158	$[-62, 535]$	> 14.68	0.749 ± 0.093
	1260.4221	$[-62, 535]$	> 14.11	0.968 ± 0.032
	1304.3702	$[-62, 535]$	> 14.61	0.358 ± 0.055
	1526.7066	$[-62, 535]$	> 14.48	0.512 ± 0.055
	1808.0130	$[-62, 386]$	15.26 ± 0.14	0.110 ± 0.035
Si III			> 14.03	
	1206.5000	$[-62, 535]$	> 14.03	1.199 ± 0.064
Si IV			13.82 ± 0.10	
	1393.7550	$[-62, 535]$	> 14.09	0.718 ± 0.049
	1402.7700	$[-62, 535]$	13.82 ± 0.10	0.188 ± 0.059
Fe II			14.02 ± 0.03	
	1608.4511	$[-62, 535]$	14.28 ± 0.06	0.222 ± 0.032
	2344.2140	$[-62, 535]$	13.91 ± 0.05	0.345 ± 0.044

Table 2.19 (cont'd)

Ion	$\lambda_{\rm rest}$ (Å)	$v_{\rm int}^a$ (km s^{-1})	$\log N_{\rm AODM}$	Rest EW (Å)
	2374.4612	$[-62, 535]$	14.32 ± 0.07	0.292 ± 0.051
	2382.7650	$[-62, 535]$	> 14.03	1.184 ± 0.051
	2586.6500	$[-62, 535]$	14.09 ± 0.05	0.400 ± 0.058
	2600.1729	$[-62, 535]$	> 13.86	0.673 ± 0.056
Fe III			< 15.13	
	1122.5260	$[-62, 535]$	< 15.13	0.416 ± 0.197

[a]Velocity interval for the AODM column density measurement. Velocities are relative to the redshift of the foreground quasar J1553+1921FG, $z_{\rm fg} = 2.0098$.

Table 2.20. Ionic Column Densities for J1627+4605FG

Ion	$\lambda_{\rm rest}$ (Å)	$v_{\rm int}^a$ (km s^{-1})	$\log N_{\rm AODM}$	Rest EW (Å)
		A		
C II			< 13.17	
	1334.5323	$[-828, -508]$	< 13.17	0.008 ± 0.010
C IV			13.63 ± 0.04	
	1548.1950	$[-828, -358]$	13.67 ± 0.04	0.168 ± 0.017
	1550.7700	$[-828, -358]$	13.47 ± 0.11	0.056 ± 0.015
O I			< 13.53	
	1302.1685	$[-828, -358]$	< 13.53	-0.002 ± 0.008
Al II			< 12.06	
	1670.7874	$[-828, -358]$	< 12.06	-0.040 ± 0.018
Si II			< 13.25	
	1304.3702	$[-828, -358]$	< 13.25	-0.007 ± 0.008
	1526.7066	$[-828, -358]$	< 13.36	0.021 ± 0.020
Si IV			< 12.66	
	1393.7550	$[-828, -358]$	< 12.66	0.020 ± 0.014
	1402.7700	$[-828, -358]$	< 12.96	-0.009 ± 0.014

[a]Velocity interval for the AODM column density measurement. Velocities are relative to the redshift of the foreground quasar J1627+4605FG, $z_{\rm fg} = 3.8137$.

Table 2.21. H I Column Density Measurements

Subsystem	Velocity Range (km s^{-1})	Adopted log $N^{a}_{\rm HI}$	Component Centroid (km s^{-1})	Component log $N_{\rm HI}$	Doppler b (km s^{-1})
J0225+0048 $z_{\rm fg} = 2.7265$ $N^{\rm total}_{\rm HI} = 17.9$					
A	$[-362, 88)$	$17.5^{+1.0}_{-1.0}$			
			-217 ± 2	17.5	34
			-59 ± 5	14.0 ± 0.2	15
			$+33 \pm 4$	14.1 ± 0.1	60
B	$[88, 498)$	$16.9^{+1.0}_{-1.0}$			
			$+303 \pm 2$	16.9 ± 0.2	60
C	$[498, 827)$	$17.5^{+0.8}_{-0.8}$			
			$+536 \pm 7$	13.4 ± 0.1	15
			$+694 \pm 2$	17.5	37
			$+905$	13.6 ± 0.2	59 ± 12
			$+1067$	13.3 ± 0.2	44 ± 16
J0341+0000 $z_{\rm fg} = 2.1233$ $N^{\rm total}_{\rm HI} = 14.2$					
A	$[-500, 200)$	$14.2^{+0.2}_{-0.2}$			
			$+264 \pm 4$	13.8 ± 0.1	15
			$+395 \pm 5$	13.9 ± 0.1	56 ± 8
J0409−0411 $z_{\rm fg} = 1.7155$ $N^{\rm total}_{\rm HI} = 14.2$					
A	$[-300, 400)$	$14.2^{+0.2}_{-0.2}$			
			-1346 ± 6	14.2 ± 0.2	51 ± 9
J0853−0011 $z_{\rm fg} = 2.4014$ $N^{\rm total}_{\rm HI} = 18.8$					
A	$[-274, -60)$	$16.8^{+0.6}_{-0.6}$			
			-163 ± 1	17.2 ± 0.4	22 ± 1
B	$[-60, 203)$	$18.6^{+0.2}_{-0.6}$			
			$+47 \pm 32$	15.5 ± 0.4	46 ± 12
			$+102 \pm 10$	18.4 ± 0.1	15 ± 3
C	$[203, 379)$	$18.2^{+0.3}_{-0.6}$			
			$+274 \pm 1$	18.3 ± 0.2	20

Table 2.21 (cont'd)

Subsystem	Velocity Range (km s^{-1})	Adopted log $N^a_{\rm HI}$	Component Centroid (km s^{-1})	Component log $N_{\rm HI}$	Doppler b (km s^{-1})
		J0932+0925 $z_{\rm fg} = 2.4170$ $N^{\rm total}_{\rm HI} = 15.7$			
A	$[-245, 307)$	$15.5^{+0.4}_{-0.4}$			
			-168 ± 1	15.4 ± 0.4	34 ± 4
			+24	14.3	55
			+146	14.1	45
B	$[307, 675)$	$15.1^{+0.3}_{-0.3}$			
			+325	13.7	40
			+438	14.0	40
			$+519 \pm 3$	15.0 ± 0.1	58 ± 3
C	$[675, 959)$	$14.3^{+0.1}_{-0.1}$			
			+775	14.0	55
			+911	13.6	45
			+985	13.9	35
		J1026+4614 $z_{\rm fg} = 3.3401$ $N^{\rm total}_{\rm HI} = 15.5$			
A	$[296, 450)$	$15.4^{+0.2}_{-0.2}$			
			$+208 \pm 4$	15.0 ± 0.1	51 ± 2
			$+308 \pm 3$	15.0 ± 0.1	20 ± 4
B	$[450, 539)$	$14.6^{+0.1}_{-0.1}$			
			$+412 \pm 2$	14.6 ± 0.1	60
		J1038+5027 $z_{\rm fg} = 3.1323$ $N^{\rm total}_{\rm HI} = 16.6$			
A	$[451, 701)$	$16.6^{+0.5}_{-0.5}$			
			$+517 \pm 7$	16.6 ± 1.4	42 ± 23
			$+671 \pm 8$	14.3 ± 0.2	29 ± 9
		J1144+0959 $z_{\rm fg} = 2.9731$ $N^{\rm total}_{\rm HI} = 18.8$			
A	$[-1696, -1483)$	$13.5^{+0.2}_{-0.2}$			
			-1674 ± 1	13.2 ± 0.1	21 ± 1
			-1637 ± 5	12.4 ± 0.1	15
			-1600 ± 2	12.8 ± 0.2	18 ± 3
			-1541 ± 12	12.5 ± 0.2	38 ± 21

Table 2.21 (cont'd)

Subsystem	Velocity Range (km s^{-1})	Adopted log $N_{\rm HI}^{a}$	Component Centroid (km s^{-1})	Component log $N_{\rm HI}$	Doppler b (km s^{-1})
B	$[-1483, -1195)$	$18.1^{+0.2}_{-0.4}$			
			-1261	18.1 ± 0.2	48
C	$[-1195, -1075)$	$18.3^{+0.2}_{-0.4}$			
			-1169	18.3 ± 0.2	26
D	$[-1075, -535)$	$17.9^{+0.5}_{-0.5}$			
			-956	17.7 ± 0.2	37 ± 1
			-801 ± 2	14.7 ± 0.1	33 ± 2
			-710 ± 1	15.2 ± 0.1	48 ± 1
			-585	14.3 ± 0.1	26
E	$[-535, -68)$	$15.6^{+0.2}_{-0.2}$			
			-513 ± 1	13.0 ± 0.1	18 ± 2
			-444 ± 2	13.2 ± 0.1	38 ± 3
			-259 ± 2	12.8 ± 0.2	26 ± 3
			-108	15.8 ± 0.1	15
F	$[-68, 197)$	$18.4^{+0.2}_{-0.4}$			
			-21 ± 3	15.4 ± 0.1	60
			$+26 \pm 5$	18.3 ± 0.1	15 ± 2
			$+127 \pm 5$	16.8 ± 0.3	28 ± 1
J1145+0322 $z_{\rm fg} = 1.7652$ $N_{\rm HI}^{\rm total} = 18.4$					
A	$[-271, 119)$	$18.4^{+0.4}_{-0.4}$			
			-75 ± 4	18.4 ± 0.1	49 ± 2
J1204+0221 $z_{\rm fg} = 2.4358$ $N_{\rm HI}^{\rm total} = 19.7$					
A	$[67, 217)$	$18.6^{+0.4}_{-0.4}$			
			$+6 \pm 2$	13.7 ± 0.1	25 ± 2
			$+144$	18.6 ± 0.1	25
B	$[217, 617)$	$19.6^{+0.2}_{-0.2}$			
			$+392$	19.8 ± 0.1	40
C	$[617, 767)$	$18.6^{+0.4}_{-0.4}$			
			$+687$	18.6 ± 0.1	22
			$+850 \pm 3$	12.8 ± 0.1	19 ± 5
			$+971 \pm 1$	13.5 ± 0.1	30 ± 1
			$+1071$	14.4 ± 0.1	25

Table 2.21 (cont'd)

Subsystem	Velocity Range (km s^{-1})	Adopted log $N^a_{\rm HI}$	Component Centroid (km s^{-1})	Component log $N_{\rm HI}$	Doppler b (km s^{-1})
			$+1297 \pm 4$	12.7 ± 0.2	30 ± 6
			$+1513 \pm 2$	12.8 ± 0.1	29 ± 3
			$+1626 \pm 1$	13.0 ± 0.1	23 ± 2
J1420+1603 $z_{\rm fg} = 2.0197$ $N^{\rm total}_{\rm HI} = 19.1$					
A	$[-656, -420)$	$15.8^{+1.0}_{-1.0}$			
			-343	16.0 ± 2.0	40 ± 28
B	$[-420, -199)$	$18.5^{+0.4}_{-0.4}$			
			-184	18.5 ± 0.1	37 ± 3
C	$[-199, 69)$	$18.0^{+0.6}_{-0.6}$			
			$+93$	17.4 ± 0.7	34 ± 40
D	$[69, 313)$	$18.6^{+0.4}_{-0.4}$			
			$+272$	18.3	15
			$+331$	18.3	15
E	$[313, 535)$	$18.6^{+0.4}_{-0.4}$			
			$+490$	18.6	46 ± 1
F	$[535, 693)$	$17.5^{+1.0}_{-1.0}$			
			$+718$	17.5 ± 0.2	16 ± 2
J1427−0121 $z_{\rm fg} = 2.2736$ $N^{\rm total}_{\rm HI} = 18.8$					
A	$[172, 293)$	$17.3^{+0.5}_{-1.0}$			
			$+232$	17.3 ± 0.1	15
B	$[293, 739)$	$18.3^{+0.2}_{-1.0}$			
			$+321$	13.2 ± 0.2	15
			$+390 \pm 3$	15.0 ± 0.4	15
			$+455 \pm 3$	18.3 ± 0.2	15
			$+524 \pm 4$	13.7 ± 0.2	15
			$+568 \pm 1$	14.7 ± 0.2	15
C	$[739, 842)$	$18.6^{+0.2}_{-1.0}$			
			$+771$	17.1 ± 0.3	15
			$+803$	18.6 ± 0.1	15
			$+899 \pm 7$	14.3 ± 0.2	41 ± 8
			$+979 \pm 1$	13.7 ± 0.1	18 ± 1

Table 2.21 (cont'd)

Subsystem	Velocity Range (km s^{-1})	Adopted log $N_{\rm HI}^{a}$	Component Centroid (km s^{-1})	Component log $N_{\rm HI}$	Doppler b (km s^{-1})
		J1553+1921 $z_{\rm fg} = 2.0098$ $N_{\rm HI}^{\rm total} = 20.2$			
A	$[-342, 258)$	$20.2^{+0.1}_{-0.1}$			
			$+323 \pm 15$	20.2 ± 0.1	15
		J1627+4605 $z_{\rm fg} = 3.8137$ $N_{\rm HI}^{\rm total} = 16.9$			
A	$[-824, -356)$	$16.9^{+0.8}_{-0.8}$			
			-862 ± 4	13.6 ± 0.1	47 ± 6
			-704 ± 1	16.6 ± 0.5	34 ± 3
			-535 ± 1	14.2 ± 0.1	36 ± 2
			-401 ± 5	13.5 ± 0.1	60

[a] The adopted $N_{\rm HI}$ values match approximately the middle of lower bounds from equivalent widths and upper bounds from wings of the Lyman series absorptions. The $N_{\rm HI}$ values of the individual components of a subsystem come from ALIS voigt profile modeling outputs, which serve as guides to our adopted $N_{\rm HI}$ for a subsystem. The two need not agree and ALIS tends to give biased high values.

Chapter 3

Quasars Probing Quasars: the Kinematics of the Circumaglactic Medium Surrounding $z \sim 2$ Quasars

We examine the kinematics of the gas in the environments of galaxies hosting quasars at $z \sim 2$. We employ 148 projected quasar pairs to study the circumgalactic gas of the foreground quasars in absorption. The sample selects foreground quasars with precise redshift measurements, using emission-lines with precision $\lesssim 300\,\mathrm{km\,s^{-1}}$ and average offsets from the systemic redshift $\lesssim |100\,\mathrm{km\,s^{-1}}|$. We stack the background quasar spectra at the foreground quasar's systemic redshift to study the mean absorption in C II, C IV, and Mg II. We find that the mean absorptions exhibit large velocity widths $\sigma_v \approx 300\,\mathrm{km\,s^{-1}}$. The observed widths are consistent with gas in gravitational motion and Hubble flow, and galactic-scale outflows are not required to explain the large widths. Furthermore, we find that the mean absorptions are asymmetric about the systemic redshift. The mean absorption centroids exhibit small redshift relative to the systemic $\delta v \approx +200\,\mathrm{km\,s^{-1}}$, with large intrinsic scatter in the centroid velocities of the individual absorption

systems. We show that the observed offsets may be produced if (i) the ionizing radiation from the foreground quasars is anisotropic or intermittent; (ii) the gas is not flowing into the galaxy.

3.1 Introduction

Galaxy formation and evolution are driven by the flows of gas into and out of their interstellar medium. Current theories demand that star-forming galaxies maintain these flows. Gas accretes, cools, and adds to the fuel supply, while star formation feedback heats gas, blows it out of galaxies, and regulates star formation (for a review see Somerville & Davé 2015).

Direct observations of galactic flows are difficult to acquire. Detecting the presence of the gas is itself challenging. Either the gas mass is too small, or the gas density is too low for the detection of line-emission, e.g. 21 cm, Lyα, or Hα from H I. Resolving the kinematics and establishing the mass flux pose an even greater challenge. These challenges are accentuated for distant, young galaxies, where flows of gas are predicted to prevail (Kereš et al. 2009; Fumagalli et al. 2011). Therefore, with rare exceptions, (e.g. Cantalupo et al. 2014; Hennawi et al. 2015), the community has relied on absorption-line spectroscopy to detect and characterize the gas surrounding galaxies (e.g. Bergeron & Boisse 1991; Steidel et al. 2010; Prochaska et al. 2011; Tumlinson et al. 2013). In a previous paper of the Qussars Probing Quasars series (Lau et al. 2016, , hereafter QPQ8), we measured the velocity field for C II 1334 and C IV 1548, finding that the circumgalactic medium frequently exhibits large velocity widths that are offset from the systemic redshift. The offsets, δv, are often positive, with the sign convention that positive velocities indicate a redshift from the systemic. From a sample of 7 C II systems and 10 C IV systems, we measured the velocity interval that encompasses 90% of the total optical depth, Δv_{90}, and the 1σ dispersion relative to the profile centroid, σ_v. The median Δv_{90} is $555\,\mathrm{km\,s^{-1}}$ for C II 1334 and is $342\,\mathrm{km\,s^{-1}}$ for C IV 1548.

The median σ_v is 249 $\mathrm{km\,s^{-1}}$ for C II 1334 and is 495 $\mathrm{km\,s^{-1}}$ for C IV 1548. These velocity fields exceed all previous measurements from galaxies and/or absorption systems at any epoch.

With absorption-line spectroscopy of background sightlines, other researchers also have had success in characterizing the flows of gas around galaxies. Rakic et al. (2012) found a net large-scale inflow around star-forming galaxies, or a Kaiser effect for gas on 1–2 Mpc scales. Ho et al. (2017) found gas spiraling inward near the disk plane of star-forming galaxies on < 100 kpc scales. Johnson et al. (2015) studied the CGM surrounding $z \sim 1$ quasars. They found large peculiar motions in the gas exceeding the expected virial velocity, with quasar-driven outflows begin one possible explanation. However, we consider that their velocity spreads can be better quantified. Other existing studies that found large velocity spreads are limited to single sightlines with most of the gas within several hundred $\mathrm{km\,s^{-1}}$ (e.g., Tripp et al. 2011; Rudie et al. 2017), or with gas tracing a higher ionization state than the QPQ absorption systems (e.g., Churchill et al. 2012), or where the average velocity spread is smaller than that measured in QPQ8. In Gauthier (2013), where a single sightline is reported, the Δv_{90} of the Mg II absorption is less than the average of the QPQ8 C II absorption. In Muzahid et al. (2015), an absorber is found with Δv_{90} smaller than 555 $\mathrm{km\,s^{-1}}$ in O VI and N V, and still smaller for other ions. The Zahedy et al. (2016) sample likewise has average Δv_{90} smaller than that of QPQ8.

A significant limitation of absorption-line analysis of transverse sightlines, especially regarding galactic-scale flows, is the inherent symmetry of the experiment. One generally lacks any constraint on the distance of the gas along the sightline. Positive or negative velocities with respect to the galaxy may be interpreted as gas flowing either toward or away from the system. “Down-the-barrel” observations break this symmetry, and have generally provided evidence for flows away from galaxies (Rupke et al. 2005; Martin 2005; Weiner et al. 2009; Rubin et al. 2014). However, these data are frequently at low spectral resolution which limits one’s sensitivity to inflowing gas.

In this paper (hereafter QPQ9), we examine the flows of gas in the environments of massive galaxies hosting quasars. Our approach leverages a large dataset of quasar pairs (Hennawi et al. 2006a, , hereafter QPQ1) to use the standard techniques of absorption-line spectroscopy with background quasars. These quasar pairs have angular separations that correspond to less than 300 kpc projected separation at the foreground quasar's redshift. Our previous publications from these quasar pairs have established that these galaxies are surrounded by a massive, cool, and enriched CGM (QPQ5, QPQ6, QPQ7: Prochaska et al. 2013b,a, 2014). We have collected a sample of 148 background spectra that are paired with foreground quasars with precisely measured redshifts. Among the sightlines in the QPQ9 sample, 13 have spectral resolution $R > 5000$ from echellette or echelle observations, and have been analyzed separately in QPQ8 (see their Figure 8, 9, and 10, and their Appendix). In QPQ8, where the individual metal-bearing absorption components are resolved, 15 out of the 21 components are at positive velocities to the systemic redshift. For this current work, we stack spectra of all resolutions instead of performing a component-by-component analysis. Our primary scientific interests are twofold: (i) search for signatures of galactic-scale outflows from the central galaxy, presumably driven by recent star formation and/or active galactic nuclei feedback; (ii) characterize the dynamics of the gas around these massive systems. We further describe an aspect of this experiment that offers a unique opportunity to study galactic-scale flows: we argue that, the anisotropic or intermittent radiation from the foreground quasars may break the symmetry in the velocity field of circumgalactic absorbers. If the ionizing radiation field is asymmetric, the absorbers may also distribute asymmetrically. Alternatively, finite quasar lifetime will result in different radiation fields impinged on the gas closer to versus further away from the background quasar, due to different light travel times. Kirkman & Tytler (2008) reported an asymmetry in H I absorption on scales larger than the CGM, and gave similar arguments on anisotropy or intermittence.

We adopt a ΛCDM cosmology with $\Omega_M = 0.26, \Omega_\Lambda = 0.74$, and $H_0 = 70\,\mathrm{km\,s^{-1}\,Mpc^{-1}}$. Distances are proper unless otherwise stated. When referring to comoving distances we include explicitly an h^{-1} term and follow modern convention of scaling to the Hubble constant $h = H_0/(70\,\mathrm{km\,s^{-1}\,Mpc^{-1}})$.

3.2 The Experiment

The goal of our experiment is to measure the average velocity fields of the absorption from C^+, C^{3+}, and Mg^+ ions associated with the CGM of the galaxies hosting $z \sim 2$ quasars.

From our QPQ survey[1], we analyze a subset of systems that pass within transverse separation $R_\perp < 300\,\mathrm{kpc}$ from a foreground quasar with $z_{\mathrm{fg}} > 1.6$. We restrict the sample to foreground quasars with redshift measured from Mg II 2800, [O III] 5007, or Hα emission, giving a precision of $300\,\mathrm{km\,s^{-1}}$ or better and an average offset from the systemic redshift of $|100\,\mathrm{km\,s^{-1}}|$ or less. According to Shen et al. (2016a), the [O III] emission-line redshifts have the smallest scatter (intrinsic scatter and measurement error combined) of $68\,\mathrm{km\,s^{-1}}$ about the systemic redshift, and we analyze the sub-sample with [O III] redshifts separately. The [O III] line has an average blueshift of $48\,\mathrm{km\,s^{-1}}$ about the systemic redshift, which has been added when we compute the redshift of the line. The scatter and average offset of [O III] redshifts reported by Shen et al. (2016a) is consistent with the numbers reported by Boroson (2005) using a larger but lower redshift sample. Systemic redshifts measured from Mg II have a precision of $226\,\mathrm{km\,s^{-1}}$ according to Shen et al. (2016a), and we have taken into account their reported median blueshift of $57\,\mathrm{km\,s^{-1}}$ of Mg II from the systemic. We note that Richards et al. (2002) reported a median redshift of $97\,\mathrm{km\,s^{-1}}$ of Mg II from [O III] using a larger but lower redshift sample. In QPQ8, we quantified the precision of Hα

---

[1] http://www.qpqsurvey.org

to be $300\,\mathrm{km\,s^{-1}}$ and the median offset from the systemic redshift is close to zero, consistent with the velocity shifts measured by Shen et al. (2011). Although Hβ is a narrow emission-line, we do not consider its redshift sufficiently reliable for use as systemic redshift. Hβ redshifts have a large scatter about the systemic $\approx 400\,\mathrm{km\,s^{-1}}$, and a large average offset about the systemic $\approx 100\,\mathrm{km\,s^{-1}}$ (Shen et al. 2016a, QPQ8). Our line-centering algorithm calculates the mode of a line given by $3 \times \mathrm{median} - 2 \times \mathrm{mean}$, applied to the upper 60% of the emission, while Shen et al. (2016a) calculates the peak of a line. We expect that our line-centering algorithm gives emission redshifts very comparable to the Shen et al. (2016a) algorithm, however. Shen et al. (2016a) states that the difference between the peak and the centroid of an emission-line is not significant except for the broad line Hβ, which we do not use in redshift measurements. To quantify the above, we further obtain individual measurements of centroids and peaks in the Shen et al. (2016a) sample through private communication. We found there is essentially no difference between using the centroid versus using the peak for [O III] emission redshifts, and there is on average $50\,\mathrm{km\,s^{-1}}$ difference for Mg II. We may expect the difference between the mode and the peak is even smaller. Hence, we argue that the average systemic bias corrections measured in Shen et al. (2016a) may be self-consistently applied to our measured emission-line redshifts to obtain systemic redshifts.

We further add to the QPQ dataset with quasar pairs selected from the public dataset of igmspec[2], which includes the spectra from the quasar catalogs based upon the Sloan Digital Sky Survey Seventh Data Release (Schneider et al. 2010) and the Twelfth Data Release (Pâris et al. 2017). We only select pairs with z_{fg} measured using a robust Mg II 2800 emission-line. We reach a final sample size of 148. Figure 3.1 summarizes the experimental design. We refer the reader to previous QPQ publications for the details on the emission-line centering algorithm, data reduction, and continuum normalization (QPQ1; QPQ6; QPQ8).

---

[2] https://github.com/specdb/igmspec

As in the previous QPQ papers, we select the quasar pairs to have redshift difference $> 3000\,\mathrm{km\,s^{-1}}$, to exclude physically associated binary quasars. The cut on velocity difference is motivated by the typical redshift uncertainty of $\approx 500\,\mathrm{km\,s^{-1}}$ of the background quasars. In QPQ8, it was required that the observed wavelengths of the metal ion transitions fall outside the Lyα forest of the background quasar. In this paper, we exclude a small window around the Lyα emission, in additional to the Lyα forest, from analysis. For stacked profile analysis, a good estimate of the continuum level is necessary. In QPQ8 we found that absorption associated to the foreground quasar occurs within $\pm 2000\,\mathrm{km\,s^{-1}}$ around z_{fg}. Therefore, it is desirable to keep a $\approx \pm 3000\,\mathrm{km\,s^{-1}}$ window relatively free of contamination from Lyα forest. Taking into account the redshift uncertainties, we decide that at least one transition among C II 1334, C IV 1548, and Mg II 2796 at z_{fg} must lie redward of $(1215.6701 + 20) \times (1 + z_{\mathrm{bg}})$ Å, for a pair to be included in the analysis.

Furthermore, we include only those spectra with average signal-to-noise ratio (S/N) exceeding 5.5 per rest-frame Å in a $\pm 3000\,\mathrm{km\,s^{-1}}$ window centered on the observed wavelengths of the metal ion transitions. This criterion is a compromise between maximizing sample size versus maintaining good data quality on the individual sightlines. We find that $\mathrm{S/N} > 5.5$ per rest-frame Å is necessary for properly estimating the continuum, as well as identifying mini-broad absorption line systems associated to the background quasar, which will significantly depress the flux level. We also require that the region of the spectrum that is $\pm 3000\,\mathrm{km\,s^{-1}}$ around a considered metal ion transition does not overlap with strong atmospheric $\mathrm{O_2}$ bands. The $\mathrm{O_2}$ A- and B-band span 7595–7680 Å and 6868–6926 Å respectively.

Table 3.1 lists the full QPQ9 sample. In Table 3.2, we first list the sample size, the median z_{fg}, and the median $R_{\perp}$ of the quasar pairs that survive the above selection criteria for C II 1334, C IV 1548, and Mg II 2796 respectively. We then provide the summary for the sub-sample with z_{fg} measured from [O III].

Table 3.1. Properties of the Projected Quasar Pairs in the QPQ9 sample

Foreground Quasar	z_{fg}	Line for z_{fg}^{a}	Background Quasar	z_{bg}	BG Quasar Instrument	$R_{\perp}$ (kpc)	g_{UV}
J003423.05−1050020	1.8388	MgII	J003423.44-104956.3	1.948	LRIS	67	11938
J004220.66+003218.7	1.9259	MgII	J004218.72+003237.1	3.048	BOSS	299	97
J004745.49+310120.3	1.9706	MgII	J004745.61+310138.3	2.695	BOSS	157	1723
J004757.26+144741.0	1.6191	MgII	J004757.88+144744.7	2.757	BOSS	82	6697
J005717.36−000113.3	2.1611	[OIII]	J005718.99-000134.7	2.511	BOSS	271	1283
J010323.84−000254.2	1.7506	MgII	J010324.37-000251.3	2.306	BOSS	74	5462
J014328.77+295436.8	1.8007	MgII	J014330.89+295439.9	2.018	BOSS	243	997
J014917.11−002141.6	1.6834	MgII	J014917.46-002158.5	2.159	SDSS	155	2390
J021416.96−005229.1	1.8002	MgII	J021416.12-005251.5	2.332	BOSS	225	564
J022447.89−004700.4	1.6959	MgII	J022448.85-004638.9	2.188	BOSS	226	293
J023018.27−033319.4	2.3817	MgII	J023019.99-033315.0	2.985	BOSS	221	1444
J023315.44−000303.6	1.7205	MgII	J023315.75-000231.4	1.839	BOSS	286	101
J023946.43−010640.4	2.299	[OIII]	J023946.45-010644.1	3.124	BOSS	32	20931
J024603.68−003211.8	1.603	MgII	J024602.35-003221.6	2.153	BOSS	195	1889
J025038.68−004739.2	1.8538	MgII	J025039.82-004749.6	2.445	BOSS	175	4007
J034138.16+000002.9	2.1246	MgII	J034139.19-000012.7	2.243	GMOS-N	190	392
J040955.87−041126.9	1.7166	MgII	J040954.21-041137.1	2.0	SDSS	235	715
J072739.55+392855.3	1.9853	MgII	J072739.72+392919.5	2.433	BOSS	210	403
J075009.25+272405.2	1.7713	MgII	J075008.27+272404.5	1.802	LRIS	114	1370
J075259.81+401128.2	1.8844	MgII	J075259.14+401118.2	2.121	SDSS	110	1060
J080049.89+354249.6	1.9825	[OIII]	J080048.74+354231.3	2.066	LRIS	201	2074
J080537.29+472339.3	1.8913	MgII	J080538.78+472404.8	2.964	BOSS	259	367
J080945.17+453918.1	2.0392	MgII	J080948.22+453929.0	2.278	BOSS	292	195
J081223.17+262000.9	1.6427	MgII	J081223.89+262012.5	2.17	BOSS	132	3442
J081419.58+325018.7	2.1744	[OIII]	J081420.38+325016.1	2.213	GMOS-N	90	2899
J081832.87+123219.9	1.7032	MgII	J081833.97+123215.4	2.234	BOSS	147	6609
J082346.05+532527.8	1.6467	MgII	J082347.49+532519.1	1.86	BOSS	136	820
J082421.01+531249.3	2.0855	MgII	J082420.02+531315.2	2.165	BOSS	237	340
J082843.37+454517.3	1.873	MgII	J082844.87+454518.2	1.987	LRIS	137	525
J083030.38+545228.8	1.6702	MgII	J083029.11+545210.3	3.337	BOSS	188	1506
J083713.56+363037.3	1.8364	MgII	J083712.69+363037.7	2.301	MODS1	92	5012
J083757.91+383727.1	2.0624	Hα	J083757.13+383722.4	2.251	LRIS	89	8609
J083854.52+462124.4	1.7596	MgII	J083852.94+462137.6	2.163	BOSS	184	673
J084158.47+392120.0	2.0414	[OIII]	J084159.26+392139.0	2.214	LRIS	183	1514
J084511.89+464135.5	1.6295	MgII	J084509.64+464113.0	1.898	BOSS	283	135
J085019.43+475538.5	1.8164	MgII	J085021.17+475516.0	1.891	BOSS	249	392
J085151.38+522901.6	1.9738	MgII	J085154.53+522910.6	2.031	BOSS	262	265

Table 3.1 (cont'd)

Foreground Quasar	$z_{\rm fg}$	Line for $z_{\rm fg}^a$	Background Quasar	$z_{\rm bg}$	BG Quasar Instrument	$R_\perp$ (kpc)	$g_{\rm UV}$
J085249.45+471423.1	1.6468	MgII	J085248.55+471419.3	1.688	BOSS	87	7078
J085358.36−001108.0	2.4016	[OIII]	J085357.49-001106.2	2.579	MagE	112	1231
J085629.48+551450.2	1.6228	MgII	J085630.45+551417.5	1.932	BOSS	296	466
J085737.58+390120.5	1.9529	MgII	J085738.00+390136.0	2.848	BOSS	150	1984
J090417.94+004148.2	1.6193	MgII	J090419.12+004205.1	1.645	SDSS	214	1035
J090657.78+100121.4	1.6965	MgII	J090657.62+100105.6	2.525	BOSS	141	6960
J091046.44+041458.5	2.0461	[OIII]	J091046.69+041448.4	2.377	MagE	95	11897
J091217.57+413933.5	1.7764	MgII	J091215.75+413948.2	2.198	BOSS	220	790
J091234.27+305616.2	1.6237	MgII	J091236.32+305626.5	2.146	BOSS	247	514
J091338.33−010708.7	2.7491	MgII	J091338.97-010704.6	2.916	XSHOOTER	89	5830
J091432.02+010912.4	2.1404	[OIII]	J091430.85+010927.5	2.475	BOSS	199	1222
J091551.72+011900.2	1.9706	MgII	J091553.37+011911.4	2.102	BOSS	236	970
J092405.06+474611.4	2.0556	MgII	J092402.85+474600.7	2.098	BOSS	214	341
J092417.65+392920.3	1.8864	MgII	J092416.72+392914.6	2.08	LRIS	106	2788
J092543.88+372504.9	2.0704	MgII	J092544.71+372503.5	2.314	BOSS	94	3890
J093226.34+092526.1	2.4172	[OIII]	J093225.66+092500.2	2.602	MagE	238	774
J093317.43+592027.4	1.8617	MgII	J093320.57+592036.5	2.633	BOSS	224	1441
J093640.35−005840.1	2.2098	MgII	J093642.12-005831.3	2.731	BOSS	250	496
J093936.83+482115.0	1.8878	MgII	J093938.97+482059.4	2.415	BOSS	230	528
J093952.56+505207.4	1.6105	MgII	J093954.75+505148.8	2.476	BOSS	242	128
J094133.64+230840.1	1.7762	MgII	J094135.61+230845.8	2.551	BOSS	243	1700
J094906.23+465938.4	1.7204	MgII	J094906.52+465909.6	2.173	BOSS	253	243
J095127.06+493248.3	1.7407	MgII	J095126.22+493218.8	1.83	BOSS	268	293
J095858.88+491253.1	2.0505	MgII	J095858.06+491307.5	2.155	BOSS	144	722
J100046.45+033708.8	1.7006	MgII	J100048.52+033708.8	2.353	BOSS	271	255
J100509.56+501929.8	1.8176	MgII	J100507.07+501929.8	2.019	LRIS	211	330
J100627.47+480420.0	2.3034	[OIII]	J100627.11+480429.9	2.597	BOSS	90	2886
J100913.91+023612.4	1.7359	MgII	J100913.33+023643.0	2.216	BOSS	287	342
J100941.35+250104.1	1.8703	MgII	J100940.58+250053.9	1.981	LRIS	127	3588
J101001.51+403755.5	2.1924	Hα	J101003.47+403754.9	2.505	BOSS	191	5421
J101323.89+033016.0	1.9401	MgII	J101322.23+033009.1	2.273	BOSS	219	426
J101753.38+622653.4	1.6528	MgII	J101750.44+622648.2	2.738	BOSS	184	922
J101947.11+494835.8	1.6224	MgII	J1019470+494849.1	1.652	LRIS	117	881
J102007.23+611955.0	1.7909	MgII	J102010.05+611950.3	2.387	BOSS	180	1817
J102259.33+491125.8	1.9757	MgII	J102259.97+491151.7	2.469	BOSS	231	212
J102821.26+240121.8	1.8709	MgII	J102822.18+240057.4	2.414	BOSS	240	834
J103443.62+085702.0	1.6395	MgII	J103442.26+085645.7	2.766	BOSS	233	700

Table 3.1 (cont'd)

Foreground Quasar	$z_{\rm fg}$	Line for $z_{\rm fg}^{a}$	Background Quasar	$z_{\rm bg}$	BG Quasar Instrument	$R_{\perp}$ (kpc)	$g_{\rm UV}$
J103628.12+501157.9	2.0097	MgII	J103630.52+501219.8	2.228	BOSS	271	1198
J103857.37+502707.0	3.1325	[OIII]	J103900.01+502652.8	3.236	ESI	233	3567
J103946.92+454716.0	1.8644	MgII	J103945.58+454707.4	2.456	BOSS	148	675
J104244.84+650002.7	1.9876	MgII	J104245.14+645936.7	2.124	BOSS	227	703
J104435.62+313950.7	1.7062	MgII	J104434.76+313957.7	2.377	BOSS	115	1873
J104955.01+231358.2	1.8439	MgII	J104953.97+231401.3	2.171	BOSS	129	1813
J105221.77+555253.5	1.9989	MgII	J105218.36+555311.3	2.278	BOSS	293	846
J105246.45+641832.2	1.6429	MgII	J105251.42+641838.5	2.936	BOSS	286	127
J111339.86+330604.8	1.8913	MgII	J111337.84+330553.3	2.413	BOSS	243	853
J111850.44+402553.8	1.9257	MgII	J111851.45+402557.6	2.317	BOSS	106	1946
J112858.89+644440.4	1.6561	MgII	J112854.14+644427.4	2.217	BOSS	289	149
J113852.65+632934.0	1.8855	MgII	J113851.73+632955.6	2.625	BOSS	196	1912
J114435.54+095921.7	2.9734	[OIII]	J114436.65+095904.9	3.16	MIKE-Red	189	2914
J114439.51+454115.8	1.687	MgII	J114442.48+454111.3	2.592	BOSS	275	78
J114546.54+032236.7	1.7664	MgII	J114546.22+032251.9	2.011	MagE	139	779
J115253.09+150706.5	1.7883	MgII	J115254.97+150707.8	3.349	BOSS	237	622
J115457.16+471149.3	1.6819	MgII	J115458.69+471209.9	1.947	SDSS	226	60
J115502.45+213235.5	1.9551	MgII	J115504.25+213254.0	2.695	BOSS	277	397
J115529.49+463413.1	1.6491	MgII	J115528.75+463442.9	2.329	BOSS	270	326
J115533.62+393359.2	1.6118	MgII	J115531.32+393415.4	2.555	BOSS	272	742
J120224.68+074800.3	1.6613	MgII	J120226.48+074739.7	2.767	BOSS	296	584
J120417.47+022104.7	2.436	[OIII]	J120416.69+022110.0	2.532	HIRES	112	2710
J120856.94+073741.2	2.1708	MgII	J120857.16+073727.3	2.616	MagE	123	3853
J121159.88+324009.0	1.978	MgII	J121201.69+324013.3	2.273	BOSS	209	1046
J121344.28+471958.7	1.8371	MgII	J121343.01+471931.0	3.275	BOSS	260	491
J1215590+571616.6	1.93	[OIII]	J121558.82+571555.5	1.964	BOSS	184	614
J121657.82+152706.6	1.9473	MgII	J121657.00+152712.7	2.318	BOSS	116	4225
J122514.29+570942.3	1.8953	MgII	J122517.89+570943.7	2.224	BOSS	255	330
J123143.01+002846.3	3.2015	[OIII]	J123141.73+002913.9	3.308	GMOS-S	271	1490
J124632.33+234531.2	1.9937	MgII	J124632.19+234509.5	2.573	BOSS	188	1886
J124846.05+405758.2	1.8265	MgII	J124846.97+405820.9	2.463	BOSS	219	897
J130124.74+475909.6	2.194	Hα	J130125.67+475930.8	2.765	SDSS	199	4932
J130605.19+615823.7	2.1089	Hα	J130603.55+615835.2	2.175	LRIS	141	1761
J130714.79+463536.6	1.6226	MgII	J130716.07+463511.2	2.248	BOSS	251	137
J131341.32+454654.6	1.6878	MgII	J131342.78+454658.2	2.241	BOSS	139	1098
J132514.97+540930.6	2.0507	MgII	J132511.07+540927.0	3.235	BOSS	298	514
J133026.12+411432.0	2.0645	MgII	J133023.67+411445.9	2.217	BOSS	271	384

Table 3.1 (cont'd)

Foreground Quasar	$z_{\rm fg}$	Line for $z_{\rm fg}^a$	Background Quasar	$z_{\rm bg}$	BG Quasar Instrument	$R_\perp$ (kpc)	$g_{\rm UV}$
J133924.02+462808.2	1.8539	MgII	J133922.31+462749.2	3.391	BOSS	226	940
J134650.08+195235.2	2.0697	MgII	J134648.19+195253.1	2.523	BOSS	278	884
J135306.35+113804.7	1.6315	MgII	J135307.90+113805.5	2.431	BOSS	213	8963
J135849.71+273806.9	1.9008	MgII	J135849.54+273756.9	2.127	LRIS	89	1765
J140208.01+470111.1	1.9161	[OIII]	J140209.52+470117.8	2.269	BOSS	140	1437
J140918.01+522552.4	1.8808	MgII	J140916.98+522535.3	2.109	SDSS	170	583
J141337.18+271517.1	1.6905	MgII	J141337.96+271511.0	1.965	BOSS	105	609
J142003.67+022726.7	3.617	[OIII]	J142004.12+022708.8	4.191	ESI	144	2291
J142054.42+160333.3	2.0221	[OIII]	J142054.92+160342.9	2.057	MagE	104	7811
J142215.57+465230.7	1.748	MgII	J142214.63+465254.6	2.338	BOSS	225	639
J142758.89−012130.4	2.2738	[OIII]	J142758.74-012136.2	2.354	MIKE	53	34208
J143109.67+572728.0	1.6802	MgII	J143109.22+572726.4	2.063	BOSS	39	5166
J143312.56+082651.8	1.8807	MgII	J143313.99+082714.0	2.432	BOSS	274	531
J143345.55+064109.0	2.294	[OIII]	J143344.55+064111.9	2.34	BOSS	122	1130
J143609.15+313426.7	1.8774	MgII	J143610.68+313418.9	2.562	BOSS	183	2188
J144211.25+530252.0	1.6461	MgII	J144209.98+530308.0	2.632	BOSS	179	439
J144232.92+013730.4	1.8079	MgII	J144231.91+013734.8	2.274	BOSS	137	1988
J144429.34+311321.2	1.7355	MgII	J144427.96+311313.0	1.795	LRIS	173	8820
J150814.06+363529.4	1.8493	MgII	J150812.78+363530.3	2.105	BOSS	133	5111
J153328.83+142542.5	2.0782	MgII	J153329.17+142537.8	2.564	BOSS	59	3898
J153456.02+215342.3	1.6712	MgII	J153455.85+215324.7	2.529	BOSS	156	1702
J153954.74+314629.3	1.8747	MgII	J153952.46+314625.2	2.235	BOSS	256	1080
J155325.61+192140.0	2.01	[OIII]	J155325.89+192137.7	2.098	MagE	44	5576
J155422.88+124438.0	1.8169	MgII	J155424.39+124431.5	2.394	BOSS	202	1349
J155947.73+494307.3	1.8615	MgII	J155946.28+494326.7	1.945	LRIS	210	1743
J160547.61+511330.5	1.783	MgII	J160546.67+511322.9	1.844	LRIS	102	4045
J161930.94+192620.9	1.7821	MgII	J161929.78+192645.4	2.39	BOSS	258	538
J162738.63+460538.4	3.8149	[OIII]	J162737.25+460609.3	4.11	ESI	253	1959
J163121.74+433317.3	2.0182	MgII	J163123.57+433317.3	2.631	BOSS	172	4090
J165442.21+251249.2	1.7207	MgII	J165444.38+251306.2	2.341	BOSS	298	459
J165716.85+310513.0	2.1331	MgII	J165716.52+310524.5	2.395	MODS1	98	5222
J214620.69−075250.6	2.1155	[OIII]	J214620.99-075303.8	2.577	MagE	120	4869
J214813.26+263059.4	1.6285	MgII	J214814.36+263129.7	3.286	BOSS	295	78
J220248.61+123645.5	2.0697	[OIII]	J220248.31+123656.3	2.512	BOSS	100	9466
J233845.19−000327.1	2.4399	[OIII]	J233845.45-000331.8	2.997	XSHOOTER	51	3674
J235505.22+320058.0	1.8159	MgII	J235505.33+320105.4	2.367	BOSS	56	2271
J235819.92+342455.8	1.6235	MgII	J235819.33+342506.5	2.02	BOSS	113	480

Table 3.1 (cont'd)

Foreground Quasar	$z_{\rm fg}$	Line for $z_{\rm fg}^a$	Background Quasar	$z_{\rm bg}$	BG Quasar Instrument	$R_\perp$ (kpc)	$g_{\rm UV}$

[a] The emission-line analyzed for measuring $z_{\rm fg}$.

3.3 Analysis

3.3.1 Stacked Profiles

We create composite spectra that average over the intrinsic scatter in quasar environments, continuum placement errors, and redshift errors. The individual spectra of background quasars are shifted to the rest-frame of the foreground quasars at the transitions of interest. Each spectrum has been linearly interpolated onto a fixed velocity grid centered at $z_{\rm fg}$ with bins of $100\,{\rm km\,s^{-1}}$. For a velocity bin of this size, it is unnecessary to smooth the data to a common spectral resolution. The individual spectra are then combined with a mean or a median statistic. Bad pixels in the individual spectra have been masked before generating the composites. Since each quasar pair gives an independent probe of the CGM, each pair has an equal weighting in the stacked profiles, i.e. we do not weight the spectra by the measured S/N near the metal ion transitions. Scatter in the stacked spectra is dominated by randomness in the CGM rather than scatter in the flux of individual observations. The mean statistic of the individual spectra yields a good estimate of the average absorption and preserves equivalent width. The median statistic is less sensitive to outliers, however the the median opacity at any velocity channel is rather small, since the discrete absorbers are spread throughout the entire velocity window. The analysis on the median velocity field is thus subject to larger uncertainty. In the following we present stacked spectra using both the mean and the median statistic.

In Figure 3.2, we present mean and median stacks of C II 1334, C IV 1548, and Mg II 2796 absorption of the QPQ9 sample. We focus on the analysis results

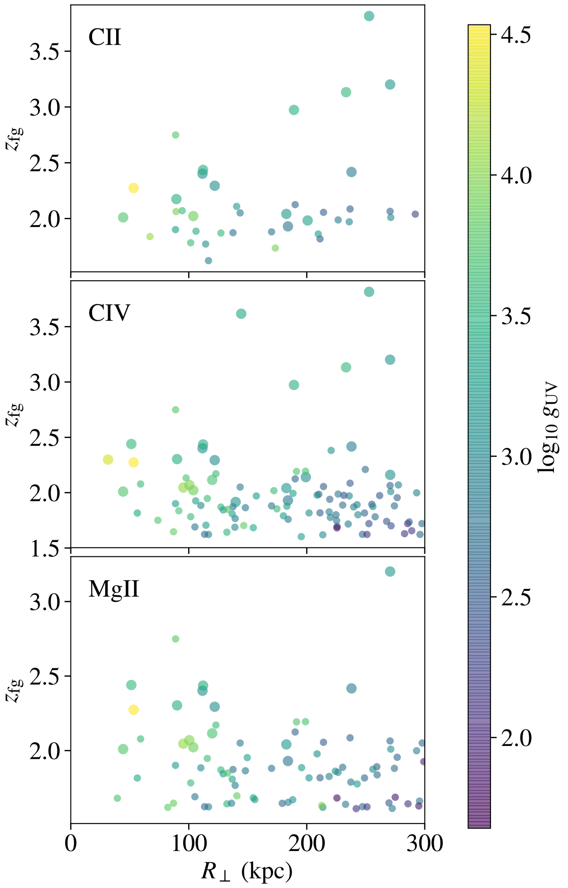

Figure 3.1 These panels summarize properties of the QPQ9 dataset. The QPQ survey selects quasar pairs of $R_\perp < 300\,$kpc and $z_{\rm fg} > 1.6$. Assuming that the foreground quasars emit isotropically and at a distance equal to the impact parameter, the enhancement in the UV flux relative to the extragalactic UV background, $g_{\rm UV}$, can be estimated. Large symbols correspond to foreground quasars with the most precise redshift measurement from [O III] 5007, while small symbols correspond to $z_{\rm fg}$ measurements from Mg II 2800, Hα, or Hβ emission. The top panel shows quasar pairs with coverage of C II 1334 at $z_{\rm fg}$ in the background quasar spectra. The middle panel shows pairs with coverage of C IV 1548. The bottom panel shows pairs with coverage of Mg II 2796.

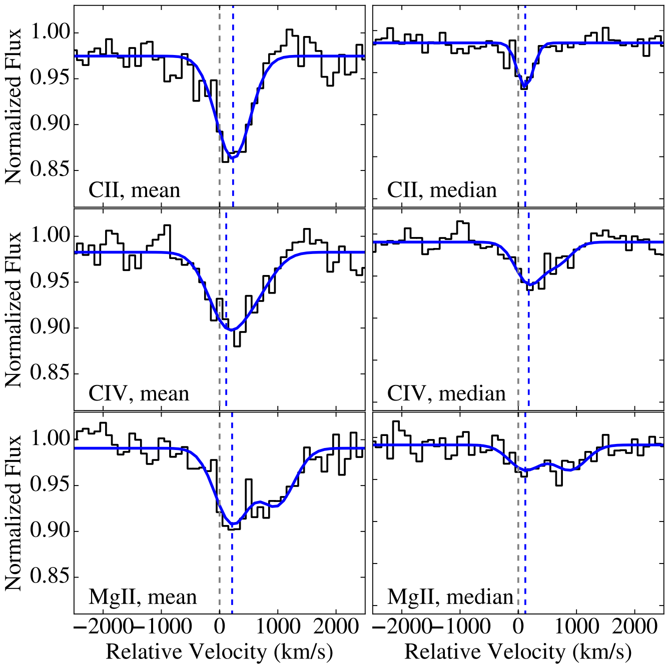

Figure 3.2 Mean and median absorption centered at C II 1334, C IV 1548, and Mg II 2796 of the foreground quasars for all QPQ9 pairs. The composites are shown in thin, black. Overplotted on the composites are Gaussian fits, normalized to pseudo-continua far away from a velocity of $0\,\mathrm{km\,s^{-1}}$ relative to z_{fg}, and are shown in thick, blue. For the doublets, a second Gaussian with a fixed mean separation and a tied standard deviation is included in the modeling. The absorptions frequently exhibit large velocity widths. The dashed lines mark the centroids, which show small positive velocity offsets from z_{fg}. The 1σ modeling error for the centroid and dispersion of the C II mean stack are $25\,\mathrm{km\,s^{-1}}$ and $27\,\mathrm{km\,s^{-1}}$ respectively, which is also the typical modeling errors of the other stacks.

of the C II mean stack. C IV and Mg II are doublet transitions and it is more challenging to analyze their kinematics. Two results are evident in Figure 3.2: (i) the mean C II stack exhibits excess absorption spanning a large velocity width; (ii) the mean absorption is likely skewed toward positive velocities. We have 40 pairs in the QPQ9 sample for C II analysis and an even larger number of pairs for C IV and Mg II analyses, and the total number of individual components can only be larger than the number of absorption systems. Hence, although QPQ8 showed the distribution of absorbing components in velocity is non-Gaussian for each individual quasar-host associated system, the central limit theorem applies and the distribution of all absorbing components should tend toward Gaussian distribution. A visual inspection of the stsack confirms that a broader absorption component is not apparent. Therefore, to model the absorption, we introduce a Gaussian profile while allowing a constant pseudo-continuum level to vary. We perform χ^2 minimization with each channel given equal weight. From the best-fit to the data, we measure the centroid of the C II stack to be $+232\,\mathrm{km\,s^{-1}}$ and the 1σ dispersion to be $293\,\mathrm{km\,s^{-1}}$. The centroid suggests an asymmetry that contradicts the standard expectation, while the dispersion suggests extreme kinematics. The median stack, on the other hand, shows weaker absorption, and the Gaussian model has a centroid with smaller offset and a more uncertain dispersion.

We also create mean and median stack for the sub-sample with [O III] redshifts and model the absorption with Gaussian best-fit. The C II mean stack for this sub-sample has a centroid at $+235\,\mathrm{km\,s^{-1}}$, and a dispersion of $330\,\mathrm{km\,s^{-1}}$, consistent with the full sample.

To model the mean and median absorption of C IV 1548 and Mg II 1796, we introduce a second Gaussian with separation equal to the doublet separation ($498\,\mathrm{km\,s^{-1}}$ and $769\,\mathrm{km\,s^{-1}}$ respectively), and tie the dispersion of the two lines in a doublet. We allow the doublet ratio to vary from 2:1 to 1:1. The modeling results show that the velocity fields of C IV and Mg II are consistent with C II, i.e. large dispersion and centroid is skewed toward positive velocities.

Table 3.2. Summary of the Data and Analysis

Measure	C II 1334	C IV 1548	Mg II 2796
For the Full QPQ9 Sample			
Number of pairs	40	110	86
Median $z_{\rm fg}$	2.04	1.89	1.87
Median $R_\perp$	157	191	184
Centroid of mean stack ($\rm km\,s^{-1}$)	$+232 \pm 98$	$+114 \pm 63$	$+215 \pm 124$
1σ dispersion of mean stack ($\rm km\,s^{-1}$)	293 ± 87	318 ± 44	295 ± 200
Centroid of median stack ($\rm km\,s^{-1}$)	$+119 \pm 240$	$+180 \pm 81$	$+121 \pm 201$
1σ dispersion of median stack ($\rm km\,s^{-1}$)	137 ± 569	231 ± 71	276 ± 215
For the Sub-sample with [OIII] Redshifts			
Number of pairs	15	23	15
Median $z_{\rm fg}$	2.29	2.29	2.27
Median $R_\perp$	183	122	112
Centroid of mean stack ($\rm km\,s^{-1}$)	$+235 \pm 118$	$+244 \pm 77$	$+210 \pm 119$
1σ dispersion of mean stack ($\rm km\,s^{-1}$)	330 ± 103	280 ± 41	235 ± 129
Centroid of median stack ($\rm km\,s^{-1}$)	$+256 \pm 191$	$+355 \pm 111$	$+244 \pm 125$
1σ dispersion of median stack ($\rm km\,s^{-1}$)	103 ± 236	252 ± 71	175 ± 114

The above analyses are summarized in Table 3.2. The Gaussian models normalized to pseudo-continuum are overplotted on the data stacks in Figure 3.2.

3.3.2 Interpretation of the asymmetric absorption

To assess the statistical significance of the measured velocity offsets. To assess the statistical significance, we perform a boostrap analysis by randomly resampling from the full sample 10000 times. We introduce a Gaussian absorption profile to model each bootstrap realization, and quote the standard deviation in the bootstrap realizations to be the scatter in the centroids of the data. The scatters $\approx 100\,\rm km\,s^{-1}$ are comparable to the measured offsets, indicating large intrinsic variation in quasar CGM environments (see also QPQ8). In Figure 3.3, we show the distribution of the absorption centroids from bootstrapping on the C II mean stack. We find that 97% of the centroids are at positive velocities. We place a generous 3σ upper limit to the small offset of the centroid from $z_{\rm fg}$ for the C II mean absorption at $\delta v < +526\,{\rm km\,s^{-1}}$. Given the large intrinsic scatter, we do not attempt to explore whether there exists relative asymmetry among the C II, C IV, and Mg II absorption.

One may also ask whether the measured positive offsets come from systematic bias in redshift measurements due to the Baldwin effect (Baldwin 1977). Shen et al. (2016b) reported that, the [O III] emission of $z \sim 2$ quasars is more asymmetric and weaker than that in typically less luminous low-z quasars. To test for this potential source of bias, we create another mean stack at C II 1334 by replacing the [O III] redshifts by a redshift measured from the more symmetric Mg II or Hα emission when available. We are able to replace for 11 out of the 15 systems with [O III] redshifts in the original sample. The new stack is similiar in velocity structure and again shows a positive offset $\approx +303\,{\rm km\,s^{-1}}$. We thus conclude that our algorithm for measuring redshifts is not severely biased by the blue wing of the [O III] emission-line.

Motivated by the study of Mg II absorbers surrounding $z \sim 1$ quasars by Johnson et al. (2015), we also generate a mean-stacked spectrum for Mg II 2796 for lower redshift quasar pairs. We select quasars with $0.4 < z_{\rm fg} < 1.6$ and use the same other selection criteria as the main QPQ9 sample. The quasar pairs are selected from the igmspec database, with $z_{\rm fg}$ measured by Hewett & Wild (2010). For quasars with $z_{\rm fg} < 0.84$, as redshift determination is dominated by [O III] emission, a shift of $+48\,{\rm km\,s^{-1}}$ is applied to bring the emission-line redshift to the systemic. For quasars with $0.84 < z_{\rm fg} < 1.6$, as redshift determination is dominated by Mg II emission, a shift of $+57\,{\rm km\,s^{-1}}$ is applied. There are 233 pairs selected, with a median $z_{\rm fg}$ of 0.90 and a median $R_\perp$ of 208 kpc. We present the mean stack in Figure 3.4. The absorption is weaker than the $z \sim 2$ main QPQ9 sample. Gaussian absorption models fitted to the stack recover a centroid of

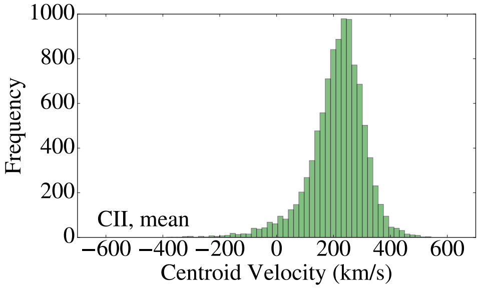

Figure 3.3 Histogram of the absorption centroids of 10000 bootstrap realizations of the data sample for the C II mean stack. 97% of the centroids are positively offset from $z_{\rm fg}$.

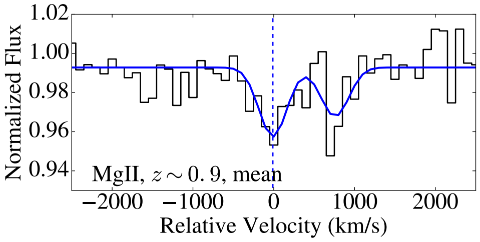

Figure 3.4 Mean stack at Mg II 2796, for a lower redshift sample of quasar pairs at $z \sim 0.9$. Line-style coding is the same as in Figure 3.2. The centroid is approximately at 0 $\rm km\,s^{-1}$, and the absorption is weaker than the main QPQ9 sample.

$-11 \pm 379\,\rm km\,s^{-1}$ and a dispersion of $172\,\rm km\,s^{-1}$. The average offset from $0\,\rm km\,s^{-1}$ is much smaller than the offsets in the $z \sim 2$ sample.

Since the large scatter in the centroids represents intrinsic variation rather than redshift errors, and the Mg II stack for lower redshift suggests a different centroid, we consider that the asymmetry signal in the $z \sim 2$ sample is likely to be real. In the Discussion section, we discuss two possible explanations for the asymmetry.

3.3.3 Interpretation of the large velocity fields

Under the assumption that the intrinsic dispersion and the redshift uncertainty add in quadrature to give the observed width, we solve for the intrinsic dispersion

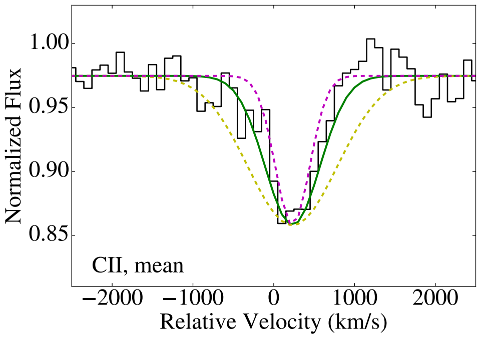

Figure 3.5 The same C II mean stack shown in the first panel of Figure 3.2 is shown in thin, black. In thick, green, we overplot the Gaussian absorption model of the Monte Carlo simulations generated from a purely clustering argument. The model from clustering analysis is multiplied to the pseudo-continuum level of the stack of the observational data, shifted to the centroid of the stack of the data, and broadened by the mean redshift error in the data. The model is a good description of the data, with a dispersion within modeling error of the dispersion in the data. We overplot in dashed, yellow an absorption profile with $\sigma_v = 554\,\mathrm{km\,s^{-1}}$, which is larger than the observed width by three times the standard deviation in the bootstrap analysis. Motions that produce a velocity width larger than this can be ruled out. We overplot in dashed, magenta an absorption profile with $\sigma_v = 214\,\mathrm{km\,s^{-1}}$, which is smaller than the observed width by three times the modeling error. Unless gravitational and Hubble flows together with redshift error broadening produce a velocity width smaller than this, extra dynamical processes (e.g. outflows) will not be required to explain the observation.

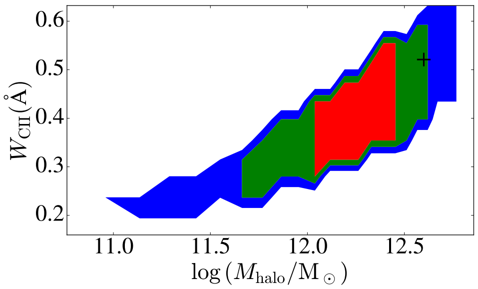

Figure 3.6 Probability distributions of the parameters W_{CII} and M_{halo}. The plot shows the degeneracy between W_{CII} and M_{halo} in recovering the intrinsic width of the absorption profile. We mark contours for points that produce an absorption profile of width that is 1, 2, and 3 times the modeling error away from the observed intrinsic width. The intrinsic velocity width corresponding to typical QPQ halo mass is marked with a plus sign, and is well contained within the 2σ contour.

in the C II mean stack. For the full QPQ9 sample, with the mean $\sigma_{\mathrm{error}(z)}^{\mathrm{full}} = 189\,\mathrm{km\,s^{-1}}$, we recover $\sigma_{\mathrm{intrinsic}}^{\mathrm{full}} = 224\,\mathrm{km\,s^{-1}}$. For the sub-sample with [O III] redshifts, we recover $\sigma_{\mathrm{intrinsic}}^{\mathrm{[OIII]}} = 323\,\mathrm{km\,s^{-1}}$.

Eftekharzadeh et al. (2015) measured the clustering of quasars in the range $2.2 < z < 2.8$ while Rodríguez-Torres et al. (2017) measured the clustering of quasars in the range $1.8 < z < 2.2$. They estimated that these quasars are hosted by dark matter halos with mass $M_{\mathrm{halo}} = 10^{12.5}\,M_\odot$ and $M_{\mathrm{halo}} = 10^{12.6}\,M_\odot$ respectively. If dark matter halos hosting QPQ9 quasars have a characteristic mass $10^{12.6}\,M_\odot$ and follow an NFW profile (Navarro et al. 1997) with concentration parameter $c = 4$, at $z \approx 2$ the maximum circular velocity is $345\,\mathrm{km\,s^{-1}}$. Tormen et al. (1997) found that the maximum circular velocity is ≈ 1.4 times the maximum of the average one-dimensional root-mean-square velocity σ_{rms}. Hence, the average line-of-sight rms velocity typical of QPQ9 halos is $\sigma_{\mathrm{rms}} = 246\,\mathrm{km\,s^{-1}}$. In QPQ8, we estimated the probability of intercepting a random optically thick absorber is 4%, and clustering would only increase that to 24%. Although motions due to Hubble flows do not dominate, they nevertheless contribute to the observed dispersion. We can investigate whether gravitational motions and Hubble flows are sufficient to reproduce the dispersion in the data, using Monte Carlo methods to simulate the absorption signals.

Since C II systems arise in optically thick absorbers, we may adopt the clustering analysis results of QPQ6. In the absence of clustering, the expected number of absorbers per unit redshift interval for Lyman limit systems, super Lyman limit systems, and damped Lyα systems are respectively $\ell_{\mathrm{IGM}}^{\mathrm{LLS}}(z) \approx 1.05((1+z)/(1+2.5))^{2.1}$, $\ell_{\mathrm{IGM}}^{\mathrm{SLLS}}(z) \approx 0.44((1+z)/(1+2.5))^{2.1}$, and $\ell_{\mathrm{IGM}}^{\mathrm{DLA}}(z) \approx 0.2((1+z)/(1+2.5))^{2.1}$. The quasar-absorber correlation functions for Lyman limit systems, super Lyman limit systems, and damped Lyα systems are respectively $\xi_{\mathrm{QA}}^{\mathrm{LLS}}(r) = (r/(12.5\,h^{-1}\,\mathrm{Mpc}))^{-1.68}$, $\xi_{\mathrm{QA}}^{\mathrm{SLLS}}(r) = (r/(14.0\,h^{-1}\,\mathrm{Mpc}))^{-1.68}$, and $\xi_{\mathrm{QA}}^{\mathrm{DLA}}(r) = (r/(3.9\,h^{-1}\,\mathrm{Mpc}))^{-1.6}$. For each quasar pair, we calculate the expected number of optically thick absorbers within $\pm 3000\,\mathrm{km\,s^{-1}}$ at a distance $R_\perp$ from the foreground quasar and at $z_{\rm fg}$. Then we generate 1000 mock sightlines. The number of absorbers for each mock spectrum is randomly selected from a Poisson distribution with mean equal to the expected number calculated as above. The absorbers are randomly assigned Hubble velocities, with a probability distribution according to the quasar-absorber correlation functions. The absorbers are randomly assigned additional peculiar velocities drawn from a normal distribution with mean equal to $0\,{\rm km\,s^{-1}}$ and scatter equal to $\sigma_{\rm rms}$. For each absorber, we assume a rest equivalent width for C II $W_{\rm CII}$ and a Gaussian absorption profile. We repeat the above procedure for all 40 quasar pairs, and create a mean stack of the 40000 mock spectra generated. We fit a Gaussian absorption profile multiplied to a constant continuum level to model the stack of mock spectra. We adjust the $W_{\rm CII}$ adopted for the absorbers until the amplitude of the best-fit Gaussian of the stack of mock spectra matches the amplitude of the stack of the observational data. We find that $W_{\rm CII} = 0.5\,$Å well reproduces the amplitude, and the dispersion of the Gaussian absorption model is insensitive to the assumed $W_{\rm CII}$ or line profile for one absorber.

In Figure 3.5, we show a comparison of the observational data stack and the Gaussian absorption model of the Monte Carlo simulations. In the figure, the Gaussian absorption model is broadened by the mean redshift error by adding it in quadrature to the dispersion in the model. The resulting stack of mock spectra has a 1σ dispersion of $282\,{\rm km\,s^{-1}}$. This is about 2 times the modeling error away from the intrinsic dispersion in the C II mean stack for the full sample, and about 2 times the modeling error away from the intrinsic dispersion in the stack of the sub-sample with [O III] redshifts as well. We also test for the sensitivity of this measured dispersion to the correlation functions adopted. The QPQ6 clustering analysis is performed on only the strongest absorber near $z_{\rm fg}$, and a low $R_\perp$ sightline may in fact intercept more than one optically thick absorber. We double the number of absorbers for each mock sightline, and find the measured dispersion only increases by several ${\rm km\,s^{-1}}$. Thus, the hypothesis that the observed velocity width is only produced by a combination of gravitational motions and Hubble flows cannot be ruled out. Extra dynamical processes are not necessary to explain the large velocity fields.

From the bootstrap analysis of the observed dispersion, a width of $\sigma_v > 554\,\mathrm{km\,s^{-1}}$ would be larger than the observed by three times the scatter (overplotted in Figure 3.5). In other words, taking into account the redshift errors, motions in addition to gravitational and Hubble flows that will produce an intrinsic dispersion $\sigma_v > 529\,\mathrm{km\,s^{-1}}$ can be ruled out.

On the contrary, $\sigma_{\mathrm{rms}} < 70\,\mathrm{km\,s^{-1}}$ together with Hubble velocities and broadening by redshift errors will result in a velocity width that is more than three times the modeling error away from the observed width (overplotted in Figure 3.5). This implies that, unless the characteristic $M_{\mathrm{halo}} < 10^{11.0}\,M_{\odot}$, additional dynamical processes are not required to explain the observed width.

In Figure 3.6, We show the probability distributions of the degenerate parameters W_{CII} and M_{halo} in recovering the intrinsic width of the absorption profile. We require that the amplitude of the absorption is reproduced within 3 times its modeling error, and mark contours for points in (W_{CII}, M_{halo})-space that produce an absorption profile of width within 1, 2, and 3 times the modeling error of the observed intrinsic width. From the figure, a higher W_{CII} means the M_{halo} that will reproduce the observed width is higher. If there are no extra dynamical processes, the intrinsic velocity width corresponding to typical QPQ halo mass is well contained within the 1σ contour.

3.4 Discussion

At low redshift, both symmetric and asymmetric ionization cones around quasars and AGNs are observed. In the extended emission-line region of 4C37.43, most of the [O III] emission is blueshifted (Fu & Stockton 2007), but there are counter examples in less extended sources in Fu & Stockton (2009). Recently, there

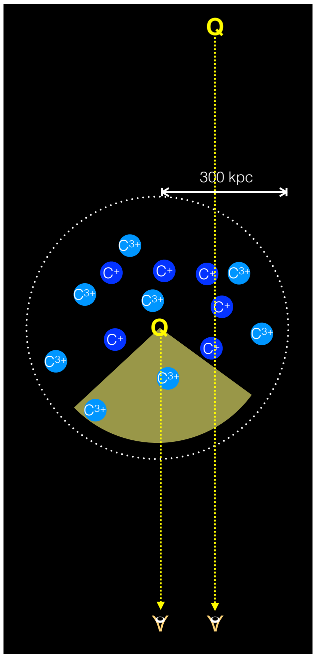

Figure 3.7 A cartoon showing a unipolar quasar. The gas observed in low- to intermediate-ion absorption preferentially lies behind the quasar, and is shadowed from the ionizing radiation.

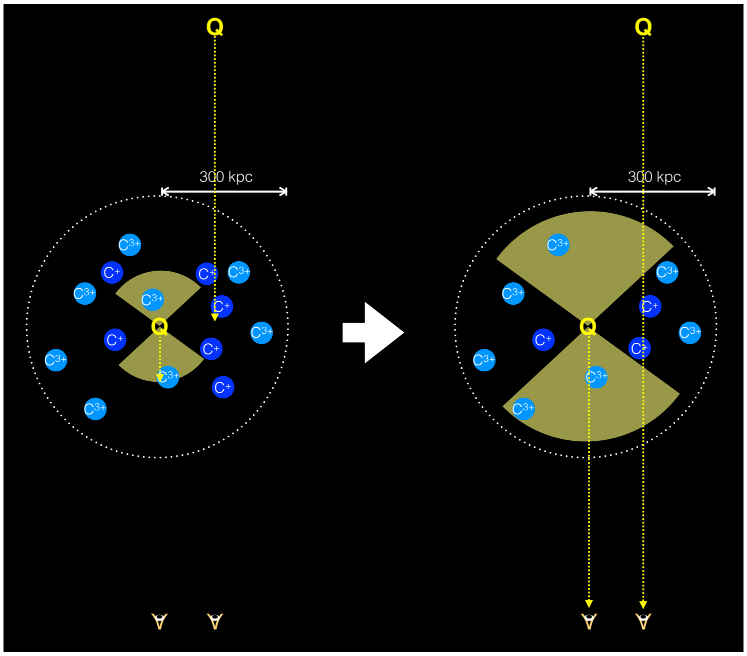

Figure 3.8 A cartoon showing the finite lifetime of quasar episodes as an explanation to the asymmetric absorption. The setup on the left shows that the foreground quasar has not been shining long enough for its ionizing radiation to reach the gas behind it, when the light from the background quasar reaches. The setup on the right shows the scenario after an amount of time comparable to the light travelling time across CGM scale. Gas in front of the foreground quasar has been ionized, by the time the light from the background quasar reaches.

has been Fabry-Perot interferometric data for less extended narrow-line regions in more nearby sources (Keel et al. 2015, 2017), which show mostly symmetric velocity fields and gas distributions. In the following, we explore two possible explanations for the putative non-dynamical process that provides the asymmetry.

One possibility is an asymmetric radiation field that preferentially ionizes the gas moving toward the observer, where the quasar is known to shine. Alternatively, the asymmetric radiation field may preferentially ionizes the gas at smaller Hubble velocity than the quasar. In Figure 3.7, we show a cartoon of a quasar that is blocked in the direction pointing away from the observer. The gas observed in absorption preferentially lies behind the quasar. The asymmetric absorption arises from a transverse proxmity effect. Roos et al. (2015) and Gabor & Bournaud (2014) performed simulations of a high-redshift disk galaxy including thermal AGN feedback and calculated radiative transfer in post-processing. They found the ionization radiation is typically asymmetric, due to either a dense clump that lies on one edge of the black hole or the black hole's location being slightly above the disk. Faucher-Giguère et al. (2016) represent the only simulations so far that is able to reproduce the substantial amount of cool gas in quasar-mass haloes. We eagerly await their group to compare the fraction of gas in inflows and outflows.

As a test of reasonableness, we calculate that, for a quasar opening angle of 120° and keeping $\sigma_{\rm rms}$ at the expected value for the typical QPQ9 halo, our Monte Carlo simulations may reproduce the observed centroid and intrinsic dispersion of the C II mean absorption to within two times the modeling error.

Another possible explanation arises from the finite lifetime of quasar episodes. Figure 3.8 presents a cartoon for a light travel time argument. Light from the background quasar will travel smaller distance to reach the gas behind the foreground quasar than the gas in front of it. The light from the background quasar may arrive at the gas behind the foreground quasar before the ionizing radiation from the foreground quasar arrives. In QPQ7 and QPQ8, we reported that the enhancement in metal ion absorption relative to IGM average extends to at least $\approx 200\,\mathrm{kpc}$. This distance corresponds to a light travelling time of $\sim 10^6\,\mathrm{yr}$, which lies within existing constraints of quasar lifetime from observations (e.g. Martini 2004) and simulations (e.g. Hopkins et al. 2005).

The first explanation above to asymmetric absorption requires that the quasars emit their ionizing radiation anisotropically, while the second explanation requires the quasars emit their ionizing radiation intermittently. Both explanations will require the line-of-sight motions of the gas to be in either outflow or Hubble flow. Were the gas flowing into the galaxy instead, the velocity centroid would be negative. Under both scenarios, lower ions should be redshifted while high ions should be blueshifted. Using Cloudy photoionization models, we find that, for the typical quasar luminosity of our sample, a CGM gas that is directly illuminated is highly ionized and shows only marginally detectable C IV absorption. The redshifted C IV may be regarded as an intermediate, an a blueshifted absorption signal needs to be searched in a higher ion.

Motivated by the asymmetry found in metal ion absorption in the CGM using precise $z_{\rm fg}$ measurements, and the asymmetry found by Kirkman & Tytler (2008) in H I on larger scales, we are assembling a sample of quasar pairs with precise $z_{\rm fg}$ measurements to study this asymmetry in H I (J. F. Hennawi et al. 2017, in preparation). In conclusion, we observe large and positively skewed velocity fields in absorption, of metal ions in the CGM of $z \sim 2$ massive galaxies hosting quasars. We argue that the velocity fields can be explained if the detected gas is in gravitational motion, Hubble flow, or outflow, and the quasars either shine preferentially toward the observer or shine intermittently.

3.5 Appendix: Line of Sight absorption

In the previous QPQ papers, we argued that optically thick absorbers in the vicinity of quasars are distributed anisotropically. We now have the means to show this anisotropic clustering explicitly. Given that the techniques for stacking spectra are established, it is straightforward to apply the same techniques to stack the foreground quasar spectra. In Figure 3.9, we present mean stacks of foreground quasar spectra for the QPQ9 sample. We require that the spectra survive a S/N cut of 5.5 per rest-frame Å at C II 1334, C IV 1548, or Mg II 2796 at $z_{\rm fg}$. In constrast to the large equivalent widths exhibited in the stacks of background spectra, C II and Mg II mean absorption along the line-of-sight to the foreground quasars is weaker, and an excess at $z_{\rm fg}$ is absent. This supports a scenario where the ionizing radiation of the foreground quasars are anisotropic and/or intermittent. For

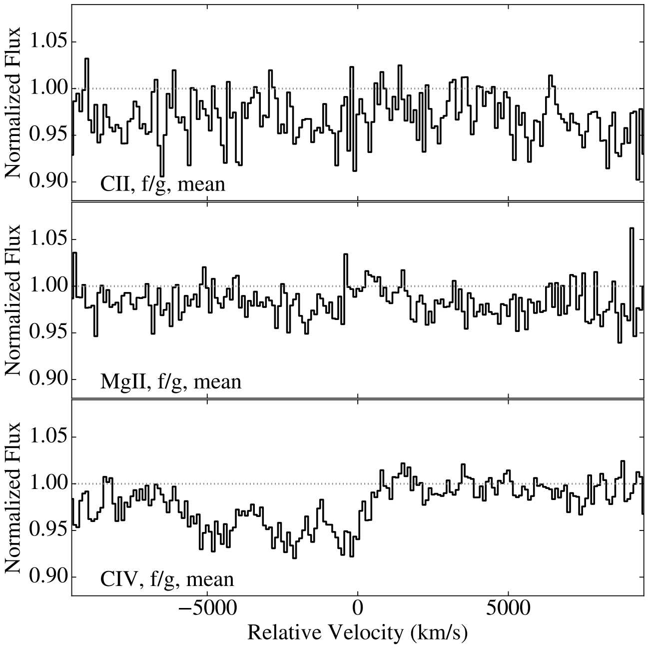

Figure 3.9 Mean stacks of the foreground quasar spectra at C II 1334, C IV 1548, and Mg II 2796 for the QPQ9 sample. For C II and Mg II, the mean absorption is weaker than that in the background stacks, and there is no evidence for an excess at $z_{\rm fg}$. The stack for C IV, which includes line-of-sight absorbers at all distances, shows a large, blueshifted mean velocity field.

C IV 1548, this stack of all line-of-sight absorbers, which include absorbers intrinsic to and far away from the quasar, shows a large, blueshifted velocity field. This excess C IV absorption has been well studied as narrow associated absorption line systems (e.g., Wild et al. 2008).

3.6 Acknowledgements

JXP and MWL acknowledge support from the National Science Foundation (NSF) grants AST-1010004 and AST-1412981. The authors gratefully acknowledge the support which enabled these observations at the Keck, Gemini, Large Binocular Telescope, Very Large Telescope, Las Campanas, and Palomar Observatories. The authors acknowledge the sharing of private data by Yue Shen. MWL thanks Hai Fu for a discussion on extended emission-line regions, T.-K. Chan for a discussion on CGM simulations, and Chi Po Choi for a discussion on statistics.

Chapter 4

Summary and Future Directions

In this thesis, several aspects of studying galaxies and their supermassive black holes have been explored, and they have all employed optical and near-infrared spectroscopy techniques. Latest work from Quasars Probing Qusars results in observational constraints on massive galaxy formation, as well as feedback from supermassive black holes on their host galaxies. As a complementary study to probe inactive supermassive black holes, which are hosted by $\approx 99.5\%$ of all galaxies observed, preliminary results and progress of a tidal disruption followed-up study are presented. As a complementary study of probing galaxy formation via stellar archeology, results and progress of a study of chemical abundance anomalies of red giants in globular clusters are presented.

In Chapter 2, from Lau et al. (2016), the results from analyzing 14 closely projected quasar pairs are presented. The low and high ions roughly trace each other in velocity structure. The H I and low ion surface densities decline with $R_{\perp}$. H I absorption is strong even beyond the virial radius. In one case, peculiar unresolved Lyα emission is detected and in another case, N V absorption is detected in one case. These peculiarities imply a small fraction of transverse sightlines are illuminated. The ionization parameter U positively correlates with $R_{\perp}$, which runs contrary to expectation should the foreground quasar dominate the ionizing radiation field. The circumgalactic medium is significantly enriched even beyond the virial radius. Within $R_\perp \approx 200\,\mathrm{kpc}$, [M/H] $= -0.6$. O/Fe is supersolar, suggestive of star formation history similar to massive ellipticals with a short starburst duration. No evolution in the total H column is found up to $R_\perp \approx 200\,\mathrm{kpc}$, within which, the median is $N_\mathrm{H} \approx 10^{20.5}\,\mathrm{cm}^{-2}$. Within the virial radius, the mass of the cool CGM is estimated to be $M_\mathrm{cool}^\mathrm{CGM} \approx 1.5 \times 10^{11}\,\mathrm{M}_\odot\,(R_\perp/(160\,\mathrm{kpc}))^2$. This substantial cool gas reservoir implies quasars are unlikely to quench star formation at $z \sim 2$. In two cases, detections of C II* allow the electron density to be estimated, and they have $n_e > 10\,\mathrm{cm}^{-3}$. Such values are characteristic of the diffuse interstellar medium.

In Chapter 3, from Lau et al. (submitted to ApJ), the kinematic results from analyzing 148 closely projected quasar pairs are presented. The mean absorption in C II, C IV, and Mg II exhibits velocity widths $\sigma_v \approx 300\,\mathrm{km\,s}^{-1}$. The large widths are consistent with gravitational motion and Hubble flow. The mean absorptions have centroids redshifted from the systemic redshift at $\delta v \approx +200\,\mathrm{km\,s}^{-1}$. The asymmetry may be explained if the ionization radiation from the quasars is anisotropic or intermittent and the gas is not flowing onto the galaxy.

Presented below are several directions for future studies.

One subsystem of the J1420+1603 is a compact clump with highly elevated electron density $n_e \approx 160\,\mathrm{cm}^{-3}$ and linear size $\ell \approx 0.2\,\mathrm{pc}$. It warrants more attention. A two-dimension spectrum of the pair is presented in Hennawi & Prochaska (2013), where some putative, fuzzy residual Lyα emission centered near the background quasar's location is detected. The H I column density modeled from Lyα absorption is $10^{17.5\pm1.0}\,\mathrm{cm}^{-2}$. Without detailed modeling, absence of Lyman-Werner bands in the background spectrum allows a generous upper limit to be placed at $N_\mathrm{H2} < 1 \times 10^{18}\,\mathrm{cm}^{-2}$. The pair also has data taken with the Atacama large Millimeter/submillimeter Array (Farina et al. 2017, in preparation), with CO emission securely detected at the location of the foreground quasar. At the location of the background quasar and at the foreground quasar's redshift, CO luminosity is not detected up to the 3σ sensitivity limit that corresponds to $L'_{\rm CO} > 10^{9.9}\,{\rm K\,km\,s^{-1}\,pc^2}$. Deeper millimeter data is desired to derive the molecular gas content of the absorption system. Deeper far-infrared data is desired to derive the star formation rate. A deep integral field spectrum is desired to map the putative Lyα-emitting gas at the location of the background quasar. This will help determining the nature of the gas and its connection with the foreground quasar.

Motivated by the asymmetry found in the metal ion absorption in the circumgalactic medium, the ongoing work of Quasars Probing Quasars is to study the same asymmetry in H I. Currently the effort is led by J. F. Hennawi.

Integral field imaging of the quasar circumgalactic medium is desired, to model the transverse proximity effect out to large scales. Borisova et al. (2016) used VLT/MUSE to determine the average opening angle or variability timescale of quasar radiation for a bright quasar at $z \approx 3.1$. A similar study at $z \sim 2$ with Keck/KCWI will help interpret the circumgalactic medium studied in Quasars Probing Quasars, in particular how often the circumgalactic gas is illuminated.

Contributors to Quasars Probing Quasars eagerly await cosmological simulations of galaxy formation that include feedback from active galactic nuclei and winds powered by star formation. Theorists are encouraged to study whether their prescriptions reproduce phyiscal properties of the observed circumgalactic medium. Faucher-Giguère et al. (2016) represent the only set of simulations that reproduce the covering fraction of Lyman limit systems in massive halos, but they do not reproduce the extreme kinemaics. Their simulations include stellar feedback, but no active galactic nuclei feedback.

Submillimeter galaxy-quasar pairs should be compared to Quasars Probing Quasars. Submillimeter galaxies show clustering strength comparable to quasars. Studying them helps isolate impact of quasar feedback. Fu et al. (2016) and Fu et al. (2017) represent the first such study. A major shortcoming is that the Herschel beam is large. For $< 5''$ separation between the pair, nearly 100%

of quasars that are selected will not be background sources but are hosted by the submillimeter galaxies. It thus becomes difficult to probe the circumgalactic medium at projected separation $< 40\,\mathrm{kpc}$. Future far-infrared and sub-millimeter surveys with better spacial resolution are desired.

Sources in Quasars Probing Quasars have not been separated for their radio properties. A quick search in the Faint Images of the Radio Sky at Twenty cm Survey catalog reveals that, 4% of the sources in Quasars Probing Quasars and the *igmspec* database are radio-loud. This value is somewhat low compared to the conventional wisdom of 10%. All the results on the circumgalactic gas properties should be compared to the radio properties, and will likely be the next step of Quasars Probing Quasars.

The line-of-sight circumgalactic medium, manifested as narrow associated absorption line systems, should be more extensively studied than is in the literature. A comparison of the line-of-sight and transverse circumgalactic medium helps identify quasar feedback. Their properties should be compared against each other other than their expected different ionization states.

The public *igmspec* database has been released. The tools for stacking spectra and modeling absorption lines in echelle and echellette spectra are built. Given these data and tools, many quasar absorption-line studies for other science goals are possible. One possibility is the diffuse interstellar bands in the Milky Way. They have been mapped in the near-infrared using star spectra in the SDSS-III/APOGEE (Zasowski et al. 2015). They have been mapped in the optical using star, galaxy, and quasar spectra in the SDSS (Baron et al. 2015b,a; Lan et al. 2015). The Na I D absorption doublet has been studied in Poznanski et al. (2012) using quasar and galaxy spectra taken by Keck/HIRES, Keck/ESI, and SDSS. The advantage of using star spectra is that the sightlines are at low Galactic latitude. Quasar and galaxy samples do not have as many such sightlines. The signal-to-noise is probably higher for a sightline that goes through the Galactic disk. However, there is no easy crude estimate as to whether SDSS or 10m class telescopes have collected more photons of background sources in total. For narrow interstellar features, a study in higher resolution than SDSS galaxy and quasar spectra is desired. Another possible project is to look for time variation of any lines in quasar absorption spectra. Boissé et al. (2015) studied VLT/UVES and Keck/HIRES spectra of five quasars for narrow lines. They found clear changes in Galactic interstellar Na I lines toward one sightline, while intervening absorption lines appear in general to be stable. With the large number of sightlines in *igmspec*, a tighter constraint on no variation may be obtained.

Bibliography

Adelberger, K. L., Shapley, A. E., Steidel, C. C., Pettini, M., Erb, D. K., & Reddy, N. A. 2005a, ApJ, 629, 636

Adelberger, K. L., Steidel, C. C., Pettini, M., Shapley, A. E., Reddy, N. A., & Erb, D. K. 2005b, ApJ, 619, 697

Alam, S., Albareti, F. D., Allende Prieto, C., Anders, F., Anderson, S. F., Anderton, T., Andrews, B. H., Armengaud, E., Aubourg, É., Bailey, S., & et al. 2015, ApJS, 219, 12

Andreon, S. 2012, A&A, 546, A6

Antonucci, R. 1993, ARA&A, 31, 473

Arrigoni Battaia, F., Hennawi, J. F., Cantalupo, S., & Prochaska, J. X. 2016, ApJ, 829, 3

Arrigoni Battaia, F., Hennawi, J. F., Prochaska, J. X., & Cantalupo, S. 2015a, ApJ, 809, 163

Arrigoni Battaia, F., Yang, Y., Hennawi, J. F., Prochaska, J. X., Matsuda, Y., Yamada, T., & Hayashino, T. 2015b, ApJ, 804, 26

Asplund, M., Grevesse, N., Sauval, A. J., & Scott, P. 2009, ARA&A, 47, 481

Baldi, A., Ettori, S., Molendi, S., Balestra, I., Gastaldello, F., & Tozzi, P. 2012, A&A, 537, A142

Baldwin, J. A. 1977, ApJ, 214, 679

Baron, D., Poznanski, D., Watson, D., Yao, Y., Cox, N. L. J., & Prochaska, J. X. 2015a, MNRAS, 451, 332

Baron, D., Poznanski, D., Watson, D., Yao, Y., & Prochaska, J. X. 2015b, MNRAS, 447, 545

Behroozi, P. S., Wechsler, R. H., & Conroy, C. 2013, ApJ, 770, 57

Bergeron, J., & Boisse, P. 1991, Advances in Space Research, 11, 241

Boissé, P., Bergeron, J., Prochaska, J. X., Péroux, C., & York, D. G. 2015, A&A, 581, A109

Boksenberg, A., & Sargent, W. L. W. 2015, ApJS, 218, 7

Borisova, E., Lilly, S. J., Cantalupo, S., Prochaska, J. X., Rakic, O., & Worseck, G. 2016, ApJ, 830, 120

Boroson, T. 2005, AJ, 130, 381

Bovy, J., Hennawi, J. F., Hogg, D. W., Myers, A. D., Kirkpatrick, J. A., Schlegel, D. J., Ross, N. P., Sheldon, E. S., McGreer, I. D., Schneider, D. P., & Weaver, B. A. 2011, ApJ, 729, 141

Bovy, J., Myers, A. D., Hennawi, J. F., Hogg, D. W., McMahon, R. G., Schiminovich, D., Sheldon, E. S., Brinkmann, J., Schneider, D. P., & Weaver, B. A. 2012, ApJ, 749, 41

Bowen, D. V., Hennawi, J. F., Ménard, B., Chelouche, D., Inada, N., Oguri, M., Richards, G. T., Strauss, M. A., Vanden Berk, D. E., & York, D. G. 2006, ApJ, 645, L105

Cai, Z., Fan, X., Noterdaeme, P., Wang, R., McGreer, I., Carithers, B., Bian, F., Miralda-Escudé, J., Finley, H., Pâris, I., Schneider, D. P., Zakamska, N. L., Ge, J., Petitjean, P., & Slosar, A. 2014, ApJ, 793, 139

Cantalupo, S., Arrigoni-Battaia, F., Prochaska, J. X., Hennawi, J. F., & Madau, P. 2014, Nature, 506, 63

Cantalupo, S., Lilly, S. J., & Haehnelt, M. G. 2012, MNRAS, 425, 1992

Cantalupo, S., Porciani, C., Lilly, S. J., & Miniati, F. 2005, ApJ, 628, 61

Chen, H.-W., Helsby, J. E., Gauthier, J.-R., Shectman, S. A., Thompson, I. B., & Tinker, J. L. 2010, ApJ, 714, 1521

Churchill, C. W., Kacprzak, G. G., Steidel, C. C., Spitler, L. R., Holtzman, J., Nielsen, N. M., & Trujillo-Gomez, S. 2012, ApJ, 760, 68

Conroy, C., Graves, G. J., & van Dokkum, P. G. 2014, ApJ, 780, 33

Cooke, R. J., Pettini, M., Jorgenson, R. A., Murphy, M. T., & Steidel, C. C. 2014, ApJ, 781, 31

Cooksey, K. L., Kao, M. M., Simcoe, R. A., O'Meara, J. M., & Prochaska, J. X. 2013, The Astrophysical Journal, 763, 37

Crighton, N. H. M., Bielby, R., Shanks, T., Infante, L., Bornancini, C. G., Bouché, N., Lambas, D. G., Lowenthal, J. D., Minniti, D., Morris, S. L., Padilla, N., Péroux, C., Petitjean, P., Theuns, T., Tummuangpak, P., Weilbacher, P. M., Wisotzki, L., & Worseck, G. 2011, MNRAS, 414, 28

Crighton, N. H. M., Hennawi, J. F., & Prochaska, J. X. 2013, ApJ, 776, L18

Crighton, N. H. M., Hennawi, J. F., Simcoe, R. A., Cooksey, K. L., Murphy, M. T., Fumagalli, M., Prochaska, J. X., & Shanks, T. 2015, MNRAS, 446, 18

Croft, R. A. C. 2004, ApJ, 610, 642

Dey, A., Bian, C., Soifer, B. T., Brand, K., Brown, M. J. I., Chaffee, F. H., Le Floc'h, E., Hill, G., Houck, J. R., Jannuzi, B. T., Rieke, M., Weedman, D., Brodwin, M., & Eisenhardt, P. 2005, ApJ, 629, 654

D'Odorico, V., Bruscoli, M., Saitta, F., Fontanot, F., Viel, M., Cristiani, S., & Monaco, P. 2008, MNRAS, 389, 1727

D'Odorico, V., Cristiani, S., Romano, D., Granato, G. L., & Danese, L. 2004, MNRAS, 351, 976

Eftekharzadeh, S., Myers, A. D., White, M., Weinberg, D. H., Schneider, D. P., Shen, Y., Font-Ribera, A., Ross, N. P., Paris, I., & Streblyanska, A. 2015, MNRAS, 453, 2779

Elias, J. H., Joyce, R. R., Liang, M., Muller, G. P., Hileman, E. A., & George, J. R. 2006, in Presented at the Society of Photo-Optical Instrumentation Engineers (SPIE) Conference, Vol. 6269, Ground-based and Airborne Instrumentation for Astronomy. Edited by McLean, Ian S.; Iye, Masanori. Proceedings of the SPIE, Volume 6269, pp. 62694C (2006).

Erb, D. K. 2008, ApJ, 674, 151

Fabian, A. C. 2012, ARA&A, 50, 455

Farina, E. P., Falomo, R., Decarli, R., Treves, A., & Kotilainen, J. K. 2013, MNRAS, 429, 1267

Farina, E. P., Falomo, R., Scarpa, R., Decarli, R., Treves, A., & Kotilainen, J. K. 2014, MNRAS, 441, 886

Faucher-Giguère, C.-A., Feldmann, R., Quataert, E., Kereš, D., Hopkins, P. F., & Murray, N. 2016, MNRAS, 461, L32

Faucher-Giguère, C.-A., Hopkins, P. F., Kereš, D., Muratov, A. L., Quataert, E., & Murray, N. 2015, MNRAS, 449, 987

Faucher-Giguère, C.-A., Kereš, D., Dijkstra, M., Hernquist, L., & Zaldarriaga, M. 2010, ApJ, 725, 633

Faucher-Giguère, C.-A., Lidz, A., Hernquist, L., & Zaldarriaga, M. 2008, ApJ, 688, 85

Faucher-Giguère, C.-A., & Quataert, E. 2012, MNRAS, 425, 605

Ferland, G. J., Porter, R. L., van Hoof, P. A. M., Williams, R. J. R., Abel, N. P., Lykins, M. L., Shaw, G., Henney, W. J., & Stancil, P. C. 2013, RMxAA, 49, 137

Finley, H., Petitjean, P., Pâris, I., Noterdaeme, P., Brinkmann, J., Myers, A. D., Ross, N. P., Schneider, D. P., Bizyaev, D., Brewington, H., Ebelke, G., Malanushenko, E., Malanushenko, V., Oravetz, D., Pan, K., Simmons, A., & Snedden, S. 2013, A&A, 558, A111

Fox, A. J., Prochaska, J. X., Ledoux, C., Petitjean, P., Wolfe, A. M., & Srianand, R. 2009, A&A, 503, 731

Fu, H., Hennawi, J. F., Prochaska, J. X., Mutel, R., Casey, C., Cooray, A., Kereš, D., Zhang, Z.-Y., Clements, D., Isbell, J., Lang, C., McGinnis, D., Michałowski, M. J., Mooley, K., Perley, D., Stockton, A., & Thompson, D. 2016, ApJ, 832, 52

Fu, H., Isbell, J., Casey, C. M., Cooray, A., Prochaska, J. X., Scoville, N., & Stockton, A. 2017, ArXiv e-prints

Fu, H., & Stockton, A. 2007, ApJ, 666, 794

—. 2009, ApJ, 690, 953

Fumagalli, M., Hennawi, J. F., Prochaska, J. X., Kasen, D., Dekel, A., Ceverino, D., & Primack, J. 2014, ApJ, 780, 74

Fumagalli, M., Prochaska, J. X., Kasen, D., Dekel, A., Ceverino, D., & Primack, J. R. 2011, MNRAS, 418, 1796

Gabor, J. M., & Bournaud, F. 2014, MNRAS, 441, 1615

Gabor, J. M., Davé, R., Oppenheimer, B. D., & Finlator, K. 2011, MNRAS, 417, 2676

Gauthier, J.-R. 2013, MNRAS, 432, 1444

Gonçalves, T. S., Steidel, C. C., & Pettini, M. 2008, ApJ, 676, 816

Haardt, F., & Madau, P. 2012, ApJ, 746, 125

Haiman, Z., & Hui, L. 2001, ApJ, 547, 27

Hamann, F. 1998, ApJ, 500, 798

Heckman, T. M., & Best, P. N. 2014, ARA&A, 52, 589

Hennawi, J. F., Myers, A. D., Shen, Y., Strauss, M. A., Djorgovski, S. G., Fan, X., Glikman, E., Mahabal, A., Martin, C. L., Richards, G. T., Schneider, D. P., & Shankar, F. 2010, ApJ, 719, 1672

Hennawi, J. F., & Prochaska, J. X. 2007, ApJ, 655, 735

—. 2013, ApJ, 766, 58

Hennawi, J. F., Prochaska, J. X., Burles, S., Strauss, M. A., Richards, G. T., Schlegel, D. J., Fan, X., Schneider, D. P., Zakamska, N. L., Oguri, M., Gunn, J. E., Lupton, R. H., & Brinkmann, J. 2006a, ApJ, 651, 61

Hennawi, J. F., Prochaska, J. X., Cantalupo, S., & Arrigoni-Battaia, F. 2015, Science, 348, 779

Hennawi, J. F., Prochaska, J. X., Kollmeier, J., & Zheng, Z. 2009, ApJ, 693, L49

Hennawi, J. F., Strauss, M. A., Oguri, M., Inada, N., Richards, G. T., Pindor, B., Schneider, D. P., Becker, R. H., Gregg, M. D., Hall, P. B., Johnston, D. E., Fan, X., Burles, S., Schlegel, D. J., Gunn, J. E., Lupton, R. H., Bahcall, N. A., Brunner, R. J., & Brinkmann, J. 2006b, AJ, 131, 1

Henry, R. B. C., Edmunds, M. G., & Köppen, J. 2000, ApJ, 541, 660

Hewett, P. C., & Wild, V. 2010, MNRAS, 405, 2302

Ho, S. H., Martin, C. L., Kacprzak, G. G., & Churchill, C. W. 2017, ApJ, 835, 267

Hodapp, K. W., Jensen, J. B., Irwin, E. M., Yamada, H., Chung, R., Fletcher, K., Robertson, L., Hora, J. L., Simons, D. A., Mays, W., Nolan, R., Bec, M., Merrill, M., & Fowler, A. M. 2003, PASP, 115, 1388

Hopkins, P. F., Cox, T. J., Kereš, D., & Hernquist, L. 2008, ApJS, 175, 390

Hopkins, P. F., Hernquist, L., Martini, P., Cox, T. J., Robertson, B., Di Matteo, T., & Springel, V. 2005, ApJ, 625, L71

Humphrey, A., Villar-Martín, M., Fosbury, R., Binette, L., Vernet, J., De Breuck, C., & di Serego Alighieri, S. 2007, MNRAS, 375, 705

Jakobsen, P., Jansen, R. A., Wagner, S., & Reimers, D. 2003, A&A, 397, 891

Johnson, S. D., Chen, H.-W., & Mulchaey, J. S. 2015, MNRAS, 452, 2553

Jones, A., Noll, S., Kausch, W., Szyszka, C., & Kimeswenger, S. 2013, A&A, 560, A91

Keel, W. C., Lintott, C. J., Maksym, W. P., Bennert, V. N., Chojnowski, S. D., Moiseev, A., Smirnova, A., Schawinski, K., Sartori, L. F., Urry, C. M., Pancoast, A., Schirmer, M., Scott, B., Showley, C., & Flatland, K. 2017, ApJ, 835, 256

Keel, W. C., Maksym, W. P., Bennert, V. N., Lintott, C. J., Chojnowski, S. D., Moiseev, A., Smirnova, A., Schawinski, K., Urry, C. M., Evans, D. A., Pancoast, A., Scott, B., Showley, C., & Flatland, K. 2015, AJ, 149, 155

Kereš, D., Katz, N., Fardal, M., Davé, R., & Weinberg, D. H. 2009, MNRAS, 395, 160

Kereš, D., Katz, N., Weinberg, D. H., & Davé, R. 2005, MNRAS, 363, 2

Kimm, T., Somerville, R. S., Yi, S. K., van den Bosch, F. C., Salim, S., Fontanot, F., Monaco, P., Mo, H., Pasquali, A., Rich, R. M., & Yang, X. 2009, MNRAS, 394, 1131

Kirkman, D., & Tytler, D. 1997, ApJ, 484, 672

—. 2008, MNRAS, 391, 1457

Konami, S., Matsushita, K., Nagino, R., & Tamagawa, T. 2014, ApJ, 783, 8

Kormendy, J., & Ho, L. C. 2013, ARA&A, 51, 511

Kormendy, J., & Richstone, D. 1995, ARA&A, 33, 581

Kravtsov, A. V., & Borgani, S. 2012, ARA&A, 50, 353

Lan, T.-W., Ménard, B., & Zhu, G. 2015, MNRAS, 452, 3629

Lanzetta, K. M., Bowen, D. V., Tytler, D., & Webb, J. K. 1995, ApJ, 442, 538

Lau, M. W., Prochaska, J. X., & Hennawi, J. F. 2016, ApJS, 226, 25

Lee, K.-G., Suzuki, N., & Spergel, D. N. 2012, AJ, 143, 51

Loewenstein, M., & Davis, D. S. 2010, ApJ, 716, 384

—. 2012, ApJ, 757, 121

Lu, Y., Mo, H. J., Katz, N., & Weinberg, M. D. 2012, MNRAS, 421, 1779

Markwardt, C. B. 2009, in Astronomical Society of the Pacific Conference Series, Vol. 411, Astronomical Data Analysis Software and Systems XVIII, ed. D. A. Bohlender, D. Durand, & P. Dowler, 251

Martin, C. L. 2005, ApJ, 621, 227

Martin, D. C., Chang, D., Matuszewski, M., Morrissey, P., Rahman, S., Moore, A., & Steidel, C. C. 2014, ApJ, 786, 106

Martini, P. 2004, Coevolution of Black Holes and Galaxies, 169

Martini, P., & Weinberg, D. H. 2001, ApJ, 547, 12

Matteucci, F. 1994, A&A, 288, 57

McLean, I. S., Becklin, E. E., Bendiksen, O., Brims, G., Canfield, J., Figer, D. F., Graham, J. R., Hare, J., Lacayanga, F., Larkin, J. E., Larson, S. B., Levenson, N., Magnone, N., Teplitz, H., & Wong, W. 1998, in Society of Photo-Optical Instrumentation Engineers (SPIE) Conference Series, Vol. 3354, Infrared Astronomical Instrumentation, ed. A. M. Fowler, 566–578

Meiksin, A., Bolton, J. S., & Tittley, E. R. 2015, MNRAS, 453, 899

Misawa, T., Charlton, J. C., Eracleous, M., Ganguly, R., Tytler, D., Kirkman, D., Suzuki, N., & Lubin, D. 2007, ApJS, 171, 1

Moehler, S., Modigliani, A., Freudling, W., Giammichele, N., Gianninas, A., Gonneau, A., Kausch, W., Lançon, A., Noll, S., Rauch, T., & Vinther, J. 2014, A&A, 568, A9

Mushotzky, R., Loewenstein, M., Arnaud, K. A., Tamura, T., Fukazawa, Y., Matsushita, K., Kikuchi, K., & Hatsukade, I. 1996, ApJ, 466, 686

Muzahid, S., Kacprzak, G. G., Churchill, C. W., Charlton, J. C., Nielsen, N. M., Mathes, N. L., & Trujillo-Gomez, S. 2015, ApJ, 811, 132

Navarro, J. F., Frenk, C. S., & White, S. D. M. 1997, ApJ, 490, 493

Neeleman, M., Wolfe, A. M., Prochaska, J. X., & Rafelski, M. 2013, ApJ, 769, 54

Noll, S., Kausch, W., Barden, M., Jones, A. M., Szyszka, C., Kimeswenger, S., & Vinther, J. 2012, A&A, 543, A92

Nomoto, K., Tominaga, N., Umeda, H., Kobayashi, C., & Maeda, K. 2006, Nuclear Physics A, 777, 424

Oosterloo, T., Fraternali, F., & Sancisi, R. 2007, AJ, 134, 1019

Oosterloo, T., & van Gorkom, J. 2005, A&A, 437, L19

Oppenheimer, B. D., & Schaye, J. 2013, MNRAS, 434, 1063

Pâris, I., Petitjean, P., Ross, N. P., Myers, A. D., Aubourg, É., Streblyanska, A., Bailey, S., Armengaud, É., Palanque-Delabrouille, N., Yèche, C., Hamann, F., Strauss, M. A., Albareti, F. D., Bovy, J., Bizyaev, D., Niel Brandt, W., Brusa, M., Buchner, J., Comparat, J., Croft, R. A. C., Dwelly, T., Fan, X., Font-Ribera, A., Ge, J., Georgakakis, A., Hall, P. B., Jiang, L., Kinemuchi, K., Malanushenko, E., Malanushenko, V., McMahon, R. G., Menzel, M.-L., Merloni, A., Nandra, K., Noterdaeme, P., Oravetz, D., Pan, K., Pieri, M. M., Prada, F., Salvato, M., Schlegel, D. J., Schneider, D. P., Simmons, A., Viel, M., Weinberg, D. H., & Zhu, L. 2017, A&A, 597, A79

Peeples, M. S., Werk, J. K., Tumlinson, J., Oppenheimer, B. D., Prochaska, J. X., Katz, N., & Weinberg, D. H. 2014, ApJ, 786, 54

Porciani, C., Magliocchetti, M., & Norberg, P. 2004, MNRAS, 355, 1010

Poznanski, D., Prochaska, J. X., & Bloom, J. S. 2012, MNRAS, 426, 1465

Prochaska, J. X. 1999, ApJ, 511, L71

Prochaska, J. X., Chen, H.-W., & Bloom, J. S. 2006, ApJ, 648, 95

Prochaska, J. X., & Hennawi, J. F. 2009, ApJ, 690, 1558

Prochaska, J. X., Hennawi, J. F., Lee, K.-G., Cantalupo, S., Bovy, J., Djorgovski, S. G., Ellison, S. L., Lau, M. W., Martin, C. L., Myers, A., Rubin, K. H. R., & Simcoe, R. A. 2013a, ApJ, 776, 136

Prochaska, J. X., Hennawi, J. F., & Simcoe, R. A. 2013b, ApJ, 762, L19

Prochaska, J. X., Lau, M. W., & Hennawi, J. F. 2014, ApJ, 796, 140

Prochaska, J. X., O'Meara, J. M., Fumagalli, M., Bernstein, R. A., & Burles, S. M. 2015, ApJS, 221, 2

Prochaska, J. X., Weiner, B., Chen, H.-W., Mulchaey, J., & Cooksey, K. 2011, ApJ, 740, 91

Prochaska, J. X., & Wolfe, A. M. 1997, ApJ, 487, 73

Rahmati, A., Schaye, J., Bower, R. G., Crain, R. A., Furlong, M., Schaller, M., & Theuns, T. 2015, MNRAS, 452, 2034

Rakic, O., Schaye, J., Steidel, C. C., & Rudie, G. C. 2012, ApJ, 751, 94

Richards, G. T., Vanden Berk, D. E., Reichard, T. A., Hall, P. B., Schneider, D. P., SubbaRao, M., Thakar, A. R., & York, D. G. 2002, AJ, 124, 1

Rodríguez-Torres, S. A., Comparat, J., Prada, F., Yepes, G., Burtin, E., Zarrouk, P., Laurent, P., Hahn, C., Behroozi, P., Klypin, A., Ross, A., Tojeiro, R., & Zhao, G.-B. 2017, MNRAS, 468, 728

Roos, O., Juneau, S., Bournaud, F., & Gabor, J. M. 2015, ApJ, 800, 19

Rosario, D. J., Trakhtenbrot, B., Lutz, D., Netzer, H., Trump, J. R., Silverman, J. D., Schramm, M., Lusso, E., Berta, S., Bongiorno, A., Brusa, M., Förster-Schreiber, N. M., Genzel, R., Lilly, S., Magnelli, B., Mainieri, V., Maiolino, R., Merloni, A., Mignoli, M., Nordon, R., Popesso, P., Salvato, M., Santini, P., Tacconi, L. J., & Zamorani, G. 2013, A&A, 560, A72

Rosdahl, J., & Blaizot, J. 2012, MNRAS, 423, 344

Rubin, K. H. R., Prochaska, J. X., Koo, D. C., Phillips, A. C., Martin, C. L., & Winstrom, L. O. 2014, ApJ, 794, 156

Rubin, K. H. R., Weiner, B. J., Koo, D. C., Martin, C. L., Prochaska, J. X., Coil, A. L., & Newman, J. A. 2010, ApJ, 719, 1503

Rudie, G. C., Newman, A. B., & Murphy, M. T. 2017, ApJ, 843, 98

Rudie, G. C., Steidel, C. C., Trainor, R. F., Rakic, O., Bogosavljević, M., Pettini, M., Reddy, N., Shapley, A. E., Erb, D. K., & Law, D. R. 2012, ApJ, 750, 67

Rupke, D. S., Veilleux, S., & Sanders, D. B. 2005, ApJS, 160, 115

Sargent, W. L. W., Young, P. J., Boksenberg, A., Carswell, R. F., & Whelan, J. A. J. 1979, ApJ, 230, 49

Sato, K., Yamasaki, N. Y., Ishida, M., Ishisaki, Y., Ohashi, T., Kawahara, H., Kitaguchi, T., Kawaharada, M., Kokubun, M., Makishima, K., Ota, N., Nakazawa, K., Tamura, T., Matsushita, K., Kawano, N., Fukazawa, Y., & Hughes, J. P. 2007, PASJ, 59, 299

Savage, B. D., & Sembach, K. R. 1991, ApJ, 379, 245

Scannapieco, E., & Oh, S. P. 2004, ApJ, 608, 62

Schneider, D. P., Richards, G. T., Hall, P. B., Strauss, M. A., Anderson, S. F., Boroson, T. A., Ross, N. P., Shen, Y., Brandt, W. N., Fan, X., Inada, N., Jester, S., Knapp, G. R., Krawczyk, C. M., Thakar, A. R., Vanden Berk, D. E., Voges, W., Yanny, B., York, D. G., Bahcall, N. A., Bizyaev, D., Blanton, M. R., Brewington, H., Brinkmann, J., Eisenstein, D., Frieman, J. A., Fukugita, M., Gray, J., Gunn, J. E., Hibon, P., Ivezić, Ž., Kent, S. M., Kron, R. G., Lee, M. G., Lupton, R. H., Malanushenko, E., Malanushenko, V., Oravetz, D., Pan, K., Pier, J. R., Price, III, T. N., Saxe, D. H., Schlegel, D. J., Simmons, A., Snedden, S. A., SubbaRao, M. U., Szalay, A. S., & Weinberg, D. H. 2010, AJ, 139, 2360

Shen, S., Madau, P., Guedes, J., Mayer, L., Prochaska, J. X., & Wadsley, J. 2013, ApJ, 765, 89

Shen, Y., Brandt, W. N., Richards, G. T., Denney, K. D., Greene, J. E., Grier, C. J., Ho, L. C., Peterson, B. M., Petitjean, P., Schneider, D. P., Tao, C., & Trump, J. R. 2016a, ApJ, 831, 7

Shen, Y., & Ho, L. C. 2014, Nature, 513, 210

Shen, Y., Horne, K., Grier, C. J., Peterson, B. M., Denney, K. D., Trump, J. R., Sun, M., Brandt, W. N., Kochanek, C. S., Dawson, K. S., Green, P. J., Greene, J. E., Hall, P. B., Ho, L. C., Jiang, L., Kinemuchi, K., McGreer, I. D., Petitjean, P., Richards, G. T., Schneider, D. P., Strauss, M. A., Tao, C., Wood-Vasey, W. M., Zu, Y., Pan, K., Bizyaev, D., Ge, J., Oravetz, D., & Simmons, A. 2016b, ApJ, 818, 30

Shen, Y., Richards, G. T., Strauss, M. A., Hall, P. B., Schneider, D. P., Snedden, S., Bizyaev, D., Brewington, H., Malanushenko, V., Malanushenko, E., Oravetz, D., Pan, K., & Simmons, A. 2011, ApJS, 194, 45

Silva, A. I., & Viegas, S. M. 2002, MNRAS, 329, 135

Simcoe, R. A., Sargent, W. L. W., & Rauch, M. 2002, ApJ, 578, 737

—. 2004, ApJ, 606, 92

Simcoe, R. A., Sargent, W. L. W., Rauch, M., & Becker, G. 2006, ApJ, 637, 648

Simionescu, A., Werner, N., Urban, O., Allen, S. W., Ichinohe, Y., & Zhuravleva, I. 2015, ApJ, 811, L25

Somerville, R. S., & Davé, R. 2015, ARA&A, 53, 51

Steidel, C. C., Erb, D. K., Shapley, A. E., Pettini, M., Reddy, N., Bogosavljević, M., Rudie, G. C., & Rakic, O. 2010, ApJ, 717, 289

Stockton, A., MacKenty, J. W., Hu, E. M., & Kim, T.-S. 2002, ApJ, 572, 735

Sukhbold, T., Ertl, T., Woosley, S. E., Brown, J. M., & Janka, H.-T. 2016, ApJ, 821, 38

Sutherland, R. S., & Dopita, M. A. 1993, ApJS, 88, 253

Thomas, D. 1999, MNRAS, 306, 655

Tinsley, B. M. 1979, ApJ, 229, 1046

Tormen, G., Bouchet, F. R., & White, S. D. M. 1997, MNRAS, 286, 865

Trager, S. C., Faber, S. M., Worthey, G., & González, J. J. 2000, AJ, 120, 165

Tripp, T. M., Meiring, J. D., Prochaska, J. X., Willmer, C. N. A., Howk, J. C., Werk, J. K., Jenkins, E. B., Bowen, D. V., Lehner, N., Sembach, K. R., Thom, C., & Tumlinson, J. 2011, Science, 334, 952

Tripp, T. M., Sembach, K. R., Bowen, D. V., Savage, B. D., Jenkins, E. B., Lehner, N., & Richter, P. 2008, ApJS, 177, 39

Trump, J. R., Hall, P. B., Reichard, T. A., Richards, G. T., Schneider, D. P., Vanden Berk, D. E., Knapp, G. R., Anderson, S. F., Fan, X., Brinkman, J., Kleinman, S. J., & Nitta, A. 2006, ApJS, 165, 1

Tumlinson, J., Thom, C., Werk, J. K., Prochaska, J. X., Tripp, T. M., Katz, N., Davé, R., Oppenheimer, B. D., Meiring, J. D., Ford, A. B., O'Meara, J. M., Peeples, M. S., Sembach, K. R., & Weinberg, D. H. 2013, ApJ, 777, 59

Tumlinson, J., Thom, C., Werk, J. K., Prochaska, J. X., Tripp, T. M., Weinberg, D. H., Peeples, M. S., O'Meara, J. M., Oppenheimer, B. D., Meiring, J. D., Katz, N. S., Davé, R., Ford, A. B., & Sembach, K. R. 2011, Science, 334, 948

Turner, M. L., Schaye, J., Steidel, C. C., Rudie, G. C., & Strom, A. L. 2014, MNRAS, 445, 794

Vernet, J., Dekker, H., D'Odorico, S., Kaper, L., Kjaergaard, P., Hammer, F., Randich, S., Zerbi, F., Groot, P. J., Hjorth, J., Guinouard, I., Navarro, R., Adolfse, T., Albers, P. W., Amans, J.-P., Andersen, J. J., Andersen, M. I., Binetruy, P., Bristow, P., Castillo, R., Chemla, F., Christensen, L., Conconi, P., Conzelmann, R., Dam, J., de Caprio, V., de Ugarte Postigo, A., Delabre, B., di Marcantonio, P., Downing, M., Elswijk, E., Finger, G., Fischer, G., Flores, H., François, P., Goldoni, P., Guglielmi, L., Haigron, R., Hanenburg, H., Hendriks, I., Horrobin, M., Horville, D., Jessen, N. C., Kerber, F., Kern, L., Kiekebusch, M., Kleszcz, P., Klougart, J., Kragt, J., Larsen, H. H., Lizon, J.-L., Lucuix, C., Mainieri, V., Manuputy, R., Martayan, C., Mason, E., Mazzoleni, R., Michaelsen, N., Modigliani, A., Moehler, S., Møller, P., Norup Sørensen, A., Nørregaard, P., Péroux, C., Patat, F., Pena, E., Pragt, J., Reinero, C., Rigal, F., Riva, M., Roelfsema, R., Royer, F., Sacco, G., Santin, P., Schoenmaker, T., Spano, P., Sweers, E., Ter Horst, R., Tintori, M., Tromp, N., van Dael, P., van der Vliet, H., Venema, L., Vidali, M., Vinther, J., Vola, P., Winters, R., Wistisen, D., Wulterkens, G., & Zacchei, A. 2011, A&A, 536, A105

Vikas, S., Wood-Vasey, W. M., Lundgren, B., Ross, N. P., Myers, A. D., AlSayyad, Y., York, D. G., Schneider, D. P., Brinkmann, J., Bizyaev, D., Brewington, H., Ge, J., Malanushenko, E., Malanushenko, V., Muna, D., Oravetz, D., Pan, K., Pâris, I., Petitjean, P., Snedden, S., Shelden, A., Simmons, A., & Weaver, B. A. 2013, ApJ, 768, 38

Weiner, B. J., Coil, A. L., Prochaska, J. X., Newman, J. A., Cooper, M. C., Bundy, K., Conselice, C. J., Dutton, A. A., Faber, S. M., Koo, D. C., Lotz, J. M., Rieke, G. H., & Rubin, K. H. R. 2009, ApJ, 692, 187

Werk, J. K., Prochaska, J. X., Thom, C., Tumlinson, J., Tripp, T. M., O'Meara, J. M., & Peeples, M. S. 2013, ApJS, 204, 17

Werk, J. K., Prochaska, J. X., Tumlinson, J., Peeples, M. S., Tripp, T. M., Fox, A. J., Lehner, N., Thom, C., O'Meara, J. M., Ford, A. B., Bordoloi, R., Katz, N., Tejos, N., Oppenheimer, B. D., Davé, R., & Weinberg, D. H. 2014, ApJ, 792, 8

Weymann, R. J., Morris, S. L., Foltz, C. B., & Hewett, P. C. 1991, ApJ, 373, 23

Whitaker, K. E., Franx, M., Leja, J., van Dokkum, P. G., Henry, A., Skelton, R. E., Fumagalli, M., Momcheva, I. G., Brammer, G. B., Labbé, I., Nelson, E. J., & Rigby, J. R. 2014, ApJ, 795, 104

White, M., Myers, A. D., Ross, N. P., Schlegel, D. J., Hennawi, J. F., Shen, Y., McGreer, I., Strauss, M. A., Bolton, A. S., Bovy, J., Fan, X., Miralda-Escude, J., Palanque-Delabrouille, N., Paris, I., Petitjean, P., Schneider, D. P., Viel, M., Weinberg, D. H., Yeche, C., Zehavi, I., Pan, K., Snedden, S., Bizyaev, D., Brewington, H., Brinkmann, J., Malanushenko, V., Malanushenko, E., Oravetz, D., Simmons, A., Sheldon, A., & Weaver, B. A. 2012, MNRAS, 424, 933

Wild, V., Kauffmann, G., White, S., York, D., Lehnert, M., Heckman, T., Hall, P. B., Khare, P., Lundgren, B., Schneider, D. P., & vanden Berk, D. 2008, MNRAS, 388, 227

Wolfe, A. M., & Prochaska, J. X. 2000, ApJ, 545, 603

Zahedy, F. S., Chen, H.-W., Rauch, M., Wilson, M. L., & Zabludoff, A. 2016, MNRAS, 458, 2423

Zasowski, G., Ménard, B., Bizyaev, D., García-Hernández, D. A., García Pérez, A. E., Hayden, M. R., Holtzman, J., Johnson, J. A., Kinemuchi, K., Majewski, S. R., Nidever, D. L., Shetrone, M., & Wilson, J. C. 2015, ApJ, 798, 35